Current and noise properties of interacting nanojunctions

Dissertation zur Erlangung des Doktorgrades der Naturwissenschaften (Dr. rer. nat.) der Fakultät für Physik der Universität Regensburg

vorgelegt von

Michael Niklas

aus Deggendorf

im Jahr 2018

Die Arbeit wurde angeleitet von: Prof. Dr. Milena Grifoni

Termin Promotionskolloquium: 27.04.2018

Prüfungsausschuss:

Vorsitzender:	Prof. Dr. Christoph Strunk
Erstgutachter:	Prof. Dr. Milena Grifoni
Zweitgutachter:	Dr. Sigmund Kohler
Weiterer Prüfer:	PD Dr. Falk Bruckmann

For science

Acknowledgements

At this point I would like to acknowledge everyone supporting me during my PhD and even making it possible in the first place.

First of all I would like to thank Milena Grifoni for introducing me into the field of condensed matter physics already during my Bachelor's thesis. Its topics are still fascinating and challenging after so many years. Thank you very much for welcoming me in your group of wonderful people and guiding me patiently through all my problems. I really enjoyed working at your chair with its wonderful atmosphere.

A special thanks goes to Andrea Donarini for answering all my "5 minutes" questions and helping me endless hours with models and numerics. Your insight and intuition in physics is what advanced large parts of the work.

Furthermore I want to thank Sigmund Kohler and his colleagues for teaching me the ways of full counting statistics during my stay in Madrid. I also enjoyed the after-work hours even though we will probably always stay opponents in football.

Thanks to all my colleagues in Regensburg: Magdalena Margańska, Paul Wenk, Ivan Dmitriev, Heng Wang, Michael Kammermeier, Felix Weiner, Matthias Stosiek, María Camarasa Gomez, Martin Wackerl, Patrick Grössing, Nico Leumer, Sebastian Pfaller, Sonja Predin, Sergey Smirnov, Benjamin Siegert, Davide Mantelli, Andreas Trottmann, Wataru Izumida and especially my two office mates Lars Milz and Daniel Hernangomez Perez.

I think our sysadmin group made a perfect team. A cheer to Felix Weiner, Raphael Kozlovsky, Josef Rammensee, Jacob Fuchs and Tobias Frank. May the cluster always run.

Without the help of Sylvia Hrdina, Claudia Zange and Robert Hrdina nobody can survive in the bureaucracy of the university, thank you.

My sincere thanks to the groups of Jean-Pierre Cleuziou from Grenoble and Christoph Strunk from Regensburg for providing our group with amazing

experiments to analyze. In particular I would like to thank Ngoc-Viet Nguyen, Wolfgang Wernsdorfer, Michael Schafberger and Nicola Paradiso.

Financial support by the Deutsche Forschungsgemeinschaft via SFB 689 and GRK 1570 as well as by the Elitenetzwerk Bayern via their international doctorate program "Topological Insulators" is acknowledged.

In particular I want to thank my wonderful girlfriend Mónica for encouraging and pushing me the whole time. Without physics I would have never found you. I love you!

Last but not least a big thanks to my family. Thanks to my parents I could enjoy the education enabling me to study physics in the first place. Thank you for supporting me the whole time. A big thanks to my brother and sister for sweetening my weekends. Without you all I would not be where I am now.

Table of Contents

List of publications

Part of the work presented in this thesis has given rise to the following publications and preprints:

P.1 *Edge-state blockade of transport in quantum dot arrays.*
M. Benito, M. Niklas, G. Platero, and S. Kohler, Phys. Rev. B **93**, 115432 (2016).

P.2 *Transport, shot noise, and topology in AC-driven dimer arrays.*
M. Niklas, M. Benito, S. Kohler and G. Platero, Nanotechnology **27**, 454002 (2016).

P.3 *Full-counting statistics of time-dependent conductors.*
M. Benito, M. Niklas and S. Kohler, Phys. Rev. B **94**, 195433 (2016).

P.4 *Blocking transport resonances via Kondo many-body entanglement in quantum dots.*
M. Niklas, S. Smirnov, D. Mantelli, M. Margańska, N. Nguyen, W. Wernsdorfer, J. Cleuziou and M. Grifoni, Nat. Commun. **7**, 12442 (2016).

P.5 *Fano stability diagram of a symmetric triple quantum dot.*
M. Niklas, A. Trottmann, A. Donarini and M. Grifoni, Phys. Rev. B **95**, 115133 (2017).

P.6 *Dark states in a carbon nanotube quantum dot.*
A. Donarini, M. Niklas, M. Schafberger, N. Paradiso, C. Strunk and M. Grifoni, arXiv:1804.02234 (2018).

Abstract

Interactions play a major role in condensed matter due to their drastic influence on the many-body physics. This thesis is devoted to understanding their impact on transport problems through quantum mechanical systems using analytical and numerical tools. It comprises two main parts.

First, we derive a quantum master equation to compute the reduced density matrix of the central system. It is based on a superoperator formalism that allows one to work in the weak coupling regime, as well as to define diagrammatic rules that can describe higher order transport. In this first part we deal with carbon nanotube (CNT) based quantum dots, whose high tuneability of the coupling strength with a back gate, allows us to study both, the weak and intermediate coupling regime.

In the latter we find an SU(2) $\otimes$ SU(2) Kondo effect in CNTs due to the presence of spin and valley degrees of freedom. By inspecting magnetotransport measurements we discover that one transition, which however, is present in the weak coupling regime, is suppressed. Further analysis shows that using a pseudospin description of the degrees of freedom, only transitions that flip this pseudospin are allowed, which results in the said blocking. Our results show a robust formation of entangled many-body states with no net pseudospin.

In the weak coupling regime we find evidence for all-electric coherent population trapping in a CNT where the electrons become blocked in a dark state. Their emergence is visible in a distinct current-voltage characteristics with missing current steps and negative differential conductance, which requires a valley (angular momentum) and lead dependent tunneling phase. Coupling to the leads results in precession between the dark and coupled states, lifting the otherwise perfect blockade and creates a smooth current behavior.

The second part examines the statistical properties of open quantum systems. Using the full counting statistics formalism withing the master equation approach allows us to obtain the current variance, called shot noise,

and higher order cumulants. We develop an efficient scheme to compute these cumulants for driven, multisite quantum dots. Interactions can affect the shot noise in two ways. Coulomb repulsion results in sequential tunneling events with little variance and a low shot noise. However, when interactions prevent electrons to leave the system, they can tunnel in bunches resulting in drastically increased shot noise.

We show that the Su-Schrieffer-Heeger model supports topological edge states that block the current. The shot noise can be used to distinguish this topological blockade from a standard blockading situation. The model requires variable hopping parameters in the chain of quantum dots to explore the topological phase transition, which might not be easily achievable in experiments. We propose an AC driving field to effectively tune these hopping parameters and use the shot noise to map out the topological phase diagram as function of the driving field parameters.

Since the shot noise can be used to unravel blocking mechanisms and their electron bunching, we apply the gained knowledge to the case of dark states. This time we find dark states in a symmetric, triangular, triple quantum dot setup, based on local tunneling. In the angular momentum basis these dark states have the same, simple form as in the CNT case, allowing us to find analytic expressions for the current and the shot noise.

Introduction

One of the most fundamental problems of physics in the beginning of the 20^{th} century was the question whether light can be described in terms of particles or as waves. Both aspects have sooner or later been proven to be right. On the one hand, light must behave like waves since it exhibits the Doppler effect as well as interference. The latter was already shown in 1801 by Young [1] in his famous double-slit experiment, sketched in Fig. 1a. The resulting interference pattern on the screen can only be explained by the wave nature of light, cfg. Fig. 1b. On the other hand, ever since the explanation of the photoelectric effect by Einstein [2], it is clear that light must consist of elementary particles, the photons. About this seemingly contradiction Einstein and Infeld [3, p.278] wrote:

> But what is light really? Is it a wave or a shower of photons? There seems no likelihood for forming a consistent description of the phenomena of light by a choice of only one of the two languages. It seems as though we must use sometimes the one theory and sometimes the other, while at times we may use either. We are faced with a new kind of difficulty. We have two contradictory pictures of reality; separately neither of them fully explains the phenomena of light, but together they do.

Actually, this wave-particle duality can be extended to all particles as shown by de Broglie [5] and is nowadays a key concept of quantum mechanics. Performing the double-slit experiment with electrons shows this duality. With a low electron density one observes single spots on the screen, revealing the localized particle nature of the electrons. This is displayed in Figs. 1c,d. Steadily increasing the measuring time unveils their wave nature since the interference pattern appears, as seen in Figs. 1e,f. Such experiments have been repeated for molecules consisting of hundreds of atoms which still show

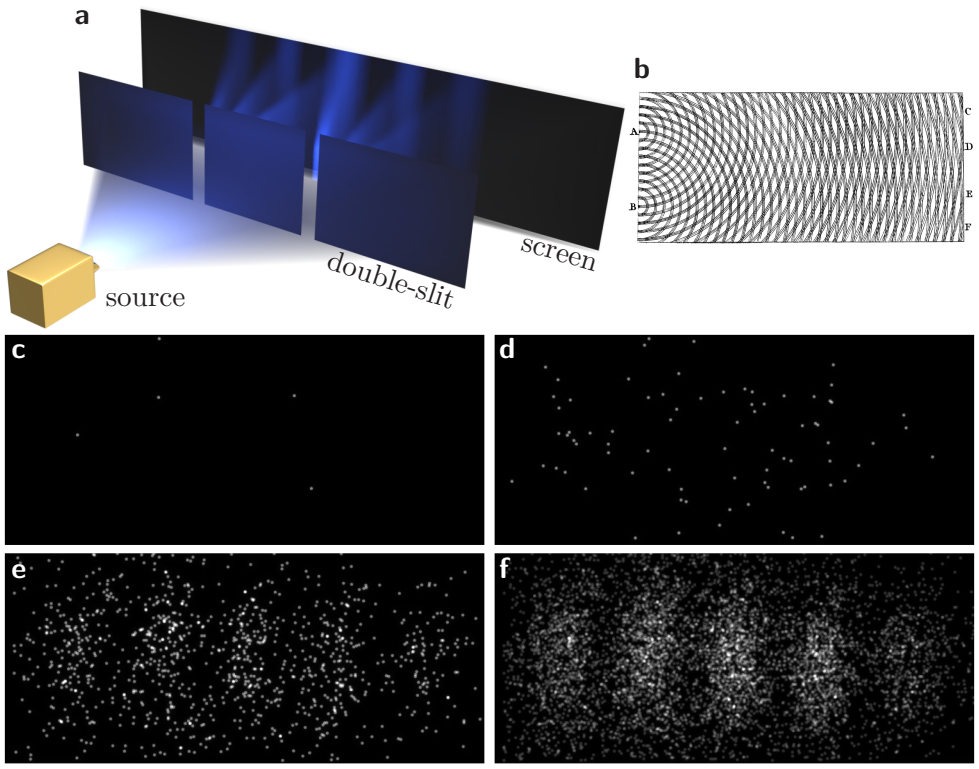

Figure 1: Double slit experiment. **a** Experimental setup. **b** Original drawing by Young [1], showing interference of waves. **c-f** Experimental images from the screen using electrons, for increasing experiment time; from Bach *et al.* [4]. **c,d** The completely random but point-like positions of the electrons highlight their particle nature. **e,f** With more electrons the interference pattern becomes apparent, underlying the wave nature of electrons.

the same results [6]. This allows one to describe the behavior of all mass-full particles by a wave equation [7]

$$i\hbar\frac{\partial}{\partial t}\left|\psi(t)\right\rangle = \hat{H}\left|\psi(t)\right\rangle, \tag{1}$$

the so called Schrödinger equation. This leads to the interesting observation that electrons can move through a barrier that they classically shouldn't be able to move through. The solutions of the Schrödinger equation don't end abruptly at a wall or barrier, they only taper off exponentially quick. Then, if the barrier is thin enough, the electron's wave function is finite on the other side. The process of an electron moving through a barrier in this fashion is called quantum tunneling and is shown in Fig. 2a. The next logical step is to analyze what happens to electrons that pass more intricate junctions, like two consecutive

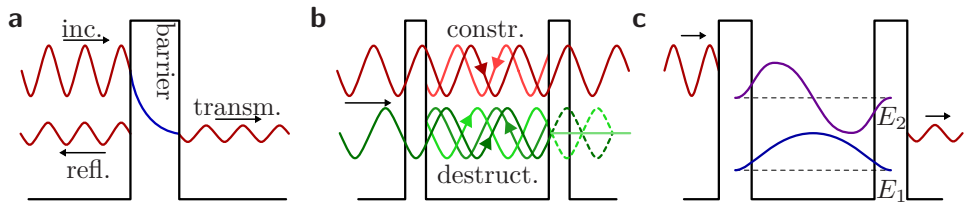

Figure 2: Transmission through junctions. **a** An incident wave splits up into a transmitted and a reflected wave, when hitting a barrier. This results in quantum tunneling. Inside the barrier the wave function decays exponentially quick. **b** Fabry-Pérot interferometer. Depending on the phase difference of the wave passing both barriers and the wave getting reflected twice or more times, these waves interfere constructively or destructively. **c** If the barriers become wide, this situation resembles a quantum well with particle in a box-like states of discrete energy values.

barriers. If these barriers are thin enough, such that a large portion of electrons can tunnel through them, but also a comparative amount gets reflected, this resembles a two-path interference experiment. Such a generalization of the double-slit experiment, is called Fabry-Pérot interferometer, named after its developers [8, 9] and displayed in Fig. 2b. The beam of particles passing through both barriers interferes with the beams that get reflected twice or more times. Whether the two waves interfere constructively or destructively solely depends on their phase difference. The results so far are quite general and work for both, light and electrons.

At this point, the natural question arises whether the same effects are observable for electrons belonging to a solid-state system. In conductors, barriers can be created simply by building heterostructures using layered materials or depletion gates. In principle, this allows to perform Fabry-Pérot experiments in patterned materials. However, electrons can behave fundamentally different than photons since they are fermions and are subject to interaction. In particular, scattering processes, e.g. mediated by phonons, can destroy the phase coherence due to their stochastic nature. Therefore, in order to see any quantum phenomena of electrons, the system's size must be small compared to the phase coherence length. At low temperatures, this allows the construction of devices at scales comparable with the electron's de Broglie wavelength and, accordingly, the observation of quantum interference effects in the solid state. For example, Fabry-Pérot interference with electrons

has been measured in carbon nanotube waveguides [10, 11]. In the limit of thin barriers, or said in other words, in the limit of large tunnel coupling, electron-electron interaction effects have almost no importance. In this regime, Green's functions based methods allow for the description of non-interacting electron transport. As the tunnel coupling becomes weaker, i.e. the barriers become thicker, the situation resembles more and more a quantum well, as seen in Fig. 2c. The electrons get confined in the region between the two barriers and form particle in a box-like states with discretized energy levels. The tunneling through the leads only acts as a weak perturbation in this case. In reality, we deal with three dimensional materials. A patterned device that spatially restricts electrons in all three dimensions, which results in bound states, is called quantum dot. Consequently, the precise geometry and level alignment of the inter-barrier region will increasingly affect the transport properties. The resulting localization of the electrons lets electron-electron interactions become more and more important. For very small sizes this interaction can even become the largest energy scale of the whole setup and separate states of different electron numbers on the quantum dot [12, 13]. In this thesis we deal with transport properties through such interacting nanojunctions. The control of the precise electron number in the quantum dot forms the basis for many realizations of spin or charge qubits [14]. While quantum information processing requires quantum coherence and therefore optimal isolation from the environment, the possibility to couple quantum dots to this environment through the barriers may be useful as well. It not only can be exploited for qubit readout [15], but also allows one to determine the relevant system parameters. Multiple qubits or more sophisticated qubits can be created by using a quantum dot with additional degrees of freedom, like the two valleys in graphene or carbon nanotubes, or simply multiple quantum dots in close proximity.

The particle wave duality will not only lead to quantum interference effects and many-body entanglement but will also influence the statistical properties of electron transport. This can be used to obtain information about the underlying transport processes by measuring e.g. the variance of the current, called shot noise. Compared to the average current, the shot noise reveals whether electrons tunnel avalanche-like or in an equidistant manner. Summarizing in the words of Landauer [16]: "The noise is the signal".

Outline

This thesis splits into two parts, dealing with transport across carbon nanotube (CNT) quantum dots and the noise properties of multiple quantum dot systems, respectively.

Part I The first part starts with an introduction into the physics of transport in quantum dots and we derive a quantum master equation that allows its theoretical description. Using the special electric properties of CNTs, we apply the theory in the intermediate coupling regime, where we find that certain resonances of the Kondo effect become blocked. In the weak coupling regime we encounter dark states as superpositions of degenerate valley states that block the current in a unique way.

Chapter 1. Carbon nanotube quantum dots

In this chapter we introduce the concept of single electron transistors. Following a simple capacitor model, one can distinguish between a Coulomb blockade regime and a transport regime. Only at Coulomb blockade a fixed number of electrons is trapped on the quantum dot, which prevents current flow. Furthermore, we obtain the electrical properties of CNT quantum dots. Starting from the dispersion of graphene and applying boundary conditions, allows us to write a model Hamiltonian using spin and valley quantum numbers.

Chapter 2. Transport theory

To calculate the current through single electron transistors we derive a quantum master equation for the reduced density matrix of the central quantum dot. We use a superoperator approach based on the Nakajima-Zwanzig projector operator formalism. This allows us to describe transport to all orders in a diagrammatic way. We show that in the weak coupling regime it gives the same result as traditional derivations. Additionally, it makes the resummation of certain diagrams possible, which enables us to, at least to some extent, describe strong coupling.

Chapter 3. Blocking Kondo resonances in quantum dots

In CNT quantum dots the coupling strength is tunable via the gate voltage. On the hole side the Kondo effect is dominant in transport. After an introduction to the spin-1/2 Kondo effect, we extend it to the SU(2) $\otimes$ SU(2) Kondo effect in CNTs. This requires an analysis of the symmetries present in the single particle spectrum of a CNT. We find time-reversal like, particle-hole like and chiral symmetries. Magnetospectroscopy experiments reveal that in the

Kondo regime the transitions to states related by particle-hole like symmetry are blocked, despite existing on the electron side in co-tunneling resonances.

Chapter 4. Dark states in a carbon nanotube quantum dot

In CNTs with vanishing spin-orbit coupling and valley mixing, the valley (orbital) degeneracy supports the formation of dark states. We find analytic expressions for these dark states build upon an orbital dependent tunneling phase. Solving a minimal model for only $N = 0 \leftrightarrow 1$ transitions, we find an analytic expression for the current. The resulting $I-V$ characteristics is unique and quantitatively fits the experiment. We give a microscopic justification of the tunneling phase, based on the surface Γ–point approximation.

Part II This part opens with an introduction to the statistical properties of transport and a theoretical framework to calculate it within the master equation approach. We apply this method to identify topological blockading situations in a dimerized chain of quantum dots. We use the noise map to unravel the influence of orbital dark states in a ring of three quantum dots.

Chapter 5. The framework of full counting statistics

In this chapter we describe full counting statistics, a way to compute all current cumulants within the master equation approach of chapter 2. The resulting generalized master equation can be solved iteratively to first compute the current, then the noise, followed by all higher order cumulants. We find a numerically effective way to compute this cumulants for driven systems.

Chapter 6. Topological blockade in a dimer chain

We introduce the key concepts of topology and the Su-Schrieffer-Heeger model. This model can be build as a dimerized chain of quantum dots which supports edge states that can block the current. We analyze certain limits of this topological blockade and find the Fano factor as an efficient indicator to measure the topological phase. An AC driving field renormalizes the hopping amplitudes and, in turn, allows one to control topological phase transitions.

Chapter 7. Dark states in a symmetric triple quantum dot

In the last chapter we analyze the simplest model that supports dark states through orbital degeneracies and at the same time allows one to treat interactions exactly: a C_{3v} symmetric triangular triple quantum dot. We find all its eigenstates in analytic form, which allows us to obtain simple expressions for the dark states, in complete analogy to chapter 4. We find certain fractional values of the Fano factor that can be explained via minimal models.

Part I

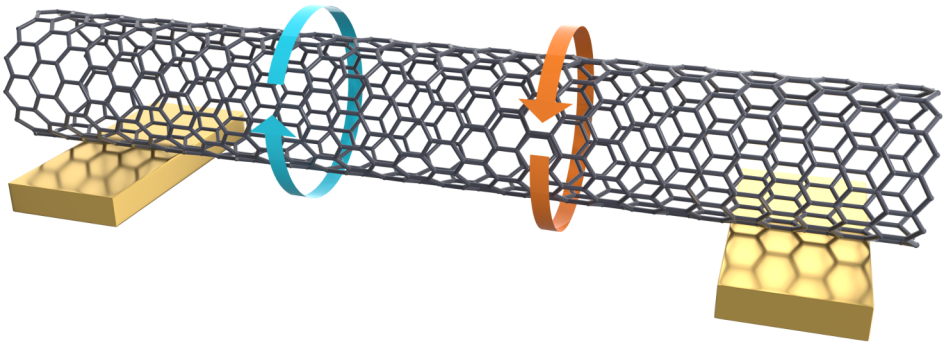

Transport across interacting carbon nanotube quantum dots

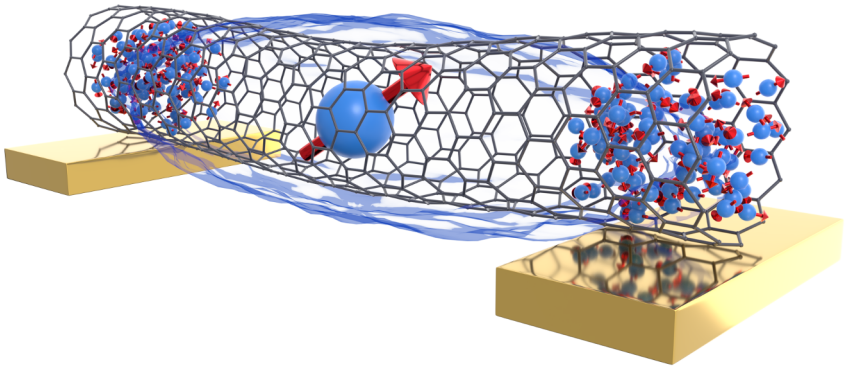

CHAPTER 1

Carbon nanotube quantum dots

The possibility of spatially restricting charge carriers on length scales comparable to their wavelength is at the very heart of mesoscopic condensed matter physics. One of the simplest realizations that takes advantage of the quantum nature of electrons are artificial atoms or quantum dots (QDs), isolated islands which are confined in all three spatial directions. Their electronic properties approximately follow from a simple particle in a box model in which the energies of the bound states depend on the size of the QD. This effect is already extensively used in optics to produce fluorescent light of a single wavelength in a controllable way. Slowly this technology even finds its way into everydays electronics like TVs. Due to the small size, interactions play a dominant role in QDs, most importantly Coulomb interaction. Adding an additional electron to a charged QD requires enough energy to overcome its Coulomb repulsion with the electrons on the dot. These striking electronic properties are also interesting for electronic applications and especially for integrated circuits. Besides from being promising candidates for Qubits used in quantum computers, they allow for a nano scale analogue to a transistor, a so called single electron transistor.

A promising candidate for such QDs are carbon nanotubes (CNTs), in the last decades they were actively studied not only in physics. Their extraordinary mechanical properties, first of all their large stiffness [17], makes them ideal candidates to build lightweight and strong materials. In medicine CNTs

are considered a likely contestant for drug delivery mechanisms [18]. With transparencies ranging from 85% [19] to only 0.01% [20] thin films of CNTs can operate as transparent electronics and prevent stray light in telescopes. We will analyze the structure of bound states in a single CNT-QD and its influence on transport.

1.1 The single-electron transistor

A transistor is a three terminal device where the current through two of these terminals, called source and drain, can be mediated via the third contact, called gate. In classical semiconductor transistors like the metal-oxide-semiconductor field-effect transistor (MOSFET) an applied gate voltage changes the charge carrier density between the source and drain and can create depletion regions which block the current flow. Scaling down MOSFETs presents the semiconductor industry with large problems since the electron number becomes small enough for quantum effects, like losses via tunneling through insulators, to play more and more important roles.

A possible solution to these problems is the implementation of a new generation of transistors that actively takes advantage of the electrons quantum nature. One of them is the so called single-electron transistor (SET) where the gate contact is capacitively coupled to a central QD and allows the control of the precise electron number on the dot up to single electrons via the gate voltage V_g. The source and drain contacts in SETs are typically coupled to the QD via tunneling barriers. A voltage applied between these two terminals is called bias voltage V_b. In Fig. 1.1 a scheme of such a SET is shown where the left (L) and right (R) leads can play the roles of source and drain depending on the bias direction. The gate voltage is often applied via a back gate contact. The behavior of a SET depends strongly on various parameters such that one can identify different transport regimes.

1.1.1 Transport regimes

The transport properties of a SET are mainly influenced by three parameters. First, the charging energy of the QD, U, which originates from the Coulomb repulsion of electrons. Second, the temperature of the environment, T, and third, the coupling strength between the contacts and the QD, usually expressed in tunneling rates Γ. In the limit of strong coupling where $U, k_\mathrm{B}T \ll \hbar\Gamma$, the two

Figure 1.1: Scheme of a single electron transistor. Two large reservoirs, L and R, are tunnel coupled to a central QD. The gate voltage V_g influences the charge on the QD.

interfaces act as semi-transparent mirrors leading to Fabry-Pérot interference. This limit is not part of this thesis but studied e.g. in CNT-QDs in Dirnaichner *et al.* [11]. Decreasing the coupling strength until $k_B T \ll \hbar\Gamma \ll U$, the contact electrons are mostly scattered by an electron in the QD which is known as the Kondo effect. We analyze and further introduce this regime in Sec. 3 at the example of a CNT-QDs. In the weak coupling regime where $\hbar\Gamma \ll k_B T \ll U$, the coupling is so much suppressed that only a single electron tunnels at a time. This so called sequential tunneling can only be extended for slightly stronger coupling strength when higher order processes like co-tunneling play a role. Most parts of this thesis are performed in this limit.

1.1.2 Capacitor model of metallic islands

A first step in understanding the influence of the three terminals on transport properties is the analysis of the classical circuit corresponding to a SET setup. There, the three leads are capacitively coupled to the QD with capacitances C_L, C_R and C_g. In addition, the left and right contact allow for tunneling to the central QD. They are considered as large reservoirs of electrons such that they stay invariant upon adding or removing electrons. Their states are filled up to the Fermi level or electro-chemical potential which are controlled by applying the bias voltage. For simplicity we refer to the electro-chemical potential only as chemical potential in the following. The bias is applied to a certain amount $0 \leq \eta \leq 1$ on the left lead and the rest to the right lead. This results in the chemical potentials $\mu_L = \mu_0 + \eta V_b$ and $\mu_R = \mu_0 + (\eta - 1)V_b$ for the left and right lead, respectively, where for convenience we set $\mu_0 = 0$.

We first consider a simple metallic QD where the electrons do not have any internal degrees of freedom, like spin, and can be added without restrictions. In this quasi classical picture the only quantum effect is the quantized charge on the dot which can be precisely controlled. The induced charge on the QD is then $Q_i = C_\mathrm{g}V_\mathrm{g} + C_\mathrm{L}\eta V_\mathrm{b} + C_\mathrm{R}(\eta - 1)V_\mathrm{b}$. Accounting for a charged QD with N electrons, the total charge is $Q = Q_i + eN$, where e is the negative elementary charge. The energy of the QD is the one of a classical capacitor

$$E_N = \frac{Q^2}{2C} = \frac{(eN + C_\mathrm{g}V_\mathrm{g} + C_\mathrm{L}\eta V_\mathrm{b} + C_\mathrm{R}(\eta - 1)V_\mathrm{b})^2}{2C}, \tag{1.1}$$

with the total capacity of the QD, $C = C_\mathrm{L} + C_\mathrm{R} + C_\mathrm{g}$. The energy required to add an additional electron or to remove one, usually defined as chemical potential, is then given by the energy difference of two consecutive states

$$\mu_N = E_N - E_{N-1} = \frac{e^2}{C}\left(N - \frac{1}{2}\right) + \alpha_\mathrm{g}V_\mathrm{g} + \alpha_\mathrm{L}\eta V_\mathrm{b} + \alpha_\mathrm{R}(\eta - 1)V_\mathrm{b}, \tag{1.2}$$

with the conversion factors $\alpha_x = eC_x/C$.

1.1.3 Coulomb blockade

For simplicity we initially allow only a minimal bias voltage $|eV_\mathrm{b}| \lesssim k_\mathrm{B}T$ to obtain a finite current I or differential conductance $G = \mathrm{d}I/\mathrm{d}V_\mathrm{b}$, for vanishing bias, called linear conductance. The condition to add electrons to the QD is that an electron with larger energy than the chemical potential of the dot is available in the leads, this means $\mu_l \gtrsim \mu_N$, for $l = \mathrm{L}$ or R. At the same time we require this electron to be able to leave to the other lead which requires free states there and therefore $\mu_{\bar{l}} \lesssim \mu_N$. The only way these two conditions can be fulfilled at the same time at almost vanishing bias is that the chemical potential of the QD is in resonance with the chemical potentials of both leads

$$\mu_\mathrm{L} \approx \mu_N \approx \mu_\mathrm{R}. \tag{1.3}$$

This situation is shown in a chemical potential landscape along the SET in Fig. 1.2a. If the chemical potential of the dot is below the lead chemical potentials the QD is filled with N electrons which cannot escape and no current can flow. This situation is called Coulomb blockade and is named after the Coulomb force, ultimately responsible for this effect. A Coulomb blocked SET is shown in Fig. 1.2b. Experimental analysis of this effect is quite easy upon realizing that the chemical potential of the QD in Eq. (1.2) depends

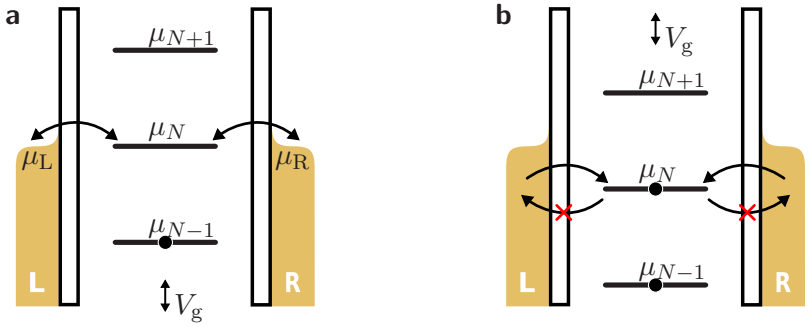

Figure 1.2: Chemical potential landscape of the SET at zero bias. **a** In the resonant case the chemical potential of N electrons μ_N is aligned with the Fermi energy of the two leads. **b** The gate voltage allows to shift the chemical potentials down such that the N-th electron can enter but not leave anymore. The QD is in Coulomb blockade.

linearly on the gate voltage. Therefore, V_g can be used to shift the chemical potential and the linear conductance as a function of V_g should show peaks exactly around the resonance conditions. The distance between two of these peaks is constant and is naturally the difference of two consecutive chemical potentials corrected by the gate conversion factor

$$\alpha_g \Delta V_g = \mu_N - \mu_{N-1} = \frac{e^2}{C} \equiv U, \tag{1.4}$$

also known as charging energy U. These repeated peaks are called Coulomb oscillations. One of the first experimental realizations from 1991 can be seen in Fig. 1.3. Between two peaks the number of electrons on the QD stays constant and increases by one with each peak. Therefore, these regions are also called stable regions. The next step in understanding the transport properties of SETs is to allow for larger bias voltages.

1.1.4 Non-linear transport

The results of Coulomb oscillations can easily be extended to the non-linear transport regime with a finite bias voltage. The plot of the current or differential conductance vs both gate and bias voltage is called (charge) stability diagram. It is best understood by looking at the chemical potential landscape again. The conditions for adding and removing electrons stay unchanged, only now

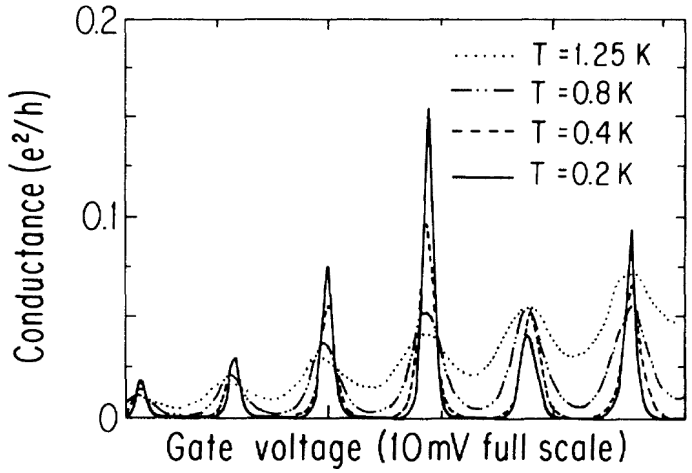

Figure 1.3: Experimental linear conductance as a function of V_g shows Coulomb oscillations in a GaAs-QD at various temperatures. Taken from Meir *et al.* [21].

allow for a larger range of current flow. The combined conditions now read

$$\begin{aligned} \mu_L \geq \mu_N \geq \mu_R \qquad & \text{for} \quad eV_b > 0, \\ \mu_L \leq \mu_N \leq \mu_R \qquad & \text{for} \quad eV_b < 0. \end{aligned} \tag{1.5}$$

As long as no chemical potential of the QD is in the bias window spanned by the two chemical potentials of the leads, the system is in Coulomb blockade. This is illustrated in Fig. 1.4a. As soon as a chemical potential enters this windows there is a peak in the differential conductance and current can flow as shown in Fig. 1.4b for positive chemical potential drop. This leads to a diamond shaped pattern of zero current in the stability diagram as shown in Fig. 1.5a. The current outside of these so called Coulomb diamonds reaches a plateau of constant current which depends on the tunneling rates and only changes once an additional chemical potential enters the bias window. The asymmetric application of the bias voltage on the two contacts with the factor $\eta = 0.4$ causes tilted Coulomb diamonds.

So far the quantum nature of the central QD has been neglected by assuming a metallic character. The inclusion of such quantum mechanical effects apart from quantized charges can have many interesting consequences. The trivial change of the energies for different particle numbers results in Coulomb diamonds of different heights. Degeneracies can influence the current height and special shapes of wave functions can even lead to annihilation of

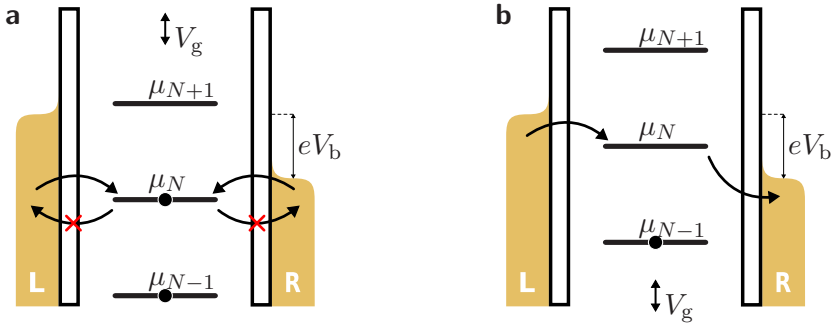

Figure 1.4: Chemical potential landscape of the SET at finite bias. **a** The chemical potential of the dot is lower than both chemical potentials of the contacts leading to Coulomb blockade. **b** Current can flow since a chemical potential of the QD is in the bias window.

tunneling matrix elements with resulting current suppression. The details then strongly depend on the underlying model. In Figs. 1.5b-d various experimental stability diagrams for different types of QDs are shown. All of them feature differently sized Coulomb diamonds. In the experimental stability diagrams additional lines outside the Coulomb diamonds can be seen. These derive from excited states that can change the current once their chemical potential enters the bias window.

1.1.5 Excited states

The next step in analyzing quantum effects in a SET is to look at the influence of excited states. In the simple case that there exists a single excited state with N electrons at an energy $E_N^* > E_N$, one can define two new chemical potentials

$$\begin{aligned} \mu_N^* &= E_N^* - E_{N-1}, \\ \mu_{N+1}^\dagger &= E_{N+1} - E_N^*, \end{aligned} \tag{1.6}$$

which both give rise to additional lines outside the Coulomb diamonds. Inside the Coulomb diamonds the current is still zero since N electrons are already trapped on the QD in the ground state and therefore the excited N-particle state is not available for transport. In Fig. 1.5a the positions of the additional lines due to an excited state with $E_N^* - E_N = \Delta E$ are marked. In the experimental stability diagrams in Figs. 1.5b-d many such excited state lines are visible suggesting complex level structures.

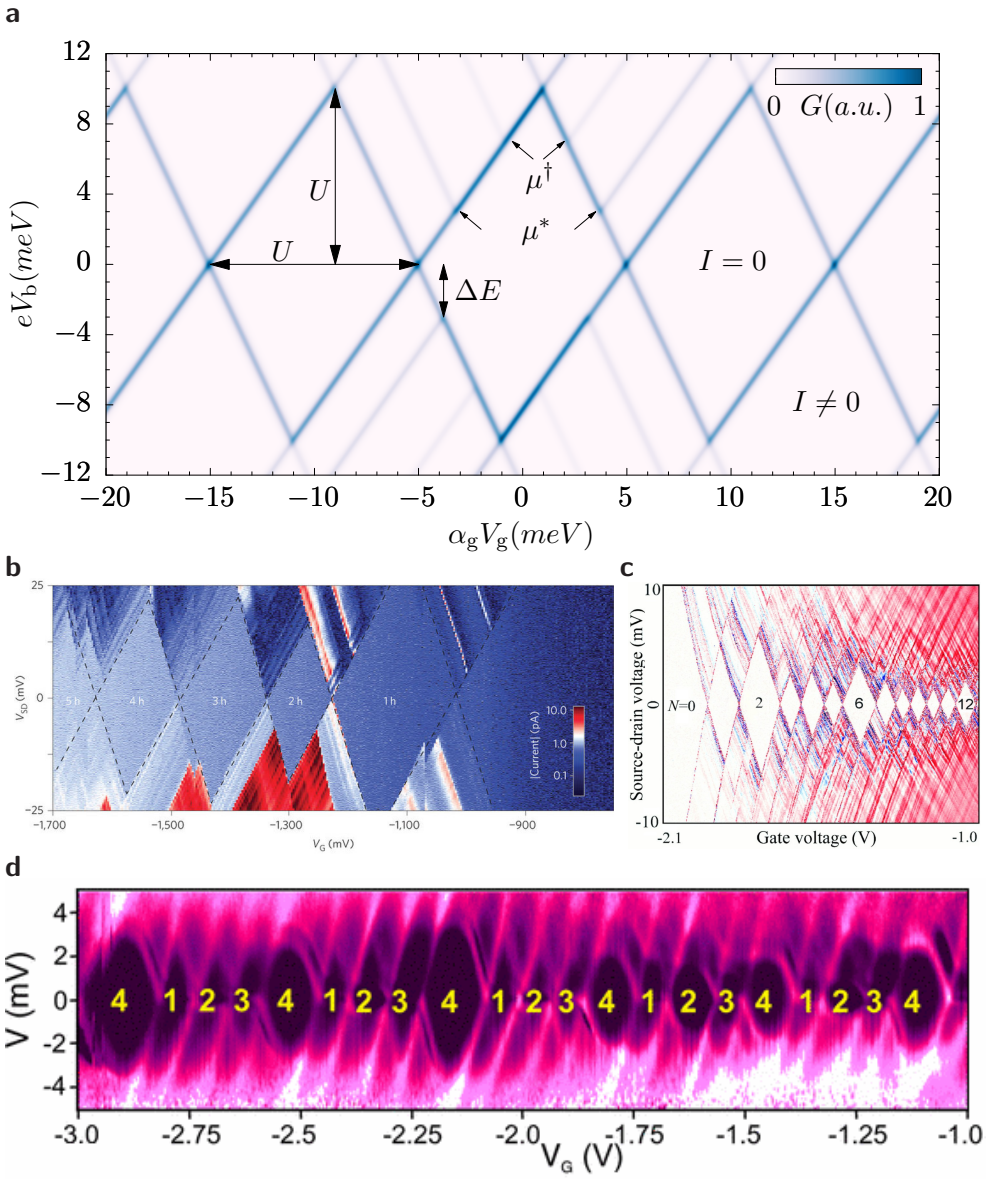

Figure 1.5: **a** Stability diagram of a QD with $U = 10meV$, $k_B T = 0.1meV$ and $\eta = 0.6$. The width and height of the Coulomb diamonds are given by the charging energy U. The central Coulomb diamond features a single excited state with $\Delta E = 3meV$. Its excitation lines are marked by arrows. **b,c,d** Experimental stability diagrams where the central QD is an InSb nanowire in the hole regime (**b**), a GaAs heterostructure (**c**), or a single-walled CNT (**d**). Figures taken from Pribiag *et al.* [22], Kouwenhoven and Oosterkamp [23], Sapmaz *et al.* [24].

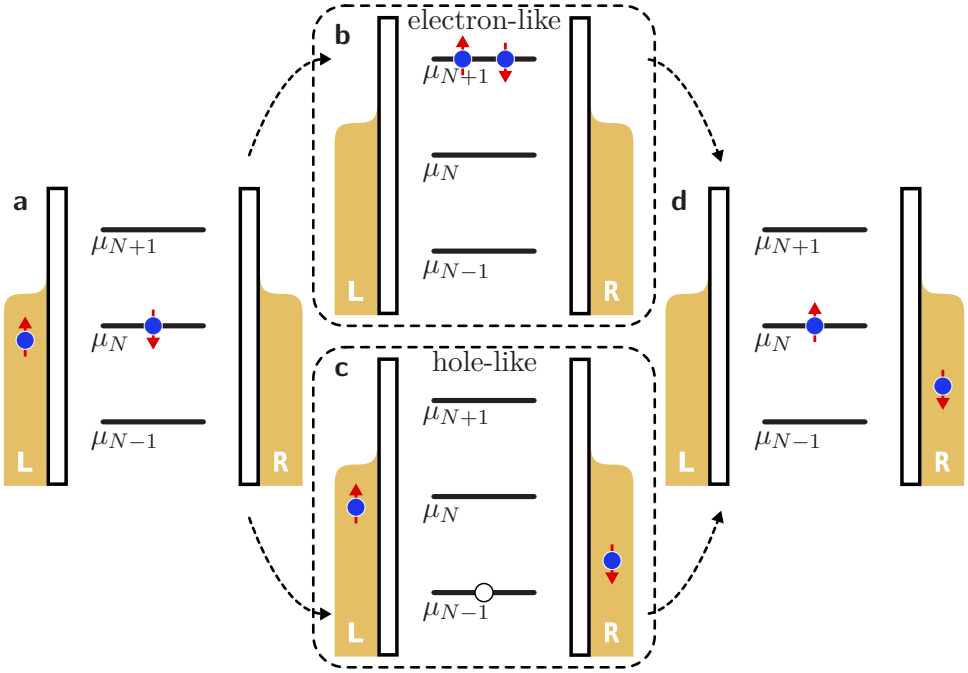

Figure 1.6: Co-tunneling process in a chemical potential landscape. **a** Starting point is N electrons in the QD. **b,c** Virtual transition state for electron-like (**b**) and hole-like (**c**) processes that temporarily violate energy conservation. **d** After the second electron tunnels the total energy of the co-tunneling process is conserved.

If the tunneling rates are not too small, higher order effects can play a role that extend the picture of sequentially tunneling electrons.

1.1.6 Co-tunneling

The next leading order correction of contributions from tunneling between the leads and the QD includes all mechanisms of fourth order in the tunneling Hamiltonian $\mathcal{O}(\hat{H}^4_{\text{tun}})$ (or analogously second order in the tunneling rate $\mathcal{O}(\Gamma^2)$) and therefore contains all processes where two electrons tunnel at the same time. This gives rise to so called *pair tunneling* which describes two electrons tunneling simultaneously from a lead onto the QD or reverse. These processes occur when the chemical potential of a lead matches the average of two subsequent charging energies, so exactly in the middle of two sequential tunneling lines [25]. The second possibility of second order processes is *co-tunneling* where again two electrons tunnel simultaneously but one starts in a lead while the

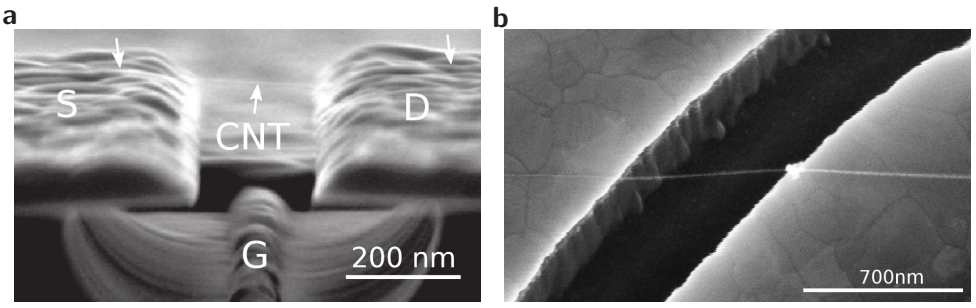

Figure 1.7: Scanning electron microscopy images of ultra-clean, suspended CNT-QD devices. Figures originate from **a** Grenoble [P.4] and **b** from Regensburg [26].

other one starts in the QD. Such tunneling events can be interpreted as two entangled tunneling events connected by a virtual state. Depending on which electron tunnels first, this virtual state can be either electron-like or hole-like. If the final state of the QD electron has the same energy as the initial one, such a process is called *elastic co-tunneling*, which is displayed in Fig. 1.6. The intermediate states are called virtual since they would violate the conservation of energy even though the total process conserves the energy. Since such processes are always possible, independent of the bias and gate voltage, this leads to a finite differential conductance inside the Coulomb diamonds. If excited state exist in the system it is possible to see *inelastic co-tunneling* which occurs if the final and initial state have different energies. This creates an additional step in the differential conductance inside the Coulomb diamond at the bias voltage that matches the level splitting of the excited state, i.e. exactly at the position where the excited state sequential tunneling line enters the Coulomb diamond.

1.2 Electronic properties of carbon nanotube quantum dots

Fullerenes are molecules of carbon, typically in a hollow form and often with high symmetry. Next to spheric molecules like C_{60}, often called buckyballs, cylindrical fullerenes are called carbon nanotubes (CNTs). They are ideal candidates for QDs since the charge carriers in CNTs are already confined in two dimensions such that contacting a tube on both ends automatically creates a QD. In Fig. 1.7 two such devices are shown where the CNT was

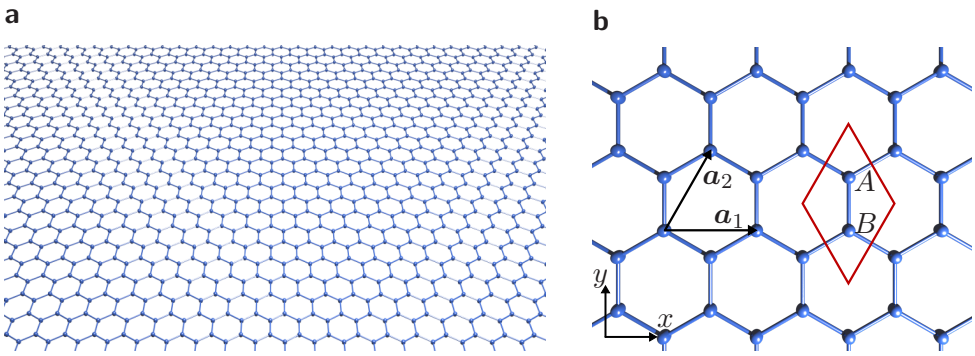

Figure 1.8: **a** A single layer of graphene is a honeycomb lattice of carbon atoms. **b** The unit cell of graphene consists of two sublattices, A and B and is marked in red. The lattice is created by repeating this unit cell with the lattice vector $\boldsymbol{a}_1$ and $\boldsymbol{a}_2$.

grown as last fabrication step over the predefined, litographically fabricated contacts which creates ultra-clean, suspended CNT-QDs. The atomic structure of CNTs is similar to graphene, a two-dimensional sheet of linked hexagonal rings. Therefore, it is quite natural to consider CNTs as rolled up graphene to derive their electronic properties.

1.2.1 Graphene

The honeycomb lattice of graphene is shown in Fig. 1.8a. It is spanned by duplicating the unit cell over and over shifted by multiples of the translational vectors $\boldsymbol{a}_{1/2}$. This unit cell consists of a two atom sublattice $p = A, B$. This is illustrated in Fig. 1.8b. Fourier transforming the graphene lattice into reciprocal space results in a hexagonal first Brillouin zone whose edges are called Fermi points. There are only two geometrical independent Fermi points labeled K and K', as shown in Fig. 1.9a. The tight binding Hamiltonian with nearest neighbor hopping between the p_z orbitals is written in sublattice basis, where it reads

$$\mathcal{H}_0 = \begin{pmatrix} 0 & \gamma(\boldsymbol{k}) \\ \gamma^*(\boldsymbol{k}) & 0 \end{pmatrix}, \tag{1.7}$$

with $\gamma(\boldsymbol{k}) = \langle A|\mathcal{H}_0|B\rangle = t(1+e^{i\boldsymbol{k}\boldsymbol{a_1}}+e^{i\boldsymbol{k}\boldsymbol{a_2}}) = t(1+e^{i\sqrt{3}k_x a_C}+e^{i(\sqrt{3}k_x+3k_y)a_C/2})$. Here, a_C is the atomic bond length and t the hopping integral. The emerging dispersion relation with a valence and a conduction band $E(\boldsymbol{k}) = \pm|\gamma(\boldsymbol{k})|$ is shown in Fig. 1.9b. Starting from this two dimensional band structure one can obtain the one dimensional bands of CNTs by rolling up a stripe of graphene.

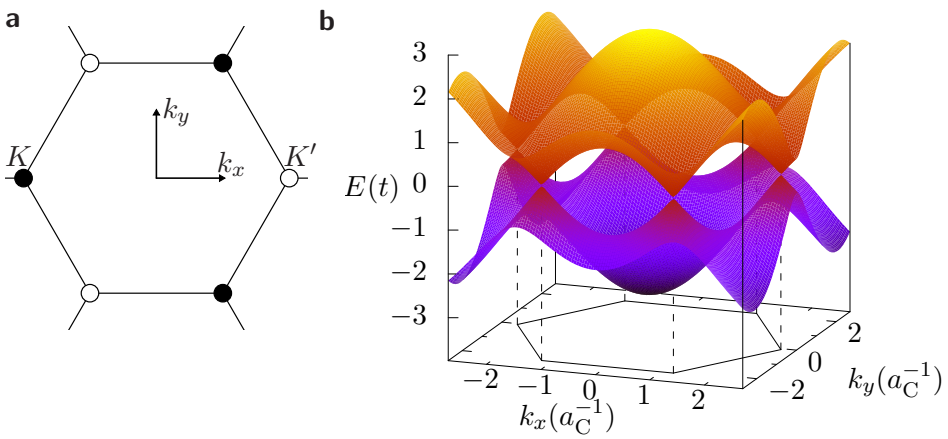

Figure 1.9: **a** First Brillouin zone of graphene in reciprocal space. The two Fermi points are K and K'. **b** Dispersion relation of graphene with the Brillouin zone highlighted. The conduction and valence band touch at the Fermi points.

1.2.2 Classification of carbon nanotubes

Starting from a large patch of graphene it is possible to construct a CNT by picking up any two non-neighboring unit cells and bringing them together by rolling up the sheet. The vector connecting these two unit cells $\boldsymbol{C} = m\boldsymbol{a}_1 + n\boldsymbol{a}_2 \equiv (m, n)$ is called chiral vector and can be written as a linear combination of the lattice vectors. The corresponding prefactors are the chiral indices and completely define the structure or chirality of the tube. Often the chirality is given by the radius of the tube $R = a_C\sqrt{3(m^2 + mn + n^2)}/2\pi$ and its chiral angle $\theta = \arcsin(\sqrt{3}n/(2\sqrt{m^2 + mn + n^2}))$, the angle between the chiral vector and the x-axis. The coordinate system of the CNT is the one of graphene rotated by the chiral angle. These coordinates are around the circumference $x_\perp$ and along the tube z. The new unit cell of the CNT is spanned by the chiral vector and the primitive translation $\boldsymbol{T}$ in z direction. This is illustrated for an $(8, 2)$ tube in Fig. 1.10. In this way one can recognize two special types of CNTs. Their names originate from the shape of edge of the tube. In *zig-zag* CNTs the second chiral index is zero $(m, 0)$ and therefore also the chiral angle is zero, $\theta = 0$. The opposite limiting case is called *armchair* CNTs where both chiral indices are the same (m, m). The chiral angle in these specimen is $\theta = 30°$. Both edge shapes are illustrated in Fig. 1.10. All intermediate tubes with $0 < \theta < 30°$ are simply called *chiral* CNTs. As we will see in a moment, the chiral CNTs can be classified into two categories: the

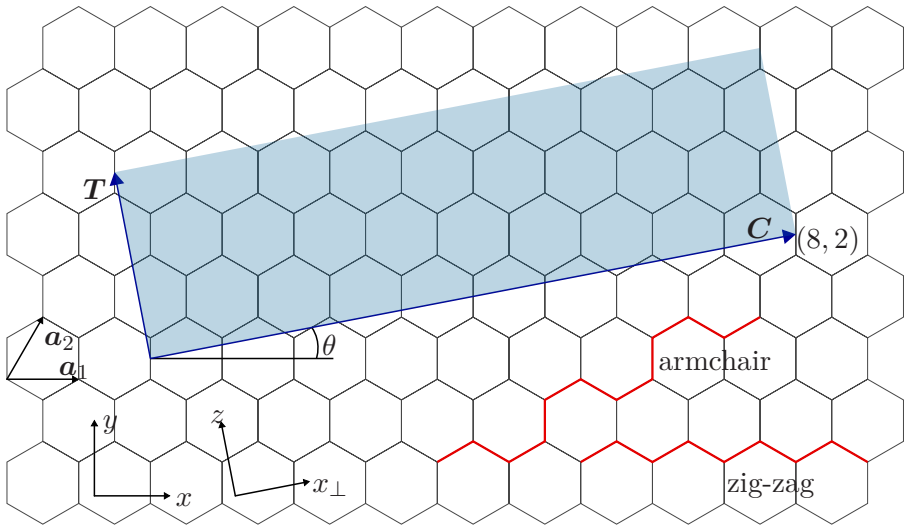

Figure 1.10: The chirality of the CNT is defined via the chiral indices at an example of a $\boldsymbol{C} = (8, 2)$ tube. The chiral angle θ rotates the coordinate system into the transversal $x_\perp$ and longitudinal z one. The blue area is the translational unit cell of the resulting CNT which is defined by the chiral vector $\boldsymbol{C}$ and the primitive translation $\boldsymbol{T}$. The edges of the two special chiralities, the zig-zag and armchair one, are highlighted in red.

ziz-zag class and the *armchair class* tubes. Examples of these three classes can be seen in Fig. 1.11. The rolling up of the graphene sheet also affects its band structure since also the coordinate system in the reciprocal space is rotated by the chiral angle into $k_\perp$ and k_z. The new Brillouin zone of CNTs is rectangular and spanned by the reciprocal vectors corresponding to the new unit cell spanned by $\boldsymbol{C}$ and $\boldsymbol{T}$. It has a width in k_z direction of $2\pi/|\boldsymbol{T}|$.

1.2.3 Transverse quantization

The wave function has to be single-valued and continuous around the CNTs circumference which implies a quantization condition on the transverse momentum

$$k_\perp(x_\perp + 2\pi R) = k_\perp x_\perp + 2\pi n_z, \quad \Rightarrow \quad k_\perp = \frac{\ell_z}{\hbar R}, \quad \text{with} \quad n_z = \frac{\ell_z}{\hbar} \in \mathbb{N}. \tag{1.8}$$

Here, ℓ_z is called angular momentum. This cuts the rectangular CNT Brillouin zone with lines parallel to k_z as is indicated in Fig. 1.12a-c by red lines for

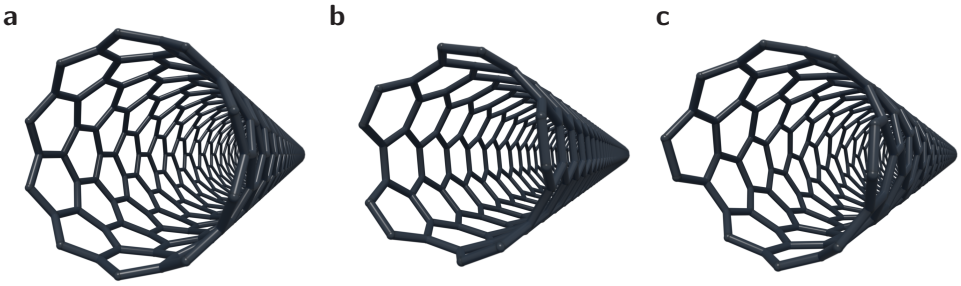

Figure 1.11: Examples of the three chirality classes. **a** A $(10, 0)$ zig-zag CNT with a chiral angle of $\theta = 0$. **b** A $(5, 5)$ armchair CNT with a chiral angle of $\theta = 30°$. **c** A $(8, 2)$ chiral CNT with a chiral angle of $\theta \approx 10.9°$.

three different CNTs. This process is called zone-folding since the bands are effectively folded from the graphene Brillouin zone into the CNT Brillouin zone. Out of these cuts one obtains one dimensional bands shown for the three cases in Fig. 1.12d-f. Here, only the conduction band is shown since the valence band just differs by a minus sign. These bands feature two Fermi points where in the case of zig-zag CNTs they fall on top of each other at $k_z = 0$. Also it is clear that this divides CNTs into two categories, semiconducting like the $(10, 0)$ one and metallic like the $(5, 5)$ and $(8, 2)$ ones, depending on whether a band gap is opened or not. The condition to obtain a metallic tube is a quantization line hitting a Fermi point of graphene. This condition can be written for a general (m, n)-CNT as

$$m - n \mod 3 \begin{cases} = 0 & \text{metallic} \\ \neq 0 & \text{semiconducting} \end{cases}, \tag{1.9}$$

which means that one in three tubes and also all armchair CNTs are metallic. In this thesis we will restrict ourself to metallic tubes only. We are interested in the low energy physics of the order of $\mathcal{O}(meV)$. Applying a commonly used value for the hopping parameter $t \approx 2.66eV$ [27], one realizes that the bands lie in energy ranges of $\mathcal{O}(eV)$ which is orders of magnitude larger than what we are interested in. This means that for the low energy physics only the lowest bands are important. The angular momentum of these bands allows to classify all CNTs into two groups, the *armchair class* tubes with $\ell_z = 0$ and the *zig-zag class* tubes with $\ell_z \neq 0$. This property can be also be extracted from the chiral indices because every CNT is symmetric under rotations of $2\pi/\tilde{n}$, where $\tilde{n} = \gcd(m, n)$. This $C_{\tilde{n}}$ symmetry allows to group all tubes according

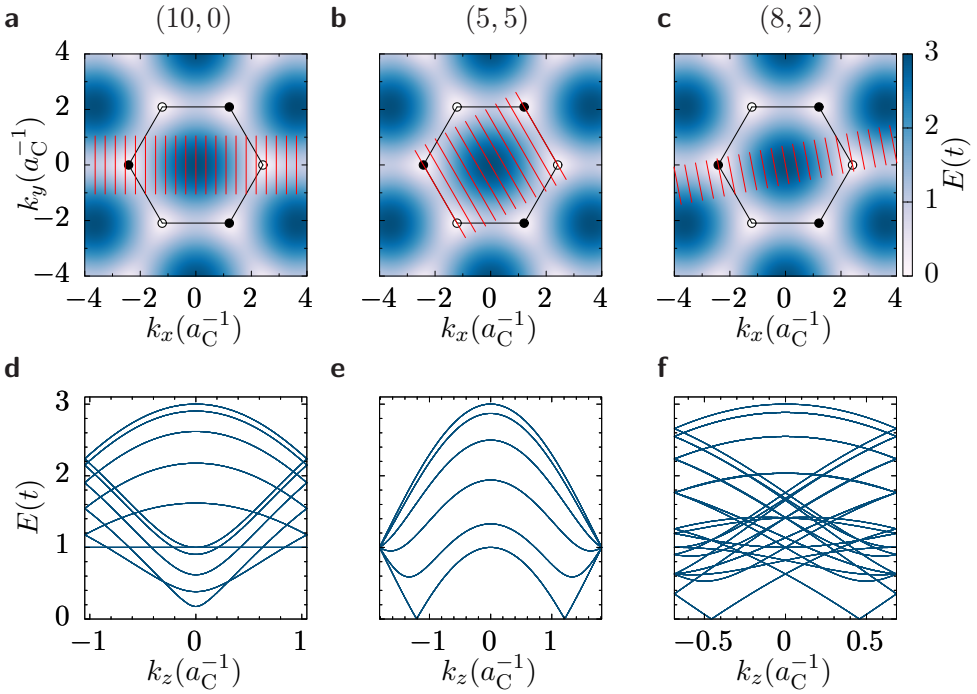

Figure 1.12: **a-c** Conduction band around the first Brillouin zone. Rolling up the graphene sheet creates quantized transverse momentum inside the CNT Brillouin zone. The resulting cuts are shown in red for a $(10, 0)$ (**a**), a $(5, 5)$ (**b**) and an $(8, 2)$ (**c**) CNT. The distance between two quantization lines is $1/R$. **d-f** Corresponding conduction bands for the same chiralities.

to [28]

$$m - n \mod 3\tilde{n} \begin{cases} = 0 & \text{armchair class} \\ \neq 0 & \text{zig-zag class} \end{cases} . \tag{1.10}$$

This shows that the $(8, 2)$ CNT from Fig. 1.12c is of the armchair class. De facto, all armchair class CNTs feature two Fermi points at opposite k_z in the zone folded momentum space, while in the case of zig-zag class tubes both Fermi points cones fall on top of each other at $k_z = 0$, like e.g. in Fig. 1.12d for a pure zig-zag tube.

1.2.4 Low energy expansion

As can be seen in Fig. 1.9b and in the lower panels of Fig. 1.12, at low energies $\mathcal{O}(meV)$ the dispersion is linear around the two Fermi points K and K'. Such band structures are usually referred to as Dirac cones since these effectively

massless electrons resemble the solutions of the relativistic Dirac equation. This introduces a new quantum number in the system called valley τ. In zig-zag class CNTs the valley is closely related to the angular momentum of the corresponding band. In armchair class tubes this assignment is not possible because both Dirac cones stem from a single band with only one angular momentum state. Therefore, the valley is not a good quantum number in armchair class CNTs. Using the fact that $\boldsymbol{K} = -\boldsymbol{K'}$, the valley is defined via $\boldsymbol{k} = \tau\boldsymbol{K} + \boldsymbol{\kappa}$ where $\tau = 1$ corresponds to the K point and $\tau = -1$ to the K' point. We know that in metallic tubes the quantization lines hit the Fermi point exactly and therefore $\kappa_\perp = 0$ when neglecting all curvature effects. Rotating the graphene Hamiltonian from Eq. (1.7) to the CNT coordinates and expanding it around the Fermi points results in

$$\mathcal{H}_\tau(\kappa_z) = \begin{pmatrix} 0 & \gamma_\tau(\kappa_z) \\ \gamma_\tau^*(\kappa_z) & 0 \end{pmatrix}, \tag{1.11}$$

where we use an extended space by defining $\hat{\tau}_3$ as the third Pauli matrix in valley space. Here,

$$\gamma_\tau(\kappa_z) = \tilde{t}(\hat{\tau}_3\kappa_x - i\kappa_y) = \tilde{t}(\hat{\tau}_3\kappa_\perp - i\kappa_z)e^{i\hat{\tau}_3(\theta+\frac{\pi}{3})}, \tag{1.12}$$

with $\tilde{t} = 3t/2$. The resulting bands feature the Dirac cones centered around the Fermi points with $E_\tau(\kappa_z) = \tilde{t}|\kappa_z|$, where the valley does not influence the energy, only the phase in the Hamiltonian. This simple picture of rolled graphene is often not enough since curvature can play a major role, especially for CNTs with a small radius.

1.2.5 Effects of curvature, magnetic fields and boundaries

The band structure of graphene is derived using only p_z orbitals and the resulting Π bonds. The other orbitals in the σ bonds do not play any role because they are hybridized into the sp^2 orbitals that build the lattice and especially they are in-plane and therefore perpendicular to the p_z orbitals. In CNTs this picture changes and hopping through σ bonds is possible due to the bending of the lattice and the resulting angles between the different orbitals. These curvature effects create a valley dependent shift of the momentum Δk^c in $k_\perp$ and k_z direction. It is important to notice that $\Delta k_\perp^c \propto \cos(3\theta)$ and $\Delta k_z^c \propto \sin(3\theta)$. Therefore, these shifts are in perpendicular direction for zig-zag CNTs and in k_z direction for armchair CNTs. The exact form and the

calculation of these shifts can be found in e.g. del Valle *et al.* [29]. This opens a small band gap in all but armchair CNTs. In all but zig-zag tubes it leads to a valley dependent shift such that the Dirac cone is not at $\kappa_z = 0$ anymore. This curvature effect also increases the strength of the spin-orbit coupling (SOC) which is negligible small in graphene [30]. The SOC is a result of the atomic spin-orbit interaction in carbon, and thus exists also for ideally infinitely long CNTs [31]. The full calculation, which is not shown here, shows that the SOC effects act as a shift in momentum in $k_\perp$ direction only. SOC couples the spin of the electrons to their orbital momentum resulting in a spin dependent energy shift Δk^{SO} [29, 31, 32]. The SOC shift splits the band into two spin dependent ones and additionally opens a gap in armchair CNTs. Therefore, the derived Hamiltonian is also extended to the spin space via

$$\gamma_{\tau\sigma}(\kappa_z) = \tilde{t}(\hat{\tau}_3\kappa'_\perp - i\kappa'_z)e^{i\hat{\tau}_3(\theta+\pi/3)}, \tag{1.13}$$

where $\kappa'_{\perp/z}$ include these shifts. The resulting dispersion relation depends now both on valley and spin, $E_{\tau\sigma}(\kappa_z) = \pm\tilde{t}\sqrt{(\kappa'_\perp)^2 + (\kappa'_z)^2}$. Furthermore we include the effects of a magnetic field which affects the electrons in two ways. First, we include the Zeeman effect which describes the interaction between an electron spin and an external magnetic field via the Hamiltonian

$$\mathcal{H}_{\mathrm{Z}} = -\boldsymbol{\mu}\boldsymbol{B} = \mu_{\mathrm{B}}\hat{\boldsymbol{\sigma}}\boldsymbol{B} = \mu_{\mathrm{B}}(\hat{\sigma}_3 B_z + \hat{\sigma}_1 B_\perp), \tag{1.14}$$

with the magnetic moment of the electron $\boldsymbol{\mu} = -g\mu_{\mathrm{B}}\hat{\boldsymbol{\sigma}}/2$, where $g \approx 2$ is the Landé g-factor, $\mu_{\mathrm{B}} = e\hbar/(2m_e)$ the Bohr magneton and $\hat{\boldsymbol{\sigma}}$ the vector of Pauli matrices in spin space. If the magnetic field has an angle ϑ with the z axis one defines $B_z = |\boldsymbol{B}|\cos\vartheta$ and $B_\perp = |\boldsymbol{B}|\sin\vartheta$. Second, if the magnetic field has a component parallel to the tube $B_z > 0$ it can also affect the electrons via the Aharonov-Bohm effect. Thereby the magnetic field influences the momentum with its vector potential $\boldsymbol{A}$ via the minimal coupling $\boldsymbol{k} \to \boldsymbol{k} - e\boldsymbol{A}/\hbar$. This influences the quantization condition along the circumference of the tube and results in a shift of the transverse momentum using $\frac{e}{\hbar}\int_0^{2\pi R}\boldsymbol{A}\mathrm{d}x_\perp = \frac{e}{\hbar}\int_S \mathrm{rot}\boldsymbol{A}\mathrm{d}S = \frac{e\pi R^2}{\hbar}B_z$, which is proportional to the magnetic field and the area of the cross section $S = \pi R^2$ of the tube. The total shifts are then [29, 33]

$$\begin{aligned}\kappa'_\perp &= \hat{\tau}_3\Delta k^c_\perp + \hat{\sigma}_3\Delta k^{\mathrm{SO}}_\perp + \frac{\pi R}{\phi_0}B_z,\\ \kappa'_z &= \kappa_z + \hat{\tau}_3\Delta k^c_z,\end{aligned} \tag{1.15}$$

where $\phi_0 = h/e$ is the flux quantum and $\hat{\sigma}_3$ is the third Pauli matrix in spin space. Therefore, a magnetic field allows to open a gap in metallic CNTs or even close a gap that arises from curvature or SOC.

Theoretical calculations have shown that scattering at the interface or disorder can mix electrons with different valley quantum numbers in finite length CNTs. A corresponding Hamiltonian reads [28, 34–37]

$$\mathcal{H}_{\mathrm{KK}'} = \hat{\tau}_1 \frac{\Delta_{\mathrm{KK}'}}{2}. \tag{1.16}$$

It is expected to be zero in disorder-free CNTs of the zig-zag class, due to angular momentum conservation rules, and finite in CNTs of the armchair class [28].

1.2.6 Finite length carbon nanotubes

Our ultimate goal in this chapter is to obtain the level structure of CNT-QDs. For this we need to consider tubes of a finite length L. In a SET setup where the CNT just lies on top of the contacts the length is actually not well defined. The length of the electrostatically defined QD can differ from the real length of the CNT and will strongly depend on the experimental setup. For simplicity we assume a CNT which has sharp ends exactly at the lead positions. This approximation turns out to often work well. The quantization condition follows from the fact that the wave function has to vanish at the missing atoms on both sides. The exact calculation is lengthy and will be skipped here, it can be found in Margańska *et al.* [28]. For zig-zag CNTs this condition reads $2\kappa_z' L = \eta_{\tau\sigma}(\kappa_z') - \eta_{\tau\sigma}(-\kappa_z') + 2\pi n$, where $\eta_{\tau\sigma} = \arg(\gamma_{\tau\sigma})$ and $n \in \mathbb{N}$. With finite $\kappa_\perp'$ this equation has to be solved self consistently, only if $\kappa_\perp' = 0$, which is the case for a metallic CNT with vanishing curvature, SOC and magnetic field, we obtain $\kappa_z' = (2n+1)\pi/L$.

This quantization of κ_z results in a shell structure of four levels per shell due to spin and valley degree of freedom. Only without curvature effects, SOC and magnetic field these four levels are degenerate. In Fig. 1.13 a sketch of a CNT-QD is shown where the two angular momentum degrees of freedom are highlighted.

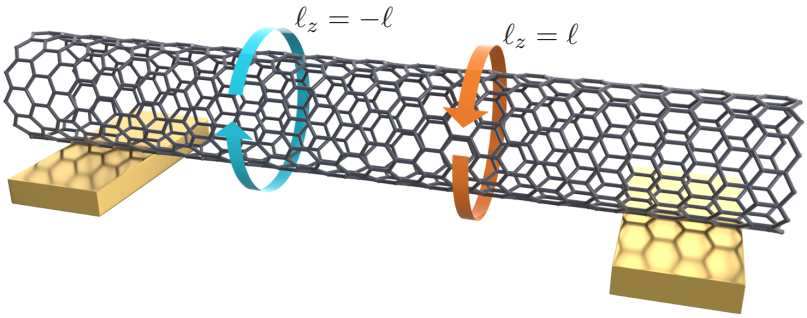

Figure 1.13: Real space model of a CNT-QD highlighting the two angular momentum states.

1.2.7 Model Hamiltonian

Since the conductance and valence band differ only by a sign due to the sublattice symmetry, it is possible to construct a model Hamiltonian for the conductance band of a single shell only $\hat{H}_{\mathrm{CNT}} = |\gamma_{\tau\sigma}| + \mathcal{H}_Z + \mathcal{H}_{\mathrm{KK}'}$. At low magnetic fields and assuming that $\Delta k_\perp^{\mathrm{SO}} \ll \Delta k_\perp^c$ we can expand $\gamma_{\tau\sigma} \approx \epsilon_0 - \hat{\tau}_3\hat{\sigma}_3\frac{\Delta_{\mathrm{SO}}}{2} + \hat{\tau}_3\mu_{\mathrm{orb}}B_z$ [34]. The exact expansion can be found in Niklas [38]. The full single particle Hamiltonian neglecting the level offset ϵ_0 then reads

$$\hat{H}_{\mathrm{CNT}} = -\hat{\tau}_3\hat{\sigma}_3\frac{\Delta_{\mathrm{SO}}}{2} + \hat{\tau}_1\frac{\Delta_{\mathrm{KK}'}}{2} + \hat{\tau}_3\mu_{\mathrm{orb}}B_z + \hat{\sigma}_3\mu_{\mathrm{B}}B_z + \hat{\sigma}_1\mu_{\mathrm{B}}B_\perp, \qquad (1.17)$$

or, written in second quantization,

$$\begin{aligned}\hat{H}_{\mathrm{CNT}} = &\frac{\Delta_{\mathrm{KK}'}}{2}\sum_{\tau\sigma} d_{\tau\sigma}^\dagger d_{\bar{\tau}\sigma} + \frac{\Delta_{\mathrm{SO}}}{2}\sum_{\tau\sigma}\sigma\tau n_{\tau\sigma} \\ &+ B_z\sum_{\tau\sigma}(\mu_{\mathrm{B}}\sigma + \mu_{\mathrm{orb}}\tau)n_{\tau\sigma} + \mu_{\mathrm{B}}B_\perp\sum_{\tau\sigma} d_{\tau\sigma}^\dagger d_{\tau\bar{\sigma}}, \qquad (1.18)\end{aligned}$$

where $d_{\tau\sigma}^{(\dagger)}$ destroys (creates) an electron in valley τ with spin σ and $n_{\tau\sigma} = d_{\tau\sigma}^\dagger d_{\tau\sigma}$. Notice that the spin and valley remain good quantum numbers in the presence of a parallel field ($\vartheta = 0, \pi$), while a perpendicular component flips the spin degrees of freedom. Often, this Hamiltonian is given in matrix form,

using the basis $\{|K\uparrow\rangle, |K'\uparrow\rangle, |K\downarrow\rangle, |K'\downarrow\rangle\}$,

$$\hat{H}_{\mathrm{CNT}} = \begin{pmatrix} -\Delta_{\mathrm{SO}}/2 & \Delta_{\mathrm{KK'}}/2 & \mu_{\mathrm{B}}B_{\perp} & 0 \\ \Delta_{\mathrm{KK'}}/2 & \Delta_{\mathrm{SO}}/2 & 0 & \mu_{\mathrm{B}}B_{\perp} \\ \mu_{\mathrm{B}}B_{\perp} & 0 & \Delta_{\mathrm{SO}}/2 & \Delta_{\mathrm{KK'}}/2 \\ 0 & \mu_{\mathrm{B}}B_{\perp} & \Delta_{\mathrm{KK'}}/2 & -\Delta_{\mathrm{SO}}/2 \end{pmatrix} + B_z \begin{pmatrix} \mu_{\mathrm{orb}} + \mu_{\mathrm{B}} & 0 & 0 & 0 \\ 0 & -\mu_{\mathrm{orb}} + \mu_{\mathrm{B}} & 0 & 0 \\ 0 & 0 & \mu_{\mathrm{orb}} - \mu_{\mathrm{B}} & 0 \\ 0 & 0 & 0 & -\mu_{\mathrm{orb}} - \mu_{\mathrm{B}} \end{pmatrix}.$$

1.2.8 Exchange interaction

So far we have obtained the single particle part of the Hamiltonian. Keeping in mind that, according to the Pauli principle, the quantum numbers of two electrons in the system have to differ, and keeping the order of the operators, we can write this Hamiltonian in the following many-body basis $\{|K\uparrow, K\downarrow\rangle, |K\uparrow, K'\uparrow\rangle, |K\downarrow, K'\uparrow\rangle, |K\uparrow, K'\downarrow\rangle, |K\downarrow, K'\downarrow\rangle, |K'\uparrow, K'\downarrow\rangle\}$, which then reads

$$\hat{H}^{2e}_{\mathrm{CNT}} = \begin{pmatrix} -2\mu_{\mathrm{orb}}B_z & 0 & -\Delta_{\mathrm{KK'}}/2 & \Delta_{\mathrm{KK'}}/2 & 0 & 0 \\ 0 & 2\mu_{\mathrm{B}}B_z & \mu_{\mathrm{B}}B_{\perp} & \mu_{\mathrm{B}}B_{\perp} & 0 & 0 \\ -\Delta_{\mathrm{KK'}}/2 & \mu_{\mathrm{B}}B_{\perp} & \Delta_{\mathrm{SO}} & 0 & \mu_{\mathrm{B}}B_{\perp} & -\Delta_{\mathrm{KK'}}/2 \\ \Delta_{\mathrm{KK'}}/2 & \mu_{\mathrm{B}}B_{\perp} & 0 & -\Delta_{\mathrm{SO}} & \mu_{\mathrm{B}}B_{\perp} & \Delta_{\mathrm{KK'}}/2 \\ 0 & 0 & \mu_{\mathrm{B}}B_{\perp} & \mu_{\mathrm{B}}B_{\perp} & -2\mu_{\mathrm{B}}B_z & 0 \\ 0 & 0 & -\Delta_{\mathrm{KK'}}/2 & \Delta_{\mathrm{KK'}}/2 & 0 & 2\mu_{\mathrm{orb}}B_z \end{pmatrix}. \tag{1.19}$$

This model can be extended to electron-electron interactions which essentially only affect this two electron subspace. This exchange interaction appears due to the fact that the two electrons are indistinguishable and the overall wave function must be antisymmetric upon exchanging the electrons. In second quantization such a general two-electron operator has the form

$$\hat{H}_{ee} = \frac{1}{2} \sum_{\tau_1\tau_2\tau_3\tau_4\sigma\sigma'} v_{ee} d^{\dagger}_{\tau_4\sigma} d^{\dagger}_{\tau_3\sigma'} d_{\tau_1\sigma} d_{\tau_2\sigma'}, \tag{1.20}$$

where the interaction matrix element is the double space integral over the symmetric two electron potential, $v(\boldsymbol{r}) = v(-\boldsymbol{r})$,

$$v_{ee} = \int \mathrm{d}\boldsymbol{r} \int \mathrm{d}\boldsymbol{r}' \varphi^*_{\tau_3\sigma'}(\boldsymbol{r}') \varphi^*_{\tau_4\sigma}(\boldsymbol{r}) v(\boldsymbol{r} - \boldsymbol{r}') \varphi_{\tau_1\sigma}(\boldsymbol{r}) \varphi_{\tau_2\sigma'}(\boldsymbol{r}'). \tag{1.21}$$

So far it has only been calculated for the case of pure armchair tubes [39], and for the zig-zag class CNTs [33, 40]. Its microscopic form is not known for different tubes. Similar to the SOC and valley mixing, this exchange interaction preserves time reversal symmetry. Using momentum conservation one can show that for zig-zag class tubes it must hold

$$\tau_1 + \tau_2 = \tau_3 + \tau_4. \tag{1.22}$$

The most common way to group these processes is to distinguish between normal processes, $\tau_1 = \tau_4$ and $\tau_2 = \tau_3$, backscattering processes, $\tau_1 = \tau_3 = -\tau_2 = -\tau_4$ and Umklapp processes, $\tau_1 = \tau_2 = -\tau_3 = -\tau_4$. However, the latter ones do not fulfill Eq. (1.22) and are therefore forbidden. The normal processes are completely diagonal and correspond to the usual Coulomb interaction with strength U. The only remaining processes are backscattering ones. We set $v^b_{ee} = J/2$ where the value is not calculated here but can be found in e.g. Sommer [41], Forster [42]. The resulting exchange Hamiltonian is

$$\hat{H}_J = -\frac{J}{2}\sum_{\sigma\sigma'} d^\dagger_{K\sigma} d^\dagger_{K'\sigma'} d_{K\sigma'} d_{K'\sigma} = J\left(\hat{\boldsymbol{S}}_K \cdot \hat{\boldsymbol{S}}_{K'} + \frac{1}{4}\hat{n}_K \hat{n}_{K'}\right), \tag{1.23}$$

where $\hat{n}_\tau = \sum_\sigma d^\dagger_{\tau\sigma} d_{\tau\sigma}$ and $\hat{\boldsymbol{S}}_\tau = \frac{1}{2}\sum_{\sigma\sigma'} d^\dagger_{\tau\sigma} \hat{\boldsymbol{\sigma}}_{\sigma\sigma'} d_{\tau\sigma'}$. The second way of writing the exchange Hamiltonian is the more commonly used version of the Heisenberg model. In matrix form this Hamiltonian reads

$$\mathcal{H}_J = -\frac{J}{2}\begin{pmatrix} 0 & 0 & 0 & 0 & 0 & 0 \\ 0 & 1 & 0 & 0 & 0 & 0 \\ 0 & 0 & 0 & 1 & 0 & 0 \\ 0 & 0 & 1 & 0 & 0 & 0 \\ 0 & 0 & 0 & 0 & 1 & 0 \\ 0 & 0 & 0 & 0 & 0 & 0 \end{pmatrix}. \tag{1.24}$$

1.2.9 Spectrum in a magnetic field

The diagonalization of the Hamiltonian in Eq. (1.19) results in the Kramers basis $\{|i\rangle\}$ with eigenenergies ϵ_i for $i = 1, 2, 3, 4$. For magnetic fields purely parallel or perpendicular to the CNT axis, this Hamiltonian is easily diagonalized. For other orientations of the field such states are a linear superposition of all the basis states and neither the spin nor the valley are good quantum numbers any more. One has to address the problem with numerical tools. For a parallel magnetic field ($B_\perp = 0$) we obtain $\epsilon_i = \pm\sqrt{{\Delta_{\mathrm{KK'}}}^2 + (\Delta_{\mathrm{SO}} \mp 2\mu_o r b B_z)^2}/2 \pm \mu_{\mathrm{B}} B_z$.

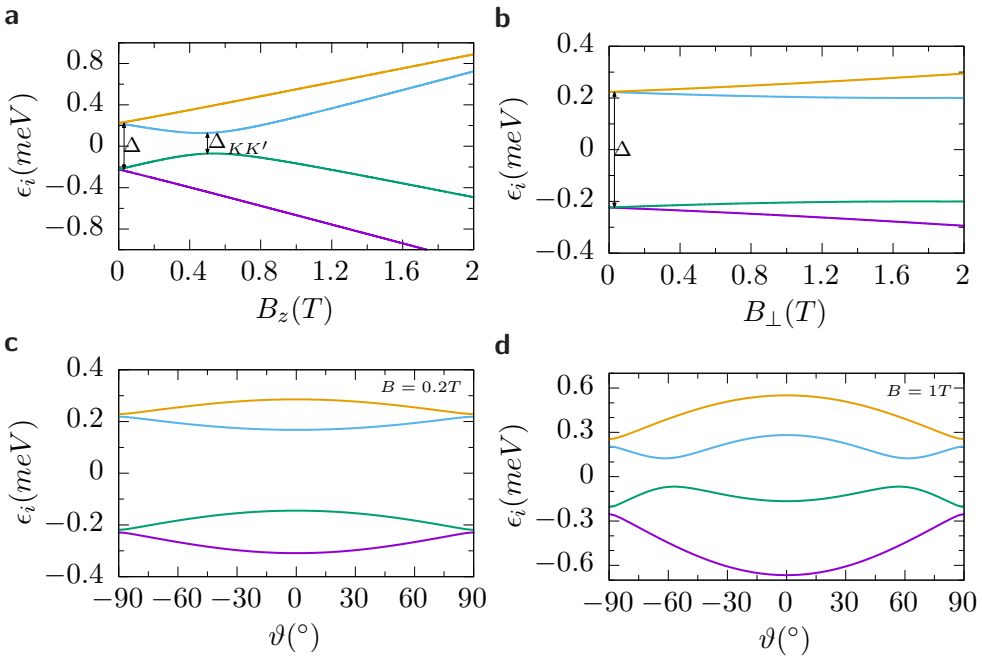

Figure 1.14: **a,b** Single particle spectrum of a CNT in a parallel (**a**) and a perpendicular (**b**) magnetic field. At zero magnetic field two Kramers pairs form which are split by Δ. Parameters are $\Delta_{\mathrm{SO}} = 0.4meV$, $\Delta_{\mathrm{KK'}} = 0.2meV$ and $\mu_{\mathrm{orb}} = 0.4meV/T$. **c,d** The dependence on the angle ϑ of the magnetic field is shown for $B = 0.2T$ (**c**) and $B = 1T$ (**d**). $\vartheta = 0°$ corresponds to a parallel field.

This spectrum can be seen in Fig. 1.14a. For a perpendicular field ($B_z = 0$) the eigenenergies are $\epsilon_i = \pm\sqrt{{\Delta_{\mathrm{SO}}}^2 + (\Delta_{\mathrm{KK'}} \pm 2\mu_{\mathrm{B}} B_\perp)^2}/2$ which is shown in Fig. 1.14b. Additionally, we present the spectrum as a function of the angle ϑ between the CNT and the magnetic field. As a convention we index the eigenenergies and eigenstates such that ϵ_1 has the highest eigenenergy and ϵ_4 the lowest. At zero magnetic field the eigenstates form two pairs of degenerate levels, the so called Kramers pairs. Their splitting is given by $\Delta = \sqrt{{\Delta_{\mathrm{SO}}}^2 + {\Delta_{\mathrm{KK'}}}^2}$. The valley mixing term $\Delta_{\mathrm{KK'}}$ mainly creates avoided crossings between states of different valley, best seen in Fig. 1.14a.

The two electrons part of the Hamiltonian in Eq. (1.19) including exchange interaction in Eq. (1.24) cannot be diagonalized analytically. The spectrum as function of parallel and perpendicular magnetic field as well as function of the angle ϑ at constant field is shown in Fig. 1.15. Comparing the spectrum in a parallel magnetic field with and without exchange interaction in Fig. 1.15a,b,

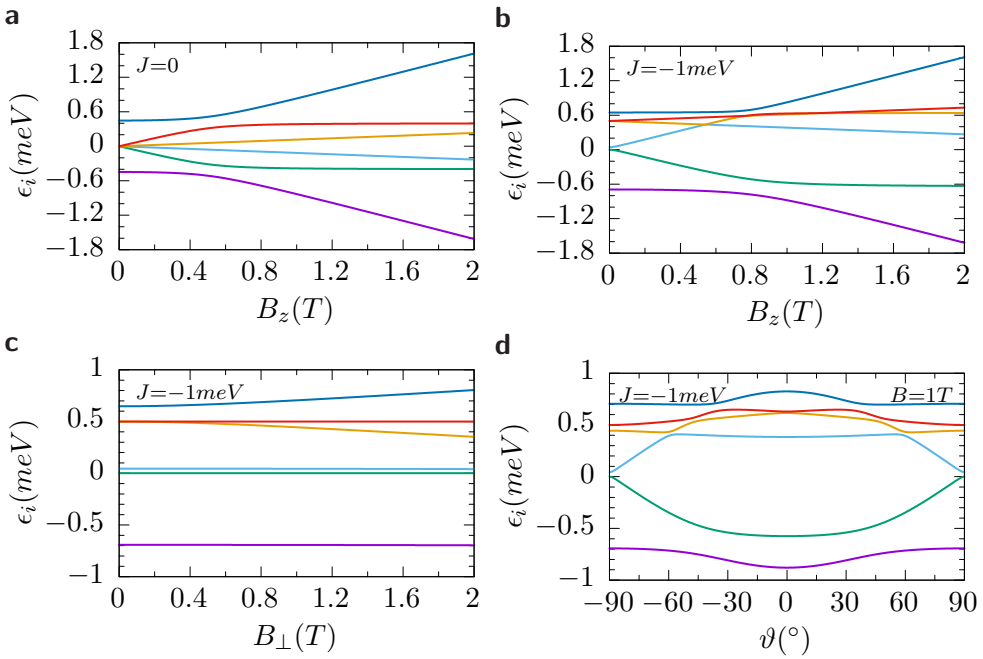

Figure 1.15: Two electron spectrum of a CNT in a magnetic field. **a** Spectrum in a parallel field without exchange interaction. **b** Including exchange interaction $J = -1meV$. **c** Spectrum in a perpendicular magnetic field with exchange. **d** Angle dependence of the spectrum at $B = 1T$ and exchange. Parameters are $\Delta_{\mathrm{SO}} = 0.4meV$, $\Delta_{\mathrm{KK'}} = 0.2meV$ and $\mu_{\mathrm{orb}} = 0.4meV/T$.

one can see that exchange has two major influences. It increases the splitting between all states at $B = 0$ and shifts the origin of the states $|K\uparrow, K'\uparrow\rangle$ and $|K\downarrow, K'\downarrow\rangle$ and thus lifts the degeneracy at $B = 0$. The sign of J also determines the direction of this shift.

CHAPTER 2

Transport theory

In classical conductors the current is directly proportional to the applied voltage $I = V/R$. This relation is known as Ohm's law and introduces the constant of proportionality, the resistance R. Though, most electric devices show an $I - V$ characteristic that is not linear like diodes or batteries. In the previous chapter we have shown that the SET features such a puzzling $I - V$ behavior with jumps of the current at certain thresholds. These effects are of quantum nature and cannot be explained by Ohm's law. In quantum mechanical systems the current is given by the expectation value of the current operator $I_l = \langle \hat{I}_l \rangle = e \langle \dot{N}_l \rangle$, where N_l is the electron number in lead l. Since the total particle number must be conserved, it holds $I_\mathrm{R} = -I_\mathrm{L} \equiv I$ and therefore in this thesis we will only consider the current at the right lead which is positive at positive bias. Theoretically the SET is closed and does not interchange information with other systems. Therefore, it is coherent and can be described by a Schrödinger equation with a corresponding Hamiltonian. In order to keep a finite current for reasonably long times, the leads need to act as a battery with sufficient capacity. Then, treating this system exactly is practically impossible due to its size. On the other hand it is possible to consider the leads themselves as an environment and only study the reduced system of the central QD in contact with this environment. This implies the appearance of incoherent processes from the coupling to the leads and a variable electron number. Such setups are called open quantum systems.

2.1 Open quantum systems

Open quantum systems and in particular SETs are at the very heart of mesoscopic physics, dealing with a substantial number of electrons in the quantum regime. The total Hamiltonian in these systems can be split into three parts

$$\hat{H} = \hat{H}_{\mathrm{S}} + \hat{H}_{\mathrm{B}} + \hat{H}_{\mathrm{tun}}, \tag{2.1}$$

a part of the central QD $\hat{H}_{\mathrm{S}}$, a part describing the environment $\hat{H}_{\mathrm{B}}$ and a coupling between these two systems $\hat{H}_{\mathrm{tun}}$. This is illustrated in Fig. 2.1 for a SET. The leads are considered as a free electron gas

$$\hat{H}_{\mathrm{B}} = \sum_{l\sigma\boldsymbol{k}} \xi_{l\boldsymbol{k}} c^{\dagger}_{l\sigma\boldsymbol{k}} c_{l\sigma\boldsymbol{k}}, \tag{2.2}$$

where $c^{(\dagger)}_{l\sigma\boldsymbol{k}}$ destroys (creates) an electron in lead $l \in \{\mathrm{L}, \mathrm{R}\}$ with spin projection $\sigma \in \{\uparrow, \downarrow\}$ and momentum $\boldsymbol{k}$ and $\xi_{l\boldsymbol{k}}$ is the single particle energy of this state. The QD Hamiltonian $\hat{H}_{\mathrm{S}}$ depends on the details of the used system, therefore we do not specify its exact form here. We only introduce a set of quantum numbers η, which, together with the spin σ, completely characterizes the single particle QD states. This defines the creation and annihilation operators of the QD $d^{(\dagger)}_{\eta\sigma}$ which allows us to write a general coupling Hamiltonian as

$$\hat{H}_{\mathrm{tun}} = \sum_{l\eta\sigma\boldsymbol{k}} t_{l\eta} c^{\dagger}_{l\sigma\boldsymbol{k}} d_{\eta\sigma} + \mathrm{h.c.} = \sum_{l\sigma\boldsymbol{k}p} p\; c^{p}_{l\sigma\boldsymbol{k}} D^{\bar{p}}_{l\sigma}, \tag{2.3}$$

with $D^{-}_{l\sigma} = \sum_{\eta} t_{l\eta} d_{\eta\sigma}$, $D^{+}_{l\sigma} = (D^{-}_{l\sigma})^{\dagger}$ and $\bar{p} = -p$. Here, we have introduced the notation where the upper index "$-$" denotes the annihilation operator, the "$+$"

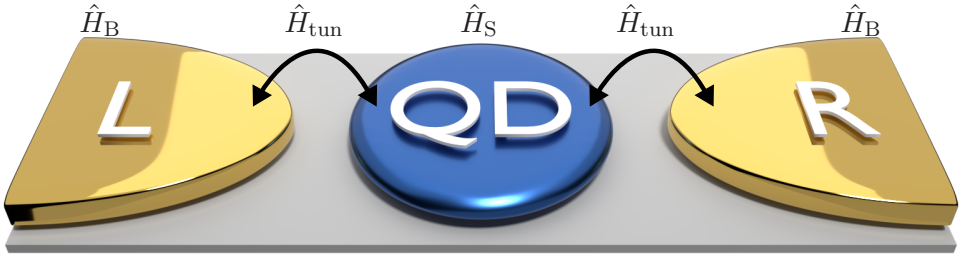

Figure 2.1: Scheme of a single electron transistor. The total Hamiltonian can be split into three parts, the QD part $\hat{H}_{\mathrm{S}}$, the lead part $\hat{H}_{\mathrm{B}}$ and a coupling between these two $\hat{H}_{\mathrm{tun}}$.

index the creation operator and we sum over $p \in \{+,-\}$. We keep in mind that the operators for bath and system anticommute $\{c^p_{l\sigma\boldsymbol{k}}, D^{\bar{p}}_{l\sigma}\} = 0$, leading to an additional minus sign in the sum, given by p. We have made the assumption that the hopping integral $t_{l\eta}$ does not depend on the momentum and spin of the transferred electron. In Sec. 4.5 we test this conjecture for the case of a CNT-QD. Integrating out the leads is not trivial since the object of interest, the current operator $\hat{I}_l$, contains lead operators. Thanks to the fact that the electron number in the leads can only change via the tunneling Hamiltonian, this change is directly connected to a corresponding variation in the QD. This will allow us to define the current operator even after integrating out the bath and work purely in the reduced system of the QD. The corresponding equation describing the dynamics is called the quantum master equation.

2.2 Quantum master equation

Expectation values like the one for the current $I = \langle \hat{I}_\mathrm{R} \rangle$ are easily defined for pure states, described by state vectors $|\psi\rangle$ on a Hilbert space. The expectation value of an operator $\hat{A}$ in this state is $\langle \hat{A} \rangle = \langle \psi | \hat{A} | \psi \rangle$. Pure states can be only defined if we have complete knowledge about the system, which often is not the case. Especially in open quantum systems the interaction with the environment causes the state of the coupled system not to be well defined. In general it can only be described as a statistical ensemble of pure states, where the expectation value of $\hat{A}$ can be written as $\langle \hat{A} \rangle = \mathrm{tr}\{\rho_\mathrm{tot} \hat{A}\}$, where we have introduced the density matrix $\rho_\mathrm{tot} = \sum_i p_i |\psi_i\rangle\langle\psi_i|$ of the full system. It describes the system with the probability p_i to be in state $|\psi_i\rangle$. Following from this definition, the properties of the density matrix can be derived. It has to be hermitian $\rho^\dagger_\mathrm{tot} = \rho_\mathrm{tot}$, normalized $\mathrm{tr}\{\rho_\mathrm{tot}\} = \sum_i p_i = 1$ and positive semidefinite $\rho_\mathrm{tot} \geq 0$ or $p_i \geq 0 \; \forall \; i$. If the system is in the pure state $|\psi_j\rangle$ the density matrix is the projector $\rho_\mathrm{tot} = |\psi_j\rangle\langle\psi_j|$ with $\rho^2_\mathrm{tot} = \rho_\mathrm{tot}$. The equation of motion for the full density matrix is the Liouville-von Neumann equation, which is the quantum mechanical analogue to the Liouville equation in classical mechanics. It can be easily derived from the Schrödinger equation and reads in the Schrödinger picture

$$\dot{\rho}_\mathrm{tot}(t) = -\frac{i}{\hbar}\left[\hat{H}, \rho_\mathrm{tot}(t)\right] =: \mathcal{L}\rho_\mathrm{tot}(t), \tag{2.4}$$

where $\mathcal{L}X = -i[\hat{H}, X]/\hbar$ is called the Liouville superoperator or Liouvillian for the full system. It consists of three parts, $\mathcal{L} = \mathcal{L}_{\mathrm{S}} + \mathcal{L}_{\mathrm{B}} + \mathcal{L}_{\mathrm{tun}}$, with the corresponding Hamiltonians. The dynamics of the central QD only is then described by a so called reduced density matrix (RDM) given by the partial trace over the leads of the full density matrix $\rho = \mathrm{tr}_{\mathrm{B}}\{\rho_{\mathrm{tot}}\}$. If we assume that the interaction between the QD and the bath is switched on at some time $t = 0$, before that time both parts are in equilibrium and closed systems. This makes the system separable and the total density matrix is simply

$$\rho_{\mathrm{tot}}(t = 0) = \rho(t = 0) \otimes \rho_{\mathrm{B}}, \tag{2.5}$$

with the equilibrium RDM of the bath $\rho_{\mathrm{B}} = e^{-\beta(\hat{H}_{\mathrm{B}} - \sum_l \mu_l \hat{N}_l)}/Z_G$ at $t = 0$. Here, $\beta = 1/k_{\mathrm{B}}T$ where T is the temperature of the bath, k_{B} the Boltzmann constant and Z_G the grand canonical partition function ensuring $\mathrm{tr}_{\mathrm{B}}\{\rho_{\mathrm{B}}\} = 1$. At times $t > 0$ the interaction is switched on and the QD and bath can mix resulting in entanglement. To obtain an effective equation for the RDM of the QD we use the Nakajima-Zwanzig projection operator technique.

2.2.1 Nakajima-Zwanzig equation

The concept of Nakajima and Zwanzig [43, 44] separates the total density matrix into two parts, a part $\mathcal{P}\rho_{\mathrm{tot}}$ where the QD and the leads are separable and a part $\mathcal{Q}\rho_{\mathrm{tot}}$ containing information about their entanglement. This is done using the projectors

$$\mathcal{P}X \equiv \mathrm{tr}_{\mathrm{B}}\{X\} \otimes \rho_{\mathrm{B}}, \qquad \mathcal{Q} = 1 - \mathcal{P}. \tag{2.6}$$

These projectors fulfill the following identities, $\mathcal{P} + \mathcal{Q} = 1$, $\mathcal{P}^2 = \mathcal{P}$, $\mathcal{Q}^2 = \mathcal{Q}$, $\mathcal{P}\mathcal{Q} = \mathcal{Q}\mathcal{P} = 0$, $\mathcal{P}\mathcal{L}_{\mathrm{B}} = \mathcal{L}_{\mathrm{B}}\mathcal{P} = 0$, $\mathcal{P}\mathcal{L}_S = \mathcal{L}_{\mathrm{S}}\mathcal{P}$, $\mathcal{P}\mathcal{L}_{\mathrm{tun}}^{2n+1}\mathcal{P} = 0$ for $n \in \mathbb{N}$. These projectors split the Liouville-von Neumann equation in (2.4) into a set of coupled differential equations

$$\mathcal{P}\dot{\rho}_{\mathrm{tot}}(t) = \mathcal{P}\mathcal{L}\mathcal{Q}\rho_{\mathrm{tot}}(t) + \mathcal{P}\mathcal{L}\mathcal{P}\rho_{\mathrm{tot}}(t), \tag{2.7}$$

$$\mathcal{Q}\dot{\rho}_{\mathrm{tot}}(t) = \mathcal{Q}\mathcal{L}\mathcal{Q}\rho_{\mathrm{tot}}(t) + \mathcal{Q}\mathcal{L}\mathcal{P}\rho_{\mathrm{tot}}(t). \tag{2.8}$$

The entangled part in Eq. (2.8) is solved with the help of the propagator $G_{\mathcal{Q}}(t) = e^{\mathcal{Q}\mathcal{L}t}$, by multiplying it with $G_{\mathcal{Q}}(-t)$ from the left, which results in

$$\frac{\mathrm{d}}{\mathrm{d}t}\left[G_{\mathcal{Q}}(-t)\mathcal{Q}\rho_{\mathrm{tot}}(t)\right] = G_{\mathcal{Q}}(-t)\mathcal{Q}\mathcal{L}\mathcal{P}\rho_{\mathrm{tot}}(t). \tag{2.9}$$

This equation can be formally integrated which, when multiplied by $G_{\mathcal{Q}}(t)$ from the left, yields

$$\mathcal{Q}\rho_{\mathrm{tot}}(t) = G_{\mathcal{Q}}(t)\mathcal{Q}\rho_{\mathrm{tot}}(0) + \int_0^t \mathrm{d}s\; G_{\mathcal{Q}}(t-s)\mathcal{Q}\mathcal{L}\mathcal{P}\rho_{\mathrm{tot}}(s). \tag{2.10}$$

Reinserting this solution into Eq. (2.7) and realizing that $\mathcal{Q}\rho_{\mathrm{tot}}(0) = 0$, due to the initial separation in Eq. (2.5), results in a single equation for $\mathcal{P}\rho_{\mathrm{tot}}$ only

$$\mathcal{P}\dot{\rho}_{\mathrm{tot}}(t) = \mathcal{P}\mathcal{L}\mathcal{P}\rho_{\mathrm{tot}}(t) + \int_0^t \mathrm{d}s\; \mathcal{P}\mathcal{L}G_{\mathcal{Q}}(t-s)\mathcal{Q}\mathcal{L}\mathcal{P}\rho_{\mathrm{tot}}(s). \tag{2.11}$$

Using $\mathcal{P}\mathcal{L}\mathcal{P} = \mathcal{L}_{\mathrm{S}}\mathcal{P}$, $\mathcal{P}\mathcal{L}\mathcal{Q} = \mathcal{P}\mathcal{L}_{\mathrm{tun}}$ and $\mathcal{Q}\mathcal{L}\mathcal{P} = \mathcal{L}_{\mathrm{tun}}\mathcal{P}$ results in the so called Nakajima-Zwanzig equation

$$\mathcal{P}\dot{\rho}_{\mathrm{tot}}(t) = \mathcal{L}_{\mathrm{S}}\mathcal{P}\rho_{\mathrm{tot}}(t) + \int_0^t \mathrm{d}s\; \mathcal{K}(t-s)\mathcal{P}\rho_{\mathrm{tot}}(s), \tag{2.12}$$

with the Kernel superoperator $\mathcal{K}(t) = \mathcal{P}\mathcal{L}_{\mathrm{tun}}\bar{G}_{\mathcal{Q}}(t)\mathcal{L}_{\mathrm{tun}}\mathcal{P}$. Here, we have introduced $\bar{G}_{\mathcal{Q}}(t) = e^{(\mathcal{L}_{\mathrm{S}}+\mathcal{L}_{\mathrm{B}}+\mathcal{Q}\mathcal{L}_{\mathrm{tun}}\mathcal{Q})t}$ by using the identity $G_{\mathcal{Q}}(t)\mathcal{Q} = \bar{G}_{\mathcal{Q}}(t)\mathcal{Q}$. This equation describes the full non-markovian dynamics to all orders in the tunneling Hamiltonian $\hat{H}_{\mathrm{tun}}$ and even considers the entangled part of the density matrix $\mathcal{Q}\rho_{\mathrm{tot}}$ exactly via the propagator $\bar{G}_{\mathcal{Q}}$ in the Kernel. In experiments often the exact time dynamics stays unresolved and only the steady state is measured.

2.2.2 Stationary solution

The Nakajima-Zwanzig equation (2.12) can be simplified by performing a Laplace transformation $\tilde{f}(\lambda) = \int_0^\infty \mathrm{d}t f(t)e^{-\lambda t}$. For the steady state of the QD, $\rho(t\to\infty) = \rho^\infty$ with $\dot{\rho}^\infty = 0$, the convolution of the Kernel with the density matrix becomes a simple product $\int_0^\infty \mathrm{d}s\; \mathcal{K}(t-s)\mathcal{P}\rho_{\mathrm{tot}}(s) = \tilde{\mathcal{K}}(\lambda)\mathcal{P}\tilde{\rho}_{\mathrm{tot}}(\lambda)$. Using the final value theorem $\lim_{t\to\infty} f(t) = \lim_{\lambda\to 0^+} \lambda\tilde{f}(\lambda)$, after multiplying the Nakajima-Zwanzig equation by λ, we obtain the master equation for the stationary solution

$$\begin{aligned} 0 &= \lim_{\lambda\to 0^+} \left(\mathcal{L}_{\mathrm{S}} + \tilde{\mathcal{K}}(\lambda)\right)\mathcal{P}\tilde{\rho}_{\mathrm{tot}}(\lambda) \\ 0 &= \mathcal{L}\rho^\infty = \left(\mathcal{L}_{\mathrm{S}} + K\right)\rho^\infty. \end{aligned} \tag{2.13}$$

In the last step we used that fact that in this equation the RDM of the bath at equilibrium, ρ_{B}, enters only via an overall tensor product and can be traced out. This results in an equation of motion for the RDM of the system ρ. Thereby, we have introduced the Liouvillian for the RDM as the sum of the coherent part $\mathcal{L}_S$ and the Kernel

$$K\rho^{\infty} = \lim_{\lambda\to 0^+} \mathrm{tr}_{\mathrm{B}} \left\{ \mathcal{L}_{\mathrm{tun}} \tilde{G}_Q(\lambda) \mathcal{L}_{\mathrm{tun}} \rho^{\infty} \otimes \rho_B \right\}. \tag{2.14}$$

In this Kernel the Laplace transform of the propagator $\bar{G}_{\mathcal{Q}}(t)$ enters which reads $\tilde{G}_Q(\lambda) = [\lambda - \mathcal{L}_{\mathrm{S}} - \mathcal{L}_{\mathrm{B}} - \mathcal{Q}\mathcal{L}_{\mathrm{tun}}\mathcal{Q}]^{-1}$. Using the Laplace transform of the free propagator $\tilde{G}_0 = \lim_{\lambda\to 0^+} \tilde{G}_0(\lambda) = \lim_{\lambda\to 0^+} [\lambda - \mathcal{L}_{\mathrm{S}} - \mathcal{L}_{\mathrm{B}}]^{-1}$, this Kernel is expanded to all powers of $\mathcal{L}_{\mathrm{tun}}$ as a geometric series (cfg. App. A)

$$K\rho^{\infty} = \mathrm{tr}_B \left\{ \mathcal{L}_{\mathrm{tun}} \sum_{n=0}^{\infty} \left(\tilde{G}_0 \mathcal{Q} \mathcal{L}_{\mathrm{tun}} \mathcal{Q} \right)^{2n} \tilde{G}_0 \mathcal{L}_{\mathrm{tun}} \rho^{\infty} \otimes \rho_B \right\}. \tag{2.15}$$

Since $\mathcal{P}\mathcal{L}_{\mathrm{tun}}^{2n+1}\mathcal{P} = 0$ for $n \in \mathbb{N}$, only an even number of $\mathcal{L}_{\mathrm{tun}}$ survives the trace. Using this quantum master equation to solve for ρ^{∞}, it is possible to calculate the main object of interest, the current.

2.2.3 Current

As introduced in the beginning of this chapter, the current is given by the expectation value of the current operator. Since observables do not depend on time in the Schrödinger picture, it is convenient to transform the current operator in the Heisenberg picture $\hat{I}_l^H(t) = U^{\dagger}(t)\hat{I}_l U(t)$ using the time-evolution operator $U(t) = e^{-i\hat{H}t/\hbar}$.

$$\hat{I}_l^H = e\dot{\hat{N}}_l^H = e\frac{i}{\hbar}\left[\hat{H}_{\mathrm{tun}}^H, \hat{N}_l^H\right], \quad \Rightarrow \quad \hat{I}_l = -e\frac{i}{\hbar}\sum_{l\sigma\boldsymbol{k}p} c_{l\sigma\boldsymbol{k}}^{p} D_{l\sigma}^{\bar{p}}, \tag{2.16}$$

where $\hat{N}_l = \sum_{\sigma\boldsymbol{k}} c_{l\sigma\boldsymbol{k}}^{\dagger} c_{l\sigma\boldsymbol{k}}$ is the particle number operator of lead l in the Schrödinger picture. This operator contains an odd number of lead operators such that its expectation value only acts on the entangled part, similarly to the tunneling Liouvillian,

$$I_l = \langle \hat{I}_l^H \rangle = \langle \hat{I}_l \rangle = \mathrm{tr}\left\{ \hat{I}_l \rho_{\mathrm{tot}} \right\} = \mathrm{tr}\left\{ \hat{I}_l \mathcal{Q}\rho_{\mathrm{tot}} \right\}. \tag{2.17}$$

Using the solution for the entangled part of the density matrix in the Nakajima-Zwanzig approach in Eq. (2.10), we obtain

$$I_l = \mathrm{tr}\left\{ \hat{I}_l \int_0^t \mathrm{d}s\, G_Q(t-s)\mathcal{Q}\mathcal{L}\mathcal{P}\rho_{\mathrm{tot}}(s) \right\} = \mathrm{tr}\left\{ \int_0^t \mathrm{d}s\, \mathcal{K}_l^I(t-s)\mathcal{P}\rho_{\mathrm{tot}}(s) \right\}, \tag{2.18}$$

with the current Kernel $\mathcal{K}_l^I(t) = \mathcal{P}\hat{I}_l\bar{G}_{\mathcal{Q}}(t)\mathcal{L}_{\rm tun}\mathcal{P}$ and $K_l^I = \lim_{\lambda\to 0^+}\tilde{\mathcal{K}}_l^I(\lambda)$. Since this current Kernel is similar to the Kernel for the RDM, following the steps of the previous sections, the stationary current can be obtained in Laplace space

$$I_l^\infty = \mathrm{tr}_{\rm S}\left\{K_l^I\rho^\infty\right\} = \mathrm{tr}_{\rm S+B}\left\{\hat{I}_l\sum_{n=0}^{\infty}\left(\tilde{G}_0\mathcal{Q}\mathcal{L}_{\rm tun}\mathcal{Q}\right)^{2n}\tilde{G}_0\mathcal{L}_{\rm tun}\rho^\infty\otimes\rho_{\rm B}\right\}. \quad (2.19)$$

Depending on the strength of the tunneling it can be sufficient to cut the series for the RDM in Eq. (2.15) and the expression for the current in Eq. (2.19) at a certain order.

2.3 Weak coupling limit

In this thesis we mostly work in the weak coupling limit where the tunneling rate is small compared to temperature and the charging energy $\hbar\Gamma \ll k_{\rm B}T, U$. The exact form of these rates will be introduced later in this section. This allows us to simplify the Kernel even further. The simplest case of a second order expansion $\mathcal{O}(\mathcal{L}_{\rm tun}^2) = \mathcal{O}(\hat{H}_{\rm tun}^2)$ is the so called sequential tunneling limit.

2.3.1 Sequential tunneling

Cutting the full Kernel from Eq. (2.15) to second order $K = K^{(2)} + \mathcal{O}(\hat{H}_{\rm tun}^4)$ we obtain the sequential tunneling Kernel

$$K^{(2)}\rho^\infty = \mathrm{tr}_{\rm B}\left\{\mathcal{L}_{\rm tun}\frac{1}{0^+ - \mathcal{L}_{\rm S} - \mathcal{L}_{\rm B}}\mathcal{L}_{\rm tun}\rho^\infty\otimes\rho_{\rm B}\right\}. \quad (2.20)$$

To account for the superoperatorial form of the Liouvillians, we introduce the following shorthand notation

$$[X,\rho] = X\rho - \rho X =: X^+\rho - X^-\rho = \sum_\alpha \alpha X^\alpha\rho, \quad (2.21)$$

with the convention that $\alpha = +$ corresponds to $X^+\rho =: X\rho$ and $\alpha = -$ corresponds to $X^-\rho =: \rho X$. This allows us to write the tunneling Liouvillian as

$$\begin{aligned}\mathcal{L}_{\rm tun}X &= -\frac{i}{\hbar}\left(\hat{H}_{\rm tun}X - X\hat{H}_{\rm tun}\right) = -\frac{i}{\hbar}\sum_{l\sigma\boldsymbol{k}p} p\left(c_{l\sigma\boldsymbol{k}}^p D_{l\sigma}^{\bar{p}}X - Xc_{l\sigma\boldsymbol{k}}^p D_{l\sigma}^{\bar{p}}\right)\\ &=: -\frac{i}{\hbar}\sum_{l\sigma\boldsymbol{k}p} p\left(c_{l\sigma\boldsymbol{k}}^{p,+}D_{l\sigma}^{\bar{p},+} + c_{l\sigma\boldsymbol{k}}^{p,-}D_{l\sigma}^{\bar{p},-}\right)X = -\frac{i}{\hbar}\sum_{l\sigma\boldsymbol{k}p\alpha} p\; c_{l\sigma\boldsymbol{k}}^{p,\alpha}D_{l\sigma}^{\bar{p},\alpha}\; X.\end{aligned} \quad (2.22)$$

The minus sign from the anticommutator with the tunneling Hamiltinian is canceled by the minus sign arising from the ordering of the operators $X^\alpha Y^\alpha = \alpha(XY)^\alpha$, using $\{c^p_{l\sigma\boldsymbol{k}}, D^{\bar{p}}_{l\sigma}\} = 0$. The rightmost bath operator in the Kernel creates or destroys an electron with energy $\xi_{l\boldsymbol{k}}$ and thereby defines the action of the bath Liouvillian in the denominator

$$K^{(2)}\rho^\infty = -\frac{i}{\hbar}\sum_{\substack{ll'\sigma\sigma'\boldsymbol{k}\boldsymbol{k}'\\ pp'\alpha\alpha'}} pp' \mathrm{tr}_\mathrm{B}\left\{c^{p,\alpha}_{l\sigma\boldsymbol{k}} D^{\bar{p},\alpha}_{l\sigma} \frac{1}{i0^+ - i\hbar\mathcal{L}_\mathrm{S} - p'\xi_{l\boldsymbol{k}}} c^{p',\alpha'}_{l'\sigma'\boldsymbol{k}'} D^{\bar{p}',\alpha'}_{l'\sigma'} \rho^\infty \otimes \rho_\mathrm{B}\right\}. \tag{2.23}$$

This allows us to separate the system and bath operators by using the commutation rule for superoperators $X^\alpha Y^{\alpha'} = -\alpha\alpha' Y^{\alpha'} X^\alpha$ (for a derivation see App. A) and the fact that the bath operators commute with the system Liouvillian and the RDM of the system. We obtain

$$\begin{aligned} K^{(2)}\rho^\infty = \frac{i}{\hbar}\sum_{\substack{ll'\sigma\sigma'\boldsymbol{k}\boldsymbol{k}'\\ pp'\alpha\alpha'}} \alpha\alpha' pp' D^{\bar{p},\alpha}_{l\sigma} \frac{1}{i0^+ - i\hbar\mathcal{L}_\mathrm{S} - p'\xi_{l\boldsymbol{k}}} D^{\bar{p}',\alpha'}_{l'\sigma'} \rho^\infty \\ \mathrm{tr}_\mathrm{B}\left\{c^{p,\alpha}_{l\sigma\boldsymbol{k}} c^{p',\alpha'}_{l'\sigma'\boldsymbol{k}'} \rho_\mathrm{B}\right\}. \end{aligned} \tag{2.24}$$

We can perform the partial trace over the bath using the bath correlators of the Fermi-Dirac statistics

$$\langle c^{p,\alpha}_{l\sigma\boldsymbol{k}} c^{p',\alpha'}_{l'\sigma'\boldsymbol{k}'}\rangle = \mathrm{tr}_\mathrm{B}\left\{c^{p,\alpha}_{l\sigma\boldsymbol{k}} c^{p',\alpha'}_{l'\sigma'\boldsymbol{k}'}\rho_\mathrm{B}\right\} = \delta_{ll'}\delta_{\sigma\sigma'}\delta_{\boldsymbol{k}\boldsymbol{k}'}\delta_{p\bar{p}'} f_l^{p\alpha'}(\xi_{l\boldsymbol{k}}), \tag{2.25}$$

with the Fermi functions $f_l^+(\epsilon) = 1/(e^{(\epsilon-\mu_l)/k_\mathrm{B}T}+1)$ and $f_l^-(\epsilon) = 1 - f_l^+(\epsilon)$. Utilizing the periodicity of the trace the result must be independent of the first bath operator. The sum over the momentum $\boldsymbol{k}$ can be replaced by an integral over the bath energy $\xi_{l\boldsymbol{k}} := \epsilon$. We obtain

$$K^{(2)}\rho^\infty = -\frac{i}{\hbar}\sum_{l\sigma p\alpha\alpha'} \alpha\alpha' \int_{-\infty}^{\infty} \mathrm{d}\epsilon\; D^{\bar{p},\alpha}_{l\sigma} \frac{f_l^{p\alpha'}(\epsilon) g_l(\epsilon)}{i0^+ - i\hbar\mathcal{L}_\mathrm{S} + p\epsilon} D^{p,\alpha'}_{l\sigma} \rho^\infty, \tag{2.26}$$

with the density of states $g_l(\epsilon)$ of lead l.

Let us assume that the system Hamiltonian $\hat{H}_\mathrm{S}$ is diagonalized with a set of eigenenergies E and corresponding eigenstates $|NEi\rangle$, where i is a set of quantum numbers which, together with the particle number N, uniquely defines all many-body states. We introduce the projectors onto the corresponding subspaces with these energies as $\Pi(E) = \sum_{N,i} |NEi\rangle\langle NEi|$. This allows us to project all operators on subspaces with fixed energy difference ω,

$$X(\omega) = \sum_{E,E'} \Pi(E) X\, \Pi(E')\delta_{E-E',\omega}. \tag{2.27}$$

We use this way of symbolizing the projection, even though ω is not a continuous variable, but a discrete one. Additionally, if X is a superoperator, we use

$$X^{\alpha}(\omega) = \sum_{E,E'} \left[\Pi(E) X \ \Pi(E')\right]^{\alpha} \delta_{E-E',\omega}. \tag{2.28}$$

The original operators can be recovered by summing over all frequencies $\sum_{\omega} X^{\alpha}(\omega) = \sum_{\omega} X^{\alpha}(-\omega) = X^{\alpha}$, since the eigenstates form a complete set. Using this notation it holds $[D_{l\sigma}^{p,\alpha}(\omega)]^{\dagger} = D_{l\sigma}^{\bar{p},\alpha}(-\omega)$. The possibility to keep the same set of frequencies for creation and annihilation operators, motivates the choice of replacing $D_{l\sigma}^{p,\alpha} \to \sum_{\omega} D_{l\sigma}^{p,\alpha}(p\omega)$.

$$K^{(2)}\rho^{\infty} = -\frac{i}{\hbar} \sum_{\substack{l\sigma p\alpha\alpha' \\ \omega\omega'\omega''}} \alpha\alpha' \int_{-\infty}^{\infty} \mathrm{d}\epsilon \ D_{l\sigma}^{\bar{p},\alpha}(\bar{p}\omega) \frac{f_l^{p\alpha'}(\epsilon) g_l(\epsilon)}{i0^+ - i\hbar\mathcal{L}_{\mathrm{S}} + p\epsilon} D_{l\sigma}^{p,\alpha'}(p\omega')\rho^{\infty}(\omega''). \tag{2.29}$$

Since the RDM of the system can be non-diagonal in energy, let us focus on a subspace of fixed energy difference $\tilde{\omega}$ of the RDM. The overall energy difference has to be the same on both sides of the equation, $\tilde{\omega} = \bar{p}\omega + p\omega' + \omega''$, which fixes e.g. ω''. Therefore, this equation yields

$$\begin{aligned}\left[K^{(2)}\rho^{\infty}\right](\tilde{\omega}) = -\frac{i}{\hbar} \sum_{\substack{l\sigma p\alpha\alpha' \\ \omega\omega'}} \alpha\alpha' \int_{-\infty}^{\infty} \mathrm{d}\epsilon \ D_{l\sigma}^{\bar{p},\alpha}(\bar{p}\omega) \frac{f_l^{p\alpha'}(\epsilon) g_l(\epsilon)}{i0^+ - i\hbar\mathcal{L}_{\mathrm{S}} + p\epsilon} \\ D_{l\sigma}^{p,\alpha'}(p\omega')\rho^{\infty}(\tilde{\omega} + p(\omega - \omega')).\end{aligned} \tag{2.30}$$

All this determines the action of the system Liouvillian in the denominator (see App. A)

$$\begin{aligned}\left[K^{(2)}\rho^{\infty}\right](\tilde{\omega}) = -\frac{i}{\hbar} \sum_{\substack{l\sigma p\alpha\alpha' \\ \omega\omega'}} \alpha\alpha' \int_{-\infty}^{\infty} \mathrm{d}\epsilon \ D_{l\sigma}^{\bar{p},\alpha}(\bar{p}\omega) \frac{f_l^{p\alpha'}(\epsilon) g_l(\epsilon)}{i0^+ + p(\epsilon - \omega - p\tilde{\omega})} \\ D_{l\sigma}^{p,\alpha'}(p\omega')\rho^{\infty}(\tilde{\omega} + p(\omega - \omega')).\end{aligned} \tag{2.31}$$

The energy integral can be split into a real and an imaginary part by using the Sokhotski-Plemelj theorem for integrals over the real line

$$\int_{-\infty}^{\infty} \mathrm{d}\epsilon \ \frac{h(\epsilon)}{i0^+ \pm (\epsilon - \omega)} = -i\pi h(\omega) \pm p.v. \int_{-\infty}^{\infty} \mathrm{d}\epsilon \ \frac{h(\epsilon)}{\epsilon - \omega}, \tag{2.32}$$

where $p.v.$ denotes the Cauchy principal value. This theorem is closely related to the Kramers-Kronig relations but does not require analyticity of the function

h in the complex plane. If the density of states is flat in the important regions around the Fermi Energy E_F, we can assume the so called wide band limit with $g_l(\epsilon) \approx g_l(E_\mathrm{F}) = g_l$. The principal value integral over the Fermi function can now be performed analytically, when regularizing it with a Lorentzian. The calculation can be found in the dissertation of Koller [45], which allows us to write

$$\begin{aligned}\left[K^{(2)}\rho^\infty\right](\tilde{\omega}) = -\frac{\pi}{\hbar}\sum_{\substack{l\sigma p\alpha\alpha'\\ \omega\omega'}} \alpha\left[\alpha' f_l^{p\alpha'}(\omega + p\tilde{\omega}) - \frac{i}{\pi}p_l(\omega + p\tilde{\omega})\right] g_l \\ D_{l\sigma}^{\bar{p},\alpha}(\bar{p}\omega) D_{l\sigma}^{p,\alpha'}(p\omega')\rho^\infty(\tilde{\omega} + p(\omega - \omega')).\end{aligned} \tag{2.33}$$

The principal value integral results in $p_l(\omega) = -\operatorname{Re}\psi[1/2 + i(\omega - \mu_l)/2\pi k_\mathrm{B}T]$, where ψ is the digamma function. Finally, we insert back the definitions $D_{l\sigma}^- = \sum_\eta t_{l\eta} d_{\eta\sigma}$ and $D_{l\sigma}^+ = \sum_\eta t_{l\eta}^* d_{\eta\sigma}^\dagger$ and define the single particle tunneling rate matrix as

$$(\mathbf{\Gamma}_l)_{\eta\eta'} = \frac{2\pi}{\hbar} g_l t_{l\eta} t_{l\eta'}^*. \tag{2.34}$$

The master equation then explicitly reads

$$\begin{aligned}0 = \dot{\rho}^\infty(\tilde{\omega}) = [\mathcal{L}\rho^\infty](\tilde{\omega}) = -\frac{i}{\hbar}\underbrace{\left[\hat{H}_\mathrm{S}, \rho^\infty\right](\tilde{\omega})}_{\tilde{\omega}\rho^\infty(\tilde{\omega})} - \frac{1}{2}\sum_{\substack{l\sigma\eta\eta'\\ \omega\omega'}} (\mathbf{\Gamma}_l)_{\eta\eta'}\Bigg\{ \\ \left[f_l^+(\omega + \tilde{\omega}) - \frac{i}{\pi}p_l(\omega + \tilde{\omega})\right] \times \\ \left[d_{\eta\sigma}(-\omega) d_{\eta'\sigma}^\dagger(\omega')\rho^\infty(\tilde{\omega} + \omega - \omega') - d_{\eta'\sigma}^\dagger(\omega')\rho^\infty(\tilde{\omega} + \omega - \omega') d_{\eta\sigma}(-\omega)\right] \\ + \left[f_l^+(\omega - \tilde{\omega}) + \frac{i}{\pi}p_l(\omega - \tilde{\omega})\right] \times \\ \left[\rho^\infty(\tilde{\omega} - \omega + \omega') d_{\eta\sigma}(-\omega') d_{\eta'\sigma}^\dagger(\omega) - d_{\eta'\sigma}^\dagger(\omega)\rho^\infty(\tilde{\omega} - \omega + \omega') d_{\eta\sigma}(-\omega')\right] \\ + \left[f_l^-(\omega - \tilde{\omega}) - \frac{i}{\pi}p_l(\omega - \tilde{\omega})\right] \times \\ \left[d_{\eta'\sigma}^\dagger(\omega) d_{\eta\sigma}(-\omega')\rho^\infty(\tilde{\omega} - \omega + \omega') - d_{\eta\sigma}(-\omega')\rho^\infty(\tilde{\omega} - \omega + \omega') d_{\eta'\sigma}^\dagger(\omega)\right] \\ + \left[f_l^-(\omega + \tilde{\omega}) + \frac{i}{\pi}p_l(\omega + \tilde{\omega})\right] \times \\ \left[\rho^\infty(\tilde{\omega} + \omega - \omega') d_{\eta'\sigma}^\dagger(\omega') d_{\eta\sigma}(-\omega) - d_{\eta\sigma}(-\omega)\rho^\infty(\tilde{\omega} + \omega - \omega') d_{\eta'\sigma}^\dagger(\omega')\right]\Bigg\}.\end{aligned} \tag{2.35}$$

Now we proceed with the same steps for the current while keeping in mind that the superoperator index of the current operator is $\alpha = +$. Furthermore,

we know that the system trace only selects the diagonal elements of the RDM, $\mathrm{tr_S}\{\sum_{\tilde{\omega}} \rho^{\infty}(\tilde{\omega})\} = \mathrm{tr_S}\{\rho^{\infty}(0)\}$. Therefore, we obtain

$$
\begin{aligned}
I_l^{\infty} &= \mathrm{tr_{S+B}}\left\{\hat{I}_l \frac{1}{0^+ - \mathcal{L}_\mathrm{S} - \mathcal{L}_\mathrm{B}} \mathcal{L}_\mathrm{tun}\rho^{\infty}\rho_\mathrm{B}\right\} \\
&= e\frac{i}{\hbar}\mathrm{tr_S}\left\{\sum_{\substack{\sigma p\alpha' \\ \omega\omega'}} p\alpha' \int_{-\infty}^{\infty} \mathrm{d}\epsilon\; D_{l\sigma}^{\bar{p},+}(\bar{p}\omega)\frac{f_l^{p\alpha'}(\epsilon)g_l(\epsilon)}{i0^+ + p(\epsilon-\omega)} D_{l\sigma}^{p,\alpha'}(p\omega')\rho^{\infty}(p(\omega-\omega'))\right\} \\
&= e\frac{\pi}{\hbar}\mathrm{tr_S}\left\{\sum_{\sigma p\alpha'\omega\omega'} p\left[\alpha' f_l^{p\alpha'}(\omega) - \frac{i}{\pi}p_l(\omega)\right] g_l \right. \\
&\qquad\qquad \left. D_{l\sigma}^{\bar{p},+}(\bar{p}\omega) D_{l\sigma}^{p,\alpha'}(p\omega')\rho^{\infty}(p(\omega-\omega'))\right\} \\
&= \frac{e}{2}\sum_{\sigma\eta\eta'\omega\omega'} (\mathbf{\Gamma}_l)_{\eta\eta'}\mathrm{tr_S}\Big\{ \\
&\quad f_l^{+}(\omega)\left[d_{\eta'\sigma}^{\dagger}(\omega)\rho^{\infty}(\omega'-\omega)d_{\eta\sigma}(-\omega') + d_{\eta'\sigma}^{\dagger}(\omega')\rho^{\infty}(\omega-\omega')d_{\eta\sigma}(-\omega)\right] \\
&- f_l^{-}(\omega)\left[d_{\eta\sigma}(-\omega)\rho^{\infty}(\omega-\omega')d_{\eta'\sigma}^{\dagger}(\omega') + d_{\eta\sigma}(-\omega')\rho^{\infty}(\omega'-\omega)d_{\eta'\sigma}^{\dagger}(\omega)\right] \\
&+ \frac{i}{\pi}p_l(\omega)\Big[d_{\eta'\sigma}^{\dagger}(\omega)\rho^{\infty}(\omega'-\omega)d_{\eta\sigma}(-\omega') - d_{\eta'\sigma}^{\dagger}(\omega')\rho^{\infty}(\omega-\omega')d_{\eta\sigma}(-\omega) \\
&\qquad + d_{\eta\sigma}(-\omega')\rho^{\infty}(\omega'-\omega)d_{\eta'\sigma}^{\dagger}(\omega) - d_{\eta\sigma}(-\omega)\rho^{\infty}(\omega-\omega')d_{\eta'\sigma}^{\dagger}(\omega')\Big]\Big\}.
\end{aligned}
\tag{2.36}
$$

While this expression seems peculiar at first glance due to the imaginary principal parts, the operator inside the trace is hermitian such that its trace is purely real.

The computation of the current requires the calculation of the full density matrix which, depending on the system size, can be numerically demanding as the Liouvillian has dimension N^4 where N is the size of the Hilbert space. Fortunately often not all coherences are required, reducing the numerical effort drastically.

2.3.2 Coherences and the secular approximation

There exist selection rules which allow to set certain coherences to zero and exclude them completely from the dynamics. In particular, if two states $|a\rangle$ and $|b\rangle$ differ only by a quantum number, associated to a variable which is conserved in the total system, the coherence $\langle a|\,\rho\,|b\rangle = 0$ can be excluded. Especially the total charge is always conserved, which for normal leads goes along with

a block structure in the number of particles of the RDM. Additionally, in this thesis we already have assumed that the leads are unpolarized or at least polarized along a certain projection direction of the spin such that the RDM is also diagonal in this spin projection. Overall it assumes the form

$$\rho = \left(\quad \right), \tag{2.37}$$

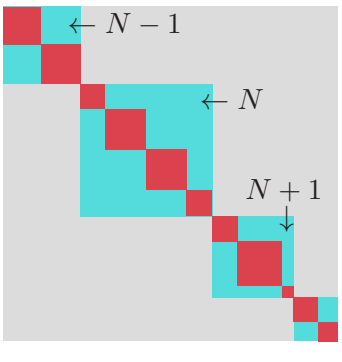

where the grey areas are zero due to the block structure in charge. Inside these blocks of constant particle number further blocks can develop as indicated in red. These can be either blocks of same spin, additional conserved quantities or, as seen in a moment, the energy.

The Bohr frequencies ω define another energy scale in the system which, in relation to the tunneling rates, can justify further elimination of coherences using the secular approximation. Already at the level of the Nakajima-Zwanzig equation in Eq. (2.12) one can see that the Kernel is negligible for coherences between states of different energies if the tunneling rates are much smaller than this energy difference $\hbar\Gamma \ll \omega$ [46]. The equation for such a coherence approximately reads $\dot{\rho}(\omega) = -i[\hat{H}_\mathrm{S}, \rho](\omega)/\hbar = -i\omega\rho(\omega)/\hbar$, which is solved by $\rho(\omega)(t) = e^{-i\omega t/\hbar}\rho_0(\omega)$, a rapidly oscillating term for large ω. Inserting this result into the equations for the populations these oscillations will quickly average to zero on an appreciable time scale. Therefore it is sufficient to eliminate these coherences completely from the equations which is called secular or rotating wave approximation. In the master equation this translates to $\omega = \omega'$ and a RDM completely diagonal in energy, $\rho^\infty_\mathrm{sec} = \rho^\infty(0)$, which

leads to the simplification

$$\begin{aligned} 0 = \mathcal{L}\rho^{\infty}_{\mathrm{sec}} = &-\frac{i}{\hbar}\left[\hat{H}_{\mathrm{LS}}, \rho^{\infty}_{\mathrm{sec}}\right] + \sum_{l\sigma\eta\eta'\omega} (\mathbf{\Gamma}_l)_{\eta\eta'} \Bigg[\\ & f_l^+(\omega)\left(d^\dagger_{\eta'\sigma}(\omega)\rho^{\infty}_{\mathrm{sec}} d_{\eta\sigma}(-\omega) - \frac{1}{2}\left\{d_{\eta\sigma}(-\omega)d^\dagger_{\eta'\sigma}(\omega), \rho^{\infty}_{\mathrm{sec}}\right\}\right) \\ & + f_l^-(\omega)\left(d_{\eta\sigma}(-\omega)\rho^{\infty}_{\mathrm{sec}} d^\dagger_{\eta'\sigma}(\omega) - \frac{1}{2}\left\{d^\dagger_{\eta'\sigma}(\omega)d_{\eta\sigma}(-\omega), \rho^{\infty}_{\mathrm{sec}}\right\}\right)\Bigg]. \end{aligned} \tag{2.38}$$

We have introduced the Lamb shift Hamiltonian that contains all principal part integrals

$$\hat{H}_{\mathrm{LS}} = \frac{\hbar}{2\pi}\sum_{l\sigma\eta\eta'\omega} (\mathbf{\Gamma}_l)_{\eta\eta'} p_l(\omega)\left[d_{\eta\sigma}(-\omega)d^\dagger_{\eta'\sigma}(\omega) + d^\dagger_{\eta'\sigma}(\omega)d_{\eta\sigma}(-\omega)\right]. \tag{2.39}$$

Eq. (2.38) is the most common form of the second order quantum master equation since it only contains Hamiltonian and Lindblad terms of the form $X^\dagger_{\eta'}\rho^\infty X_\eta - \{X_\eta X^\dagger_{\eta'}, \rho^\infty\}/2$. In the case that no degenerate levels exist in the system the rate matrix becomes a number $\Gamma_{l,\eta} = (\mathbf{\Gamma}_l)_{\eta\eta}$ and the summation over η' can be dropped. Additionally in this case the Lamb shift Hamiltonian commutes with the RDM and therefore can be dropped as well. The current in the secular approximation is simply the difference of in- and outgoing rates, weighted with the density matrix

$$I^\infty_l = e\sum_{\sigma\eta\eta'\omega} (\mathbf{\Gamma}_l)_{\eta\eta'} \mathrm{tr}_{\mathrm{S}}\left\{f_l^+(\omega)d^\dagger_{\eta'\sigma}(\omega)\rho^{\infty}_{\mathrm{sec}} d_{\eta\sigma}(-\omega) - f_l^-(\omega)d_{\eta\sigma}(-\omega)\rho^{\infty}_{\mathrm{sec}} d^\dagger_{\eta'\sigma}(\omega)\right\}. \tag{2.40}$$

We now turn to higher order contributions to the Kernel.

2.3.3 Co-tunneling

The next leading order in the expansion of the Kernel in Eq. (2.15) is correct to fourth order in the tunneling Hamiltonian $K = K^{(2)} + K^{(4)} + \mathcal{O}(\hat{H}^6_{\mathrm{tun}})$. The fourth order Kernel reads

$$K^{(4)}\rho^\infty = \mathrm{tr}_{\mathrm{B}}\left\{\mathcal{L}_{\mathrm{tun}}\tilde{G}_0\mathcal{Q}\mathcal{L}_{\mathrm{tun}}\mathcal{Q}\tilde{G}_0\mathcal{Q}\mathcal{L}_{\mathrm{tun}}\mathcal{Q}\tilde{G}_0\mathcal{L}_{\mathrm{tun}}\ \rho^\infty\otimes\rho_{\mathrm{B}}\right\}. \tag{2.41}$$

Since $\mathcal{P}\mathcal{L}^{2n+1}_{\mathrm{tun}}\mathcal{P} = 0$ for $n \in \mathbb{N}$, only the central $\mathcal{Q}$ projectors survive in the trace. Inserting the expressions for the tunneling Liouvillains from Eq. (2.22)

and the propagators, we get

$$K^{(4)}\rho^{\infty} = \frac{1}{\hbar^4}\sum_{\substack{\{l_i\}\{\sigma_i\}\{\boldsymbol{k}_i\}\\ \{p_i\}\{\alpha_i\}}}\left(\prod_i p_i\right)\mathrm{tr}_B\Bigg\{c^{p_3,\alpha_3}_{l_3\sigma_3\boldsymbol{k}_3}D^{\bar{p}_3,\alpha_3}_{l_3\sigma_3}\frac{1}{0^+-\mathcal{L}_\mathrm{S}-\mathcal{L}_\mathrm{B}}c^{p_2,\alpha_2}_{l_2\sigma_2\boldsymbol{k}_2}D^{\bar{p}_2,\alpha_2}_{l_2\sigma_2}$$
$$\frac{1}{0^+-\mathcal{L}_\mathrm{S}-\mathcal{L}_\mathrm{B}}\mathcal{Q}c^{p_1,\alpha_1}_{l_1\sigma_1\boldsymbol{k}_1}D^{\bar{p}_1,\alpha_1}_{l_1\sigma_1}\frac{1}{0^+-\mathcal{L}_\mathrm{S}-\mathcal{L}_\mathrm{B}}c^{p_0,\alpha_0}_{l_0\sigma_0\boldsymbol{k}_0}D^{\bar{p}_0,\alpha_0}_{l_0\sigma_0}\rho^{\infty}\otimes\rho_\mathrm{B}\Bigg\}, \tag{2.42}$$

where $i\in\{0,1,2,3\}$. Using the additional commutation rules for the free propagator $[\tilde{G}_0,\mathcal{P}]=[\tilde{G}_0,\mathcal{Q}]=0$ and $\mathcal{Q}=1-\mathcal{P}$, the $\mathcal{Q}$ projector splits the expression into two parts, the full and the reducible part. Then, the Kernel is the difference of the full and the reducible part

$$\begin{aligned}K^{(4)}\rho^{\infty} = -\frac{i}{\hbar}\sum_{\substack{\{l_i\}\{\sigma_i\}\{\boldsymbol{k}_i\}\\ \{p_i\}\{\alpha_i\}}}\left(\prod_i p_i\alpha_i\right)\Bigg[&D^{\bar{p}_3,\alpha_3}_{l_3\sigma_3}\frac{1}{i0^+-i\hbar\mathcal{L}_\mathrm{S}-\sum_{j=0}^{2}p_j\xi_{l_j\boldsymbol{k}_j}}\\ &D^{\bar{p}_2,\alpha_2}_{l_2\sigma_2}\frac{1}{i0^+-i\hbar\mathcal{L}_\mathrm{S}-\sum_{j=0}^{1}p_j\xi_{l_j\boldsymbol{k}_j}}D^{\bar{p}_1,\alpha_1}_{l_1\sigma_1}\\ &\frac{1}{i0^+-i\hbar\mathcal{L}_\mathrm{S}-p_0\xi_{l_0\boldsymbol{k}_0}}D^{\bar{p}_0,\alpha_0}_{l_0\sigma_0}\rho^{\infty}\langle c^{p_3,\alpha_3}_{l_3\sigma_3\boldsymbol{k}_3}c^{p_2,\alpha_2}_{l_2\sigma_2\boldsymbol{k}_2}c^{p_1,\alpha_1}_{l_1\sigma_1\boldsymbol{k}_1}c^{p_0,\alpha_0}_{l_0\sigma_0\boldsymbol{k}_0}\rangle\\ &-D^{\bar{p}_3,\alpha_3}_{l_3\sigma_3}\frac{1}{i0^+-i\hbar\mathcal{L}_\mathrm{S}-p_2\xi_{l_2\boldsymbol{k}_2}}D^{\bar{p}_2,\alpha_2}_{l_2\sigma_2}\frac{1}{i0^+-i\hbar\mathcal{L}_\mathrm{S}}D^{\bar{p}_1,\alpha_1}_{l_1\sigma_1}\\ &\frac{1}{i0^+-i\hbar\mathcal{L}_\mathrm{S}-p_0\xi_{l_0\boldsymbol{k}_0}}D^{\bar{p}_0,\alpha_0}_{l_0\sigma_0}\rho^{\infty}\langle c^{p_3,\alpha_3}_{l_3\sigma_3\boldsymbol{k}_3}c^{p_2,\alpha_2}_{l_2\sigma_2\boldsymbol{k}_2}\rangle\langle c^{p_1,\alpha_1}_{l_1\sigma_1\boldsymbol{k}_1}c^{p_0,\alpha_0}_{l_0\sigma_0\boldsymbol{k}_0}\rangle\Bigg].\end{aligned} \tag{2.43}$$

Extending Wick's theorem for fermionic operators of noninteracting particles to superoperators (for derivation see App. A)

$$\begin{aligned}\langle c^{\alpha_3}_3c^{\alpha_2}_2c^{\alpha_1}_1c^{\alpha_0}_0\rangle = \langle c^{\alpha_3}_3c^{\alpha_2}_2\rangle\langle c^{\alpha_1}_1c^{\alpha_0}_0\rangle&-\alpha_1\alpha_2\langle c^{\alpha_3}_3c^{\alpha_1}_1\rangle\langle c^{\alpha_2}_2c^{\alpha_0}_0\rangle\\ &+\alpha_1\alpha_2\langle c^{\alpha_3}_3c^{\alpha_0}_0\rangle\langle c^{\alpha_2}_2c^{\alpha_1}_1\rangle,\end{aligned} \tag{2.44}$$

and applying it to the full part of the Kernel enables further simplification, since the reducible part exactly cancels with the first group of the Wick theorem. Therefore, the $\mathcal{Q}$ projectors specifically rule out the reducible part and only

leave an irreducible part

$$K^{(4)}\rho^{\infty} = \frac{i}{\hbar} \sum_{\substack{l_0 l_1 \sigma_0 \sigma_1 \\ p_0 p_1 \{\alpha_i\}}} \alpha_3 \alpha_0 \int_{-\infty}^{\infty} \mathrm{d}\epsilon_0 \int_{-\infty}^{\infty} \mathrm{d}\epsilon_1 \Bigg[D^{p_1,\alpha_3}_{l_1\sigma_1} \frac{f^{-p_1\alpha_1}_{l_1}(\epsilon_1) g_{l_1}(\epsilon_1)}{i0^+ - i\hbar\mathcal{L}_{\mathrm{S}} - p_1\epsilon_1} D^{p_0,\alpha_2}_{l_0\sigma_0}$$
$$\frac{1}{i0^+ - i\hbar\mathcal{L}_{\mathrm{S}} - \sum_{j=0}^{1} p_j\epsilon_j} D^{\bar{p}_1,\alpha_1}_{l_1\sigma_1} \frac{f^{-p_0\alpha_0}_{l_0}(\epsilon_0) g_{l_0}(\epsilon_0)}{i0^+ - i\hbar\mathcal{L}_{\mathrm{S}} - p_0\epsilon_0} D^{\bar{p}_0,\alpha_0}_{l_0\sigma_0} \rho^{\infty}$$
$$- D^{p_0,\alpha_3}_{l_0\sigma_0} \frac{f^{-p_1\alpha_1}_{l_1}(\epsilon_1) g_{l_1}(\epsilon_1)}{i0^+ - i\hbar\mathcal{L}_{\mathrm{S}} - p_0\epsilon_0} D^{p_1,\alpha_2}_{l_1\sigma_1}$$
$$\frac{1}{i0^+ - i\hbar\mathcal{L}_{\mathrm{S}} - \sum_{j=0}^{1} p_j\epsilon_j} D^{\bar{p}_1,\alpha_1}_{l_1\sigma_1} \frac{f^{-p_0\alpha_0}_{l_0}(\epsilon_0) g_{l_0}(\epsilon_0)}{i0^+ - i\hbar\mathcal{L}_{\mathrm{S}} - p_0\epsilon_0} D^{\bar{p}_0,\alpha_0}_{l_0\sigma_0} \rho^{\infty} \Bigg]. \tag{2.45}$$

These integrals can still be performed analytically when the density of states is flat. We will analyze an exemplary Kernel element in Sec. 2.6.3 and show that the superoperator approach yields exactly the same results as found in the dissertation of Koller [45]. All results are not shown here since they are quite lengthy but can be found in said thesis. Also the current Kernel for lead l can be obtained following the same steps. The only differences with respect to the Kernel are the replacements of $\alpha_3 \to p_1$ and $D^{p_1,\alpha_3}_{l_1\sigma_1} \to D^{p_1,+}_{l\sigma_1}$ and the additional trace over the system. The secular approximation is only valid for terms containing the highest order in the expansion of the series of the Kernel. However, it was shown by Leijnse and Wegewijs [47] that these non-secular terms produce correction of the order of $\hbar\Gamma$ and can be effectively accounted for while still neglecting coherences between non-degenerate states. In the course of this thesis we use a program called KinEq which was written by M. Leijnse, M. R. Wegewijs and S. Koller [45, 48]. It includes all second and fourth order terms within the secular approximation.

2.3.4 Remarks

In this section we will highlight some interesting properties and relations of the second order quantum master equation as well as some tools for effective analytical and numerical analysis.

2.3.4.1 Infinite bias limit

Often the exact gate and bias voltage dependence is not the main object of interest, especially when one can effectively reduce the dimension of the

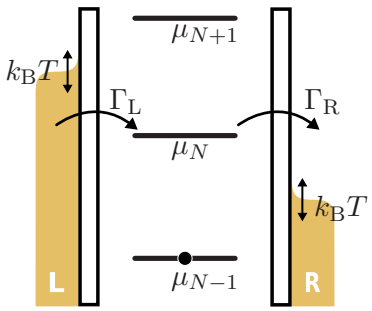

Figure 2.2: Chemical potential landscape in the infinite bias limit. The bias voltage is large enough that all chemical potentials of the systems are far away, compared to the temperature, from the chemical potentials of the leads. All channels above and below both reservoirs stay unchanged, leading to an effectively reduced Fock space and unidirectional transport.

Fock space due to strong interaction. Then the current reaches plateaus of constant height where the Fermi functions can be approximated as Heaviside step functions, if far enough away from all resonant lines. For a large positive potential drop at the leads this means $f_\mathrm{L}^+(\omega) = f_\mathrm{R}^-(\omega) \approx 1$ and $f_\mathrm{R}^+(\omega) = f_\mathrm{L}^-(\omega) \approx 0$. Such a situation is shown in Fig. 2.2 in a chemical potential landscape. Applying this to the master equation, including non-secular terms in Eq. (2.35) and neglecting the principal parts, results in

$$0 = \mathcal{L}\rho^\infty = -\frac{i}{\hbar}\left[\hat{H}_\mathrm{S}, \rho^\infty\right] + \sum_{\sigma\eta\eta'}\left\{(\mathbf{\Gamma}_\mathrm{L})_{\eta\eta'}\left(d^\dagger_{\eta'\sigma}\rho^\infty d_{\eta\sigma} - \frac{1}{2}\left\{d_{\eta\sigma}d^\dagger_{\eta'\sigma}, \rho^\infty\right\}\right)\right.$$
$$\left. +(\mathbf{\Gamma}_\mathrm{R})_{\eta\eta'}\left(d_{\eta\sigma}\rho^\infty d^\dagger_{\eta'\sigma} - \frac{1}{2}\left\{d^\dagger_{\eta'\sigma}d_{\eta\sigma}, \rho^\infty\right\}\right)\right\}. \quad (2.46)$$

We could replace the summation over $\tilde{\omega}$ by a summation over $\tilde{\omega}+\omega-\omega'$. Then, we obtain three independent sums in each term of tunneling part, which can be performed using $\sum_\omega X(\pm\omega) = X$. Notice that, even though this equation contains non-secular terms, it has Lindblad form. Since the eigenenergies never enter explicitly in this equation, it is also possible to transform this master equation into a different basis than the energy eigenbasis. For SETs where the central system consists of multiple QDs it is common to work in a local basis since typically the tunneling is local as well. However, the system part of the Liouvillian is not diagonal anymore and couples different local states. This method is a trade-off between comfortably writing the Liouvillian but keeping

the coherences and a numerically fast method working in the eigenbasis where the secular approximation might hold.

2.3.4.2 Time-local quantum master equation

So far we were only interested in the stationary solution ρ^∞ of the quantum master equation. However, it might be also useful to know the explicit time dependence of the RDM. This is achievable by applying the Markov approximation to the Nakajima-Zwanzig equation (2.12). Substituting the time integration by $s \to t - s$ now indicates how far back in time we go

$$\mathcal{P}\dot{\rho}_{\mathrm{tot}}(t) = \mathcal{L}_{\mathrm{S}}\mathcal{P}\rho_{\mathrm{tot}}(t) + \int_0^t \mathrm{d}s\; \mathcal{K}(s)\mathcal{P}\rho_{\mathrm{tot}}(t-s). \tag{2.47}$$

This accounts for memory effects which we assume to have a characteristic timescale τ_{B} over which bath correlations decay. The Markov approximation now assumes that these memory effects are short-lived compared to all relevant time scales of the system $\{\tau_{\mathrm{S}}\} \gg \tau_{\mathrm{B}}$ and therefore the integrand decays quickly for $s \gg \tau_{\mathrm{B}}$. This allows us to neglect the s dependence of the density matrix and extend the upper bound of the integral to ∞. This results in the time-local master equation

$$\mathcal{P}\dot{\rho}_{\mathrm{tot}}(t) = \mathcal{L}_{\mathrm{S}}\mathcal{P}\rho_{\mathrm{tot}}(t) + \underbrace{\int_0^\infty \mathrm{d}s\; \mathcal{K}(s)}_{\tilde{\mathcal{K}}(0^+)}\mathcal{P}\rho_{\mathrm{tot}}(t),$$

$$\dot{\rho} = \mathcal{L}\rho = (\mathcal{L}_{\mathrm{S}} + K)\,\rho. \tag{2.48}$$

In the case of sequential tunneling and simple tunneling systems, the bath correlation time is mostly given by the temperature $\tau_{\mathrm{S}} \propto \hbar/k_{\mathrm{B}}T$ [49]. The relevant timescale of the dynamics of this master equation is characterized by $\tau_{\mathrm{tun}} \propto 1/\Gamma$ which restricts the validity of the Markov approximation to $\hbar\Gamma \ll k_{\mathrm{B}}T$ which is typically fulfilled in the sequential tunneling regime. Therefore, we have shown that the derived Liouvillian also allows to calculate the Markovian time dependence of the RDM.

2.3.4.3 Time-dependent systems

An interesting extension of the derived master equation is to allow a time-dependent system Hamiltonian $\hat{H}_{\mathrm{S}}(t)$. This requires us to redefine the propa-

gator in a more general way

$$G_{\mathcal{Q}}(t,t') = \mathcal{T} e^{\mathcal{Q}\int_{t'}^{t} \mathrm{d}s\ \mathcal{L}(s)}, \tag{2.49}$$

where $\mathcal{T}$ is the time-ordering operator. This prevents from taking the simple Laplace transform and complicates the calculation. Simplifications are possible in the case of adiabatic driving or in the opposite limit of fast driving. For the former, and in the case of a periodic perturbation with frequency ω, this amounts to $\hbar\omega \ll k_{\mathrm{B}}T, \hbar\Gamma$. This approximation assumes that the system has enough time to adapt itself to the time-dependent perturbation, such that its dynamics at each time is approximately given by the instantaneous eigenstates $\hat{H}_{\mathrm{S}}(t)|n(t)\rangle \approx E_n(t)|n(t)\rangle$, instead of solving the time-dependent Schrödinger equation. This translates into an approximate constant Liouvillian in the time integral of the propagator, such that one obtains

$$G_{\mathcal{Q}}(t,t') = \mathcal{T} e^{\mathcal{Q}\int_{t'}^{t} \mathrm{d}s\ \mathcal{L}(s)} \approx e^{\mathcal{Q}\mathcal{L}(t)(t-t')}, \tag{2.50}$$

which makes a simpler treatment of the master equation possible. On the other hand, in the high frequency limit a time average of the propagator can be performed, which yields an effective time-independent problem. This case will be discussed e.g. in Sec. 6.5.

Finally, we also comment on the the infinite bias limit in the driven case. Starting from the Nakajima-Zwanzig equation, including the generalized propagator for the time-dependent system Liouvillian, this equation reads

$$\begin{aligned}
\dot{\rho}(t) &= \mathcal{L}_{\mathrm{S}}(t)\rho(t) + \int_0^t \mathrm{d}t'\ \mathcal{K}^{(2)}(t,t')\rho(t'), \\
\mathcal{K}^{(2)}(t,t')\rho(t') &= \mathrm{tr}_{\mathrm{B}}\left\{\mathcal{L}_{\mathrm{tun}}\mathcal{T} e^{\int_{t'}^{t} \mathrm{d}s\ (\mathcal{L}_{\mathrm{S}}(s)+\mathcal{L}_{\mathrm{B}})}\mathcal{L}_{\mathrm{tun}}\rho(t')\otimes\rho_{\mathrm{B}}\right\} \\
&= \sum_{\substack{ll'\sigma\sigma'\boldsymbol{k}\boldsymbol{k}' \\ pp'\alpha\alpha'}} pp' \mathrm{tr}_B\left\{c^{p,\alpha}_{l\sigma\boldsymbol{k}} D^{\bar{p},\alpha}_{l\sigma}\mathcal{T} e^{\int_{t'}^{t} \mathrm{d}s\ (\mathcal{L}_{\mathrm{S}}(s)+\mathcal{L}_{\mathrm{B}})} c^{p',\alpha'}_{l'\sigma'\boldsymbol{k}'} D^{\bar{p}',\alpha'}_{l'\sigma'}\rho(t')\otimes\rho_{\mathrm{B}}\right\}.
\end{aligned} \tag{2.51}$$

Using the fact that the system Liouvillian commutes with the bath operators at all times, we can perform the trace over the leads. At this point we apply the infinite bias limit, such that the Fermi functions are simply either one or zero, $\langle c^{p,\alpha}_{l\sigma\boldsymbol{k}} c^{p',\alpha'}_{l'\sigma'\boldsymbol{k}'}\rangle = \delta_{ll'}\delta_{\sigma\sigma'}\delta_{\boldsymbol{k}\boldsymbol{k}'}\delta_{p\bar{p}'}(\delta_{p\alpha'}\delta_{l\mathrm{L}} + \delta_{\bar{p}\alpha'}\delta_{l\mathrm{R}})$. Replacing the sum over

the momentum again by an integral, this yields

$$\begin{aligned}\mathcal{K}^{(2)}(t,t')\rho(t') &= -\sum_{l\sigma p\alpha\alpha'}\alpha\alpha'\int_{-\infty}^{\infty}\mathrm{d}\epsilon\; g_l D_{l\sigma}^{\bar{p},\alpha}\mathcal{T}e^{\int_{t'}^{t}\mathrm{d}s\;\mathcal{L}_{\mathrm{S}}(s)-ip\epsilon(t-t')/\hbar}D_{l\sigma}^{p,\alpha'}\rho(t') \\ &= -\frac{2\pi}{\hbar}\sum_{l\sigma p\alpha\alpha'}\alpha\alpha' g_l(\delta_{p\alpha'}\delta_{l\mathrm{L}}+\delta_{\bar{p}\alpha'}\delta_{l\mathrm{R}})D_{l\sigma}^{\bar{p},\alpha}D_{l\sigma}^{p,\alpha'}\delta(t-t')\rho(t).\end{aligned} \tag{2.52}$$

In this step we performed the energy integral before the time integral. We used the Fourier transform of the Dirac delta $\int_{-\infty}^{\infty}\mathrm{d}\epsilon\; e^{i\epsilon t}=2\pi\delta(t)$, to show that the complete propagator vanishes in this limit. This additionally allows us to compute the final time integral

$$\begin{aligned}\dot{\rho}(t) &= \mathcal{L}_{\mathrm{S}}(t)\rho(t)+\int_{0}^{t}\mathrm{d}t'\;\mathcal{K}^{(2)}(t,t')\rho(t') \\ &= \mathcal{L}_{\mathrm{S}}(t)\rho(t)-\frac{\pi}{\hbar}\sum_{l\sigma p\alpha\alpha'}\alpha\alpha' g_l(\delta_{p\alpha'}\delta_{l\mathrm{L}}+\delta_{\bar{p}\alpha'}\delta_{l\mathrm{R}})D_{l\sigma}^{\bar{p},\alpha}D_{l\sigma}^{p,\alpha'}\rho(t),\end{aligned} \tag{2.53}$$

where the half-sided integral results in a factor 1/2. This expression finally results in the master equation (2.46), where we have shown that it also holds for a time-dependent system Hamiltonian, since the Kernel becomes time-independent.

2.3.4.4 Liouville space

While the density matrix is easily defined in a Hilbert space as a $d\times d$ matrix, the Liouvillian is difficult to represent since it is a superoperator. The analysis of its tensor structure is complicated. A way out, is to work in the so called Liouville space, where the density matrix is mapped onto a vector $\rho\to|\rho\rangle\!\rangle$. Now, the Liouvillian can be written as a $d^2\times d^2$ matrix acting on the vector $|\rho\rangle\!\rangle$. Depending on the block structure of the RDM this size can be reduced. In this way, the coherent part of the Liouvillian can be written as $\mathcal{L}_{\mathrm{S}}=-i(\hat{H}_{\mathrm{S}}\otimes\mathbb{1}_{d\times d}-\mathbb{1}_{d\times d}\otimes\hat{H}_{\mathrm{S}})/\hbar$. In general, terms in the Liouvillian that are composed of left standing (X^+) and right standing (X^-) superoperators, one obtains the matrix $\mathcal{L}=(X^-)^T\otimes X^+$. Note that the trace over the system transforms into a scalar product $\mathrm{tr}_{\mathrm{S}}\{A\}\to\langle\!\langle 1|A\rangle\!\rangle$, where $|1\rangle\!\rangle$ is the mapped identity matrix $\mathbb{1}_{d\times d}$. This method allows for advanced numerical routines that are existing for matrices to compute the RDM.

2.3.4.5 Relaxation

Relaxation mechanisms that bring excited states into the ground state are independent of tunneling events and, in general, cannot be neglected. Even though we are not considering phonons or other processes explicitly in the system Hamiltonian, we can still introduce a phenomenological relaxation Liouvillian [50]

$$\mathcal{L}_{\mathrm{rel}}\rho = -\Gamma_{\mathrm{rel}}\left(\rho - \sum_N \rho^N_{\mathrm{th}}\mathrm{tr}\{\rho^N\}\right), \tag{2.54}$$

with the relaxation rate Γ_{rel}. This process brings the N–particle subblock ρ^N of the RDM closer to its thermal distribution ρ^N_{th}, which is given by

$$\rho^N_{\mathrm{th}} = \sum_i \frac{e^{-\beta E_{Ni}}}{\sum_j e^{-\beta E_{Nj}}} \left|Ni\right\rangle\left\langle Ni\right|, \tag{2.55}$$

where $\hat{H}_{\mathrm{S}}\left|Ni\right\rangle = E_{Ni}\left|Ni\right\rangle$. This mechanism is often the reason why in experiments transition lines between two excited states are highly suppressed and only transitions starting from the ground state are visible, e.g. in the co-tunneling excitation spectrum.

2.4 Diagrammatics

Starting from the full Kernel in Eq. (2.15) and repeatedly applying the simplifications of the previous sections it is possible to obtain a diagrammatic representation of this Kernel. In the following, we shall first recall a diagrammatics which makes use of two time lines, describing forward and backward propagation on a Keldysh contour [45, 48, 51, 52]. In a second step, we shall introduce a single time line diagrammatics which will turn out to be useful especially for higher order diagrams, due to its compactness. The two time lines diagrams are defined via the master equation for a single entry of the RDM

$$\left\langle b\right|\dot{\rho}^{\infty}\left|b'\right\rangle = \dot{\rho}^{\infty}_{bb'} = 0 = \sum_{aa'} K^{aa'}_{bb'}\,\rho^{\infty}_{aa'} =: \sum_{aa'} \left(\begin{array}{ccc} b & \longleftarrow & a \\ & & \\ b' & \longrightarrow & a' \end{array} \right) \rho^{\infty}_{aa'}. \tag{2.56}$$

The gray block in the diagram represents the sum over all possible diagrams arising from all orders of the perturbation expansion in the tunneling Hamiltonian plus all possible Wick contractions. As seen in the previous sections,

a diagram of n-th order always contains n system operators $D^{p,\alpha}_{l\sigma}$. These operators are called vertices in the diagrammatic language and are represented as a dot on a contour where the superoperator index α determines on which contour they are placed. For $\alpha = +$ the vertex is on the upper contour and for $\alpha = -$ on the lower contour. These operators are ordered in the exact same order as they appear in the equation. Performing a Wick contraction connects each two of these vertices and defines their lead, spin and direction degree of freedom. Furthermore, it introduces an integral over their bath energy together with a Fermi function, cfg. Eq. 2.45. This is indicated by a dashed line connecting the two vertices, where by convention the direction p is resolved as an arrow. Keeping the summation over the spin and lead degrees of freedom, while dropping the matrix element indices, results in eight different diagrams for the second oder Kernel

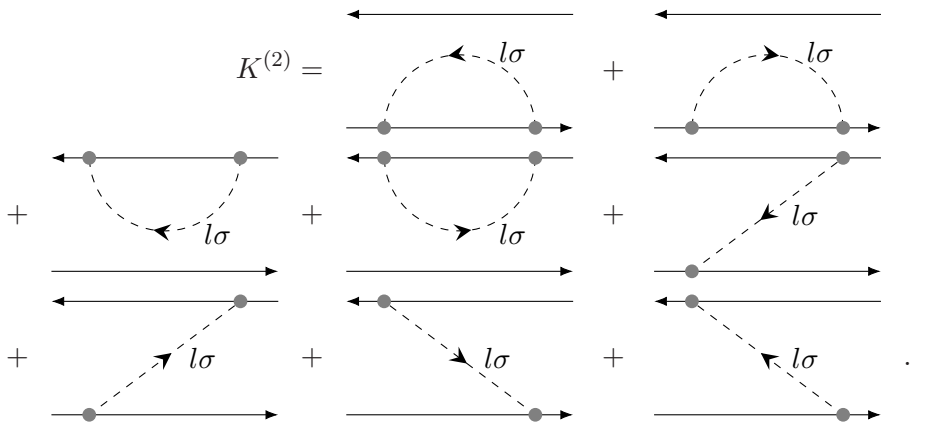

(2.57)

An n-th order diagram also contains $n-1$ propagators that can be obtained by cutting the diagram in the middle of all neighboring vertices. Its denominator is then given by the sum over all bath energies of fermion lines, that are cut, weighted by their direction p and the difference of the system energy of the upper and lower contour. The complete set of rules can be found in Koller [45] or Mantelli [53].

Let us now turn to the simplified diagrammatics which naturally arises from the superoperator formalism. Here we project the two contours onto a single contour such that each vertex has the contour index α. Additionally, we sum over the direction of the fermion lines, labeled by p. This allows us to

represent all eight second order contributions in the single diagram

$K^{(2)} =$ 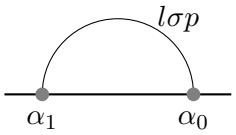

. (2.58)

The same simplifications hold for the fourth order diagrams

$K^{(4)} =$ 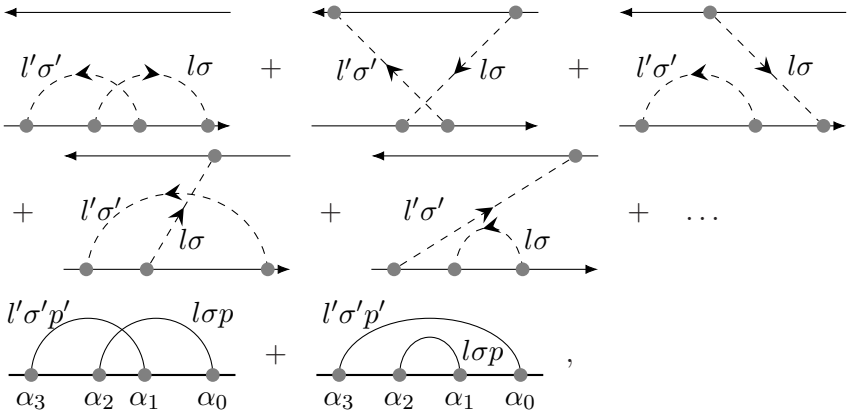

, (2.59)

where we do not show all 128 fourth order diagrams in the Keldysh contour way, they are presented e.g. in Koller [45]. In fact, all fourth order diagrams can now be written as the sum of only two diagrams. One can also omit the Fermi line indices for lead l, spin σ and direction p. All sixth order diagrams are given by

$K^{(6)} =$ 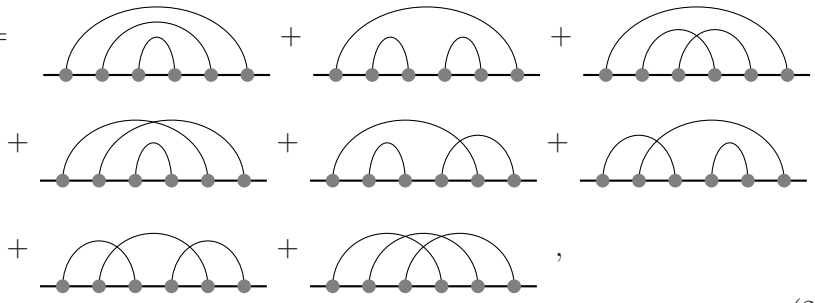

, (2.60)

which in practice are too many to include numerically and, additionally, some of the integrals cannot be calculated analytically anymore, like in the last contribution. In App. A we present diagrammatic rules that allow one to find the Kernel expressions of all diagrams. It is apparent that it is impossible to include all higher order diagrams. However, a certain subset of these diagrams can be summed up in an infinite series that converges, allowing us to predict at least to some extent strong coupling contributions.

2.5 The dressed second order

In this section we want to obtain a correction to the Kernel that cannot be captured by a perturbative approach. We consider the simplest infinite series that can be summed, which is called the generalized dressed second order (DSO$^+$). It is an extension of the work by Kern and Grifoni [54] on the two time lines diagrams. It renormalizes the second order diagram by including all non-crossing "bubbles" inside the main fermion line

$K^{\mathrm{DSO}} =:$ 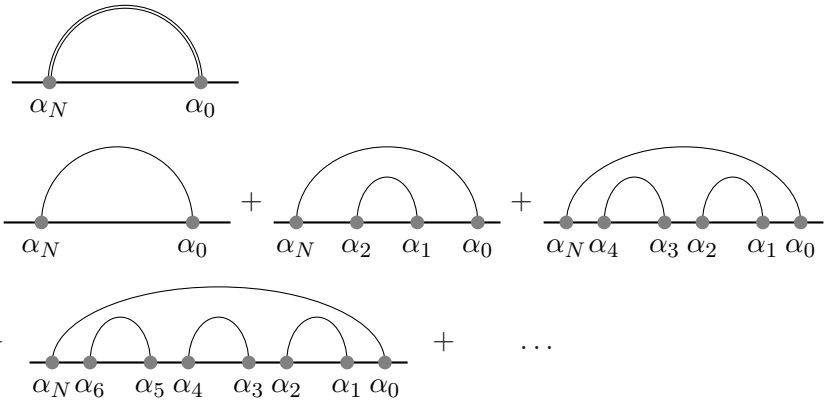

(2.61)

We indicate this renormalized second order diagram via a double fermion line. Within the superoperator formalism we obtain

$$
\begin{aligned}
K^{\mathrm{DSO}}\rho^{\infty} = -\frac{i}{\hbar}\sum_{\substack{l_0\sigma_0 p_0\\ \alpha_0\alpha_N}} \alpha_0\alpha_N \int_{-\infty}^{\infty} \mathrm{d}\epsilon_0\; D^{p_0,\alpha_N}_{l_0\sigma_0}
\Bigg[1 + \sum_{\substack{l_1\sigma_1 p_1\\ \alpha_1\alpha_2}} \int_{-\infty}^{\infty} \mathrm{d}\epsilon_1 \frac{f^{-p_1\alpha_1}_{l_1}(\epsilon_1) g_{l_1}}{i0^+ - i\hbar\mathcal{L}_{\mathrm{S}} - p_0\epsilon_0} D^{p_1,\alpha_2}_{l_1\sigma_1} \frac{1}{i0^+ - i\hbar\mathcal{L}_{\mathrm{S}} - p_0\epsilon_0 - p_1\epsilon_1} D^{\bar{p}_1,\alpha_1}_{l_1\sigma_1} \\
+ \left(\sum_{\substack{l_3\sigma_3 p_3\\ \alpha_3\alpha_4}} \int_{-\infty}^{\infty} \mathrm{d}\epsilon_3 \frac{f^{-p_3\alpha_3}_{l_3}(\epsilon_3) g_{l_3}}{i0^+ - i\hbar\mathcal{L}_{\mathrm{S}} - p_0\epsilon_0} D^{p_3,\alpha_4}_{l_3\sigma_3} \frac{1}{i0^+ - i\hbar\mathcal{L}_{\mathrm{S}} - p_0\epsilon_0 - p_3\epsilon_3} D^{\bar{p}_3,\alpha_3}_{l_3\sigma_3} \right) \\
\left(\sum_{\substack{l_1\sigma_1 p_1\\ \alpha_1\alpha_2}} \int_{-\infty}^{\infty} \mathrm{d}\epsilon_1 \frac{f^{-p_1\alpha_1}_{l_1}(\epsilon_1) g_{l_1}}{i0^+ - i\hbar\mathcal{L}_{\mathrm{S}} - p_0\epsilon_0} D^{p_1,\alpha_2}_{l_1\sigma_1} \frac{1}{i0^+ - i\hbar\mathcal{L}_{\mathrm{S}} - p_0\epsilon_0 - p_1\epsilon_1} D^{\bar{p}_1,\alpha_1}_{l_1\sigma_1} \right) \\
+ \quad \cdots \quad \Bigg] \frac{f^{-p_0\alpha_0}_{l_0}(\epsilon_0) g_{l_0}}{i0^+ - i\hbar\mathcal{L}_{\mathrm{S}} - p_0\epsilon_0} D^{\bar{p}_0,\alpha_0}_{l_0\sigma_0} \rho^{\infty}.
\end{aligned}
$$

(2.62)

One can see that the way the diagrams were chosen, ensures that any vertical cut crosses at most two fermion lines, such that all integrals are still solvable analytically. Already here one realizes that this results in a geometric series that converges to $\sum_k r^k = 1/(1-r)$. This yields the expression of the infinite sum

$$K^{\mathrm{DSO}}\rho^{\infty} = -\frac{i}{\hbar}\sum_{\substack{l_0\sigma_0 p_0\\ \alpha_0\alpha_N}} \alpha_0\alpha_N \int_{-\infty}^{\infty} \mathrm{d}\epsilon_0 \; D_{l_0\sigma_0}^{p_0,\alpha_N}$$
$$\left[1 - \sum_{\substack{l_1\sigma_1 p_1\\ \alpha_1\alpha_2}} \int_{-\infty}^{\infty} \mathrm{d}\epsilon_1 \frac{f_{l_1}^{-p_1\alpha_1}(\epsilon_1) g_{l_1}}{i0^+ - i\hbar\mathcal{L}_{\mathrm{S}} - p_0\epsilon_0} D_{l_1\sigma_1}^{p_1,\alpha_2} \frac{1}{i0^+ - i\hbar\mathcal{L}_{\mathrm{S}} - p_0\epsilon_0 - p_1\epsilon_1} D_{l_1\sigma_1}^{\bar{p}_1,\alpha_1}\right]^{-1}$$
$$\frac{f_{l_0}^{-p_0\alpha_0}(\epsilon_0) g_{l_0}}{i0^+ - i\hbar\mathcal{L}_{\mathrm{S}} - p_0\epsilon_0} D_{l_0\sigma_0}^{\bar{p}_0,\alpha_0}\rho^{\infty}. \tag{2.63}$$

By using $(XY)^{-1} = Y^{-1}X^{-1}$, where $X = i0^+ - i\hbar\mathcal{L}_{\mathrm{S}} - p_0\epsilon_0$ and Y^{-1} is the full inverse, this Kernel can be simplified to

$$K^{\mathrm{DSO}}\rho^{\infty} = -\frac{i}{\hbar}\sum_{\substack{l_0\sigma_0 p_0\\ \alpha_0\alpha_N}} \alpha_0\alpha_N \int_{-\infty}^{\infty} \mathrm{d}\epsilon_0 \; D_{l_0\sigma_0}^{p_0,\alpha_N}$$
$$\left[i0^+ - i\hbar\mathcal{L}_{\mathrm{S}} - p_0\epsilon_0 - \sum_{\substack{l_1\sigma_1 p_1\\ \alpha_1\alpha_2}} \int_{-\infty}^{\infty} \mathrm{d}\epsilon_1 D_{l_1\sigma_1}^{p_1,\alpha_2} \frac{f_{l_1}^{-p_1\alpha_1}(\epsilon_1) g_{l_1}}{i0^+ - i\hbar\mathcal{L}_{\mathrm{S}} - p_0\epsilon_0 - p_1\epsilon_1} D_{l_1\sigma_1}^{\bar{p}_1,\alpha_1}\right]^{-1}$$
$$f_{l_0}^{-p_0\alpha_0}(\epsilon_0) g_{l_0} D_{l_0\sigma_0}^{\bar{p}_0,\alpha_0}\rho^{\infty}. \tag{2.64}$$

Finally, this allows us to write the DSO$^+$ Kernel as

$$K^{\mathrm{DSO}}\rho^{\infty} = -\frac{i}{\hbar}\sum_{\substack{l\sigma p\\ \alpha_0\alpha_N}} \alpha_0\alpha_N \int_{-\infty}^{\infty} \mathrm{d}\epsilon \; D_{l\sigma}^{p,\alpha_N} \frac{f_l^{-p\alpha_0}(\epsilon) g_l}{i0^+ - i\hbar\mathcal{L}_{\mathrm{S}} - p\epsilon - \Sigma^{\mathrm{DSO}}(p\epsilon)} D_{l\sigma}^{\bar{p},\alpha_0}\rho^{\infty}, \tag{2.65}$$

by introducing the self-energy

$$\Sigma^{\mathrm{DSO}}(p\epsilon) = \sum_{\substack{l'\sigma' p'\\ \alpha\alpha'}} \int_{-\infty}^{\infty} \mathrm{d}\epsilon' \; D_{l'\sigma'}^{p',\alpha'} \frac{f_{l'}^{-p'\alpha'}(\epsilon') g_{l_1}}{i0^+ - i\hbar\mathcal{L}_{\mathrm{S}} - p\epsilon - p'\epsilon'} D_{l'\sigma'}^{\bar{p}',\alpha}. \tag{2.66}$$

Eq. (2.65) shows that, indeed, this infinite sum is closely related to the second order expression by renormalizing the propagator with a self-energy. Notice

that this derivation of the DSO$^+$ Kernel is an extension of the one obtained by Kern and Grifoni [54] and Mantelli [53], as it also includes diagrams that are crossed in the Keldysh contour representation. Mantelli tests the scaling behavior of the differential conductance analytically and numerically. Similar to Kern and Grifoni [54], he finds a universal scaling behavior as function of the temperature which, however, is not the correct one when compared to DM-NRG calculations. Nevertheless, the Coulomb peaks show indeed a tunneling induced broadening. The DSO$^+$ is valid in the range $U \gg \hbar\Gamma, k_\mathrm{B}T \gtrsim k_\mathrm{B}T_\mathrm{K}$. In summary, the DSO$^+$ is capable of capturing many interesting effects in the intermediate coupling regime, $k_\mathrm{B}T \approx \hbar\Gamma$, but is not suitable to quantitatively describe e.g. the Kondo effect. Whether the inclusion of further diagrams, as derived in this work, corrects the scaling behavior has yet to be tested.

Let us now turn to some simple test models in the weak coupling regime to see the master equation at work.

2.6 Minimal models

In this section we will apply the derived quantum master equation for increasingly complex test models.

2.6.1 Single resonant level

The most simple model for a SET setup is a single, spinless level between the two leads. The gate voltage can shift its energy $E = \alpha_\mathrm{g} V_\mathrm{g}$ via the capacitive coupling which allows to switch between the transport regime and a non-conducting regime. The corresponding chemical potential landscape in both regimes is shown in Fig. 2.3a,b. The master equation in this simple case follows directly from the one including the secular approximation in Eq. (2.38) and, since there exists only one Bohr frequency in the system, it can be written as

$$\mathcal{L}\rho = \sum_l \Gamma_l \left[\left(d^\dagger \rho d - \frac{1}{2}\{dd^\dagger, \rho\} \right) f_l^+(E) + \left(d\rho d^\dagger - \frac{1}{2}\{d^\dagger d, \rho\} \right) f_l^-(E) \right], \tag{2.67}$$

where the RDM ρ is completely diagonal since no degenerate states exist. It is convenient to write this Liouvillian in Liouville space in matrix form

$$\mathcal{L} = \sum_l \Gamma_l \begin{pmatrix} -f_l^+(E) & f_l^-(E) \\ f_l^+(E) & -f_l^-(E) \end{pmatrix}, \tag{2.68}$$

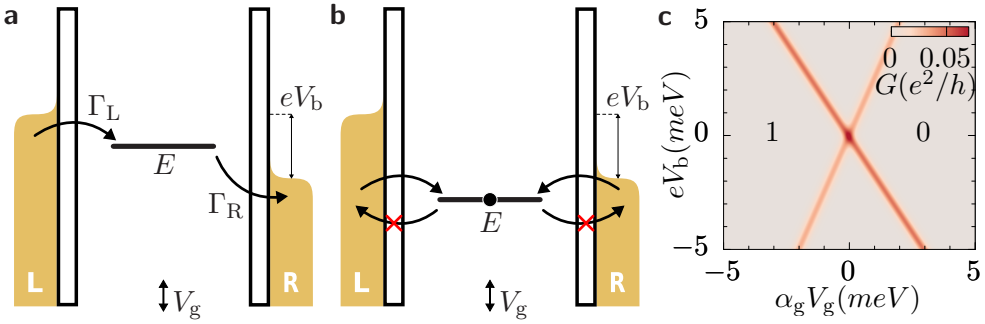

Figure 2.3: Chemical potential landscape of a single resonant level at finite bias. **a** The energy of the level is in the bias window and current can flow. **b** In the non-conductive regime the energy of the level is below both chemical potentials. **c** The resulting stability diagram at $T = 0.1meV$, $\eta = 0.4$ and $\hbar\Gamma_L = \hbar\Gamma_R = 10\mu eV$. In the region of vanishing current the average population of the level is displayed.

where now the stationary solution $\mathcal{L}\rho^\infty = 0$ is easy to find

$$\rho^\infty = \begin{pmatrix} P_0^\infty \\ P_1^\infty \end{pmatrix} = \frac{1}{\Gamma_L + \Gamma_R} \begin{pmatrix} \Gamma_L f_L^-(E) + \Gamma_R f_R^-(E) \\ \Gamma_L f_L^+(E) + \Gamma_R f_R^+(E) \end{pmatrix}. \tag{2.69}$$

Using these stationary populations, the current is simply the probability of an occupied level times the difference of outgoing and ingoing rates

$$I = e\left[f_L^+(E) - f_R^+(E)\right] \frac{\Gamma_L \Gamma_R}{\Gamma_L + \Gamma_R}. \tag{2.70}$$

This results in the stability diagram in Fig. 2.3c. At low temperatures it is often sufficient to approximate the Fermi functions as step functions far enough away from resonant lines. The plateau of constant current in the transport regime in this so called infinite bias limit has the simple expression for the current $I = \pm e\Gamma_L\Gamma_R/(\Gamma_L + \Gamma_R)$, where the sign is determined by the bias direction.

2.6.2 Quasi-degenerate level

To test the validity of the secular approximation we add an excited state to the resonant level with a minimal level splitting $\Delta E = E_e - E_g \ll k_B T$. Furthermore we allow for state- and lead dependent hopping parameters such that the rate matrices are non diagonal and different for the left and right lead. The master equation in the secular approximation and without the Lamb shift

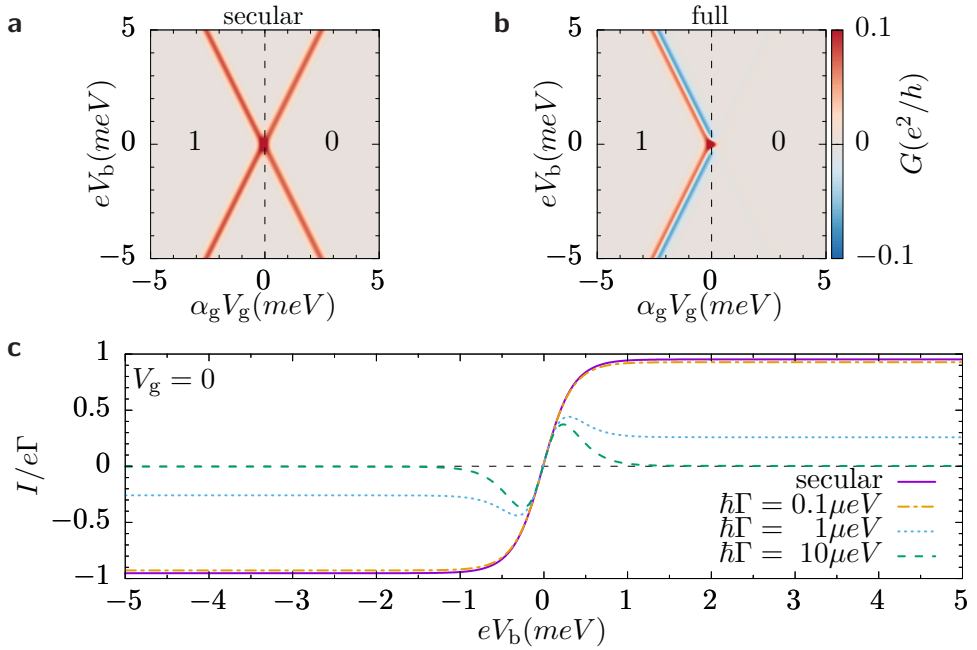

Figure 2.4: **a,b** Stability diagram of two quasi-degenerate levels with a splitting $\Delta E = 1\mu eV$ and state dependent tunneling at $\hbar\Gamma = 10\mu eV$, $k_B T = 0.1meV$ and $\eta = 0.5$. In the region of vanishing current the electron numbers on the QD are displayed. **a** In the secular approximation. **b** Including coherences between ground and excited state. **c** Current traces at $V_g = 0$ of the secular approximation and several full calculations at different tunneling rates.

reads

$$\begin{aligned}\dot{\rho}_{gg} &= \sum_l (\mathbf{\Gamma}_l)_{gg} \left[f_l^-(E_g)\rho_0 - f_l^+(E_g)\rho_{gg} \right], \\ \dot{\rho}_{ee} &= \sum_l (\mathbf{\Gamma}_l)_{ee} \left[f_l^-(E_e)\rho_0 - f_l^+(E_e)\rho_{ee} \right],\end{aligned} \tag{2.71}$$

together with $\rho_{gg} + \rho_{ee} + \rho_0 = 1$. For simplicity we have discarded the gate term in the Fermi functions $f_l^{\pm}(\omega) \leftrightarrow f_l^{\pm}(\alpha_g V_g + \omega)$. Since the RDM is now completely diagonal only the diagonal entries of the rate matrices enter. Including the coherences between ground and excited state gives the non-secular

master equation, again without Lamb shift

$$\begin{aligned}
\dot{\rho}_{gg} &= \sum_l (\mathbf{\Gamma}_l)_{gg} \left[f_l^-(E_g)\rho_0 - f_l^+(E_g)\rho_{gg} \right] - \frac{1}{2} f_l^+(E_e) \left[(\mathbf{\Gamma}_l)_{ge}\rho_{ge} + (\mathbf{\Gamma}_l)_{eg}\rho_{eg} \right], \\
\dot{\rho}_{ee} &= \sum_l (\mathbf{\Gamma}_l)_{ee} \left[f_l^-(E_e)\rho_0 - f_l^+(E_e)\rho_{ee} \right] - \frac{1}{2} f_l^+(E_g) \left[(\mathbf{\Gamma}_l)_{ge}\rho_{ge} + (\mathbf{\Gamma}_l)_{eg}\rho_{eg} \right], \\
\dot{\rho}_{ge} &= i\Delta E \rho_{ge} - \sum_l \Big[(\mathbf{\Gamma}_l)_{gg} f_l^+(E_g)\rho_{ge} + (\mathbf{\Gamma}_l)_{ee} f_l^+(E_e)\rho_{ge} \\
&\qquad - \frac{1}{2} (\mathbf{\Gamma_l})_{eg} \left(f_l^-(E_g)\rho_0 + f_l^-(E_e)\rho_0 - f_l^+(E_g)\rho_{gg} - f_l^+(E_e)\rho_{ee} \right) \Big].
\end{aligned} \tag{2.72}$$

In Fig. 2.4 we plot the stability diagram and current traces comparing the secular approximation to the full master equation when the ground state is coupled twice as good to the right lead as the excited state and reverse for the left lead, $t_{\mathrm{L}e} = t_{\mathrm{R}g} = 2t_{\mathrm{L}g} = 2t_{\mathrm{R}e}$. This results in the rate matrices

$$\mathbf{\Gamma}_{\mathrm{L}} = \Gamma \begin{pmatrix} 1 & 2 \\ 2 & 4 \end{pmatrix}, \qquad \mathbf{\Gamma}_{\mathrm{R}} = \Gamma \begin{pmatrix} 4 & 2 \\ 2 & 1 \end{pmatrix}. \tag{2.73}$$

As seen in Fig. 2.4c, the secular approximation breaks down for $\hbar\Gamma \gtrsim \Delta E$ and fails to reproduce the negative differential conductance. This effect is related to dark states which will be discussed in detail in chapters 4 and 7.

2.6.3 Single-impurity Anderson model

A more realistic model of a single QD is the so called single-impurity Anderson model (SIAM), a spin-full QD with interactions. Originally this model was used to describe magnetic impurities in metals and Kondo-type problems. The SIAM with two degenerate levels is often referred to as the SU(2) Anderson model. There also exist models with more degenerate levels like the SU(4) Anderson model, which is important for CNTs. In this section we will focus on a Anderson model with non-degenerate levels, whose Hamiltonian reads

$$\hat{H}_{\mathrm{SIAM}} = \sum_\sigma E_\sigma \hat{n}_\sigma + U \hat{n}_\uparrow \hat{n}_\downarrow, \tag{2.74}$$

where $\hat{n}_\sigma = d_\sigma^\dagger d_\sigma$. We choose the level splitting to be $E_\uparrow = -E_\downarrow = \Delta E/2$, which for example might come from an external magnetic field. The interaction strength U is the energy originating from Coulomb repulsion when two electrons are occupying the QD. This Hamiltonian is already diagonal, such that its eigenenergies and eigenstates are trivially determined, they are summarized in

N	Eigenenergy	Eigenstate
0	0	$\|0\rangle$
1	$-\Delta E/2$	$\|\downarrow\rangle$
1	$\Delta E/2$	$\|\uparrow\rangle$
2	U	$\|2\rangle$

Table 2.1: Eigenenergies and eigenstates of the single-impurity Anderson model with level splitting ΔE and interaction strength U.

Tab. 2.1. For $\Delta E \neq 0$ there are no degenerate states in the SIAM therefore again no coherences play a role and one works purely with populations. The quantum master equation reads

$$\begin{aligned}
\dot{P}_0 &= \sum_l \Gamma_l \left[f_l^-(E_\uparrow)P_\uparrow - f_l^+(E_\uparrow)P_0 + f_l^-(E_\downarrow)P_\downarrow - f_l^+(E_\downarrow)P_0 \right], \\
\dot{P}_\uparrow &= \sum_l \Gamma_l \left[f_l^+(E_\uparrow)P_0 - f_l^-(E_\uparrow)P_\uparrow + f_l^-(U-E_\uparrow)P_2 - f_l^+(U-E_\uparrow)P_\uparrow \right], \\
\dot{P}_\downarrow &= \sum_l \Gamma_l \left[f_l^+(E_\downarrow)P_0 - f_l^-(E_\downarrow)P_\downarrow + f_l^-(U-E_\downarrow)P_2 - f_l^+(U-E_\downarrow)P_\downarrow \right], \\
\dot{P}_2 &= \sum_l \Gamma_l \left[f_l^+(U-E_\downarrow)P_\downarrow - f_l^-(U-E_\downarrow)P_2 + f_l^+(U-E_\uparrow)P_\uparrow - f_l^-(U-E_\uparrow)P_2 \right],
\end{aligned} \tag{2.75}$$

where for simplicity we have discarded the gate term in the Fermi functions $f_l^\pm(\omega) \leftrightarrow f_l^\pm(\alpha_g V_g + \omega)$. These equations can in principle still be solved completely analytically. However, the expressions for the populations and the current are quite lengthy and therefore we will not write them down. Applying this quantum master equation results in the stability diagram shown in Fig. 2.5a. It displays the Coulomb diamonds with increasing electron number from right to left. The one electron state with spin up is an excited state resulting in additional resonant lines outside the central Coulomb diamond. Again some limiting cases of the infinite bias limit can be obtained. In the region where only $|0\rangle \leftrightarrow |\downarrow\rangle$ transitions are open the current has the same form as the single resonant level at infinite bias $I_{0\leftrightarrow\downarrow} = \pm e\Gamma_L\Gamma_R/(\Gamma_L + \Gamma_R)$. Lowering the gate or increasing the bias voltage, until transitions to the excited state $|0\rangle \leftrightarrow |\uparrow\rangle$ are opening, results in $I_{0\leftrightarrow\downarrow\uparrow} = \pm e2\Gamma_L\Gamma_R/(2\Gamma_L + \Gamma_R)$. This expression can be understood as an effective single level, where the rate from the left lead is twice as large as the one from the right, or as two degenerate levels such that the chance of electrons to enter is twice as high. Both regions

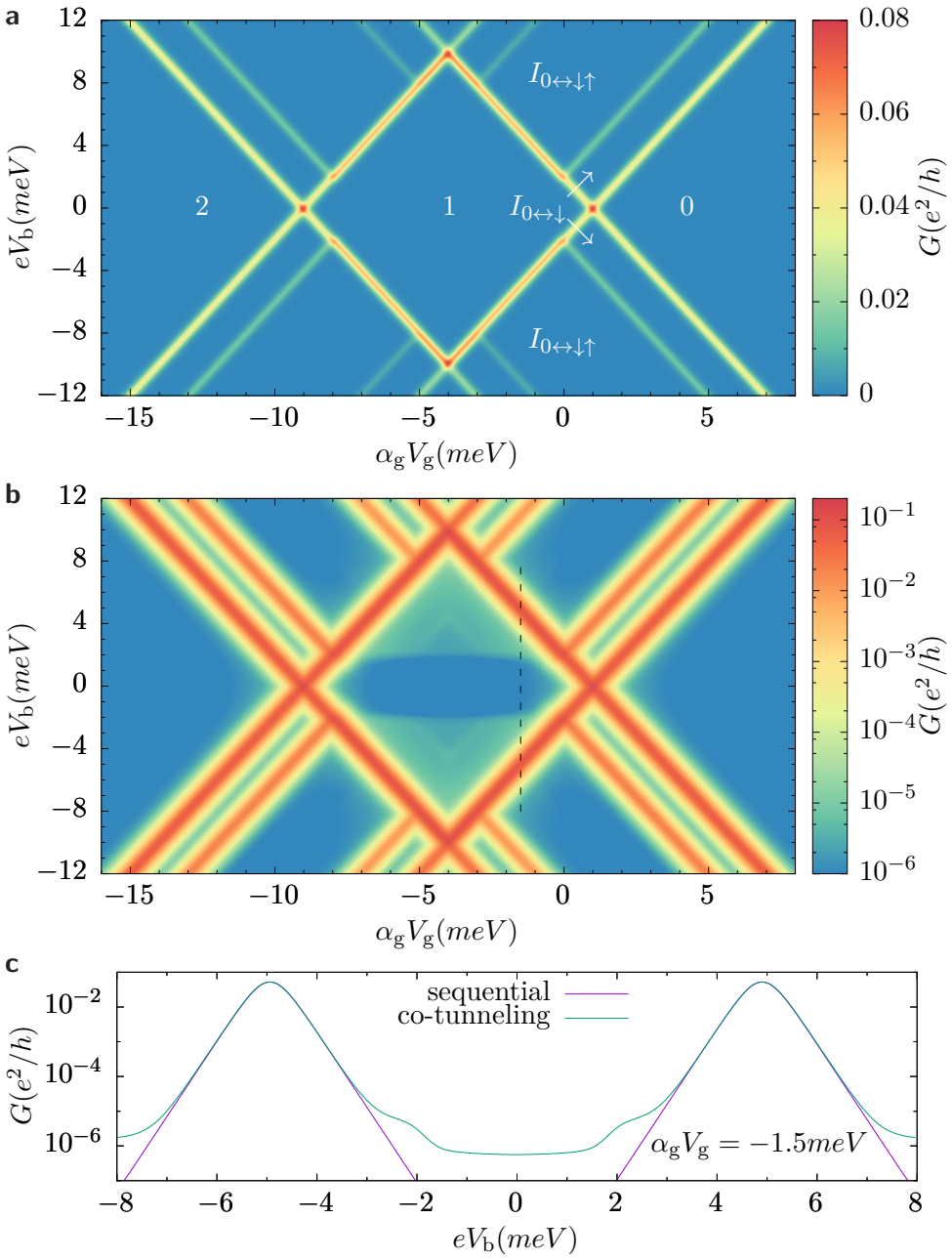

Figure 2.5: Stability diagram of the single-impurity Anderson model with $U = 8meV$, $\Delta E = 2meV$, $k_B T = 0.1meV$, $\hbar\Gamma_{L/R} = 10\mu eV$ and $\eta = 0.5$. **a** A sequential tunneling calculation features Coulomb diamonds. The number of electrons on the QD and some plateaus of constant current are highlighted. **b** Including co-tunneling horizontal features inside the central Coulomb diamond appear. **c** Bias trace of the differential conductance with and without co-tunneling at $\alpha_g V_g = -1.5meV$ as indicated by the dashed line in **b**.

are indicated in Fig. 2.5a.

Co-tunneling contributions can be included in this model. Fig. 2.5b shows the numerically computed stability diagram using KinEq. Inelastic co-tunneling results in horizontal features inside the central Coulomb diamond at $eV_\mathrm{b} = \pm\Delta E$. This energy corresponds also to the point where the excited state lines hit the Coulomb diamond borders. Elastic co-tunneling is also observed below this threshold although it is difficult to resolve in the plot. In Fig. 2.5c a bias trace of the differential conductance is shown with and without co-tunneling. In sequential tunneling the current drops exponentially in the Coulomb blockade regions, while elastic co-tunneling creates a threshold of constant differential conductance, even deep in Coulomb blockade.

To show that the superoperator formalism yields the same results, as previously obtained by Koller [45], we focus on the example diagram

$$\left(K^{(4)}\right)^{22}_{22} =$$

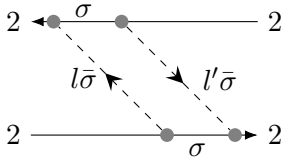

$$\equiv$$

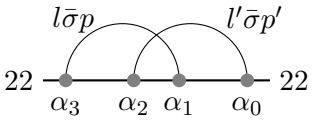

, (2.76)

where $p = +$, $p' = -$, $\alpha_3 = \alpha_2 = +$ and $\alpha_1 = \alpha_0 = -$. Starting from the Kernel expression in Eq. (2.45) we obtain for this single diagram

$$\begin{aligned}
\left(K^{(4)}\right)^{22}_{22}\rho_{22} = -\frac{i}{\hbar}\sum_{ll'\sigma}\int_{-\infty}^{\infty}\mathrm{d}\epsilon\int_{-\infty}^{\infty}\mathrm{d}\epsilon'\ \langle 2|\, D^{+,+}_{l\bar\sigma}\frac{g_l f_l^+(\epsilon)}{i0^+ - i\hbar\mathcal{L}_\mathrm{S} - \epsilon}D^{-,+}_{l'\bar\sigma} \\
\frac{1}{i0^+ - i\hbar\mathcal{L}_\mathrm{S} + \epsilon' - \epsilon}D^{-,-}_{l\bar\sigma}\frac{g_{l'} f_{l'}^-(\epsilon')}{i0^+ - i\hbar\mathcal{L}_\mathrm{S} + \epsilon'}D^{+,-}_{l'\bar\sigma}\rho_{22}\,|2\rangle \\
= -\frac{i}{\hbar}\sum_{ll'\sigma\{\omega_i\}}\int_{-\infty}^{\infty}\mathrm{d}\epsilon\int_{-\infty}^{\infty}\mathrm{d}\epsilon'\ \langle 2|\, D^{+,+}_{l\bar\sigma}(\omega_3)\frac{g_l f_l^+(\epsilon)}{i0^+ - \omega_0 + \omega_1 + \omega_2 - \epsilon}D^{-,+}_{l'\bar\sigma}(-\omega_2) \\
\frac{1}{i0^+ - \omega_0 + \omega_1 + \epsilon' - \epsilon}D^{-,-}_{l\bar\sigma}(-\omega_1)\frac{g_{l'} f_{l'}^-(\epsilon')}{i0^+ - \omega_0 + \epsilon'}D^{+,-}_{l'\bar\sigma}(\omega_0)\rho_{22}\,|2\rangle \\
= -\frac{i}{\hbar}\sum_{ll'\sigma\{\omega_i\}}\int_{-\infty}^{\infty}\mathrm{d}\epsilon\int_{-\infty}^{\infty}\mathrm{d}\epsilon'\ \frac{g_l f_l^+(\epsilon)}{i0^+ - \omega_0 + \omega_1 + \omega_2 - \epsilon}\frac{1}{i0^+ - \omega_0 + \omega_1 + \epsilon' - \epsilon} \\
\frac{g_{l'} f_{l'}^-(\epsilon')}{i0^+ - \omega_0 + \epsilon'}\,\langle 2|\, D^\dagger_{l\bar\sigma}(\omega_3)\,|\sigma\rangle\langle\sigma|\, D_{l'\bar\sigma}(-\omega_2)\rho_{22}D^\dagger_{l'\bar\sigma}(\omega_0)\,|\sigma\rangle\langle\sigma|\, D_{l\bar\sigma}(-\omega_1)\,|2\rangle \\
= -\frac{i}{\hbar}\sum_{ll'\sigma}\int_{-\infty}^{\infty}\mathrm{d}\epsilon\int_{-\infty}^{\infty}\mathrm{d}\epsilon'\frac{g_l f_l^+(\epsilon)}{i0^+ + E_2 - E_\sigma - \epsilon}\frac{|t_l|^2|t_{l'}|^2}{i0^+ + \epsilon' - \epsilon}\frac{g_{l'} f_{l'}^-(\epsilon')}{i0^+ + E_\sigma - E_2 + \epsilon'}\rho_{22},
\end{aligned}$$

where in the first step we have inserted the projectors onto the eigenenergies of the system, which determines the actions of the system Liouvillians in the denominators. Since the RDM is completely diagonal in the SIAM we use $\rho_{22} = \rho_{22}(0)$. In the next step we have realized that only the states $|\sigma\rangle$ can be reached from $|2\rangle$ and therefore inserted two times $|\sigma\rangle\langle\sigma|$ between the system operators, which results in $\omega_i = E_2 - E_\sigma$. The final expression, after reinserting $D_{l\sigma}^{(\dagger)} = t_l^{(*)} d_\sigma^{(\dagger)}$, is exactly the same as derived before by Koller [45], where also the final integral is calculated.

CHAPTER 3

Blocking Kondo resonances in quantum dots

The discovery of the Kondo effect dates back to the 1930s, when scientists all over the world performed current measurements in metals at low temperatures. The resistance of a pure metal should drop with lowering temperature since traveling through a crystal is eased when phononic vibrations are small. Some metals like copper and gold remain conducting with a finite resistance even at the lowest temperatures possible where the value of this resistance depends on the defect number in the material. Interestingly, other metals like lead, niobium or aluminium suddenly can loose all their resistance and become perfect conductors as discovered by Onnes [55] in 1911. This effect appears below a certain critical temperature of a few Kelvin and lead to additional findings such as the Meissner-Ochsenfeld effect where a magnetic field gets expelled from a superconductor [56]. In 1934 W. J. de Haas, J. H. de Boer and G. J. van de Berg found another intriguing behavior of metals, below a critical temperature the resistance starts rising again [57]. Its origin was a longstanding puzzle for 30 years. This critical temperature is now known as the Kondo temperature T_{K} after Jun Kondo, who managed to explain the underlying mechanism: scattering on magnetic impurities [58], which now is called the Kondo effect. In recent years this effect has drawn great attention again after its discovery in QDs [59–61]. If an unpaired electron is Coulomb blocked in the QD, it can screen the lead electrons leading to an increase in conductance, exactly the opposite consequence as the Kondo effect in metals.

The underlying many-body entanglement is at the heart of the Kondo effect, which has its hallmark as a zero-bias conductance peak at low temperatures. While the original Kondo effect deals only with the spin degree of freedom of the electrons, one observes that the ubiquity of Kondo resonances in QDs relies on the presence of degenerate dot states, whose degeneracy is associated to any conserved degrees of freedom during the tunneling from and to the dot [62]. In CNT-QDs the additional valley degree of freedom introduces a four-fold spin-valley degeneracy which yields the exotic spin plus orbital SU(4) Kondo effect [63–69]. Spin-orbit coupling (SOC) and valley mixing remove this degeneracy and hence reduce the total symmetry to SU(2) $\otimes$ SU(2) [65, 68–74]. Magnetic fields can be used to break time-reversal symmetry related degeneracies and unravel the nature of the Kondo effect by tracking the evolution of split Kondo peaks [59, 64–66, 73, 75–79]. Large parts of this chapter rely on the publication Niklas *et al.* [P.4].

In the recent work by Schmid *et al.* [74] the striking report was made that specific transport resonances of such split Kondo peaks are not observable in CNTs, despite being expected from theoretical predictions [63, 70, 71]. Even more intriguing is the fact that those resonances were recorded in cotunneling measurements in the weak coupling regime [35]. A closer inspection of other experimental works in the Kondo regime [64, 68, 73, 77] reveals that the absence of some resonances seems systematic. In this chapter we utilize the extreme scalability of the coupling strength in CNT-QDs and study the low-temperature nonlinear electron transport in a very clean CNT-QD [33]. Details of the device fabrication for the suspended CNT were reported previously [68]. All the measurements were performed at a mixing chamber temperature of about $T_{\mathrm{exp}} = 30mK$, which sets a lower bound to the actual electronic temperature. By sweeping the gate voltage, the chemical potential is moved from above (electron sector) to below (hole sector) the charge neutrality point and quadruplets of states are thus successively emptied. This allows to tune the same CNT device from a weak coupling regime, where Coulomb diamonds and inelastic co-tunneling are observed, to a Kondo regime with strong many-body correlations to the leads and clear zero-bias peaks at odd fillings [66, 80]. This pattern is visible in a typical measurement of the differential conductance $G = \mathrm{d}I/\mathrm{d}V_{\mathrm{b}}$ versus the bias voltage V_{b} and the gate voltage V_{g}, Fig. 3.1, which exhibits the characteristic four-fold periodicity. We use nonlinear magneto-spectroscopy in the two regimes to identify and model all expected virtual

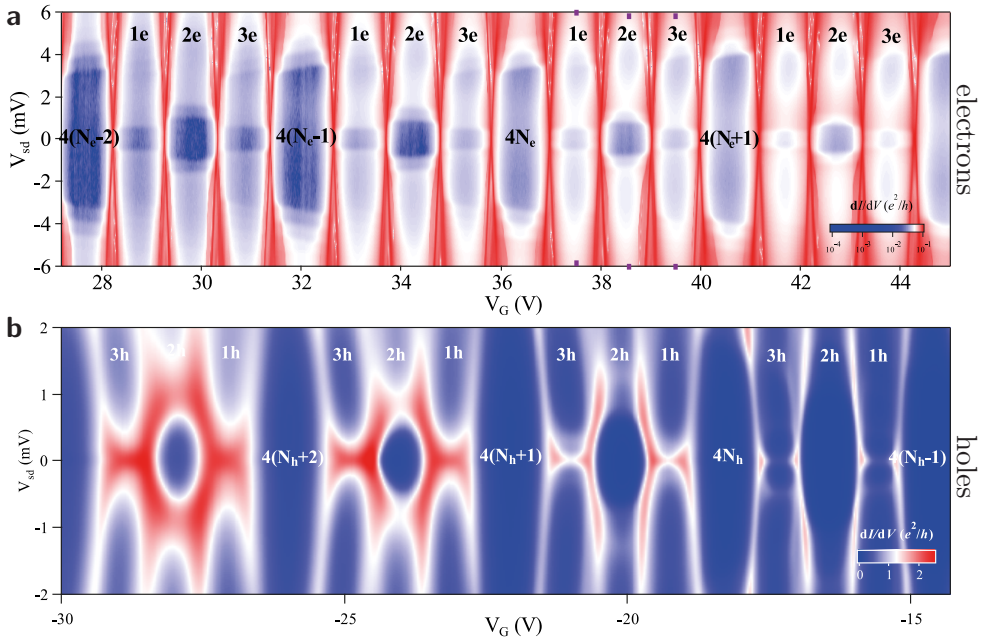

Figure 3.1: Experimental stability diagram of four shells each in the electron and hole regime of the same CNT-QD device. **a** At positive V_g clear Coulomb diamonds with co-tunneling lines inside appear. **b** At negative V_g Kondo ridges emerge in Coulomb diamonds with an odd number of electrons.

transitions of the CNT spectrum and describe the two regimes using accurate transport calculations based on perturbative and non-perturbative approaches in the coupling, respectively. The missing resonances in the Kondo regime have been clearly identified, and their suppression fully taken into account by the transport theory. In virtue of an effective exchange interaction, we show that virtual transtions which flip the Kramers pseudospins yield low-energy many-body singlet states with no net Kramers pseudospin. This result in turn reveals that the transport resonances suppressed in the deep Kondo regime are associated to virtual processes which do not flip the Kramers pseudospin. Let us start with understanding the original spin-1/2 Kondo problem.

3.1 The spin-1/2 Kondo effect in quantum dots

To grasp the concept of the Kondo effect, it is best to start with the original one that only considers the spin degree of freedom, often referred to as the SU(2) Kondo problem. The corresponding model of a QD is the single-impurity

Anderson model (SIAM) as considered before in Sec. 2.6.3 with the Hamiltonian at zero magnetic field

$$\hat{H}_{\mathrm{SIAM}} = \sum_{\sigma} E_d \hat{n}_\sigma + U \hat{n}_\uparrow \hat{n}_\downarrow, \tag{3.1}$$

together with the usual Hamiltonians for the leads and tunneling. We have seen in Fig. 3.1b that the Kondo effect only appears in Coulomb diamonds with an odd number of electrons. Therefore, we introduce the projectors onto the subspaces with $N = 0, 1, 2$ electrons, $P_0 = \prod_\sigma (1 - \hat{n}_\sigma)$, $P_1 = \sum_\sigma \hat{n}_\sigma (1 - \hat{n}_{\bar{\sigma}})$ and $P_2 = \hat{n}_\uparrow \hat{n}_\downarrow$, which allows us to separate the Hamiltonian $\hat{H} = \hat{H}_{\mathrm{SIAM}} + \hat{H}_{\mathrm{B}} + \hat{H}_{\mathrm{tun}}$ into

$$\hat{H}|\psi\rangle = \begin{pmatrix} H_{00} & H_{01} & 0 \\ H_{10} & H_{11} & H_{12} \\ 0 & H_{21} & H_{22} \end{pmatrix} \begin{pmatrix} \psi_0 \\ \psi_1 \\ \psi_2 \end{pmatrix} = E \begin{pmatrix} \psi_0 \\ \psi_1 \\ \psi_2 \end{pmatrix}, \tag{3.2}$$

with $H_{ij} = P_i \hat{H} P_j$. Finally we derive an effective equation for the one-particle subspace

$$\hat{H}_{\mathrm{eff}} \psi_1 = \Big[H_{11} + \underbrace{H_{12}(E - H_{22})^{-1} H_{21}}_{\text{electron like}} + \underbrace{H_{10}(E - H_{00})^{-1} H_{01}}_{\text{hole like}} \Big] \psi_1 = E \psi_1, \tag{3.3}$$

that includes transitions to electron and hole like virtual states. These transition amplitudes can be calculated to lowest order in the tunnel coupling as [62]

$$\begin{aligned} H_{12}(E - H_{22})^{-1} H_{21} &= \sum_{\boldsymbol{k}\boldsymbol{k}'\sigma\sigma'} t_{\boldsymbol{k}} d_\sigma c^\dagger_{\boldsymbol{k}\sigma} \frac{1}{E - 2E_d - U - \hat{H}_{\mathrm{B}}} t^*_{\boldsymbol{k}'} c_{\boldsymbol{k}'\sigma'} d^\dagger_{\sigma'} \\ &= - \sum_{\boldsymbol{k}\boldsymbol{k}'\sigma\sigma'} t^*_{\boldsymbol{k}} t_{\boldsymbol{k}'} \frac{1}{E_d + U - \xi_{\boldsymbol{k}}} c^\dagger_{\boldsymbol{k}\sigma} c_{\boldsymbol{k}'\sigma'} d_\sigma d^\dagger_{\sigma'} \hat{n}_{\bar{\sigma}'} + \mathcal{O}(t^4_{\boldsymbol{k}}), \\ H_{10}(\tilde{E} - H_{00})^{-1} H_{01} &= \sum_{\boldsymbol{k}\boldsymbol{k}'\sigma\sigma'} t^*_{\boldsymbol{k}} d^\dagger_\sigma c_{\boldsymbol{k}\sigma} \frac{1}{E - \hat{H}_{\mathrm{B}}} t_{\boldsymbol{k}'} c^\dagger_{\boldsymbol{k}'\sigma'} d_{\sigma'} \\ &= - \sum_{\boldsymbol{k}\boldsymbol{k}'\sigma\sigma'} t^*_{\boldsymbol{k}} t_{\boldsymbol{k}'} \frac{1}{\xi_{\boldsymbol{k}'} - E_d} c_{\boldsymbol{k}'\sigma'} c^\dagger_{\boldsymbol{k}\sigma} d^\dagger_{\sigma'} d_\sigma (1 - \hat{n}_{\bar{\sigma}}) + \mathcal{O}(t^4_{\boldsymbol{k}}). \end{aligned} \tag{3.4}$$

Expanding the inverses as a geometric series in $E - \hat{H}_{\mathrm{B}} - E_d$, which contains at least one tunneling amplitude $t_{\boldsymbol{k}}$, allows us to only keep the lowest order term $\mathcal{O}(t^2_{\boldsymbol{k}})$, if the tunneling is small enough. This enables the transformation of the SIAM Hamiltonian (3.1) into an effective Kondo Hamiltonian

$$\hat{H}_{\mathrm{eff}} \approx H_{11} - J \boldsymbol{S} \cdot \boldsymbol{s}, \tag{3.5}$$

with the antiferromagnetic Heisenberg coupling J. In the wide band limit, $t_{\boldsymbol{k}} \to t$, this exchange coupling reads

$$J_{\boldsymbol{k},\boldsymbol{k}'} = -\left(\frac{t^*_{\boldsymbol{k}} t_{\boldsymbol{k}'}}{\xi_{\boldsymbol{k}'} - E_d} + \frac{t^*_{\boldsymbol{k}} t_{\boldsymbol{k}'}}{E_d + U - \xi_{\boldsymbol{k}}}\right) \to J = \frac{t^2 U}{E_d(E_d + U)} < 0. \tag{3.6}$$

For conduction band energies close to the Fermi energy, $\xi_{\boldsymbol{k}} \to 0$, can be neglected while $E_d < 0$ and $E_d + U > 0$. This Hamiltonian couples the spin of the QD electron, $S_z = (\hat{n}_\uparrow - \hat{n}_\downarrow)/2$ with the collective spin of the leads, $s_z = \sum_{\boldsymbol{k}\boldsymbol{k}'\sigma} \sigma c^\dagger_{\boldsymbol{k}\sigma} c_{\boldsymbol{k}'\sigma}/2$. Keep in mind that $\boldsymbol{S}\cdot\boldsymbol{s} = S_z s_z + (S_+ s_- + S_- s_+)/2$. This analysis yields the same result as the transformation by Schrieffer and Wolff [81]. Writing a general state of the full system as a product state of a QD and a bath part, $|S_z\rangle \otimes |s_z\rangle_{\mathrm{B}}$, allows to write the eigenstates of the Kondo Hamiltonian, $\hat{H}_{\mathrm{K}} = -J\boldsymbol{S}\cdot\boldsymbol{s}$, as the singlet state $|S\rangle = (|{\uparrow}\rangle\otimes|{\downarrow}\rangle_{\mathrm{B}} - |{\downarrow}\rangle\otimes|{\uparrow}\rangle_{\mathrm{B}})/\sqrt{2}$ and the triplet states $|T^1\rangle = |{\uparrow}\rangle \otimes |{\uparrow}\rangle_{\mathrm{B}}$, $|T^0\rangle = (|{\uparrow}\rangle \otimes |{\downarrow}\rangle_{\mathrm{B}} + |{\downarrow}\rangle \otimes |{\downarrow}\rangle_{\mathrm{B}})/\sqrt{2}$ and $|T^{-1}\rangle = |{\downarrow}\rangle \otimes |{\downarrow}\rangle_{\mathrm{B}}$. The eigenenergies are $\hat{H}_{\mathrm{K}}|S\rangle = \frac{3}{4}J|S\rangle$ and $\hat{H}_{\mathrm{K}}|T\rangle = -\frac{1}{4}J|T\rangle$ which shows that for antiferromagnetic coupling, $J < 0$, the ground state is a singlet. Strictly speaking, this analysis requires an odd number of electrons in the leads, such that their combined spin is $S_{\mathrm{B}} = 1/2$. However, in metals with magnetic impurities local screening results in conduction electrons getting trapped around the impurity, antialigning their collective spin with the impurity's spin, forming what is known as the Kondo cloud. This trapping leads to a reduced conductivity. In QDs the effect of the Kondo cloud is the opposite, because it connects the QD with the contacts leading to increased conductivity and ultimately in the zero bias resonance. In Fig. 3.2 an artist impression of this Kondo cloud in a CNT-QD is shown. To extend the SU(2) Kondo model to the SU(2) $\otimes$ SU(2) problem of CNTs we have to understand their symmetries.

3.2 Fundamental symmetries of carbon nanotubes

Let us recall the Hamiltonian of a CNT accounting for SOC, valley mixing, onsite and exchange Coulomb interactions, and an external magnetic field

$$\hat{H}_{\mathrm{CNT}} = \hat{H}_{\mathrm{d}} + \hat{H}_{\mathrm{SO}} + \hat{H}_{\mathrm{KK}'} + \hat{H}_{\boldsymbol{B}} + \hat{H}_{\mathrm{U}} + \hat{H}_{\mathrm{J}}. \tag{3.7}$$

Here $\hat{H}_{\mathrm{d}} + \hat{H}_{\mathrm{U}}$ is the SU(4) invariant component, which reads

$$\hat{H}_{\mathrm{d}} + \hat{H}_{\mathrm{U}} = \varepsilon_{\mathrm{d}} \sum_{\tau,\sigma} n_{\tau,\sigma} + \frac{U}{2} \sum_{(\tau,\sigma)\neq(\tau',\sigma')} n_{\tau,\sigma} n_{\tau',\sigma'}, \tag{3.8}$$

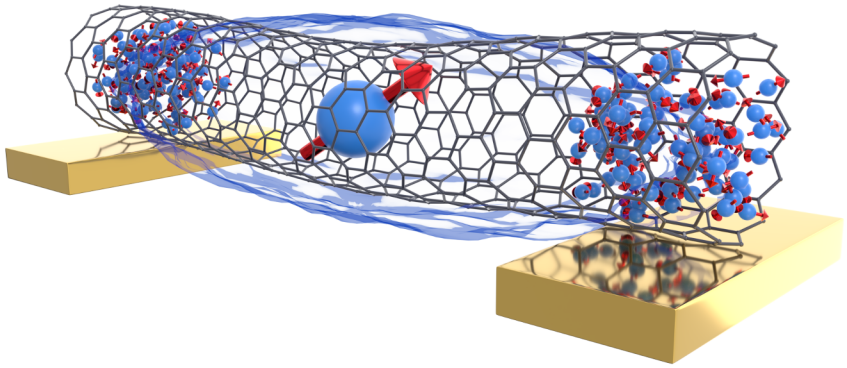

Figure 3.2: Artist's impression of the Kondo effect in a CNT-QD. The electrons in the leads get screened by the QD electron due to the antiferromagnetic coupling which forms a Kondo cloud. This results in increased conductivity.

with ε_d the energy of the quantized longitudinal mode, which can be tuned through the applied gate voltage, and U accounting for charging effects. Valley mixing and SOC break the SU(4) symmetry with characteristic energies $\Delta_{\mathrm{KK}'}$ and Δ_SO, respectively. The corresponding contributions including the one for a magnetic field and the exchange interaction can be found in detail in Sec. 1.2 in Eqs. (1.18) and (1.23). In the experiment, according to Tab. 3.1, the valley mixing is small, which favors tubes of the zig-zag class. Therefore, we choose in the following the form of Eq. (1.23) for the exchange interaction with the exchange coupling $J < 0$. We call the basis $\{|i\rangle\}$, $i = 1, 2, 3, 4$ which diagonalizes the single particle part $\hat{H}_0 = \hat{H}_\mathrm{d} + \hat{H}_{\mathrm{KK}'} + \hat{H}_\mathrm{SO} + \hat{H}_{\boldsymbol{B}}$ of the CNT Hamiltonian the Kramers basis. Despite the complexity of $\hat{H}_0$, a closer inspection reveals the existence of conjugation relations among the quadruplet of states $i = 1, 2, 3, 4$ generated by the time-reversal operator $\hat{\mathcal{T}}$, as well as by the particle-hole like and chirality operators $\hat{\mathcal{P}}$ and $\hat{\mathcal{C}} = \hat{\mathcal{P}}\hat{\mathcal{T}}^{-1}$, respectively [74]. Specifically, the states are ordered such that $(1, 2)$ and $(3, 4)$ are time-reversal partners, while $(1, 4)$ and $(2, 3)$ are particle-hole partners. In the $\{|\tau, \sigma\rangle\}$ basis

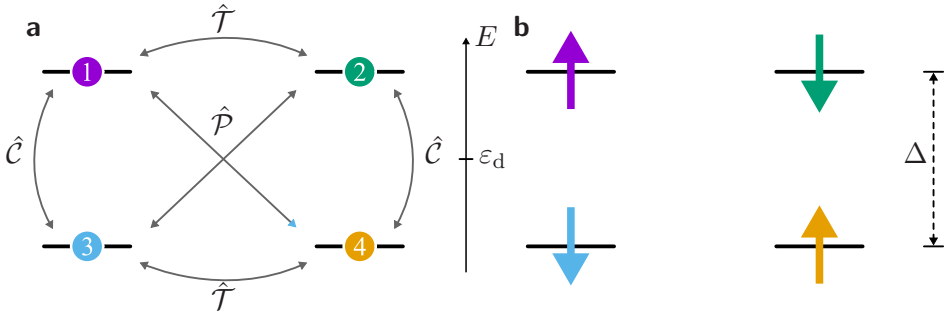

Figure 3.3: Single particle eigenstates of a CNT-QD in an energy landscape without magnetic field. **a** The four eigenstates $i = 1, 2, 3, 4$ form two Kramers doublets, split by Δ and are related via $\hat{\mathcal{T}}$, $\hat{\mathcal{P}}$ and $\hat{\mathcal{C}}$ conjugations. **b** In the symmetric description these states are defined via their pseudospin.

these operators read

$$\hat{\mathcal{T}} = \hat{\kappa} \sum_{\tau,\sigma} \sigma d^{\dagger}_{\bar{\tau},\bar{\sigma}} d_{\tau,\sigma}, \tag{3.9}$$

$$\hat{\mathcal{P}} = \hat{\kappa} \sum_{\tau,\sigma} \sigma\tau d^{\dagger}_{\bar{\tau},\sigma} d_{\tau,\sigma}, \tag{3.10}$$

$$\hat{\mathcal{C}} = \sum_{\tau,\sigma} (-\tau) d^{\dagger}_{\tau,\bar{\sigma}} d_{\tau,\sigma}, \tag{3.11}$$

where $\hat{\kappa}$ stands for the complex conjugation operator. In the absence of a magnetic field, $\hat{\mathcal{T}}$ commutes with the total CNT Hamiltonian, resulting in a single-particle spectrum with two degenerate Kramers doublets $(1, 2)$ and $(3, 4)$ separated by the inter-Kramers splitting $\Delta = \sqrt{{\Delta_{\mathrm{SO}}}^2 + {\Delta_{\mathrm{KK'}}}^2}$. In the following we call them the upper (u) and lower (d) Kramers channels. At zero magnetic field $\hat{\mathcal{P}}$ and $\hat{\mathcal{C}}$ are only symmetries in the absence of SOC and valley mixing. Since both anticommute with $\hat{H}_{\mathrm{SO}} + \hat{H}_{\mathrm{KK'}}$, for $\mathcal{P}$-conjugated pairs it holds $\varepsilon_{1,2}(\Delta) = \varepsilon_{4,3}(-\Delta)$. All these properties of the eigenstates are summarized in Fig. 3.3a. One finds a U(1) $\otimes$ U(1) $\otimes$ SU(2) $\otimes$ SU(2) symmetry related to the existence of two pairs of time-reversal degenerate doublets. The U(1) symmetries reflect charge conservation in each Kramers pair with generators

$$\hat{Q}_{\kappa} = \frac{1}{2} \sum_{j \in \kappa} (\hat{n}_j - \frac{1}{2}), \tag{3.12}$$

which measure the charge of the pair with respect to the half-filling. Here is $j = (1, 2)$ or $(3, 4)$ for $\kappa =$ u or d, respectively. The SU(2) symmetries are

generated by the spin-like operators

$$\hat{\boldsymbol{J}}_\kappa = \frac{1}{2} \sum_{j,j' \in \kappa} d_j^\dagger \boldsymbol{\sigma}_{j,j'} d_{j'}. \tag{3.13}$$

Here $\boldsymbol{\sigma}$ is the vector of Pauli matrices. Physically, $\hat{J}^z_{\rm u} = (n_1 - n_2)/2$ and $\hat{J}^z_{\rm d} = (n_4 - n_3)/2$ account for the charge unbalance within a Kramers pair. Thus, an isolated CNT with one electron or a hole only in the quadruplet has a net Kramers pseudospin (and charge). We introduce the notation for writing a general state using the pseudospin as $|J^z_{\rm d}; J^z_{\rm u}\rangle$, where the pseudospin can be either $\Uparrow$, $\Downarrow$ or "$-$" if the corresponding Kramers pair is unoccupied. The two degenerate ground state configurations of an isolated CNT, without a magnetic field are then $|\Downarrow; -\rangle$ and $|\Uparrow; -\rangle$.

A magnetic field breaks the time-reversal symmetry and hence also the SU(2) symmetries. However, because $\hat{H}_{\rm B}$ anticommutes with $\hat{\mathcal{T}}$, formerly degenerate Kramers states are still related to each other by Kramers conjugation. For an arbitrary magnetic field $\boldsymbol{B}$ time-reversal conjugation and particel-hole conjugation imply [74] $\varepsilon_{1,4}(\boldsymbol{B}) = \varepsilon(\boldsymbol{B}) \pm \frac{1}{2}\Delta(\boldsymbol{B})$ and $\varepsilon_{2,3}(-\boldsymbol{B}) = \varepsilon_{1,4}(\boldsymbol{B})$, where $\varepsilon(\boldsymbol{B})$ and $\Delta(\boldsymbol{B})$ reduce to the longitudinal energy and Kramers splitting $\varepsilon_{\rm d}$ and Δ, respectively, at zero field. Introducing the average quantities $\bar{\Delta}(\boldsymbol{B}) := (\Delta(\boldsymbol{B}) + \Delta(-\boldsymbol{B}))/2$ and $\bar{\varepsilon}(\boldsymbol{B}) := (\varepsilon(\boldsymbol{B}) + \varepsilon(-\boldsymbol{B}))/2$, as well as the differences $\delta\Delta(\boldsymbol{B}) := (\Delta(\boldsymbol{B}) - \Delta(-\boldsymbol{B}))/2$ and $\delta\varepsilon(\boldsymbol{B}) := (\varepsilon(\boldsymbol{B}) - \varepsilon(-\boldsymbol{B}))/2$, the single particle part of the CNT Hamiltonian can be easily recast in terms of total charge and pseudospin of a Kramers pair. It reads

$$\hat{H}_0 = \sum_\kappa \left(\bar{\varepsilon}(\boldsymbol{B}) + \kappa \frac{\bar{\Delta}(\boldsymbol{B})}{2} \right) \hat{N}_\kappa + \left[2\delta\varepsilon(\boldsymbol{B}) + \kappa\delta\Delta(\boldsymbol{B}) \right] \hat{J}^z_\kappa, \tag{3.14}$$

where $\kappa = {\rm u/d} = +/-$, $\hat{N}_\kappa = 2\hat{Q}_\kappa + 1$, and at zero magnetic field $\bar{\Delta}(B = 0) = \Delta$, $\bar{\varepsilon}(B = 0) = \varepsilon_{\rm d}$ and $\delta\varepsilon = \delta\Delta = 0$. Therefore, the CNT states can still be characterized according to the eigenvalues of the $\hat{Q}_\kappa$ and $\hat{J}^z_\kappa$ operators, since they commute with this single-particle CNT Hamiltonian. Finite bias and finite magnetic field spectroscopy allows us to clearly identify the relevant elastic and inelastic virtual processes according to the involved Kramers charge and spin.

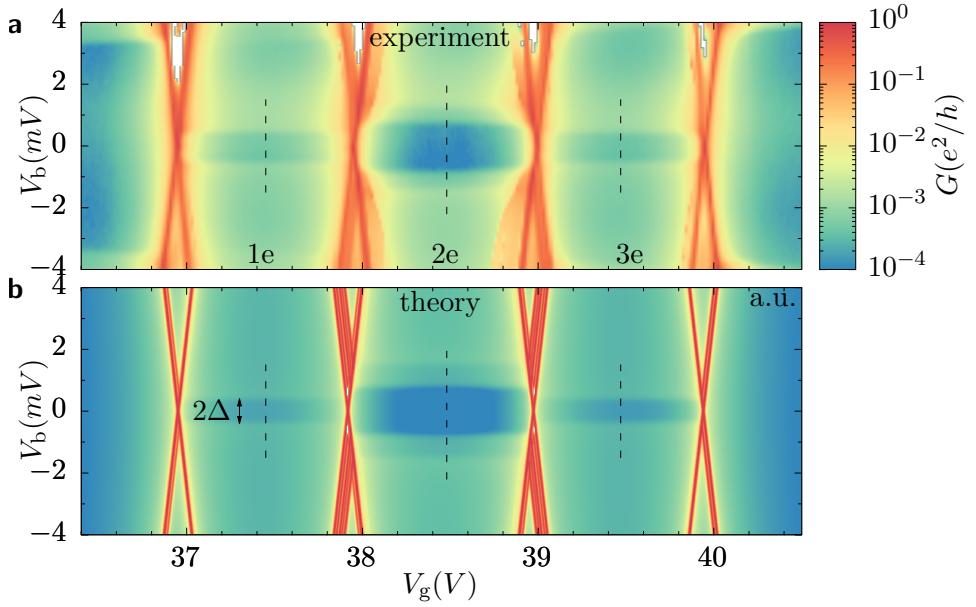

Figure 3.4: Stability diagram of a single shell at the electron side at zero magnetic field. **a** Experiment compared to **b** numerical calculations. Clear inelastic co-tunneling lines are visible in all three Coulomb diamonds. Vertical lines mark the positions of the magnetotransport cuts.

3.3 Virtual transitions revealed by magnetospectroscopy

To understand the fundamental differences between the electron and the hole side, we analyze the magnetic field spectroscopy performed in both regimes.

3.3.1 Electron side: co-tunneling

Fig. 3.4a displays the stability diagram for the electron sector of a single shell ($N_e = 6$) at zero magnetic field, where Coulomb diamonds and inelastic co-tunneling excitation lines are visible. This indicates large charging energies U and a parameter regime where Kondo correlations are not relevant yet. All transport calculations in the electron regime use the KinEq code based on perturbation theory (PT) which contains all contributions up to second order in the tunnel coupling Γ. It is expected to give accurate results for small ratios $\hbar\Gamma/k_BT$ and $\hbar\Gamma/U$ [48] and to qualitatively capture the dominant sequential tunneling and cotunneling mechanisms [82]. Due to its perturbative nature

	holes (shell $N_h = 6$)	electrons (shell $N_e = 6$)
$\Delta_{\mathrm{SO}}(meV)$	-0.21	-0.4
$\Delta_{\mathrm{KK'}}(meV)$	0.08	0.04
$\mu_{\mathrm{orb}}(meV/T)$	(2h, 3h) 0.51, (1h) 0.55	0.43
$U(meV)$ PT		26.5
$U(meV)$ DM-NRG	4.7	
$U(meV)$ KEA	(1h, 3h) ∞	
$J(meV)$ PT	-1.35	-1.4
$\Delta_\mu B_\parallel(meV/T)$	-0.05	-0.06
$\Delta V_{\mathrm{b}}(mV)$	0.12	0.28

Table 3.1: Parameters used to fit the electronic transport spectra of the CNT. It corresponds to the valence quadruplet $N_h = 6$ (hole transport), and the conduction quadruplet $N_e = 6$ (electron transport), counting the Coulomb diamonds from the band gap. The experimental data for each Coulomb valley are offset by ΔV_{b}, and tilted in the magnetic field by $\Delta_\mu B_\parallel$, resulting in an asymmetry between the measurement in fields parallel and antiparallel to the CNT axis. In all the plots presented in the work both the offset and the tilt have been removed.

though, it fails to account for a broadening of the conductance traces being larger than the nominal experimental temperature as a thermal broadening is expected from PT. This large broadening signals that also higher order charge fluctutation processes might influence transport, yielding a width governed by Γ rather than by the temperature and a Lamb shift of the experimental peaks [54, 83–85]. From the experimental curves we extract an average half width at half maximum of $0.15meV$. In the perturbative simulations, much smaller values of the tunneling coupling had to be chosen in order to fulfill the theoretical requirement $\hbar\Gamma \ll k_{\mathrm{B}}T$ for the application of the PT; therefore we only compare the results qualitatively. Since the calculations also include an exchange splitting, it was convenient in this regime to work in the $\{|\tau, \sigma\rangle\}$ basis. Besides the parameters shown in Tab. 3.1, the additional parameters used in the simulations are $T = 232mK$, and symmetric leads with tunneling couplings $\hbar\Gamma_{K,\uparrow} = \hbar\Gamma_{K',\downarrow} = 0.06\mu eV$, $\hbar\Gamma_{K,\downarrow} = \hbar\Gamma_{K',\uparrow} = 0.047\mu eV$. The result of the calculations for the differential conductance is shown in Fig. 3.4b and correctly reproduces the positions of the inelastic co-tunneling thresholds. We are interested in the evolution of the co-tunneling resonances in magnetic

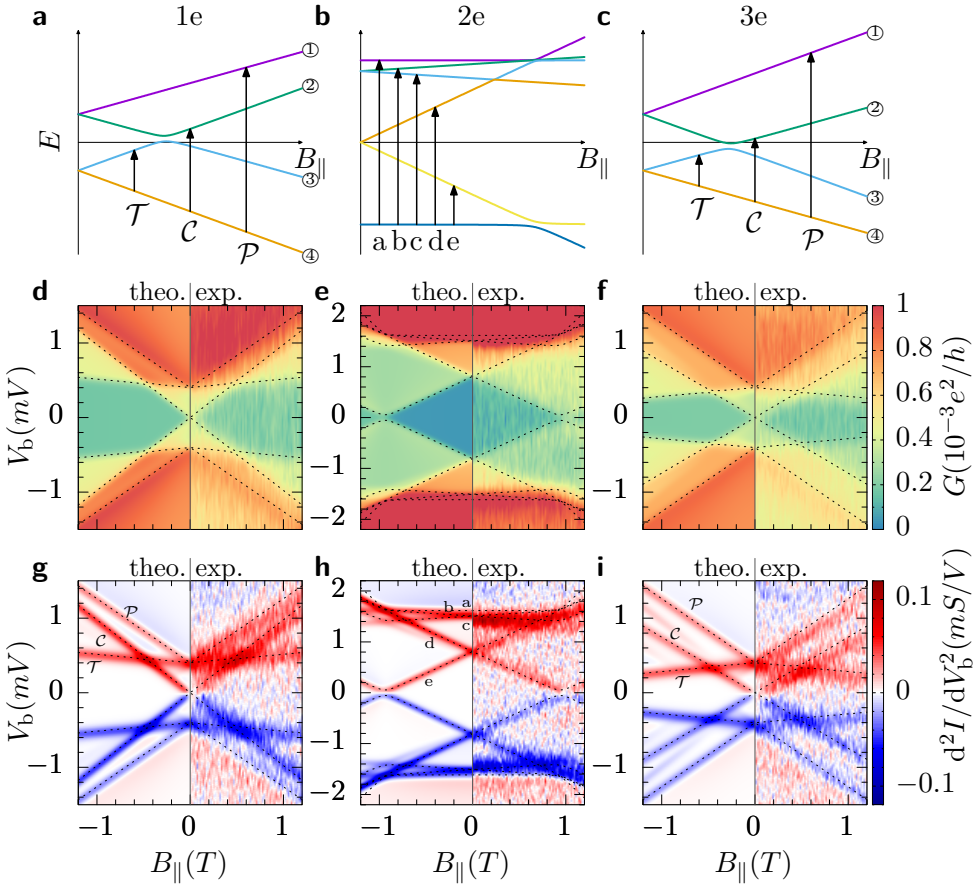

Figure 3.5: **a-c** Energy spectra for fillings $n_e = 1, 2, 3$ from left to right. **a** The single particle eigenstates are related via the $\mathcal{T}$, $\mathcal{C}$ and $\mathcal{P}$ operations which define the corresponding co-tunneling lines. **d-f** Differential conductance co-tunneling magnetotransport in the electron regime. **g-i** Current second derivative d^2I/dV_b^2 for better visibility of the inelastic co-tunneling lines. **d-i** The dotted lines correspond to the transition energies from the ground state calculated directly from the spectra. Each panel reports experimental data (positive magnetic field, adapted from Cleuziou *et al.* [68]) and our numerical calculations (negative field).

field, which is well captured by the perturbative approach as long as Kondo ridges have not yet formed. To this extent we look at bias traces in the center of the Coulomb diamonds, as indicated in Fig. 3.4 by dashed lines and plot them as function of a parallel magnetic field. The magnetospectrum corresponding to electron filling $n_e = 1, 2, 3$ of a longitudinal quadruplet, as expected for the perturbative regime, is shown in Fig. 3.5. In Fig. 3.5a-c we

recall the spectrum of a CNT-QD in a parallel magnetic field, now highlighting the eigenstates and their transitions from the ground state. The inelastic co-tunneling excitation spectrum consists of the energy differences in the spectrum within the same electron number to the ground state. Therefore each co-tunneling excitation can be labeled by the corresponding transition name. For the case of odd occupancies, we call $\mathcal{T}$ the transitions within a Kramers pair, $\mathcal{C}$ and $\mathcal{P}$ operations are associated to inter-Kramers transitions. These transitions connect exactly the states of the corresponding symmetry operations. The states with three electrons are closely related to the ones with one electron as they can be described by a single hole within a shell. For the case of two electrons we simply label the transitions from a to e. Figs. 3.5d-f show magnetotransport measurements and theoretical predictions in the electron regime. In Figs. 3.5g-i the current second derivative $\mathrm{d}^2I/\mathrm{d}V_\mathrm{b}^2$ is reported. We have included this quantity on top of the more conventional differential conductance to enhance eye visibility of the excitation spectra. At odd filling, all three possible ground state transitions are observed in the experiment as well as in the PT approach. Being signaled by co-tunneling steps in the differential conductance, they yield maxima/minima in the second derivative. Likewise for even occupation, except for the "a" transition at high field, forbidden by selection rules. This picture changes drastically for negative gate voltages since, due to the increased ratio of the tunnel coupling to the charging energy $\hbar\Gamma/U$, Kondo physics dominates for odd hole number and Kondo ridges form, cfg. Fig. 3.1b.

3.3.2 Hole side: Kondo peaks

To analyze the Kondo effect in our CNT we focus on a single shell on the hole side ($N_h = 6$) whose stability diagram is shown in Fig. 3.6a. Clear Kondo peaks at zero bias have formed in the center of the 1h and 3h Coulomb diamonds with values of the differential conductance of the order of the conductance quantum $2e^2/h$. The theoretical trace in Fig. 3.6b is the outcome of our scheme for the non-perturbative density matrix-numerical renormalization group (DM-NRG) code [86] from Budapest which uses the same model Hamiltonian but with slightly different parameters. The strong suppression of the conductance in the valley with even hole occupancy is an indication of the breaking of the SU(4) symmetry in the presence of SOC and valley mixing to an SU(2) $\otimes$ SU(2) one [72, 87]. In the larger stability diagram in Fig. 3.1b one can see that by

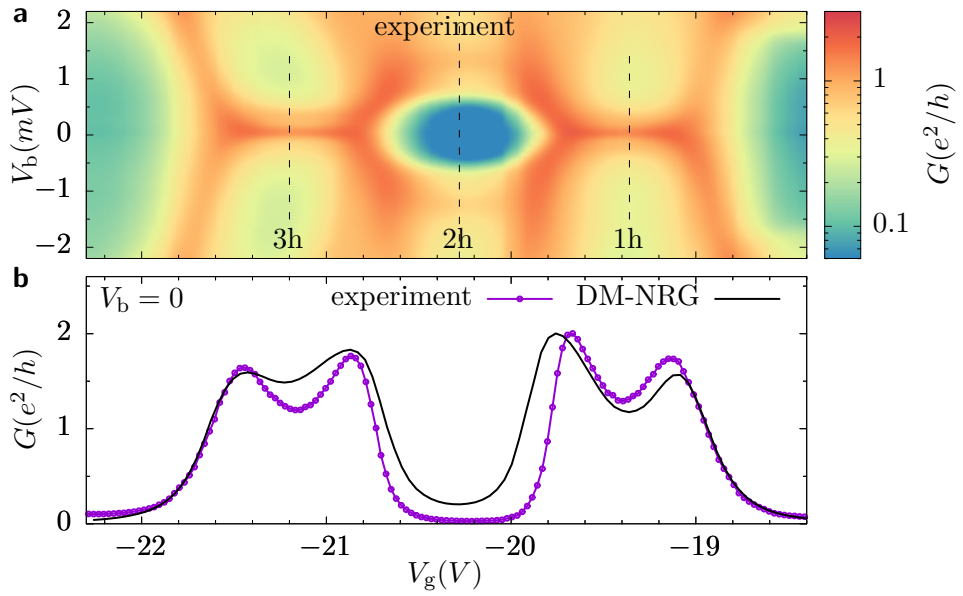

Figure 3.6: **a** Experimental stability diagram of a single shell at the hole side at zero magnetic field. Kondo ridges are forming in the center of the 1h and 3h Coulomb diamonds. Vertical lines mark the positions of the magnetotransport cuts. **b** Zero bias trace comparing experiment with DM-NRG calculations.

applying more negative gate voltage Kondo correlations are strengthened and the system approaches more and more the SU(4) Kondo regime.

In the DM-NRG calculations the two-particles exchange J was not included due to high computational costs. The latter further reduces the symmetry in the 2h valley, and hence the experimental conductance is stronger suppressed in that valley, as predicted by our simulations. On the other hand, J is not relevant for describing the spectrum in the 3h and 1h cases, which is the focus of this chapter. In the DM-NRG calculations the experiment was fitted assuming a temperature of $T = 30mK$. From the so extracted parameters we evaluate the temperature dependence of the conductance at $-\varepsilon_d = U/2 - \Delta/2$, and $-\varepsilon_d = 5U/2 + \Delta/2$, corresponding to gate voltage values located roughly in the middle of the 1h and 3h Coulomb diamonds, respectively, and extract the Kondo temperatures, see Fig. 3.7. At such values of ε_d the Kondo temperature takes its minimal value in a given valley, which sets a lower bound for T_K [87]. We find $T_K = 84mK$ and $T_K = 160mK$ for the 1h and 3h valleys, respectively. Correspondingly, $0.1 < T_{exp}/T_K < 1$, suggesting that the experiment is in the so-called Kondo crossover regime [62] also for the actual electronic and

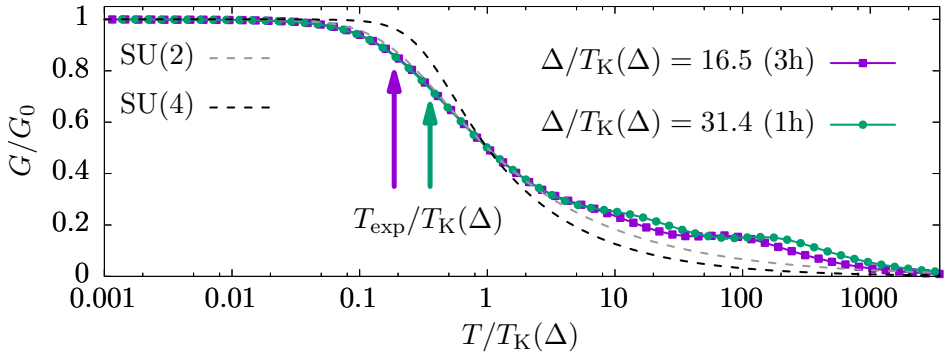

Figure 3.7: Scaling behavior of the linear conductance in the middle of the valleys with odd hole numbers, $G_0 \approx 2e^2/h$. The system lies in the crossover regime ($0.1 < T_{exp}/T_K(\Delta) < 1$), as pointed out by the arrows. T_K is the Kondo temperature determined from the DM-NRG calculation according to $G(T_K) = G_0/2$.

Kondo temperatures. We allow for an Kramers pair internal asymmetry $\alpha = 4\tan\gamma/(1+\tan\gamma)^2$ between the left and right leads, with $\tan\gamma = \Gamma_{R\kappa}/\Gamma_{L\kappa}$, which also fixes the height of the $2-3$ peak in the linear conductance trace of Fig. 3.6b. This fit yields $\alpha = 0.9$ and $\hbar\Gamma_{Lu} = 0.50meV$ and $\hbar\Gamma_{Ld} = 0.64meV$ for the u/d Kramers channels coupled to the left lead. Furthermore, we find $U = 4.7meV$, which in turn yields the Kondo temperatures $T_K(\Delta)$, as shown in Fig. 3.7. Notice that a different choice of the temperature T would have implied a different set of parameters for fitting to the experiment, and hence also different Kondo temperatures. Nevertheless, we are confident that our estimate of the ratio T/T_K is close to the experimental one, as is this ratio, for example, which determines how pronounced are the minima of the linear conductance in valley 1h and 3h.

Once again we analyze the magnetotransport measurements in the center of the Coulomb diamonds as highlighted in Fig.3.6a by the dashed lines. The result can be seen in Fig. 3.8. The spectrum in Figs. 3.8a-c is exactly the same as in the electron side when exchanging 1e↔ 3h and 3e↔ 1h and different parameters, cfg. Tab. 3.1. Upon inspection it is clear that only for the 2h case in Figs. 3.8e,h, the experimental data can be interpreted by means of a simple co-tunneling excitation spectrum. Moreover, the 2e and 2h co-tunneling spectra are very similar such that we can use the PT approach to qualitatively reproduce the experiment. In the 1h and 3h cases in Figs. 3.8d,f,g,i Kondo

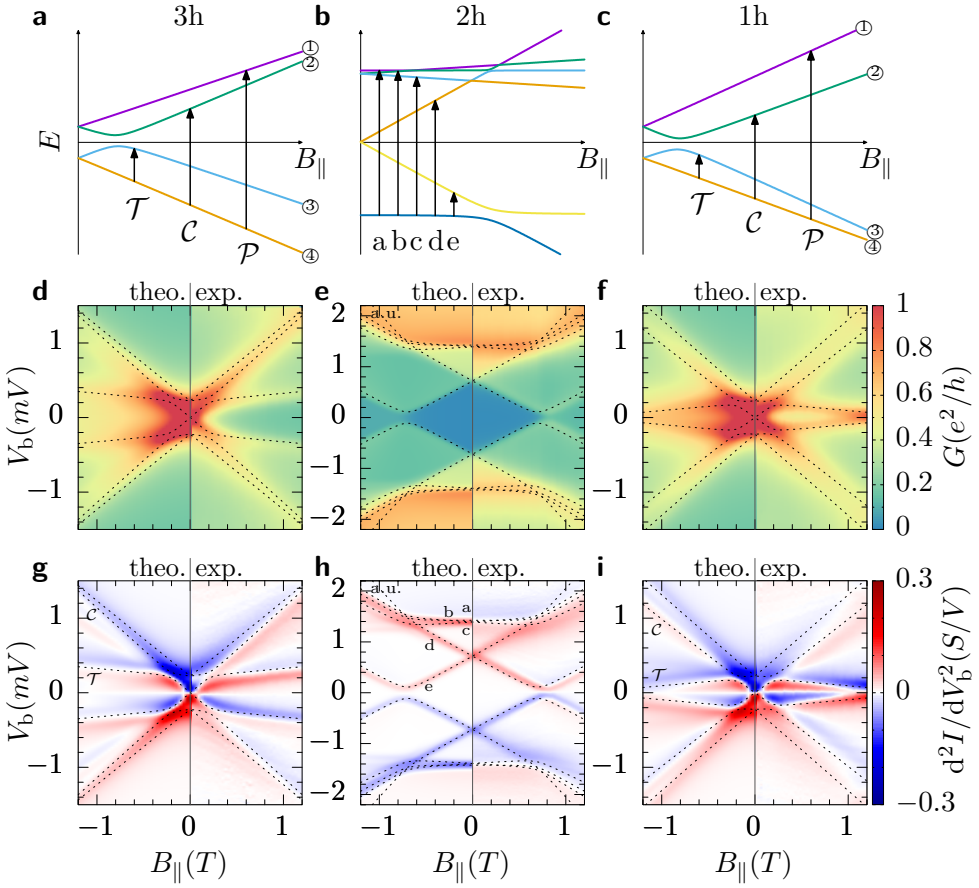

Figure 3.8: **a-c** Energy spectra for fillings $n_h = 3, 2, 1$ from left to right. **a,c** The single hole eigenstates are related via the $\mathcal{T}$, $\mathcal{C}$ and $\mathcal{P}$ operations. **d-f** Differential conductance magnetotransport in the hole regime. **g-i** Current second derivative d^2I/dV_b^2 for better visibility of the inelastic co-tunneling lines and Kondo ridges. **d-i** The dotted lines correspond to the transition energies from the ground state calculated directly from the spectra. Each panel reports experimental data (positive magnetic field, adapted from Cleuziou *et al.* [68]) and our numerical calculations (negative field). **e,h** The experimental results for the 2h and 2e cases are similar since no Kondo peaks are appearing in even numbered Coulomb diamonds and we can use the PT approach. **d,f,g,i** The $\mathcal{P}$ transitions are no longer experimentally resolved, as predicted by the transport theory, due to the Kondo effect. In the Kondo-regime $\mathcal{T}$ and $\mathcal{C}$ transitions yield maxima in the differential conductance, and hence zeros in the second derivative. Near maxima (minima) of G the second derivative decreases (increases), i.e., it changes from red to blue (blue to red) upon increasing the bias.

correlations dominate the low energy transport, and differences with respect to the electron sector are seen. The zero-bias Kondo peak does not immediately split as the field is applied. Rather the splitting occurs at a critical field such that the energy associated to the inelastic $\mathcal{T}$ transition is of the order of the Kondo temperature [62]. In the 1h valley the lowest pair of levels merges again for values of the field of about 1.2 Tesla, yielding a Kondo revival [64, 72]. In the Kondo-regime $\mathcal{T}$ and $\mathcal{C}$ transitions yield maxima in the differential conductance, and hence zeros in the second derivative. Near maxima (minima) of $\mathrm{d}I/\mathrm{dV}$ the second derivative decreases (increases), i.e., it changes from red to blue (blue to red) upon increasing the bias. Striking here is the observation that, in contrast to the 1e and 3e cases, *only one* of the two inter-Kramers transitions is resolved in the experimental data for the 3h and 1h valley. However, in particular for the 1h case, the $\mathcal{P}$ and $\mathcal{C}$ excitation lines as expected from the excitation spectrum should be separated enough to be experimentally distinguishable, similar to the 3e case. Note that maxima or minima in the second derivative do not mark excitation lines. By comparing with the excitation spectrum, we conclude that it is the $\mathcal{P}$ transition which is not resolved.

In order to describe also finite bias effects, and hence account for the inelastic transitions, one has to resort to non-perturbative transport approaches to the Kondo effect valid out of equilibrium. To this extent we have used the Keldysh effective action (KEA) approach, recently developed by S. Smirnov and M. Grifoni [74, 88]. The KEA is based on a slave boson field integral formulation, where a truncation of the effective action to terms quadratic in the slave boson fields enables us to evaluate the tunneling density of state of the Kondo quantum dot in analytic form. Due to such truncation, some cotunneling terms which become relevant at high bias voltage or large magnetic fields are neglected. As such, the KEA is expected to quantitatively describe the positions of the inelastic Kondo peaks at finite bias and magnetic field, but only qualitatively their shapes [74]. For the KEA calculations symmetric and equal couplings $\Gamma_{l\kappa} = \Gamma$ were assumed, an infinite charging energy U and no exchange coupling. This parameter choice necessarily yields a different Kondo temperature than in the experiments, which e.g. naturally have a finite charging energy and different couplings $\Gamma_{l\mathrm{u}}$ and $\Gamma_{l\mathrm{d}}$. Moreover, due to the choice of infinite U, our calculations well describe Kondo behavior when the effects of the fluctuations to states with double occupancy can be neglected, i.e. away from the middle of the diamonds with one or three holes. The experimental

curves shown in Fig. 3.8, however, correspond to gate voltages in the middle of the 1h and 3h diamonds. Nevertheless, due to the universal scaling properties of the differential conductance in the Kondo regime, the predictions of the KEA theory can become quantitative when both the experimental data and the theoretical curves are scaled by the respective Kondo voltage [89], or by an energy scale proportional to it, as long as only universal features are relevant. The KEA transport theory qualitatively reproduces these experimental features. These results naturally reconcile the apparently contradictory observations by Schmid *et al.* [74] and Jespersen *et al.* [35]. Furthermore, they suggest that the inhibition of selected resonances in the Kondo regime is of fundamental nature.

To understand why the $\mathcal{P}$ transition is being blocked, we have to extend the original spin-1/2 Kondo effect to the case of CNTs using their symmetries, as discussed in the next section.

3.4 Role of Kramers pseudospin

We have shown that in the electron regime the ground state is doubly degenerate at zero magnetic field. Only transitions involving the same state or its Kramers partner contribute to the linear conductance, where these virtual transitions are denoted via their corresponding symmetry relations, $\mathcal{I}$ or $\mathcal{T}$, respectively. This is shown in Fig. 3.9a. As illustrated in Fig. 3.9b, in the weak tunneling regime only energy differences matter, and hence both intra-Kramers ($\mathcal{I}$, $\mathcal{T}$) and inter-Kramers ($\mathcal{P}$, $\mathcal{C}$) transitions are expected in transport if the bias voltage overcomes the required threshold. This also holds true at finite magnetic field where one can resolve all three inelastic transitions independently. In the Kondo regime this picture changes. To this aim we observe that, when a sizable tunnel coupling to the leads is included, the CNT charge and pseudospin operators $\hat{Q}_\kappa$ and $\hat{\boldsymbol{J}}_\kappa$ are no longer symmetries of the coupled system, since the tunneling does not conserve the dot particle number. The occurrence of the Kondo effect, however, suggests that the CNT quantum numbers $j = 1, 2, 3, 4$ are carried also by the conduction electrons and conserved during tunneling [63]. For example, this is the case when the dot is only a segment of the CNT. Following Mantelli *et al.* [87], we hence introduce charge and pseudospin

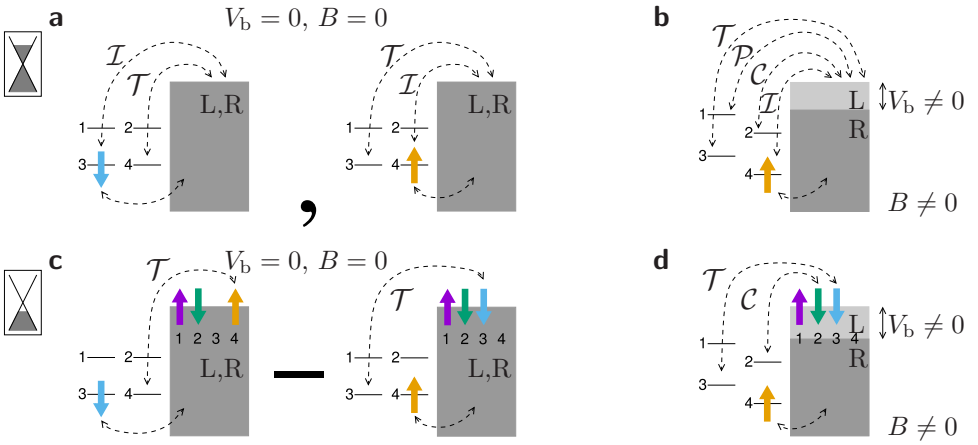

Figure 3.9: Ground state configurations and virtual processes of a CNT-QD with one electron filling in the co-tunneling and Kondo regimes. **a** Elastic co-tunneling processes to the left (L) and right (R) leads (grey areas) involving the same pseudospin, $\mathcal{I}$, and its Kramers partner, $\mathcal{T}$, contribute to the linear transport. **b** Kramers degeneracy is broken by a magnetic field. A finite bias allows us to identify the three inelastic processes $\mathcal{T}$, $\mathcal{P}$ and $\mathcal{C}$ which connect the bound states within a quadruplet. **c** The ground state in the Kondo regime is a singlet with no net Kramers pseudospin. Only virtual $\mathcal{T}$ fluctuations which involve a pseudospin flip matter at low energies. **d** At finite bias voltages only the inelastic $\mathcal{T}$, $\mathcal{C}$ transitions, which involve a pseudospin flip, are relevant in the deep Kondo regime.

operators of the coupled CNT plus bath system

$$\hat{\mathcal{Q}}_\kappa = \hat{Q}_\kappa + \hat{Q}_{\mathrm{B},\kappa}, \tag{3.15}$$

$$\hat{\boldsymbol{\mathcal{J}}}_\kappa = \hat{\boldsymbol{J}}_\kappa + \hat{\boldsymbol{J}}_{\mathrm{B},\kappa}. \tag{3.16}$$

Under the assumption that the tunneling couplings are the same within each Kramers channel $\kappa = \mathrm{u/d}$, the total Hamiltonian commutes with $\hat{\mathcal{Q}}_\kappa$ and $\hat{\boldsymbol{\mathcal{J}}}_\kappa$, which generates a global U(1) $\otimes$ U(1) $\otimes$ SU(2) $\otimes$ SU(2) symmetry of the coupled system. As a consequence, many-body states can be characterized by the quadruplet of eigenvalues $(\mathcal{Q}_\mathrm{d}, \mathcal{Q}_\mathrm{u}; \mathcal{J}_\mathrm{d}, \mathcal{J}_\mathrm{u})$, where the highest eigenvalue $\mathcal{J}_\kappa$ of $\hat{\mathcal{J}}^z_\kappa$ is indicated in the quadruplet. This notation gives direct access to the eigenvalues $\mathcal{J}_\kappa(\mathcal{J}_\kappa + 1)$ of $\hat{\boldsymbol{\mathcal{J}}}^2_\kappa$. Such quadruplets can be numerically calculated within the DM-NRG calculations [90], and yield for a single hole a singlet ground state characterized by the quadruplet $(0, 0; 0, 0)$. Thus "0" is also eigenvalue of $\hat{\boldsymbol{\mathcal{J}}}^2_\mathrm{u}$ and $\hat{\boldsymbol{\mathcal{J}}}^2_\mathrm{d}$. Due to $\mathcal{Q}_\kappa = 0$, the Kramers channels are half-filled (two charges per channel) whereby one charge arises from the electron trapped

in the CNT. For $\Delta = 0$ this CNT charge is equally distributed among the two channels, while for large values of $\Delta/T_{\rm K}(\Delta)$, as in our calculation in Fig. 3.7, it is mainly in the lowest Kramers channel. Thus at zero temperature the localized CNT pseudospin is fully screened by an opposite net pseudospin in the leads. In the basis $\{|\mathcal{J}_d^z;\mathcal{J}_u^z\rangle \otimes |\mathcal{J}_d^z;\mathcal{J}_u^z\rangle_{\rm B}\}$ spanned by the pseudospin eigenstates of CNT and leads this ground state is

$$\frac{1}{\sqrt{2}}\Big(|\Uparrow;-\rangle \otimes |\Downarrow;\Downarrow,\Uparrow\rangle_{\rm B} - |\Downarrow;-\rangle \otimes |\Uparrow;\Downarrow,\Uparrow\rangle_{\rm B} \Big), \tag{3.17}$$

a unique ground state with no net pseudospin. This situation is illustrated in Fig. 3.9c. In the standard spin-1/2 Kondo effect the appearance of a unique singlet ground state with no net spin is the result of the screening of the quantum impurity spin by the conduction electrons spins, due to the antiferromagnetic character of the coupling constant between such degrees of freedom [62]. Also for the more complex case of a CNT effective Kondo Hamiltonians have been derived, with positive coupling constants for Kramers channels identified by orbital and spin degrees of freedom [63, 91]. The antiferromagnetic character of the coupling constants remains also when, as in our case, the more abstract Kramers pseudospin is used. A natural consequence of the antiferromagnetic nature of the correlations is that at low temperatures and zero bias elastic virtual transitions which flip the pseudospin, i.e., $\mathcal{T}$ transitions, are favoured, as depicted in Fig. 3.9c. Similarly, $\mathcal{C}$ transitions are inelastic processes which flip the pseudospin and become accessible at finite bias, as shown in Fig. 3.9d. They connect the singlet ground state to an excited state where the CNT charge is located in the upper Kramers channel. Our results suggest that $\mathcal{P}$ transitions are inhibited because they involve virtual transitions which conserve the pseudospin.

Magnetotransport measurements performed for other quadruplets both in the electron and hole regimes exhibit qualitatively similar features, and hence confirm the robustness of the suppression of $\mathcal{P}$ transitions in the Kondo regime. This can be found in App. B. A further proof of pseudospin screening can be obtained by varying the angle between the magnetic field and the CNT.

3.5 Angular dependence

While an axial field sets the same spin quantization axis as the SOC [31], this is no longer the case for a generic orientation of the magnetic field. To further

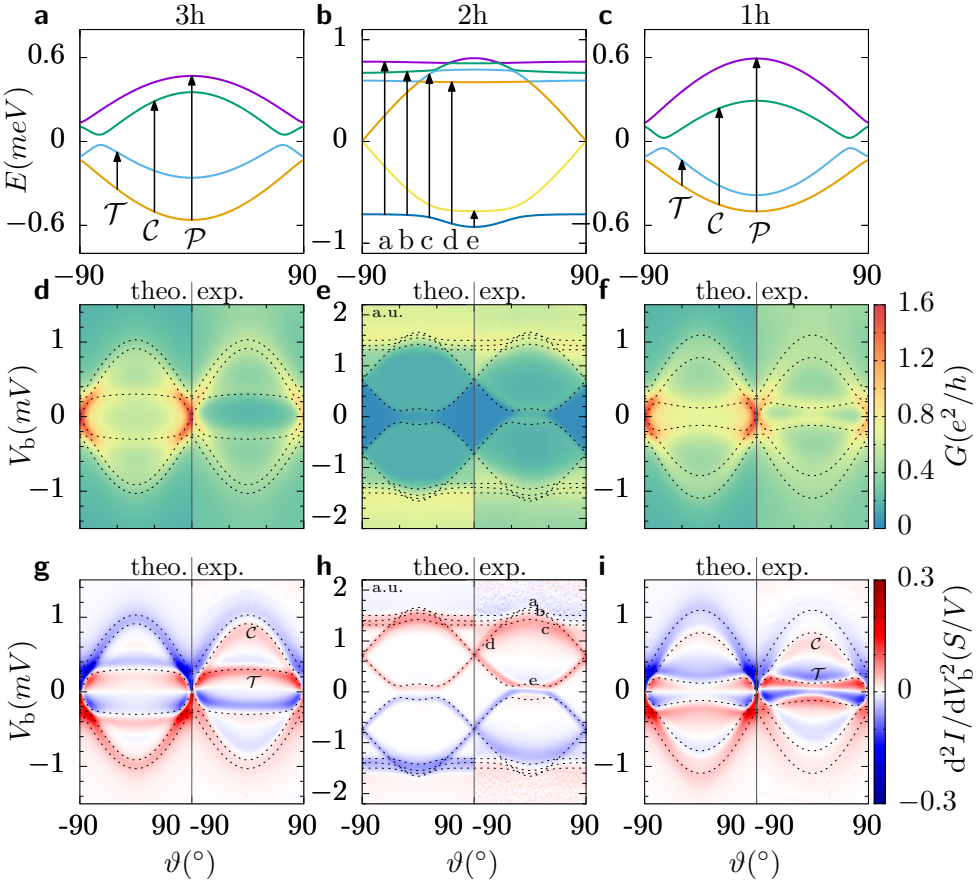

Figure 3.10: Angular dependence of the spectrum and magnetotransport in the Kondo regime. The magnetic field is fixed at $|\boldsymbol{B}| = 0.8T$. **a-c** Spectrum as function of the angle ϑ between the magnetic field and the CNT for 3h, 2h and 1h from left to right. **d-f** Differential conductance magnetotransport. **g-i** Second current derivative for better visibility. **d-i** Only $\mathcal{T}$ and $\mathcal{C}$ transitions are resolved both in experiment (right sides) and theory (left sides).

confirm that it is the Kramers pseudospins and not distinct spin or orbital degrees of freedom which should be considered in the most general situations, we report results for the differential conductance as function of the angle ϑ formed by the magnetic field and the CNT's axis. The combined action of SOC, valley mixing and non collinear magnetic field mixes spin and valley degrees of freedom which, in general, are no longer good quantum numbers to classify CNTs states. Nevertheless, the three discrete $\mathcal{T}$, $\mathcal{P}$ and $\mathcal{C}$ operations still enable us to identify the inelastic transitions in the 1h and 3h case, independent of the direction of the magnetic field. The angular dependence of the spectrum for a fixed magnetic field amplitude is shown in Figs. 3.10a-c. The corresponding magnetotransport results are shown in Figs. 3.10d-i. A perpendicular magnetic ($\vartheta = \pm 90°$) field almost restores (for our parameter set) Kramers degeneracy, thus revitalizing the Kondo resonance for this angle. As the field is more and more aligned to the CNT's axis, the degeneracy is removed, which also enables us to distinguish between $\mathcal{P}$ and $\mathcal{C}$ transitions. As in the axial case only the inelastic resonance associated to the $\mathcal{C}$ transition is clearly resolved in both the experiment and theory, while the $\mathcal{P}$ transition is blocked.

3.6 Conclusions and Outlook

The ability to tune the strength of the electronic interactions in a CNT-QD has enabled us to unravel the Kondo screening of degrees of freedom of a CNT-QD. Our results show that specific low-energy inelastic processes, while observed in the perturbative co-tunneling regime, tend to be blocked in the Kondo regime due to antiferromagnetic correlations, which at zero temperature yield a many-body ground state with net zero Kramers pseudospin involving degrees of freedom of the QD and of the leads. In specific it is possible to relate all processes to existing symmetries of the CNT and find that it is the particle-hole like $\mathcal{P}$ transition that gets blocked. This signature of the Kondo effect is universal, in the sense that it does not depend on the degree of the SOC or valley mixing specific to a given CNT. As such, it is also expected for SU(4) correlated CNTs, which explains the missing inelastic resonance in the seminal work [64]. Furthermore, we believe that such pseudospin selective suppression should be detectable also in a variety of other tunable QD systems with emergent SU(4) and SU(2) $\otimes$ SU(2) Kondo effects [76, 79, 92–95].

An additional exchange coupling further breaks the SU(2) symmetries in

the 2h valley. For our DM-NRG calculations in the Kondo regime we have neglected the exchange coupling J. Its inclusion would have been possible but at the expense of a significant increase in the computational cost, due to the reduced symmetry. Likewise J was not included in the KEA. Further work might investigate the influence of such an exchange interaction. Because the screening is progressively suppressed by increasing the temperature or the bias voltage, it should be possible to recover the $\mathcal{P}$ transitions by continuously tuning those parameters. Indeed, signatures of the re-emergence of the $\mathcal{P}$ transition are seen in the KEA calculations and experimental traces at fields around $0.9T$ in the form of an emerging shoulder, App. B. Experiments at larger magnetic fields, not accessible to our experiment, are required to record the evolution of this shoulder, and thus the suppression of Kondo correlations. Additional asymmetries in the coupling strengths $\Gamma_{\mathrm{L/R,u/d}}$, especially in the KEA calculations might lead to stronger revivals of the $\mathcal{P}$ transitions.

CHAPTER 4

Dark states in a carbon nanotube quantum dot

Coherent preparation by laser light of quantum states in atoms, molecules or QDs can lead to quantum interference in the amplitudes of optical transitions. One such destructive interference effect is coherent population trapping (CPT) which is observable in systems with at least two low–lying ground states and a common excited state. Illumination by resonant lasers can pump electrons into a coherent superposition of the ground states which can no longer absorb the light [96, 97]. The minimal system with three states is referred to as Λ–type system owing to its energy level alignment as seen in Fig. 4.1a. Within the dipole approximation the system and laser Hamiltonian read $\hat{H}_\Lambda = \hat{H}_0 + \hat{H}_{\rm dip} = \sum_i \epsilon_i \left|i\right\rangle\!\left\langle i\right| - \sum_{j=1}^{2} \boldsymbol{\mu}_j \cdot \boldsymbol{E}_j$ which is often expressed in terms of the Rabi frequencies $\Omega_j = \boldsymbol{\mu}_j \cdot \boldsymbol{E}_j^0/\hbar$ with $\boldsymbol{E}_j^0$ being the amplitude of the electric field $\boldsymbol{E}_j$ and $\boldsymbol{\mu}_j$ the electric dipole moment. It is written in the basis of the two ground states $|1\rangle$, $|2\rangle$ and the excited state $|3\rangle$, where dipole transitions between the two ground states are forbidden, $\hat{H}_{\rm dip} = -\hbar \sum_{j=1}^{2} \Omega_j (e^{i\omega_j t} + e^{-i\omega_j t}) \left|j\right\rangle\!\left\langle 3\right| + \text{h.c.}$. Applying the rotating wave approximation results in $\hat{H}_{\rm dip}^{\rm RWA} = -\hbar \sum_{j=1}^{2} \Omega_j e^{i\omega_j t} \left|j\right\rangle\!\left\langle 3\right| + \text{h.c.}$. The full Hamiltonian with two laser fields, rotated by $U = \exp\{-i \sum_{j=1}^{2} \omega_j t \left|j\right\rangle\!\left\langle j\right|\}$, $\tilde{H}_\Lambda^{\rm RWA} = U^\dagger \hat{H}_\Lambda^{\rm RWA} U - i\dot{U}U^\dagger - \epsilon_1 + \omega_1$, reads

$$\tilde{H}_\Lambda^{\rm RWA} = \hbar \begin{pmatrix} 0 & 0 & -\Omega_1 \\ 0 & \Delta_1 - \Delta_2 & -\Omega_2 \\ -\Omega_1 & -\Omega_2 & \Delta_1 \end{pmatrix}, \tag{4.1}$$

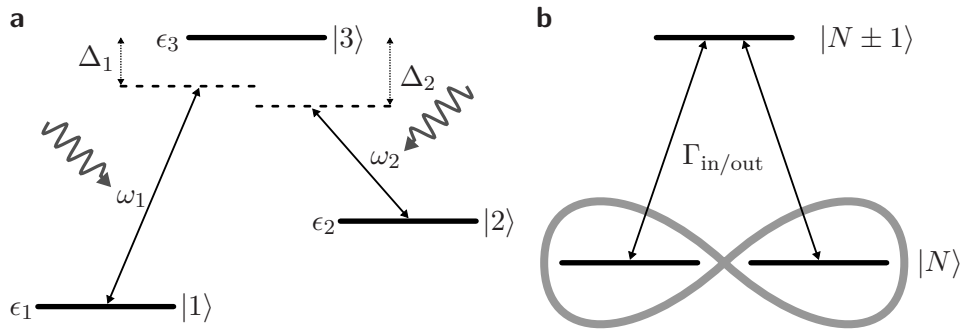

Figure 4.1: Schematic representation of a three level Λ–system. **a** In atoms the two driving frequencies $\omega_{1/2}$ show mismatches $\Delta_{1/2}$ to the corresponding excitation energies. **b** An applied bias voltage can take the role of the laser fields when the excited state is replaced with a level of different particle number connected by tunneling rates $\Gamma_{\text{in/out}}$. In both cases a coherent superposition of the ground states results in DSs.

where $\hbar\Delta_i = \epsilon_3 - \epsilon_i - \hbar\omega_i$ are the detunings of the laser frequencies from the corresponding atomic transitions. This situation is sketched in Fig. 4.1a. For the case of a two-photon resonance, where the detuning of the two laser modes matches the ground state splitting $\hbar(\omega_2 - \omega_1) = \epsilon_1 - \epsilon_2$, there always exists one eigenstate

$$|\text{DS}\rangle = \frac{\Omega_2}{\Omega}|1\rangle - \frac{\Omega_1}{\Omega}|2\rangle\,, \tag{4.2}$$

with $\Omega = \sqrt{\Omega_1^2 + \Omega_2^2}$. This state features the interesting property that it is decoupled from the light

$$\langle 3|\,\tilde{H}_\Lambda^{\text{RWA}}\,|\text{DS}\rangle = 0. \tag{4.3}$$

Because fluorescent light emission is then suppressed, this coherent superposition is known as a dark state (DS). One has to note here that usually additional relaxation mechanisms are required to end up in this DS.

QDs offer the possibility to engineer artificial atoms and molecules by proper circuit design, and hence to probe CPT in effective Λ–systems. Early proposals [98–100] have considered a microwave irradiated double QD analogs of the seminal experiment [101]. Since localization of the electrons in the DS also implies a vanishing current through the double dot, this allows the electrical detection of CPT by recording variations of the current as the microwaves parameters are tuned. This situation is sketched in Fig. 4.2a.

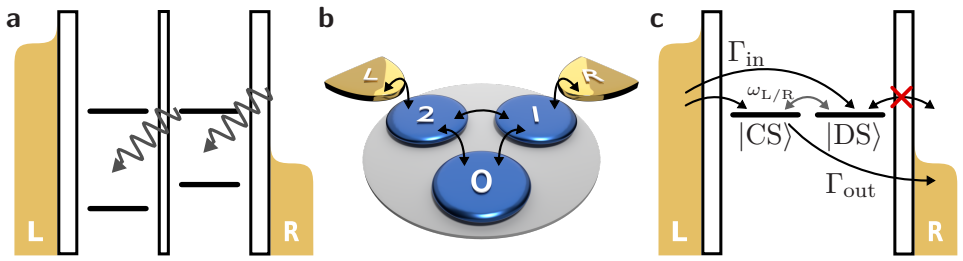

Figure 4.2: QD realizations of CPT. **a** A driven double QD enables electrical read out of DS formation. **b** A triple QD features all-electric dark states. **c** The general chemical potential landscape in the presence of dark and coupled states. For the chosen bias voltage polarity, an electron can enter a DS from the left lead but it can not leave it by tunneling to the right lead. Precession allows population transfer from the dark state to the coupled state (CS).

Quantum dots in ring geometries [102–108] or single-molecules with orbital degeneracies [46, 109, 110], however, also allow an all-electrical realization of CPT, being the topic of this chapter. In Fig. 4.2b the example of a triple QD is shown which will be analyzed in detail in chapter 7. Here, an applied bias voltage allows tunneling of electrons in and out of the dot, which in turn changes the charge state of the system; thus the bias takes the role of the optical fields, see Fig. 4.1b. If, due to symmetry, the quantum-dot complex has (quasi)-degenerate states with the same charge, they can form coherent superpositions which are decoupled from one of the two leads. Fig. 4.2c shows the chemical potential landscape for a positive potential drop between left and right leads, and a DS which is decoupled from the right lead. This situation allows electrons to enter the DS from the left while preventing them to leave it to any of the two leads. CPT occurs and current is suppressed.

Despite the large number of theoretical proposals, the experimental observation of CPT in quantum dot setups has remained elusive so far. In this chapter we report for the first time its occurrence in a CNT-QD. Let us recall some results of chapter 1.2. Similar to graphene, CNTs posses an orbital (valley) degree of freedom, arising from the two inequivalent Dirac points in the honeycomb lattice. In CNTs of the zig-zag class, such orbital degree of freedom is also the longitudinal orbital momentum ℓ_z, accounting for clockwise ($\ell_z = -\ell$) or anti-clockwise ($\ell_z = \ell$) rotations along the tube waist [33], see Fig. 4.3. The finite length of the CNT-QD results in the quantization of the longitudinal momentum, characterized by a natural number m, and hence in a

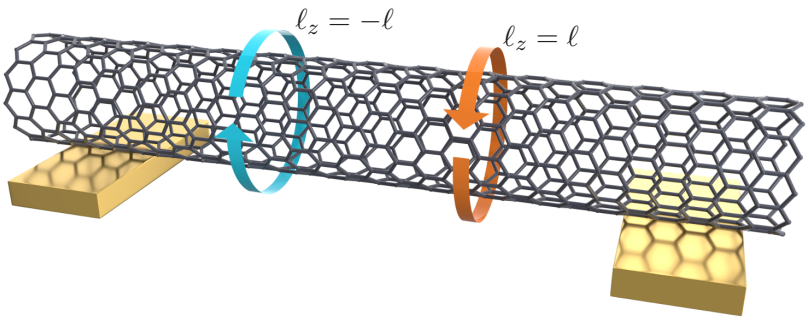

Figure 4.3: Angular momentum states of a CNT-QD for clockwise ($\ell_z = -\ell$) or anti-clockwise ($\ell_z = \ell$) rotations of the electrons.

shell structure like for the atomic bound states. In the absence of spin-orbit coupling [31, 32, 34] and valley mixing [28, 34, 35, 37], each shell consists of four degenerate bound states with spin, $\sigma = \uparrow, \downarrow$, and angular momentum degree of freedom, $\ell_z = \pm\ell$. Thus each shell can accommodate up to $N = 4$ electrons.

This chapter is based on Donarini *et al.* [P.6]. We show that for a CNT-QD near the $N = 0 \leftrightarrow 1$ resonance we find such DSs and, due to the particle-hole symmetry of the many-body spectrum, if the voltage polarity is reversed, CPT is also expected near the $N = 3 \leftrightarrow 4$ resonance. We give analytical expressions for these DSs and analyze the dependence on gate and bias voltages of the resulting current suppression. A microscopical picture justifies the main ingredient to obtain DSs: an angular momentum dependent tunneling phase.

4.1 Experimental signatures of CPT

We report on an experiment performed in the group of Prof. Strunk in Regensburg. On a highly p-doped Si substrate with a $300nm$ thermally grown SiO_2 layer, ring-like electrode structures were defined by electron beam lithography and evaporation of $20nm$ Re and $40nm$ Co. A catalyst for the CVD process was deposited in the center of the electrode ring structure to increase the chance of a CNT connecting the contacts. The CNT growth was performed as the last sample fabrication step to ensure the production of ultra clean devices [80]. MOKE measurements showed no magnetic behavior of the Re/Co contacts after CVD, ruling out spin valve effects with a similar $I - V$ characteristics [111]. The current as well as the differential conductance were

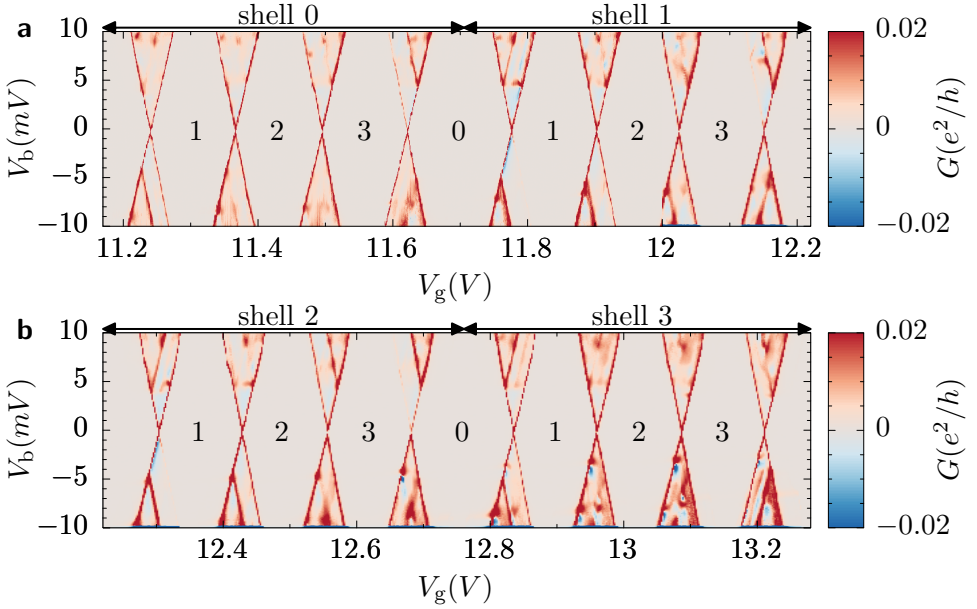

Figure 4.4: Experimental differential conductance as function of back-gate voltage V_g and bias voltage V_b. The 16 consecutive Coulomb diamonds can be assigned to four CNT shells (**a** shells 0 and 1, **b** shells 2 and 3). With increasing V_g these shells get progressively occupied with $N = 1$ to $N = 4$ electrons, as highlighted.

measured using an Ithaca 1211 IV-converter.

In Fig. 4.4 we show the experimentally measured differential conductance G as function of the applied bias voltage V_b and of a back-gate voltage V_g. Coulomb diamonds are clearly visible, with a characteristic 4–fold periodicity, a signature of the successive filling of CNT shells with four electrons each. Noticeably, three almost identical diamonds are followed by a larger one. For the small diamonds only a charging energy has to be paid, which indicates almost degenerate states within a shell and therefore negligibly small SOC and valley mixing, as well as a small exchange energy for the middle diamond. By closer inspection of the current voltage characteristics in shell 1 and shell 2, we observe signatures of current suppression in the form of faint Coulomb diamond edges and negative differential conductance for the $0 \leftrightarrow 1$ transitions. The same pattern occurs also at the $3 \leftrightarrow 4$ transition for opposite bias polarity. To understand whether such current suppression is due to the formation of a DS, we have compared experimental gate traces and bias traces with theoretical calculations for the stationary current where coherences between orbitally

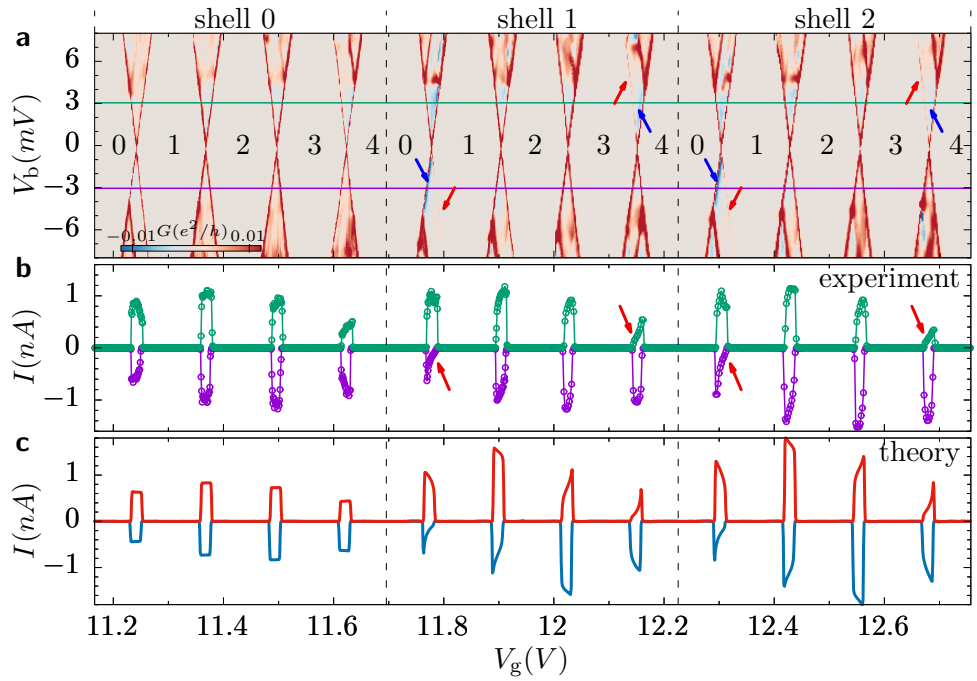

Figure 4.5: **a** Stability diagram of shells $0-2$ with highlighted negative differential conductance and faint Coulomb diamond borders, indicated by blue and red arrows, respectively. **b** Current vs gate voltage for the two values $V_b = \pm 3.045mV$ of the bias voltages corresponding to the green/purple lines in panel (**a**). Current suppression associated to coherent population trapping is indicated by red arrows. **c** Numerically evaluated stationary current qualitatively reproducing the experiment. The parameters used in the simulation are in Tab. 4.1.

degenerate states are fully retained for shells 0-2 in Fig. 4.5. Fig. 4.5b shows experimental gate traces for $V_b = \pm 3.045mV$ (green/purple line in Fig. 4.5a). The numerical calculations are depicted in Fig. 4.5c. We use a transport code which contains terms of first order in the tunneling rate Γ and keeps coherences also between states of different energy, so called non-secular terms, based on Eq. (2.35). The used parameters can be found in Tab. 4.1. A current suppression is clearly visible at the $0 \leftrightarrow 1$ and $3 \leftrightarrow 4$ transitions, and is indicated by the red arrows in the experimental traces. The same outcome is seen in the theoretical traces. Since most of the displayed shells behave similarly, we have focused on the $0 \leftrightarrow 1$ and $3 \leftrightarrow 4$ transitions of shell 1. The respective experimental stability diagrams are shown on an enlarged gate voltage scale in Figs. 4.6a,b, the corresponding numerical results are depicted

parameter	shell 0	shell 1	shell 2
ε_0		4.35meV	
U		20meV	
J		10μeV	
$k_\mathrm{B}T$		0.5meV	
$\hbar\Gamma_\mathrm{R}$	$2\mu eV$	10μeV	10μeV
$\hbar\Gamma_\mathrm{L}$		4μeV	
$\hbar\Gamma_\mathrm{rel}$		0.1μeV	
$\Delta\phi$	0.01π	0.11π	0.07π
η		0.55	

Table 4.1: Numerical parameters to fit all three shells of the experiment. Only Γ_R and $\Delta\phi$ vary with the shell, all other parameters are the same for all shells.

in Figs. 4.6c,d. We observe similar behavior within a range of $3mV$ around zero bias. At larger bias voltages the experimental curves display extra features which are not understood at present (see also in Fig. 4.4). Experimental and theoretical gate traces are shown together in Figs. 4.6e,f. At the $0 \leftrightarrow 1$ resonance both the experimental and theoretical gate traces show a rectangular shaped current at positive bias, typical of QD behavior in the sequential tunneling regime. However, at negative bias the current abruptly decreases as the gate increases, indicating trapping of a single electron. At the $3 \leftrightarrow 4$ resonance similar current shapes are observed for opposite bias voltage polarity and upon gate voltage mirroring, a signature of trapping of a single hole. As discussed below, all the features observed in Figs. 4.5 and 4.6 can be explained in terms of CPT in a DS, combined with a precessional motion which transfers population between the dark and the coupled state, as sketched in Fig. 4.2c.

4.2 Model and dark states

The peculiarity of the isolated spectrum, e.g. the presence of orbital degeneracies (or quasi-degeneracies), is decisive for the occurrence of CPT. As discussed above, the single particle energy spectrum of a CNT of finite length is fully characterized by a shell quantum number m and the pair (σ, ℓ_z), accounting for the spin and orbital degrees of freedom. Curvature-induced SOC and valley-mixing remove the intra-shell degeneracy. The amplitude of the SOC is

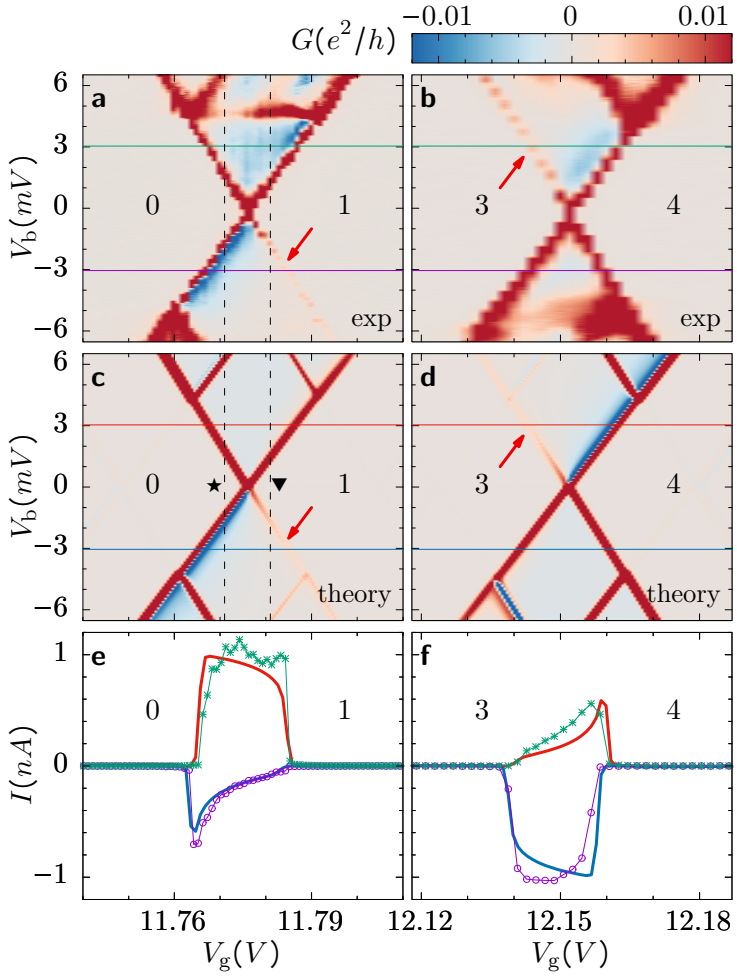

Figure 4.6: **a,b** Experimental stability diagrams for shell 1. Current suppression features observed for single-electron tunneling in panel (**a**), also occur for single-hole tunneling under reverted bias polarity and mirroring of the gate voltage, as shown in panel (**b**). **c,d** Theoretical stability diagrams for the $0 \leftrightarrow 1$ and $3 \leftrightarrow 4$ dynamical regimes reproducing the experimental observation. **e,f** Comparison of experimental and numerical current-gate traces at bias voltage set to $V_b = \pm 3.045mV$.

largest near the Dirac point and of the order of a fraction of meV. However, it strongly decreases for states away from the bottom of the CNT conduction band [35], which is possibly the reason why its effects are not relevant in our experiment. Similarly, valley mixing due to disorder is strongly suppressed in ultraclean CNTs, and is forbidden by symmetry in CNTs of the zig-zag class [28], which suggests that we have measured such kind of tube in our experiment. We neglect both perturbations in the following. We include a charging term U and the exchange interaction J. The latter strongly depends on the CNT chirality and radius and was assumed to be $10\mu eV$. The CNT-QD Hamiltonian then reads

$$\hat{H}_{\mathrm{CNT}} = \sum_{m\ell_z} \left(m\varepsilon_0 - e\alpha_{\mathrm{g}} V_{\mathrm{g}}\right) \hat{n}_{m\ell_z} + \frac{U}{2}\hat{N}^2 + J\sum_{m}\left(\hat{\mathbf{S}}_{m\ell}\cdot\hat{\mathbf{S}}_{m-\ell} + \frac{1}{4}\hat{n}_{m\ell}\hat{n}_{m-\ell}\right), \tag{4.4}$$

where in the numerical calculations only 3 shells ($m \in \{0,1,2\}$) are considered with an inter-shell spacing ε. The gate voltage V_{g} applied with a level arm α_{g} ensures particle-hole symmetry of Eq. (4.4) with respect to shell $m = 1$ for $e\alpha_{\mathrm{g}}V_{\mathrm{g}} = \varepsilon_0 + 6U + J/4$. Further, the occupation operator $\hat{n}_{m\ell_z} = \sum_\sigma d^\dagger_{m\ell_z\sigma} d_{m\ell_z\sigma}$, and the spin operator $\hat{\mathbf{S}}_{m\ell_z} = \frac{1}{2}\sum_{\sigma\sigma'} d^\dagger_{m\ell_z\sigma}\boldsymbol{\sigma}_{\sigma\sigma'} d_{m\ell_z\sigma'}$ are defined in terms of creation (destruction) operators $d^{(\dagger)}_{m\ell_z\sigma}$. The CNT Hamiltonian can be diagonalized analytically by using the basis corresponding to the eigenstates of the total particle number $\hat{N} = \sum_{m\ell_z}\hat{n}_{m\ell_z}$, total spin $S^2 = \sum_{m\ell_z}\hat{\mathbf{S}}^2_{m\ell_z}$, total spin projection $S_z = \frac{1}{2}\sum_{m\ell_z\sigma}\sigma d^\dagger_{m\ell_z\sigma} d_{m\ell_z\sigma}$, and total angular momentum operator $L_z = \sum_{m\ell_z}\ell_z\hat{n}_{m\ell_z}$. Accordingly, many-body states are defined by the vector set $\{|N, E; S, S_z, L_z\rangle\}$ using additionally the eigenenergy E. In our three-shells model, we have fixed the energy E_0 and the particle number of the configuration with the shell $m = 0$ completely full, and the upper two shells $m = 1, 2$ completely empty. The $N = 0$ ground state is therefore

$|0, E_0; 0, 0, 0\rangle \equiv |0\rangle =$ 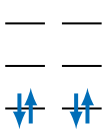 . (4.5)

The left (right) states are for angular momentum values $\ell_z = +(-)\,\ell$ and the up/down arrows indicate opposite spin direction. The $N = 1$ ground state is four-fold degenerate. A basis is the quadruplet of states $\{|1, E_1; \frac{1}{2}, \sigma, \ell_z\rangle \equiv |\sigma, \ell_z\rangle\}$ obtained by adding one electron with quantum numbers (σ, ℓ_z) on shell

$m = 1$

$$|1, E_{1_0} = \varepsilon_0; \frac{1}{2}, \pm\frac{1}{2}, \pm\ell\rangle = \left\{ \right.$$ 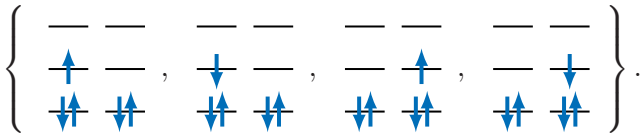 $$\left. \right\}.$$ (4.6)

Many-body excited states are obtained by creating electron-hole pairs starting from a given ground state configuration for fixed electron number, as exemplary shown below for the case $N = 0$ (left) and $N = 3$ (right).

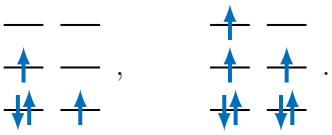 (4.7)

In App. C all such eigenstates can be found up energies of $\varepsilon_0 \pm J$ above the ground state. Excited many-body states have been considered in the numerics up to a cut-off of $1.5\varepsilon_0$ with respect to the ground state.

The tunneling Hamiltonian allows the system to make transitions between dot states with different particle number, and plays the role of the resonant laser fields inducing transitions in the atomic Λ–systems. We assume the standard form of Eq. (2.3) where now we account for the dependence of the tunneling amplitude $t_{l\boldsymbol{k}m\ell_z}$ on the momentum. In general it is a complex quantity which accounts for the overlap between an electron wave function in lead l, characterized by the momentum $\boldsymbol{k}$, and a CNT wave function for shell m and angular momentum ℓ_z in the contact region. We show later in Sec. 4.5 that the single particle rate matrix $(\mathbf{\Gamma}_l^m)_{\ell_z\ell_z'}(\Delta E) := 2\pi \sum_{\boldsymbol{k}} t^*_{l\boldsymbol{k}m\ell_z} t_{l\boldsymbol{k}m\ell_z'} \delta(\xi_{l\boldsymbol{k}} - \Delta E)/\hbar$ is in general no-diagonal in the angular momentum basis. For a single atom contact, or in the more general surface Γ-point approximation, it takes the simple form

$$(\mathbf{\Gamma}_l^m)_{\ell_z\ell_z'} = \Gamma_l^m (\mathcal{R}_l^m)_{\ell_z\ell_z'} = \Gamma_l^m e^{i\phi_l^m(\ell_z - \ell_z')}, \tag{4.8}$$

where the phase ϕ_l^m describes a global property of contact l for shell m. For later usage we defined the hermitian coherence matrices $\mathcal{R}_l^m$ and the bare tunneling rate Γ_l^m. Using this form of the rate matrix allows the construction of DSs.

4.2.1 One-electron dark states

Eq. (4.6) allows one to construct linear combinations $|\mathrm{DS}, \sigma; l\rangle$ of the single-particle ground states $|\sigma, \ell_z\rangle$ which are decoupled from lead l and hence may

act as DS for a given bias polarity. Since shells 0 and 2 are frozen in this consideration we focus on shell 1 only and drop the shell index m. Such states are determined through the requirement

$$\langle 0|\, d_{l\sigma}\, |\mathrm{DS}, \sigma; l\rangle \equiv 0, \tag{4.9}$$

where $d_{l\sigma}$ destroys a CNT electron of spin σ at lead l. We express such operators in the angular momentum basis, $d_{l\sigma} = \sum_{\ell_z} e^{i\phi_l \ell_z} d_{\ell_z \sigma}$, motivated by the choice of the rate matrix in Eq. (4.8). In Sec. 4.5 we will show that this phase is defined up to an overall phase that can be gaged away. For the DS we find the anti-bonding linear combination

$$\left.\begin{matrix} |\mathrm{DS}, \tfrac{1}{2}; l\rangle \\ |\mathrm{CS}, \tfrac{1}{2}; l\rangle \end{matrix}\right\} = \frac{1}{\sqrt{2}}\Big(e^{i\ell\phi_l}$$ 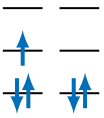 $$\mp e^{-i\ell\phi_l}$$ 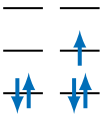 $$\Big),$$

$$\left.\begin{matrix} |\mathrm{DS}, -\tfrac{1}{2}; l\rangle \\ |\mathrm{CS}, -\tfrac{1}{2}; l\rangle \end{matrix}\right\} = \frac{1}{\sqrt{2}}\Big(e^{i\ell\phi_l}$$ 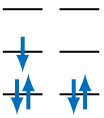 $$\mp e^{-i\ell\phi_l}$$ 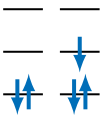 $$\Big), \tag{4.10}$$

where the bonding linear combination is the corresponding CS. Given this form for the DS at lead l, one finds $\langle 0|\, d_{\bar{l}\sigma}\, |\mathrm{DS}, \sigma; l\rangle \propto \sin(\ell(\phi_\mathrm{R} - \phi_\mathrm{L}))$ for the matrix element involving the destruction operator at the opposite lead $\bar{l}$. Thus the requirement $\phi_\mathrm{R} \neq \phi_\mathrm{L}$ is necessary for a dark state to have vanishing transition amplitude only at one lead.

4.2.2 Two-electrons dark states

The results of the $0 \leftrightarrow 1$ transitions can be easily extended to higher electron numbers since a dark state which blocks transitions to 2-electrons states can also be constructed. For $N = 2$ we find a spin-singlet ground state

$$|2, E_{2_0} = 2\varepsilon_0 - \frac{J}{2}; 0, 0, 0\rangle = \frac{1}{\sqrt{2}}\Big($$ 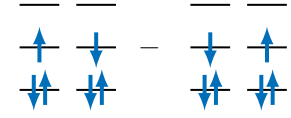 $$\Big), \tag{4.11}$$

a doublet of angular momentum first excited states

$$|2, E_{2_1} = 2\varepsilon_0; 0, 0, 2\ell\rangle =$$ 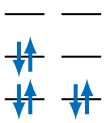 $$, \quad |2, E_{2_1} = 2\varepsilon_0; 0, 0, -2\ell\rangle =$$ 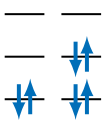 $$, \tag{4.12}$$

and a spin-triplet of second excited states with energy $E_{2_2} = 2\varepsilon_0 + J/2$,

$$|2, E_{2_2}; 1, -1, 0\rangle = \quad , \quad |2, E_{2_2}; 1, 1, 0\rangle = \quad ,$$

$$|2, E_{2_2}; 1, 0, 0\rangle = \frac{1}{\sqrt{2}} \left(\quad + \quad \right). \tag{4.13}$$

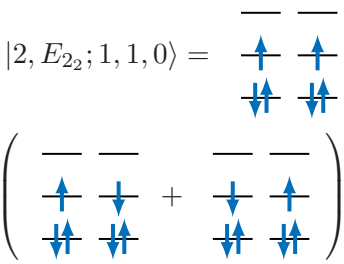

The one-particle dark states in Eq. (4.10) can block transitions to the two-electron ground-state. However, whether the blocking is effective crucially depends on the exchange energy J. In fact, as soon as the two-particles first excited doublet enters the transport window, interference is destroyed since transport through the doublet can occur. In our simulations we took indeed $J \simeq \hbar\Gamma \simeq eV_\mathrm{b}$, such that the splitting of ground- and excited state is large enough to destroy CPT at least partially and small enough to not see an additional excitation line appearing. Notice that in this situation the secular approximation breaks down, and the dynamics of the reduced density matrix is governed by a more general set of equations accounting also for non-secular terms.

Interestingly, for $J = 0$ (or at least $J \ll \Gamma_l$), the two-particle ground state, which now is a sextuplet, can form a dark state itself

$$|2, \mathrm{DS}\rangle = \frac{1}{2}\Big(e^{2i\ell\phi_\alpha} \quad - \quad + \quad + e^{-2i\ell\phi_\alpha} \quad \Big), \tag{4.14}$$

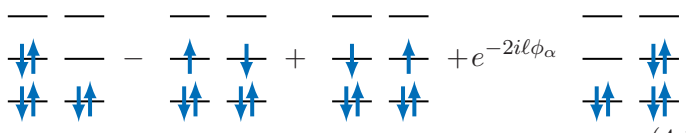

which blocks transitions to the one-particle ground state at lead l since $\langle 1, E_{1_0}; \frac{1}{2}, \pm\frac{1}{2}, \pm\ell |\, d_{l\sigma}\, |2, \mathrm{DS}\rangle = 0$. Again we require that this dark state is not completely decoupled from the dynamics and can be reached from the other lead $\langle 1, E_{1_0}; \frac{1}{2}, \pm\frac{1}{2}, \pm\ell |\, d^\dagger_{\bar{l}\sigma}\, |2, \mathrm{DS}\rangle \propto \sin(\ell(\phi_\mathrm{R} - \phi_\mathrm{L})) \neq 0$.

With our parameter choice of J the main features are found close to the $0 \leftrightarrow 1$ resonance. Therefore, we focus on the one-electron dark states and set up a minimal model for this case.

4.3 Dark state dynamics

Here we exemplary focus on CPT at the $0 \leftrightarrow 1$ resonance, which involves the $N = 0$ and the $N = 1$ ground states of a single shell. For general values of the gate and bias voltages such equations have to be solved numerically. Analytical solutions are possible when the system is tuned near the resonance, which is the case of interest here. In the $N = 0$ subspace, which only has one configuration (cfg. Eq. (4.5)), the density matrix is a number, ρ_0. In the $N = 1$ subspace, it is block-diagonal in spin but *not* in angular momentum. The contributions from different spin configurations can be summed up in the dynamical equations using the Wigner-Eckart theorem [112] yielding a set of coupled equations for ρ_0 and a 2×2 matrix $\rho_1(E_1)$. Away from the exact resonance (i.e. from the border of the Coulomb diamond), one finds for positive chemical potential drop between left and right lead, $eV_\mathrm{b} \gg k_\mathrm{B}T$, the master equation

$$\begin{aligned} 0 = \dot{\rho}_1 &= -\frac{i}{\hbar}\Big[\hat{H}_\mathrm{LS}, \rho_1\Big] + 2\Gamma_\mathrm{L}\mathcal{R}_\mathrm{L}\rho_0 - \frac{\Gamma_\mathrm{R}}{2}\Big\{\mathcal{R}_\mathrm{R}, \rho_1\Big\} - \Gamma_\mathrm{rel}[\rho_1 - \rho_{1,\mathrm{th}}\mathrm{tr}\{\rho_1\}], \\ 0 = \dot{\rho}_0 &= \Gamma_\mathrm{R}\mathrm{tr}\left\{\mathcal{R}_\mathrm{R}\rho_1\right\} - 4\Gamma_\mathrm{L}\rho_0, \end{aligned} \tag{4.15}$$

where in this subset the secular approximation holds since the one-electron states are degenerate. This equation accounts for precession through the Lamb shift contribution

$$\hat{H}_\mathrm{LS} = \frac{\hbar}{2}\sum_l \omega_l \mathcal{R}_l, \tag{4.16}$$

with precession frequencies $\omega_{\mathrm{L/R}}$. We add a relaxation part with relaxation rate Γ_rel to account for inelastic processes due to e.g. phonons. Here $\rho_{1,\mathrm{th}} = 1/2$ is the thermal density matrix for the one-electron sub-block. Due to the non-diagonal form of the $\mathcal{R}_l$ in the angular momentum basis, also the stationary density matrix ρ_1^∞ is not diagonal there. Notice that $\mathcal{R}_\mathrm{R}$ and $\mathcal{R}_\mathrm{L}$ cannot be diagonalized simultaneously as $\phi_\mathrm{R} \neq \phi_\mathrm{L}$. In the DS and CS basis from Eq. (4.10) for a DS that is decoupled from the right lead these coherence matrices read

$$\mathcal{R}_\mathrm{R} = \begin{pmatrix} 0 & 0 \\ 0 & 2 \end{pmatrix}, \qquad \mathcal{R}_\mathrm{L} = 2\begin{pmatrix} \sin^2\Delta\phi & -i\sin\Delta\phi\cos\Delta\phi \\ i\sin\Delta\phi\cos\Delta\phi & \cos^2\Delta\phi \end{pmatrix}, \tag{4.17}$$

with $\Delta\phi = \phi_\mathrm{L} - \phi_\mathrm{R} \neq 0$. For vanishing relaxation and neglecting the Lamb shift contribution this results in a DS that is completely decoupled from the right

lead with population 1. Therefore, in this case the current will be completely suppressed.

Let us now turn to the impact of the Lamb shift term in Eq. (4.15). It introduces a precession of the Bloch vector in the DS/CS basis with population transfer between dark and coupled states with frequencies [46]

$$\omega_l(V_\mathrm{g}, V_\mathrm{b}) = \frac{\Gamma_l}{\pi}\left[p_l(-e\alpha_\mathrm{g}V_\mathrm{g}) - p_l\left(U - \frac{J}{2} - e\alpha_\mathrm{g}V_\mathrm{g}\right)\right], \tag{4.18}$$

where $p_l\left(\Delta E\right) := -\operatorname{Re}\psi\left[1/2 + i(\Delta E - \mu_l)/2\pi k_\mathrm{B}T\right]$ where ψ is the digamma function. These precession frequencies clearly depend on the gate voltage and, via the chemical potentials, also on the bias voltage. For the situation indicated in Fig. 4.2c, $\omega_\mathrm{L} \neq 0$ allows the electrons in a DS to precess into the CS and from there to escape, yielding a small stationary current $I = 4e\Gamma_\mathrm{L}\rho_0^\infty$. Eq. (4.15) can be solved completely analytically, however, the resulting expression is too long, so we focus on some limiting cases. We find the expression at zero relaxation

$$I(\Gamma_\mathrm{rel} = 0) = \frac{4e\Gamma_\mathrm{R}\omega_\mathrm{L}^2\cos^2\Delta\phi}{8\Gamma_\mathrm{R}^2 + 2(\omega_\mathrm{L} - \omega_\mathrm{R})^2 + \omega_\mathrm{L}\left(\omega_\mathrm{L}\Gamma_\mathrm{R}/\Gamma_\mathrm{L} + 4\omega_\mathrm{R}\right)\cos^2\Delta\phi}, \tag{4.19}$$

for $\Delta\phi = (\phi_\mathrm{L} - \phi_\mathrm{R}) \neq 0$. Because the precession frequencies strongly depend on gate and bias voltage, also the effectiveness of CPT does. The current dependence on the bias voltage is analyzed in more detail in Fig. 4.7. We show the current for the $0 \leftrightarrow 1$ transition at $V_\mathrm{g} = 11.771V$ and $V_\mathrm{g} = 11.781V$ in Figs. 4.7a,b, respectively. These positions are marked in Fig. 4.6 by vertical lines and the corresponding symbols. The negative differential conductance and the faint (almost missing) resonant line are highlighted by a blue and red arrow, respectively. Again, the agreement between theory and experiment is remarkable, which gives us confidence on the fact that these are all signatures of CPT. Clearly, at negative bias voltages (corresponding to positive potential drop eV_b), CPT is more pronounced in panel (b) than in panel (a), indicating a smaller ω_L. As the bias polarity is changed, also the role of the precession frequencies is exchanged. The fact that at positive bias the current shows standard Coulomb steps, is because of large ω_R for both of the chosen V_g values.

We observe that, due to the particle-hole symmetry of the spectrum with respect to half-filling (valley with $N = 2$), the equations for the reduced density operator near the $3 \leftrightarrow 4$ transition immediately follow from Eq. (4.15) upon

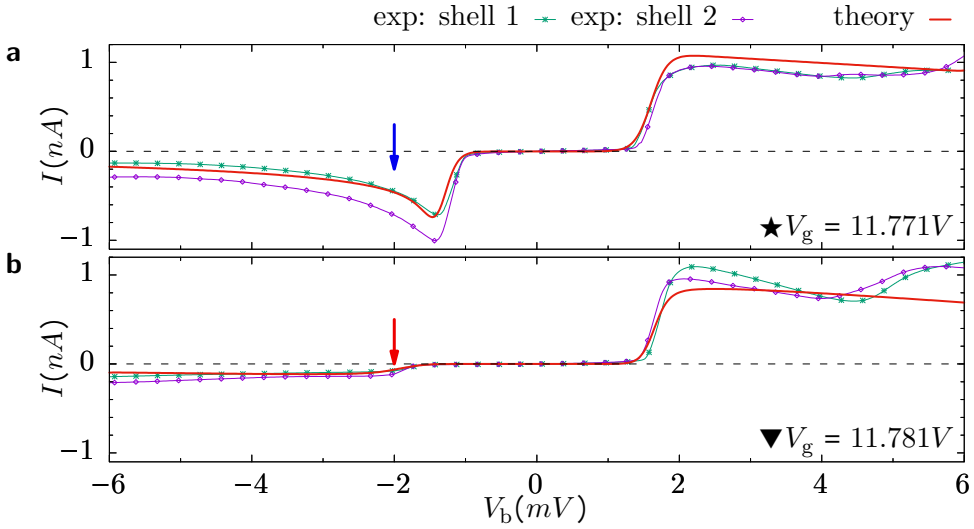

Figure 4.7: I-V characteristics in the presence of dark states. \a,b Experimental current-bias characteristics around the $0 \leftrightarrow 1$ resonance for shell 1 at voltages $V_g = 11.771V$ (**a**) and $V_g = 11.781V$ (**b**) are compared to numerical results. These gate voltages correspond to the vertical dashed lines in Fig. 4.6. The behavior at positive voltages is similar. At negative bias, however, one observes a pronounced negative differential conductance in panel (**a**) and almost vanishing current in panel (**b**). The current measured in shell 2 displays similar behavior.

exchanging R with L and letting $V_b \to -V_b$. This implies that the CPT features at the $3 \leftrightarrow 4$ transition can be obtained from the ones at the $0 \leftrightarrow 1$ resonance by mirroring of both V_b and V_g, as observed in Fig. 4.6.

If $\phi_L = \phi_R$ and $\Gamma_{rel} = 0$ the dark state is completely decoupled from the dynamics and therefore the stationary solution is not uniquely defined but rather depends on the initial state. Any finite relaxation rate solves this problem which is the second limit that can be analyzed. Interestingly, the dependence of the current on the relaxation rate drops completely and we obtain

$$I(\Delta\phi = 0) = e\frac{4\Gamma_L\Gamma_R}{4\Gamma_L + \Gamma_R}. \tag{4.20}$$

Notice that this same expression for the current holds true for transport through four fold degenerate levels in the absence of interference, therefore we call this the incoherent limit.

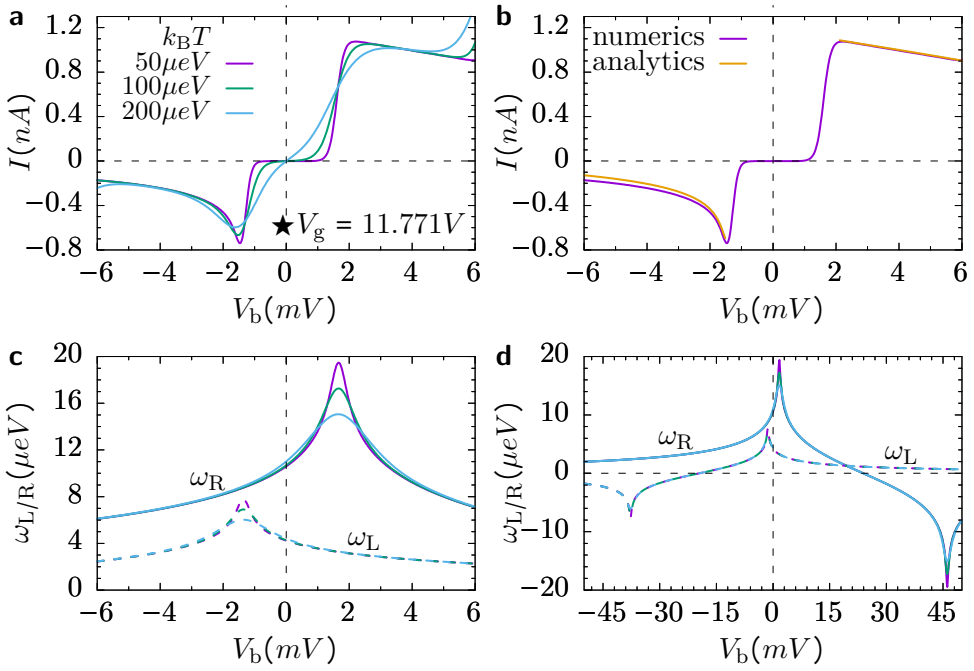

Figure 4.8: **a** Numerical current bias traces around the $0 \leftrightarrow 1$ resonance at $V_g = 11.771V$ for different temperatures. **b** Comparison between the numerically calculated current and the analytic approximation valid for vanishing relaxation. The thermal energy was set to $k_BT = 50\mu eV$. **c** Precession frequencies s $\omega_{L/R}$ for the same temperatures as in (**a**). **d** Precession frequencies in a larger bias range. Their zeros occurs for energies $|eV_b|$ of the order of the charging energy U.

4.4 Impact of precession, temperature and relaxation on coherent population trapping

In this section we give a closer look at the role played by the precession frequencies $\omega_{L/R}$, on the shape of the current as a function of the bias voltage. Furthermore, we investigate the role of temperature and inelastic relaxation. We focus on the vicinity of the $0 \leftrightarrow 1$ resonance where, as seen from the comparison in Fig. 4.8b, the analytical expression for the current in Eq. (4.19) well reproduces the numerics.

Fig. 4.8a shows the bias dependence of the current for different temperatures. While the traditional step-like behavior of the current at positive bias for is temperature broadened via the Fermi function, the interference peak at negative bias is not. To understand this feature, we have depicted in Fig. 4.8c the

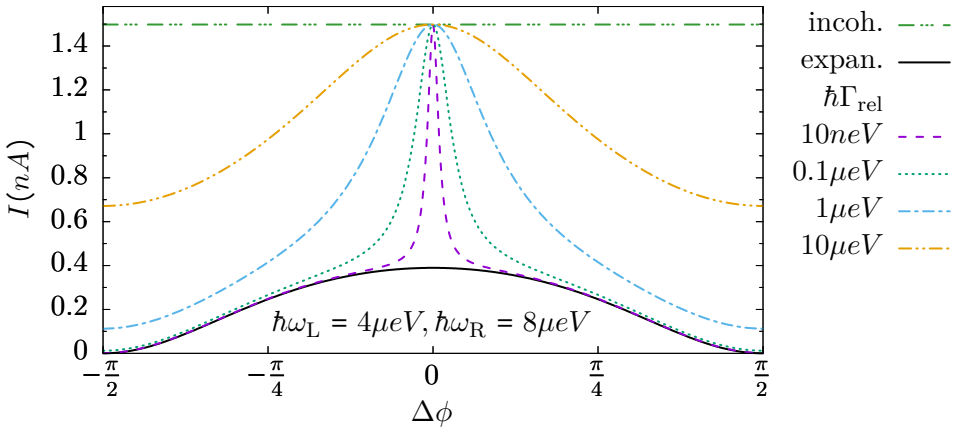

Figure 4.9: The current is plotted for various values of the relaxation rate $\Gamma_{\rm rel}$. At low relaxation the current is well approximated by the analytical expansion obtained for vanishing relaxation rate. At large relaxation, the incoherent limit is approached where the current is independent of the phase difference. The precession frequencies are fixed at $\hbar\omega_{\rm L} = 4\mu eV$ and $\hbar\omega_{\rm R} = 8\mu eV$. All other parameters are the same as in Tab. 4.1.

precession frequencies $\omega_{\rm L/R}$ in the same bias voltage range of panel (a) and for the same temperatures. It is clear that the current changes occur in the correspondence of changes in the peaks in the precession frequencies. In particular, the temperature basically only changes the height of the resonance peaks and leaves the tails invariant.

We observe that at fixed temperature the broadening of the precession frequencies peaks is largely dominated by the charging energy U, since $\omega_{\rm L/R}$ vanish when the bias becomes of the order of U/e, as shown in Fig. 4.8d. Eq. (4.19) proofs that the current is dominated by a single precession frequency in the numerator, where the bias direction defines which one. If this precession frequency becomes zero, interference perfectly blocks the current. In the experiment U is so large that this behavior cannot be seen since excited states enter the bias window before this value of the bias voltage is reached. Eq. 4.19 also shows that the current is completely suppressed for $\Delta\phi = \pi/2$ despite finite Lamb shift. We display the full analytical current in Fig. 4.9 and compare it to the two limiting cases of zero relaxation and the incoherent one. As an example we choose a large negative bias with precession frequencies $\hbar\omega_{\rm L} = 3\mu eV$ and $\hbar\omega_{\rm R} = 2\mu eV$. For low relaxation rates ($\Gamma_{\rm rel} \ll \Gamma_{\rm L/R}$) the

simple limit of Eq. 4.19 is recovered at $\Delta\phi \neq 0$. This agreement is expected since in the shown bias range excited states are far-off in energy. At $\Delta\phi = 0$ the current is always given by the incoherent limit from Eq. (4.20).

All considerations so far are based on the form of the single particle rate matrix from Eq. (4.8) $(\mathbf{\Gamma}_l^m)_{\ell_z\ell_z'} = \Gamma_l^m(\mathcal{R}_l^m)_{\ell_z\ell_z'}$ with $|(\mathcal{R}_l^m)_{\ell_z\ell_z'}| = 1$. However, this crucial assumption should be tested.

4.5 The tunneling rate matrix

In this section we want to show that, in general, the rate matrix in Eq. (4.8), defined via

$$(\mathbf{\Gamma}_l^m)_{\ell_z\ell_z'}(\Delta E) := \frac{2\pi}{\hbar}\sum_{\boldsymbol{k}} t^*_{l\boldsymbol{k}m\ell_z} t_{l\boldsymbol{k}m\ell_z'}\delta(\xi_{l\boldsymbol{k}} - \Delta E), \tag{4.21}$$

is non-diagonal in the angular momentum basis.

4.5.1 Tunneling amplitude

The tunneling amplitude $t_{l\boldsymbol{k}m\ell_z}$ in the tunneling Hamiltonian is proportional to the overlap of a wave function of the CNT $\phi_{m\ell_z\sigma}(\boldsymbol{r}) = \langle \boldsymbol{r}|m\ell_z\sigma\rangle$ and one of the lead $\psi_{l\boldsymbol{k}\sigma}(\boldsymbol{r}) = \langle \boldsymbol{r}|l\boldsymbol{k}\sigma\rangle$. Explicitly, $\langle l\boldsymbol{k}\sigma|\,\hat{h}\,|m\ell_z\sigma'\rangle = t_{l\boldsymbol{k}m\ell_z\sigma}\delta_{\sigma\sigma'}$, where $\hat{h} = \frac{p^2}{2m_{\mathrm{el}}} + v(\boldsymbol{r})$ is the single-particle Hamiltonian of the CNT–plus-leads complex. By decomposing the electrostatic potential into a contribution from the CNT and one from the leads, $v(\boldsymbol{r}) = v_{\mathrm{CNT}}(\boldsymbol{r}) + v_{\mathrm{leads}}(\boldsymbol{r})$, see the schematics in Fig. 4.10, the tunneling amplitude can be written as

$$\begin{aligned} t_{l\boldsymbol{k}m\ell_z\sigma} &= \int \mathrm{d}\boldsymbol{r}\ \psi^*_{l\boldsymbol{k}\sigma}(\boldsymbol{r})\left(\frac{p^2}{2m_{\mathrm{el}}} + v(\boldsymbol{r})\right)\phi_{m\ell_z\sigma}(\boldsymbol{r}) \\ &= \langle l\boldsymbol{k}\sigma|\,\hat{h}_{\mathrm{CNT}}\,|m\ell_z\sigma\rangle + \underbrace{\langle l\boldsymbol{k}\sigma|\,v_{\mathrm{leads}}\,|m\ell_z\sigma\rangle}_{\approx 0} \\ &= \underbrace{(m\varepsilon_0 - e\alpha_{\mathrm{g}}V_{\mathrm{g}})}_{=\varepsilon_m}\langle l\boldsymbol{k}\sigma|m\ell_z\sigma\rangle\,, \end{aligned} \tag{4.22}$$

where $\hat{h}_{\mathrm{CNT}}$ is the single particle part of the CNT Hamiltonian from Eq. (4.4). Since the wave functions of the CNT are much more localized than the lead ones, the contribution containing the overlap of lead and CNT wave function in the lead region (where the potential v_{leads} is finite) can be neglected, yielding the simple expression

$$t_{l\boldsymbol{k}m\ell_z\sigma} = \varepsilon_m \int \mathrm{d}\boldsymbol{r}\ \psi^*_{l\boldsymbol{k}\sigma}(\boldsymbol{r})\phi_{m\ell_z\sigma}(\boldsymbol{r}). \tag{4.23}$$

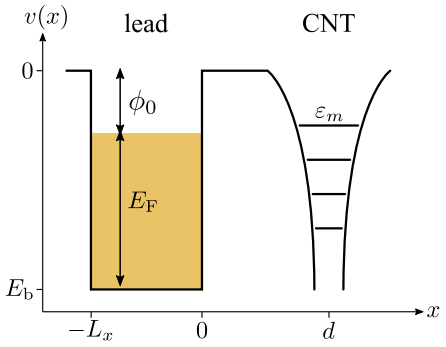

Figure 4.10: Electrostatic potential along the tunneling direction, chosen to be along the x-axis. In the lead, the electrons are considered to be free electrons in the direction parallel to the surface while they experience a confinement potential in the x-direction. E_b is the energy at the band bottom, E_F the Fermi energy and ϕ_0 the work function. Notice that the zero of the energy has been set to the vacuum. The CNT is located at a distance d from the lead and features localized bound states.

Hence, the evaluation of the tunneling amplitude requires to take a closer look at the CNT wave functions as well as the lead wave functions in the tunneling region.

We start from the latter. We assume an adiabatically smooth variation of the lead surface in the contact region, such that the lead wave functions locally factorize in a contribution parallel to the surface and in an exponentially decaying part perpendicular to it

$$\psi_{l\boldsymbol{k}\sigma}(\boldsymbol{r}) = \psi^{\parallel}_{lk_yk_z\sigma}(y,z)\psi^{\perp}_{lk_x\sigma}(x) = \frac{1}{\sqrt{L_x}}\psi^{\parallel}_{lk_yk_z\sigma}(y,z)e^{-\kappa_x x}. \tag{4.24}$$

Conservation of energy in the lead's potential well and in the tunneling region yields $E_\mathrm{el} = E_\parallel - \frac{\hbar^2\kappa_x^2}{2m_\mathrm{el}} = E_\parallel + E_b + \frac{\hbar^2 k_x^2}{2m_\mathrm{el}}$, where E_el is the energy of the lead electron with respect to the vacuum. Moreover, the energy at the band bottom is $E_\mathrm{b} = -(E_\mathrm{F} + \phi_0)$, with E_F the Fermi energy and ϕ_0 the lead work function, see Fig. 4.10. Hence,

$$\kappa_x = \sqrt{\frac{2m_\mathrm{el}}{\hbar^2}\left(E_F^l + \phi_0\right) - k_x^2}. \tag{4.25}$$

Thus, the smallest values of κ_x, and hence the largest penetration in the CNT, are obtained when $k_x \approx k_F$ yielding $\kappa_x \approx \sqrt{2m_\mathrm{el}\phi_0/\hbar^2}$. Since the total energy is bound to be E_F^l, this simultaneously implies that the longitudinal components k_y, k_z should be vanishingly small (i.e. in the vicinity of the Γ point).

Regarding the CNT wave functions, we assume that they are well described as a linear combination of atomic orbitals (LCAO) localized at the atomic positions $\boldsymbol{R}_j = (X_j, Y_j, Z_j)$. In particular, the low energy properties are already well captured by considering a single p-orbital for each atomic position [113]. We denote $|j\sigma\rangle$ such atomic state and the associated wave function as $p_\sigma(\boldsymbol{r}-\boldsymbol{R}_j) = \langle \boldsymbol{r}|j\sigma\rangle$. Hence, $|m\ell_z\sigma\rangle = \sum_{j\sigma}|j\sigma\rangle\langle j\sigma|m\ell_z\sigma\rangle = \sum_{j\sigma}|j\sigma\rangle\, c_j(m\ell_z\sigma)$, where the LCAO coefficients $c_j(m\ell_z\sigma) \equiv \langle j\sigma|m\ell_z\sigma\rangle$ have been introduced. Notice that they are chosen in such a way that the CNT wave functions obey proper boundary conditions at the ends of the tube [28]. Furthermore, due to time reversal symmetry, it holds $c_j(m\ell_z\sigma) = c_j^*(m-\ell_z-\sigma)$. It follows

$$t_{l\boldsymbol{k}m\ell_z\sigma} = \varepsilon_m \sum_j c_j(m\ell_z\sigma) \int \mathrm{d}\boldsymbol{r}\ \psi^*_{l\boldsymbol{k}\sigma}(\boldsymbol{r}) p_\sigma(\boldsymbol{r}-\boldsymbol{R}_j). \tag{4.26}$$

In the *absence* of SOC, as in our case, the spatial and spin parts factorize both for the leads as well as the CNT wave functions, yielding spin independent coefficients $c_j(m\ell_z\sigma) = c_j(m\ell_z)$. Similarly, the scalar product $\langle lk\sigma|j\sigma\rangle$ becomes spin independent, yielding the final form for the tunneling amplitude

$$t_{l\boldsymbol{k}m\ell_z} = \varepsilon_m \sum_j c_j(m\ell_z) \int \mathrm{d}\boldsymbol{r}\ \psi^*_{l\boldsymbol{k}}(\boldsymbol{r}) p(\boldsymbol{r}-\boldsymbol{R}_j) \approx \varepsilon_m a \sum_j c_j(m\ell_z)\psi^*_{l\boldsymbol{k}}(\boldsymbol{R}_j), \tag{4.27}$$

where in the last step we approximated the localized p-orbitals to Dirac-delta functions, $p(\boldsymbol{r}) = a\delta(\boldsymbol{r})$, centered at the atomic position $\boldsymbol{R}_j$. Here a is a normalization factor. The last approximation neglects the nodal plane of the p_z orbitals, but it is justified by i) the selection of j given by the lead wave function and ii) the negligible contribution to the integral given by the CNT wave function inside the tube.

4.5.2 Single particle rate matrix

We calculate the rate matrix according to Eqs. (4.21) and (4.27), i.e., in the absence of SOC. We then obtain

$$\begin{aligned}
(\boldsymbol{\Gamma}^m_l)_{\ell_z\ell'_z}(\Delta E) &= \\
&= \frac{2\pi}{\hbar}\varepsilon_m^2|a|^2 \sum_{jj'} c_j^*(m\ell_z)c_{j'}(m\ell'_z) \sum_{\boldsymbol{k}} \psi_{l\boldsymbol{k}}(\boldsymbol{R}_j)\psi^*_{l\boldsymbol{k}}(\boldsymbol{R}_{j'})\delta(\xi_{l\boldsymbol{k}} - \Delta E) \\
&= \frac{2\pi}{\hbar}\varepsilon_m^2\frac{|a|^2}{L_x} \sum_{jj'} c_j^*(m\ell_z)c_{j'}(m\ell'_z) \sum_{\boldsymbol{k}} \psi^{\parallel}_{lk_yk_z}(Y_j, Z_j)\psi^{\parallel *}_{lk_yk_z}(Y_{j'}, Z_{j'}) \\
&\qquad \times e^{-\kappa_x(X_j+X_{j'})}\delta(\xi_{l\boldsymbol{k}} - \Delta E).
\end{aligned} \tag{4.28}$$

Whether the rate matrix is diagonal in the angular momentum basis, crucially depends on the geometry of the contact region. The exponential $e^{-\kappa_x(X_j+X_{j'})}$ in fact selects in the sums over the atomic positions those CNT atoms closest to the leads. Furthermore, in the summation over the momenta $\boldsymbol{k}$, it selects the smallest values of κ_x compatible with the requirement that the energy of the tunneling lead electron is resonant with the CNT chemical potential ΔE. As discussed before, this yields $k_y, k_z \approx 0$ and $\kappa_x \approx \sqrt{2m_{\rm el}\phi_0/\hbar^2} := \kappa_{\rm min}$, such that

$$(\mathbf{\Gamma}_l^m)_{\ell_z\ell_z'}(\Delta E) \approx \frac{2\pi}{\hbar}\varepsilon_m^2\frac{|a|^2}{L_x}\sum_{jj'} c_j^*(m\ell_z)c_{j'}(m\ell_z')e^{-\kappa_{\rm min}(X_j+X_{j'})} \times \psi^{\parallel}_{lk_\parallel=0}(Y_j,Z_j)\psi^{\parallel *}_{lk_\parallel=0}(Y_{j'},Z_{j'})\sum_{\boldsymbol{k}}\delta(\xi_{l\boldsymbol{k}}-\Delta E). \quad (4.29)$$

Thus, this so called surface Γ-point approximation [114] enables us to decouple the sums over j and j' into two independent sums. We introduce the density of states at the Fermi level $g_l = \sum_{\boldsymbol{k}}\delta(\xi_{l\boldsymbol{k}} - E_{\rm F}^l)$ and the tunneling coefficients

$$\tau_l(m\ell_z) = \varepsilon_m\frac{a}{\sqrt{L_x}}\sum_{j'} c_{j'}(m\ell_z)e^{-\kappa_{\rm min}X_{j'}}\psi^{\parallel *}_{lk_\parallel=0}(Y_{j'},Z_{j'}), \quad (4.30)$$

yielding

$$(\mathbf{\Gamma}_l^m)_{\ell_z\ell_z'} = \frac{2\pi}{\hbar}g_l\tau_l^*(m\ell_z)\tau_l(m\ell_z'). \quad (4.31)$$

In the surface Γ-point approximation, the wave function $\psi^{\parallel}(Y_j,Z_j)$ is independent of k_y and k_z and hence real. Furthermore, the LCAO coefficients are related by time-reversal symmetry, $c_j(m,\ell_z) = c_j^*(m,-\ell_z)$, yielding the result $\tau_l(m\ell_z) = \tau_l^*(m-\ell_z)$. Accounting for this symmetry we finally obtain the final form for the rate matrix

$$(\mathbf{\Gamma}_l^m)_{\ell_z\ell_z'} = \Gamma_l^m e^{i\phi_l^m(\ell_z-\ell_z')},\ \Gamma_l^m = \frac{2\pi}{\hbar}g_l|\tau_l(m\ell_z)|^2,\ \phi_l^m := arg\{\tau_l(m\ell)\}. \quad (4.32)$$

This result strongly relies on the surface Γ-point approximation, which allows one to decouple the double sum over the atomic positions j and j'. If it does not hold the amplitude of the off-diagonal elements are reduced with respect to the diagonal entries. In general one can write the rate matrix as $\mathbf{\Gamma}_l = \Gamma_l\mathcal{R}_l$ where the coherence matrices fulfill $|(\mathcal{R}_l)_{\ell_z\ell_z}| = 1$ and $0 \le |(\mathcal{R}_l)_{\ell_z-\ell_z}| \le 1$. In Appendix D we have explored the consequences of keeping a finite contribution for the parallel momenta k_y and k_z on the example of a ring of carbon atoms

coupled in three different ways to a metal. As we shall see, if the ring is lying flat on the substrate, such that all atoms are equally distant from the lead, the rate matrix becomes diagonal. The result in Eq. (4.8) is in contrast recovered when the ring is orthogonal to the substrate, in a way that tunneling is dominated by only one closest atom. When two atoms are equally close to the surface, the rate matrix is off-diagonal, but the modulus of the diagonal elements is smaller than that of the diagonal ones. From this we conclude that in the CNT case, where only few atoms are close to the leads, the rate matrix is not diagonal. How good the simple form Eq. (4.8) describes the experiment, depends on various factors, among which tube's chirality. In the case of our experiment, we consider CNTs of the zig-zag class, which at the tube's end have non vanishing weights only for atoms of a given sublattice [28]. Thus, if at the left end only A atoms have non vanishing LCAO coefficients, this implies that the neighboring B atoms are not tunneling coupled, hence effectively achieving the single atom limit. At the right lead, the same considerations apply upon exchange of the role of atoms A and B. This insight into the microscopic origin of the single particle rate matrix allows a closer look at the DSs we described before.

4.5.3 Dark states

Eq. (4.6) allows one to construct linear combinations $|\mathrm{DS}, \sigma; l\rangle$ of the single-particle ground states $|\ell_z \sigma\rangle$ which are decoupled at given positions $\boldsymbol{r}_l$, and hence may act as DS for a given bias polarity. Such states have the generic form $|\mathrm{DS}, \sigma; l\rangle = a(\boldsymbol{r}_l)\,|\ell\sigma\rangle + b(\boldsymbol{r}_l)\,|-\ell\sigma\rangle$, where the coefficients satisfy the normalization condition $|a(\boldsymbol{r}_l)|^2 + |b(\boldsymbol{r}_l)|^2 = 1$ and are determined through the requirement

$$\langle 0|\, d_{\sigma l}\, |\mathrm{DS}, \sigma; l\rangle \equiv 0, \tag{4.33}$$

where $d_{\sigma l}$ destroys a CNT electron of spin σ in shell 1 at position $\boldsymbol{r}_l$. Such operators read in angular momentum basis, $d_{\sigma l} = \sum_{\ell_z} \langle \boldsymbol{r}_l | \ell_z \sigma\rangle\, d_{1\ell_z\sigma}$. Notice that such DSs are possible to construct also for higher and lower shells starting from e.g. a state where shells 0 and 1 are completely filled. Additionally, the orbital part $\phi_{m\ell_z\sigma}(\boldsymbol{r}_l) = \langle \boldsymbol{r}_l | m\ell_z\sigma\rangle$ of the CNT wave function is complex, $\phi_{m\ell_z\sigma}(\boldsymbol{r}_l) = |\phi_{m\ell_z\sigma}(\boldsymbol{r}_l)| e^{i\theta_l(m,\ell_z)}$ and furthermore, $|\phi_{m\ell_z\sigma}(\boldsymbol{r}_l)| = |\phi_{m-\ell_z-\sigma}(\boldsymbol{r}_l)|$ due to time-reversal symmetry. Then, insertion in Eq. (4.33) yields for the coefficients the simple form $a(\boldsymbol{r}_l) = e^{-i\theta_l(m,\ell)}/\sqrt{2}$, $b(\boldsymbol{r}_l) = -e^{-i\theta_l(m,-\ell)}/\sqrt{2}$.

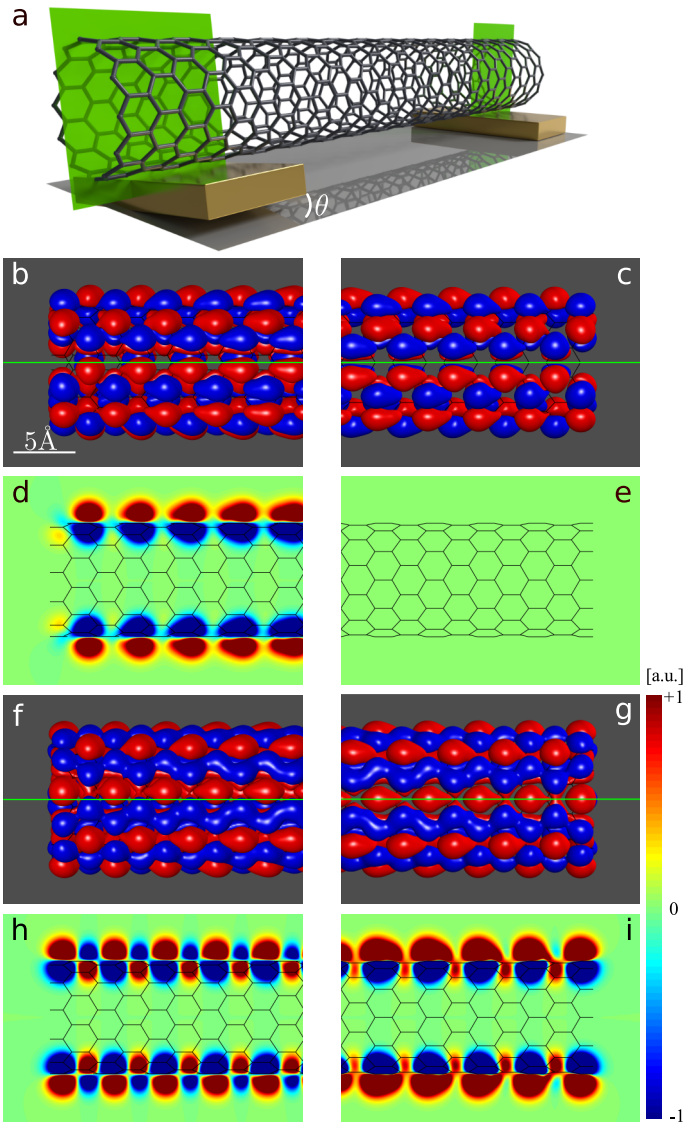

Figure 4.11: **a** Sketch of the nanotube-lead configuration at the left and right contacts. The left lead is rotated by an angle $\theta = \pi/24$ with respect to the right lead. The intersection of the green rectangles with the leads define in both leads the contact region. **b,c** Equiamplitude surfaces of the CNT wave function as seen from the left (**b**) and right (**c**) contact region. At the left lead, a nodal line is seen which coincides with the green contact line. At the right lead, in contrast, the nodal line and the contact line do not coincide. **d,e** Projection of the wave function amplitudes on the intersection rectangle. The DS has a vanishing amplitude at the right lead but not at the left lead. **f-i** The same features discussed for the DS are here shown for its associated orthogonal CS.

Introducing the angles $\bar{\theta}_l^m = [\theta_l(m,\ell) + \theta_l(m,-\ell)]/2$, and $\Delta\theta_l^m = [\theta_l(m,\ell) - \theta_l(m,-\ell)]/2$, we find

$$\left.\begin{matrix} |\mathrm{DS},\sigma;l\rangle \\ |\mathrm{CS},\sigma;l\rangle \end{matrix}\right\} = \frac{e^{-i\bar{\theta}_l^m}}{\sqrt{2}}\left[e^{i\ell\phi_l^m}\,|\ell,\sigma\rangle \mp e^{-i\ell\phi_l^m}\,|-\ell,\sigma\rangle\right], \tag{4.34}$$

where $\phi_l^m = -\Delta\theta_l^m/\ell$. This shows that DSs are possible to construct in all shells at both leads. An example of dark and coupled states is shown in Fig. 4.11 for the case of a $(12,0)$ CNT. The CNT was chosen to be 100 unit cells long, corresponding to about $50nm$. Moreover, the states shown correspond to the first excited state above the band gap. We have assumed the angular coordinate of the contact atoms at the right and left lead to be rotated by an angle $\theta = \pi/24$. The DS has a node at the contact positions at the right lead but not at the left lead, cfg. Figs. 4.11b-e. The corresponding CS is shown in Figs. 4.11f-i and has finite weight at both contacts.

4.6 Conclusions

Our results demonstrate for the first time CPT by all-electric means in a QD with orbital degeneracies. The presented results show a remarkable quantitative agreement between the experimental data and the theoretical predictions, strongly supporting the claim that the observed current suppression features are due to CPT. In the case considered here such degeneracies result from the interplay of the tubular nanotube geometry and the underlying graphene honeycomb lattice. However, the phenomenon is rather generic and is expected to occur in other QD systems in the weak tunneling regime, as the main requirement are i) the presence of a symmetry of the system yielding degenerate energy states (for weak symmetry breaking the level splitting should be smaller than the tunnel couplings Γ_l), ii) tunneling matrices being not diagonal in the basis associated to the symmetry and with modulus of the off-diagonal elements of the coherence matrices $\mathcal{R}_l$ close to one, iii) strong Coulomb interaction enforcing single electron tunneling. The above requirements are for CNTs strongly interconnected with each other, and are met at best for n-doped (electron conduction) CNTs of the zig-zag class, whose bound states have angular momentum (valley) degeneracy. For this nanotube class, symmetry breaking perturbations are SOC and valley mixing. While the former is an intrinsic property of the CNT and decreases away from the

band gap, valley mixing is due to disorder or to perturbations which break the rotational symmetry. Suspended ultraclean CNTs [80] have very weak disorder and symmetry breaking mostly occurs due to the presence of contact leads in the non-suspended portion of the tube. In a realistic experimental set-up the curvature of the tube and some roughness of the contacts causes tunneling to occur locally through few single carbon atoms. This ensures on the one hand that the tunneling matrix is not diagonal in the angular momentum basis, and on the other that the tunneling is a small perturbation and hence that valley mixing is small. The arising dark states are a coherent superposition of valley (angular momentum) states which are decoupled from either the left or the right lead. Their emergence is visible through a distinct current-voltage characteristics, with missing current steps or current suppression depending on the sign of the applied bias voltage.

Since energy conservation is required only within an accuracy dictated by $\Delta E \approx \hbar\Gamma$, in the strong coherent tunneling regime, where Γ is the largest scale in the problem, the CPT discussed here looses its significance. Rather, other kind of interference effects are expected in transport, based on a coherent superposition of different tunneling paths and visible also at level of the linear conductance [115]. Experimental signatures of destructive [116] and constructive [117] zero-bias interference have been reported in the transport through molecular junctions. Similarly, the zero-bias interference discussed for off-resonant transport through single molecules requires energy-nonconserving virtual transitions [118]. Other CNTs systems have shown current suppression induced by coupling asymmetries between different states [119]. All these phenomenon are qualitatively distinct from our presented work as we require weak incoherent tunneling in and out of the leads, charging effects and a finite bias ensuring directed transport.

Part II

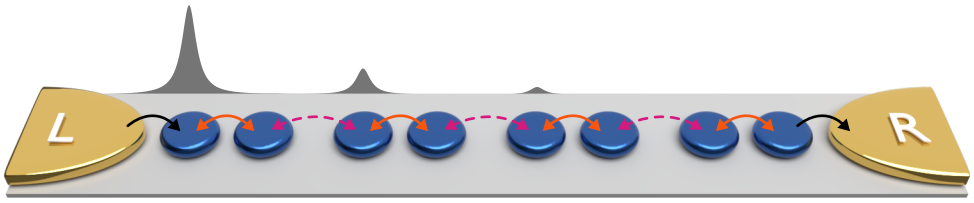

Full counting statistics for multisite conductors

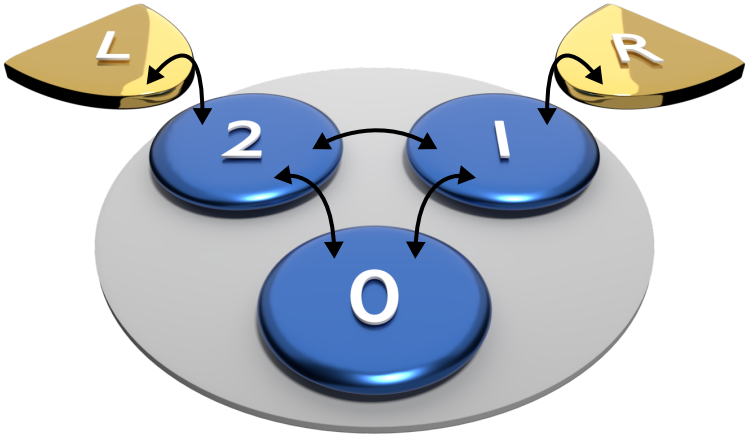

CHAPTER 5

The framework of full counting statistics

So far we have calculated the current through open quantum systems as the mean value of the current operator $I = e\langle \dot{N} \rangle$. However, an experimental more realistic scenario is the measurement of the total charge or electron number that accumulates in a lead during a certain measuring time. Then, each individual measurement does not necessarily return the average $\langle N \rangle$ but rather some value N. These current fluctuations occur due to the stochastic nature of single electron tunneling events. While typically undesirable in technical applications, they can be useful for understanding quantum-mechanical transport processes [120] not accessible from the knowledge of the average current only [16]. The complete characterization of transport is given by full counting statistics (FCS) which quantifies the probability of measuring N electrons [121–125]. This is expressed via the probability distribution function $P(N)$. Figs. 5.1a,b shows two fictional measurements that feature the same current but different distribution functions as seen in Fig. 5.1c. This highlights the importance of understanding current fluctuations. A quantitative measure of this distribution is given by the full set of moments or cumulants. The first cumulant is the mean value $\kappa_1 = \langle N \rangle$ and related to the current. The second cumulant is the variance $\kappa_2 = \langle N^2 \rangle - \langle N \rangle^2$ and the most important measurement for current fluctuations since they correspond to the low-frequency limit of the current correlation function [126]. Its time derivative is called shot noise. In many cases it is enough to analyze the shot noise but of course one can

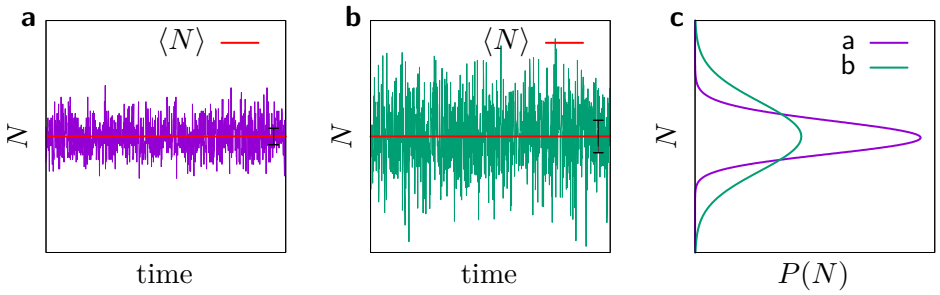

Figure 5.1: Current fluctuations lead to random distribution of the measured electron number N over time. **a,b** While both fictional measurements show the same average number and therefore the same current as shown in red, their distributions are quite different. **c** The corresponding distribution function $P(N)$.

measure and calculate higher order cumulants as well. In this chapter we derive a generalized master equation to compute the cumulants for driven systems in the Markovian sequential tunneling regime. Some parts of the theoretical framework have been published in Niklas *et al.* [P.2] and Benito *et al.* [P.3].

5.1 Counting variable

To achieve a compact notation we drop the lead index in the electron number operator $\hat{N}_l = N$. The replacement of the probability distribution function $P(N)$ by moments requires the definition of a moment generating function that contains all existing moments. This introduces a counting variable $\chi_l = \chi$, which is the conjugated variable to N, that allows us to define the moment generating function as

$$Z(\chi) = \langle e^{i\chi N} \rangle = \sum_{k=0}^{\infty} \frac{(i\chi)^k}{k!} \mu_k, \tag{5.1}$$

with the moments $\mu_k = \langle N^k \rangle = (\partial/\partial i\chi)^k Z|_{\chi=0}$. Their irreducible parts, the cumulants κ_k, are generated from $\log Z(\chi)$ [127]. For Markovian time-independent transport problems, the cumulants normally grow linearly in time [124] which motivates the definition of the *current cumulants* as the time derivatives $c_k = \dot{\kappa}_k$, which are our main quantities of interest. Their generating function reads

$$\phi(\chi) = \frac{\mathrm{d}}{\mathrm{d}t} \log Z(\chi) \equiv \sum_{k=1}^{\infty} \frac{(i\chi)^k}{k!} c_k, \tag{5.2}$$

which implies $c_k = (\partial/\partial i\chi)^k \phi|_{\chi=0}$. Thus, the moments and cumulants are given via the Tailor expansion coefficients of their associated generating functions and can be calculated as derivatives of those with respect to the counting variable.

5.2 Poissonian Noise and the Fano factor

The benchmark of FCS is the Poissonian distribution where all tunneling events occur independently from each other at a fixed rate γ. The probability of having N electrons after a measuring time t is then given by the Poissonian distribution

$$P(N,t) = \frac{(\gamma t)^N}{N!} e^{-\gamma t}. \tag{5.3}$$

It is easy to show that the current cumulant generating function is given by $\phi(\chi, t) = \gamma(e^{i\chi} - 1)$ and therefore all cumulants are the same, $c_k = \gamma$. It is natural to define cumulant ratios $F_k = c_{k+1}/c_k$ as the ratio of each cumulant divided by its Poissonian value for a dimensionless quantization of the statistics. We have shown that the Poissonian value of all cumulants is the same and therefore in this case all cumulant ratios are equal to one, $F_k = 1$. The most important cumulants are the first two since they correspond to current $I = ec_1$ and shot noise $S = e^2 c_2$. This additionally determines the most essential cumulant ratio $F = F_1$ that is commonly known as the Fano factor [123]

$$F = \left| \frac{S}{eI} \right|. \tag{5.4}$$

Notice that often in literature the Fano factor is defined with an additional factor 1/2 coming from a different definition of the noise by Schottky [123, 128]. In general a Fano factor of $F = 1$ does not prove a Poissonian behavior but already gives a strong indication in its favor. Values of $F < 1$ are assigned to sub-Poissonian noise and $F > 1$ holds for super-Poissonian behaviour. This classification can be useful for understanding quantum mechanical transport processes [120]. For instance, an open transport channel with transmission close to unity has sub-Poissonian noise, while super-Poissonian noise may hint at electron bunching [123], the size of the charge carriers [129], or bistabilities [50, 115, 125]. External driving allows the control of the noise via the driving amplitude and frequency [130]. Examples are pumps that transport a fixed charge per cycle which feature a low noise [131–134].

5.3 Generalized master equation

The calculation of the FCS can be formulated as a non-Hermitian eigenvalue problem with a consecutive computation of derivatives with respect to the counting variable in *time-independent* transport problems [124]. For small system sizes, this may provide all cumulants analytically [124, 125]. For a numerical treatment, however, the computation of higher-order derivatives should be avoided, which can be done using an iterative scheme based on Rayleigh-Schrödinger perturbation theory [135, 136]. For single-electron transistors (SETs) with an arbitrary *time-dependence* such eigenvalue based methods are in general not applicable, so that alternatives are required. One idea is to introduce the number of transported electrons as an additional degree of freedom in the number-resolved master equations [137–139]. However, the computational effort may become tremendous due to the possible broad distribution of this number. A more efficient way is based on a density matrix like object containing information about the second moment of the transported charge [100]. To solve the corresponding equations provides the current and its variance with moderate numerical effort. Extending this idea to higher order moments and cumulants results in an efficient way to use the framework of FCS in a master equation approach. While the master equation (2.38) contains the full information about the central quantum dot (QD), the leads' degrees of freedom have been traced out in the course of its derivation. To nevertheless keep track of the electron number in the lead, one multiplies the total density matrix by a counting factor $e^{i\chi N}$ for the lead electrons to obtain the generalized reduced density matrix of the system $R(\chi) = \mathrm{tr}_B\{e^{i\chi N}\rho_{\mathrm{tot}}\}$. In this way its trace is the moment generating function $Z(\chi) = \mathrm{tr}\{R(\chi)\}$. To obtain a master equation for $R(\chi)$ we multiply the Liouville-von Neumann equation (2.4) by the counting factor from the left and proceed with the Nakajima-Zwanzig projection operator technique as before. Since this counting factor commutes with the system and bath Hamiltonians, it is only important to consider the Kernel, which to second order in the tunnel coupling can be derived analogously to Eq. (2.23). It has the form

$$K_\chi^{(2)} R(\chi) = -\frac{1}{\hbar^2} \sum_{\substack{ll'\sigma\sigma'\boldsymbol{k}\boldsymbol{k}' \\ pp'\alpha\alpha'}} pp' \mathrm{tr}_B \left\{ e^{i\chi N} c_{l\sigma\boldsymbol{k}}^{p,\alpha} D_{l\sigma}^{\bar{p},\alpha} \tilde{G}_0 c_{l'\sigma'\boldsymbol{k}'}^{p',\alpha'} D_{l'\sigma'}^{\bar{p}',\alpha'} \rho^\infty \otimes \rho_B \right\}. \tag{5.5}$$

Using the commutation rule $e^{i\chi N}c^{p,\alpha}_{l\sigma\boldsymbol{k}} = c^{p,\alpha}_{l\sigma\boldsymbol{k}}e^{i\chi(N+p\delta_{\alpha+})}$, we end up with an generalized equation for $R(\chi)$, similar to Eq. (2.33), in the secular approximation

$$K^{(2)}_{\chi}R(\chi) = -\frac{\pi}{\hbar}\sum_{\substack{l\sigma p\alpha\alpha'\\ \omega\omega'}}\alpha\left[\alpha' f_l^{p\alpha'}(\omega) - \frac{i}{\pi}p_l(\omega)\right]g_l e^{i\chi p(\delta_{\alpha+}-\delta_{\alpha'+})} D^{\bar{p},\alpha}_{l\sigma}(\bar{p}\omega)D^{p,\alpha'}_{l\sigma}(p\omega')R(\chi). \tag{5.6}$$

The counting field term in the exponential can only be $i\chi p(\delta_{\alpha+}-\delta_{\alpha'+}) = 0, \pm i\chi$, which allows to split this Kernel into a sum of the original Liouvillian for the reduced density matrix (RDM) in Eq. (2.38) and a term that contains the counting field [124, 140]

$$\dot{R}(\chi) = \left[\mathcal{L} + \mathcal{J}(\chi)\right]R(\chi). \tag{5.7}$$

The additional term in this generalized master equation

$$\mathcal{J}(\chi) = \left(e^{i\chi}-1\right)\mathcal{J}^{+} + \left(e^{-i\chi}-1\right)\mathcal{J}^{-}, \tag{5.8}$$

is composed of the forward and backward current operators

$$\begin{aligned}\mathcal{J}^{+}\rho &= \sum_{\sigma\eta\eta'\omega}(\boldsymbol{\Gamma_l})_{\eta\eta'}f_l^{-}(\omega)d_{\eta\sigma}(-\omega)\rho\, d^{\dagger}_{\eta'\sigma}(\omega),\\ \mathcal{J}^{-}\rho &= \sum_{\sigma\eta\eta'\omega}(\boldsymbol{\Gamma_l})_{\eta\eta'}f_l^{+}(\omega)d^{\dagger}_{\eta'\sigma}(\omega)\rho\, d_{\eta\sigma}(-\omega).\end{aligned} \tag{5.9}$$

To achieve a compact notation we again omit the lead index of these superoperators.

5.3.1 Hierarchy of master equations

The generalized master equation (5.7) together with the generating functions (5.1) and (5.2) in principle already provides the current cumulants c_k. However, the direct numerical evaluation of these expressions is hindered by two obstacles. First, the numerical computation of derivatives becomes increasingly difficult with the order. Second, the relation between moments and cumulants is only known implicitly via the Taylor series for $Z(\chi)$ and $\phi(\chi)$. Our goal is therefore, to bring the generalized master equation into a form that allows the direct calculation of the cumulants c_k. From $\phi = \log\dot{Z}$ and $Z = \mathrm{tr}\{R(\chi)\}$ together with the generalized master equation (5.7), it follows

$$\phi(\chi) = \frac{1}{Z(\chi)}\mathrm{tr}\{\mathcal{J}(\chi)R(\chi)\} = \mathrm{tr}\{\mathcal{J}(\chi)X(\chi)\}, \tag{5.10}$$

with the auxiliary operator $X(\chi) = Z^{-1}(\chi)R(\chi)$. Additionally, we find the equation of motion

$$\dot{X}(\chi) = \mathcal{L}X(\chi) + [\mathcal{J}(\chi) - \phi(\chi)]X(\chi). \tag{5.11}$$

The dependence on the counting variable χ is substituted by the Taylor coefficients X_k and $\mathcal{J}_k$ which are defined via the series $X(\chi) = \sum_{k=0}^{\infty}(i\chi)^k X_k/k!$ and $\mathcal{J}(\chi) = \sum_{k=1}^{\infty}(i\chi)^k \mathcal{J}_k/k!$. Keep in mind that $\mathcal{J}_k = \mathcal{J}^+ + (-1)^k\mathcal{J}^-$ for $k > 0$ and $\mathcal{J}_0 = 0$. Ultimately, we obtain from Eqs. (5.2) and (5.11) the hierarchy of equations

$$c_k = \sum_{k'=0}^{k-1} \binom{k}{k'} \mathrm{tr}\{\mathcal{J}_{k-k'}X_{k'}\}, \tag{5.12}$$

$$\dot{X}_k = \mathcal{L}X_k + \sum_{k'=0}^{k-1} \binom{k}{k'} (\mathcal{J}_{k-k'} - c_{k-k'})X_{k'}. \tag{5.13}$$

Notice that in the limit $\chi \to 0$, $X(\chi)$ becomes the RDM, i.e., for $k = 0$, Eq. (5.13) is identical to the master equation (2.38). Furthermore, as an important consequence of $\mathcal{J}_0 = 0$ and $c_0 = 0$, the summations on the r.h.s. of these equations terminate at $k' = k - 1$, which implies that X_k and c_k depend only on terms of lower order. This allows the truncation at arbitrary order and, thus, the iterative computation of the current cumulants. In particular, the first step is to solve the master equation $\mathcal{L}\rho = 0$ for the RDM $\rho = X_0$ and use it to compute the current

$$I/e \equiv c_1 = \mathrm{tr}\left\{\left(\mathcal{J}^+ - \mathcal{J}^-\right)\rho\right\}. \tag{5.14}$$

This result is required to solve the equation

$$\dot{X}_1 = \mathcal{L}X_1 + \left(\mathcal{J}^+ - \mathcal{J}^- - c_1\right)\rho, \tag{5.15}$$

for X_1 which is then needed to compute the noise

$$S/e^2 \equiv c_2 = 2\mathrm{tr}\left\{\left(\mathcal{J}^+ - \mathcal{J}^-\right)X_1\right\} + \mathrm{tr}\left\{\left(\mathcal{J}^+ + \mathcal{J}^-\right)\rho\right\}. \tag{5.16}$$

This strategy can be repeated until the requested order of cumulants is achieved.

The numerical effort of this scheme can be estimated as follows. Let us assume that the Liouvillian $\mathcal{L}$ can be written as a $d \times d$-matrix and that its smallest decay rate is $\gamma_{\min}$. Then, to compute the first $k_{\max}$ cumulants, we have to propagate $k_{\max}d$ scalar equations for a time $\tau \approx 3/\gamma_{\min}$, where one

is typically interested in the first $k_{\max} = 5$–10 cumulants. To highlight the efficiency of our method, we compare this effort with that of the number-resolved master equation [137–139], for which the density operator is extended by a variable $n = 0, \ldots, n_{\max}$ that accounts for the number of transported electrons, truncated at $n_{\max}$. Since coherences between different n do not play a role, one essentially has to replace ρ by the $n_{\max} + 1$ density operators $\rho^{(n)}$, where $\mathrm{tr}\rho^{(n)}$ is the probability that n electrons have arrived at the lead. During a time τ, on average $I\tau$ electrons flow, so that one would have to employ a number-resolved master equation with $n_{\max} \approx 2I\tau = 6I/\gamma_{\min}$, i.e., one has to integrate $\sim 6Id/\gamma_{\min}$ scalar equations. This means that whenever $I \gtrsim \gamma_{\min}$, our method outperforms this alternative significantly. This is for example the case when the system infrequently switches between two states with different conductance [50, 115, 125]. A further advantage of our method is that it provides direct access to the cumulants, such that the detour via the moments can be avoided.

5.3.2 Relation to the iterative scheme for static transport

Equations (5.12) and (5.13) resemble the iterative scheme derived by Flindt *et al.* [135, 136] for the cumulants of *time-independent* transport problems and therefore represent a generalization of these works to *time-dependent* problems. If the Liouvillian $\mathcal{L}$ is time-independent, there exists a stationary solution ρ^∞ which for $k = 0$ also solves Eq. (5.13). For $k > 0$ it holds $\mathrm{tr}\{X_k\} = \delta_{k,0}$ because $\mathrm{tr}\{X(\chi)\} = 1$. Consequently, Eq. (5.13) possesses a stationary solution also for $k > 0$. Formally it can be written with the help of the pseudo-inverse of the Liouvillian $Q/\mathcal{L}$, where $Q = 1 - \rho^\infty \mathrm{tr}$ projects onto the subspace in which $\mathcal{L}$ is regular. Therefore, the condition $\dot{X}_k = 0$ together with $\mathrm{tr}\{X_k\} = \delta_{k,0}$ results in

$$X_k = -\frac{Q}{\mathcal{L}} \sum_{k'=0}^{k-1} \binom{k}{k'} \left(\mathcal{J}_{k-k'} - c_{k-k'}\right) X_{k'}, \tag{5.17}$$

while $X_0 = \rho^\infty$. Equations (5.12) and (5.17) represent the known iteration scheme for the time-independent case [135, 136].

5.3.3 Hierarchy of equations for the moments

While the advantage of this scheme is the direct access to the current cumulants, it is valuable to compare it with the corresponding iteration for the time-

dependent moments derived in Kambly *et al.* [141] and Kambly and Flindt [142]. It can be obtained from the Taylor expansions of moment generating function (5.1) and of the generalized master equation (5.7). It reads

$$\mu_k = \mathrm{tr}\{R_k\}, \tag{5.18}$$

$$\dot{R}_k = \mathcal{L}R_k + \sum_{k'=0}^{k-1} \binom{k}{k'} \mathcal{J}_{k-k'} R_{k'}, \tag{5.19}$$

respectively. While these equations appear simpler than the corresponding expressions for the cumulants, the following computation of the current cumulants is cumbersome. It can be achieved by the recurrence relation that follows directly from Eqs. (5.1) and (5.2)

$$c_k = \dot{\mu}_k - \sum_{k'=1}^{k-1} \binom{k-1}{k'-1} c_{k'} \dot{\mu}_{k-k'}. \tag{5.20}$$

Notice that in contrast to Refs. [141, 142], we are considering current cumulants and not number cumulants, which requires the computation of the time derivative of the moments

$$\dot{\mu}_k = \mathrm{tr}\{\dot{R}_k\} = \sum_{k'=0}^{k-1} \binom{k}{k'} \mathrm{tr}\left\{\mathcal{J}_{k-k'} R_{k'}\right\}. \tag{5.21}$$

The calculation of the c_k from Eqs. (5.18)–(5.21) can be numerically challenging, especially when, e.g., for strong bunching the cumulants grow rapidly with their order. In such cases Eq. (5.20) includes small differences of large numbers, which typically is sensitive to rounding errors.

5.4 Matrix-continued fractions

The most straightforward way to solve the hierarchy of equations is the numerical integration of the master equation for the RDM followed by the computation of the current $I(t)$ and the numerical integration of Eq. (5.15). While being flexible, such numerical propagation methods often lack efficiency, especially when dealing with driven systems. For systems with a single driving frequency there exist more sophisticated ways of computing the dynamics. The matrix-continued fraction method has been employed recently for the efficient computation of time-averaged currents [143] in the context of mesoscopic transport. Our goal is to extend this scheme to the computation of the shot

noise. For convenience, we write the two equations of motion in block matrix notation,

$$\begin{pmatrix} \dot{\rho} \\ \dot{X}_1 \end{pmatrix} = \begin{pmatrix} \mathcal{L}(t) & 0 \\ \mathcal{J}^+ - \mathcal{J}^- - c_1(t) & \mathcal{L}(t) \end{pmatrix} \begin{pmatrix} \rho \\ X_1 \end{pmatrix} \equiv M(t)\boldsymbol{b}(t), \tag{5.22}$$

with the shorthand notation $\boldsymbol{b} = (\rho, X_1)^T$. To derive a matrix-continued fraction scheme, this equation has to be brought into the form of a tridiagonal recurrence relation [144]. This is hindered by the fact that $M(t)$ depends on the time-dependent current $I(t)$ which may contain higher-order harmonics. Here, however, we find that reliable results for the noise can still be obtained when $I(t)$ is replaced by its time average. This assumtion is tested in Niklas *et al.* [P.2]. Since the remaining time-dependence in $M(t)$ stems from the Liouvillian of the driving in the system Hamiltonian with frequency ω, the Fourier decomposition of the terms in Eq. (5.22) reads

$$M(t) = M_0 + M_+ e^{i\omega t} + M_- e^{-i\omega t}, \tag{5.23}$$

$$\boldsymbol{b}(t) = \sum_{n=-\infty}^{\infty} e^{in\omega t} \mathbf{b}_n. \tag{5.24}$$

By inserting Eq. (5.24) into Eq. (5.22) we obtain the tridiagonal recurrence relation

$$M_+ \boldsymbol{b}_{n-1} + (M_0 - in\omega)\, \mathbf{b}_n + M_- \mathbf{b}_{n+1} = 0. \tag{5.25}$$

Our interest lies in the time-average of $\boldsymbol{b}(t)$, i.e., in the Fourier component $\boldsymbol{b}_0$. To this end, we define the transfer matrices S_k and R_k via the ansatz

$$\mathbf{b}_n = \begin{cases} R_n \boldsymbol{b}_{n+1} & \text{for } n < 0, \\ S_n \boldsymbol{b}_{n-1} & \text{for } n > 0. \end{cases} \tag{5.26}$$

Consistency with Eq. (5.25) is ensured by the recurrence relations

$$S_n = -\left[M_0 - in\omega + M_- S_{n+1}\right]^{-1} M_+, \tag{5.27}$$

$$R_n = -\left[M_0 - in\omega + M_+ R_{n-1}\right]^{-1} M_-, \tag{5.28}$$

together with

$$(M_0 + M_+ R_{-1} + M_- S_1)\boldsymbol{b}_0 = 0. \tag{5.29}$$

For practical purposes, we have to truncate the Fourier components of $\boldsymbol{b}(t)$ assuming $\boldsymbol{b}_n = 0$ for $|n| > n_0$ which holds for $S_{n_0+1} = R_{-(n_0+1)} = 0$. With the

latter condition we compute R_{-1} and S_1 by iterating Eqs. (5.27) and (5.28) which finally provides an explicit expression for Eq. (5.29). In a last step we solve this homogeneous equation under the trace conditions $\mathrm{tr}\{\rho_0\} = 1$ and $\mathrm{tr}\{X_1\} = 0$. This method can easily be extended to higher order cumulants by including higher order X_k into $\boldsymbol{b}$.

5.5 Minimal models

In this section we will apply the FCS to increasingly complex test models to understand certain values that the Fano factor can assume and how higher order cumulants are behaving.

5.5.1 Single resonant level

Let us start again with the simplest possible SET, the single resonant level. This time we are not interested in the gate and bias dependence but in the behavior of the Fano factor and higher order cumulants in the infinite bias limit. The Liouvillian and current operators read

$$\mathcal{L} = \begin{pmatrix} -\Gamma_\mathrm{L} & \Gamma_\mathrm{R} \\ \Gamma_\mathrm{L} & -\Gamma_\mathrm{R} \end{pmatrix}, \qquad \mathcal{J}^+ = \begin{pmatrix} 0 & \Gamma_\mathrm{R} \\ 0 & 0 \end{pmatrix}, \tag{5.30}$$

and $\mathcal{J}^- = 0$. Here we measure the current at the right lead $\mathcal{J}^+ = \mathcal{J}^+_\mathrm{R}$. The stationary solution of the RDM is $\rho^\infty = (\Gamma_\mathrm{R}, \Gamma_\mathrm{L})^T/(\Gamma_\mathrm{L} + \Gamma_\mathrm{R})$ which results in the current $I = e\Gamma_\mathrm{L}\Gamma_\mathrm{R}/(\Gamma_\mathrm{L} + \Gamma_\mathrm{R})$. Solving Eq. (5.15) determines $X_1^\infty = \Gamma_\mathrm{L}^2\Gamma_\mathrm{R}(1, -1)^T/(\Gamma_\mathrm{L} + \Gamma_\mathrm{R})^3$ and finally with Eq. (5.16), the shot noise $S = e^2\Gamma_\mathrm{L}\Gamma_\mathrm{R}(\Gamma_\mathrm{L}^2 + \Gamma_\mathrm{R}^2)/(\Gamma_\mathrm{L} + \Gamma_\mathrm{R})^3$. Putting everything together we find the Fano factor at infinite bias

$$F = \frac{\Gamma_\mathrm{L}^2 + \Gamma_\mathrm{R}^2}{(\Gamma_\mathrm{L} + \Gamma_\mathrm{R})^2}. \tag{5.31}$$

For the symmetric case, $\Gamma_\mathrm{L} = \Gamma_\mathrm{R} \equiv \Gamma$, the Fano factor is $F = 1/2$. In the situation of strong asymmetry the Fano factor approaches $F \lesssim 1$. Therefore, in the resonant level the Fano factor strongly indicates sub-Poissonian statistics. All higher order cumulants are known analytically as $c_k = 2^{-k}\Gamma$ [124], which makes this system an ideal test case. Consequently, all cumulant ratios $F_k = 1/2$ are identical to the Fano factor. For any $\Gamma_\mathrm{L} \neq \Gamma_\mathrm{R}$, the cumulants cannot be written in a closed form, but exhibit a generic behavior: While cumulants of

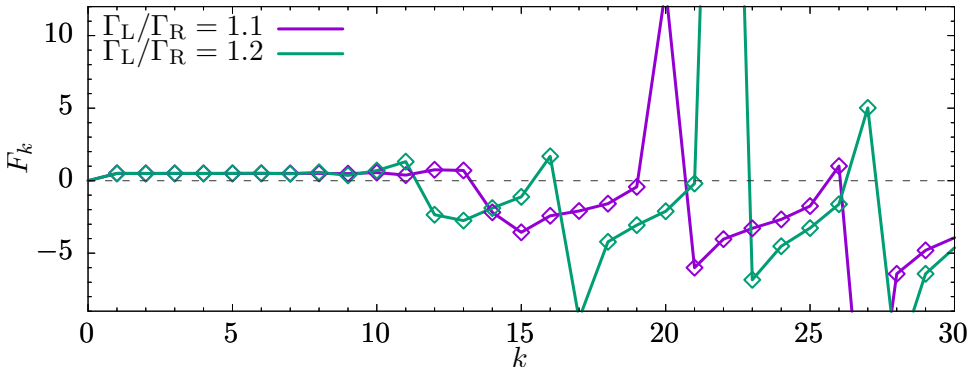

Figure 5.2: Cumulant ratios $F_k = c_{k+1}/c_k$ of a resonant level at infinite bias with asymmetric tunneling rates $\Gamma_{L/R}$. The symbols are obtained with the hierarchy of master equations, while the lines interpolate the results of the iteration scheme based on Eq. (5.17).

low order reflect the nature of the transport process, high-order cumulants oscillate in a universal manner [145]. Therefore the symmetric case with its constant $F_k = 1/2$ is rather special and should be sensitive to numerical errors. By solving Eqs. (5.12) and (5.13) numerically, we have found that for $\Gamma_L = \Gamma_R$, the first $\gtrsim 30$ cumulant ratios agree with the analytical prediction with a precision $\lesssim 1$ (not shown). For slight asymmetries, we compare in Fig. 5.2 our results with those obtained by the traditional iteration scheme. Both agree rather well also for orders at which the cumulants exhibit universal oscillations.

Solving the finite bias master equation (2.68) also for the shot noise results in the stability diagram together with the Fano map in Figs. 5.3a,b, respectively. Deep inside the non-conductive regions we obtain a Fano factor of $F = 1$ since the current is only given by thermal excitation of the trapped electron. These processes are uncorrelated and thus follow the Poissonian distribution. In the transport region we find exactly the value obtained before in the infinite bias limit $F = 1/2$. Expanding the expressions for current and noise to lowest order in the bias voltage we find a linear behavior of the current while the shot noise reaches a constant value

$$I = e\frac{\Gamma_L\Gamma_R}{4k_BT(\Gamma_L+\Gamma_R)}\mathrm{sech}^2\left(\frac{\alpha_g V_g}{2k_BT}\right)V_b + \mathcal{O}(V_b^2), \tag{5.32}$$

$$S = e^2\frac{\Gamma_L\Gamma_R}{(\Gamma_L+\Gamma_R)\left[1+\cosh\left(\frac{\alpha_g V_g}{k_BT}\right)\right]} + \mathcal{O}(V_b). \tag{5.33}$$

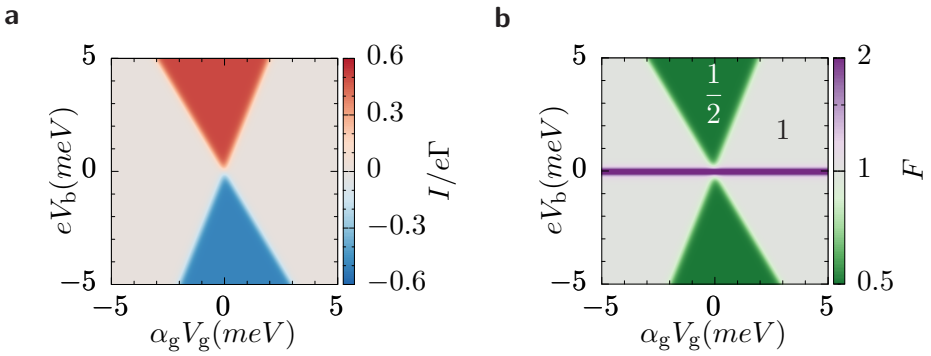

Figure 5.3: **a** Stability diagram of the single resonant level. **b** Corresponding Fano map with highlighted analytical values. The used parameters are $k_B T = 0.1meV$, $\eta = 0.4$ and $\hbar\Gamma_L = \hbar\Gamma_R = \hbar\Gamma = 10\mu eV$.

This noise is usually called Johnson-Nyquist noise or thermal noise [146, 147]

$$S = 2k_B T \frac{I}{V_b}, \tag{5.34}$$

and results in a diverging Fano factor for $V_b \lesssim k_B T$, as seen in Fig. 5.3b.

5.5.2 Fast and slow channel model

A minimal system that can exhibit super-Poissonian noise via electron bunching features two levels, a fast and a slow one. In the context of SETs this happens for example in the Coulomb blockade region where an excited state lies inside the bias window [125]. The chemical potential landscape of this situation is shown in Fig. 5.4. Here, the current is mainly governed by the slow channel since the electrons spend most of the time occupying the ground state due to Coulomb blockade. Therefore, the current is given by the rate at which these electrons leave the state, which is only possible via thermal excitation due to the finite temperature and defines the bottleneck of tunneling. Once the ground state is empty the next electron can enter one of the two levels. If by chance the electron enters the excited state, it will leave this level at a fast rate since it lies inside the bias window. This process will be repeated until an electron enters again in the ground state and blocks transitions for a long time. This repeated process leads to bunches of electrons tunneling separated by long waiting times which features a super-Poissonian noise. The Liouvillian in this situation in the basis $\{|0\rangle\langle 0|, |s\rangle\langle s|, |f\rangle\langle f|\}$, far away from resonant lines,

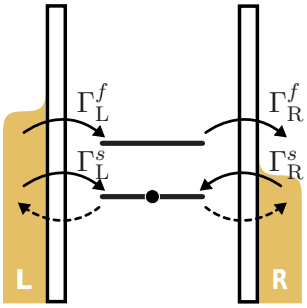

Figure 5.4: Chemical potential landscape of a system with a fast and a slow channel. The bottleneck processes of thermal excitation of the Coulomb blocked level are indicated by dashed arrows.

reads

$$\mathcal{L} = \begin{pmatrix} -\Gamma^f_{\rm L} & 0 & \Gamma^f_{\rm R} \\ 0 & 0 & 0 \\ \Gamma^f_{\rm L} & 0 & -\Gamma^f_{\rm R} \end{pmatrix} + \sum_l \begin{pmatrix} -\Gamma^s_l & \Gamma^s_l f^-_l & 0 \\ \Gamma^s_l & -\Gamma^s_l f^-_l & 0 \\ 0 & 0 & 0 \end{pmatrix}, \tag{5.35}$$

with the tunneling rates $\Gamma^{f/s}_{\rm L/R}$ of the fast and slow channel, respectively. The Fermi functions $f^-_l \approx 0$ of the ground state define the bottleneck processes, therefore we keep them to obtain a finite current and noise. The current operators of the right lead read

$$\mathcal{J}^+ = \begin{pmatrix} 0 & \Gamma^s_{\rm R} f^-_{\rm R} & \Gamma^f_{\rm R} \\ 0 & 0 & 0 \\ 0 & 0 & 0 \end{pmatrix}, \qquad \mathcal{J}^- = \begin{pmatrix} 0 & 0 & 0 \\ \Gamma^s_{\rm R} & 0 & 0 \\ 0 & 0 & 0 \end{pmatrix}. \tag{5.36}$$

To lowest order in the small Fermi functions f^-_l the current in the right lead is

$$I = e\frac{\left(\Gamma^f_{\rm L} + \Gamma^s_{\rm L}\right)\Gamma^s_{\rm R} f^-_{\rm R} + \left(\Gamma^f_{\rm L} - \Gamma^s_{\rm R}\right)\Gamma^s_{\rm L} f^-_{\rm L}}{\Gamma^s_{\rm L} + \Gamma^s_{\rm R}}. \tag{5.37}$$

In a CB situation with $f^-_{\rm R} \gg f^-_{\rm L}$, and for large asymmetry between the couplings to the leads, $\Gamma^s_{\rm L} \gg \Gamma^s_{\rm R}$, the current simplifies to $I = e\Gamma^s_{\rm R} f^-_{\rm R}(1 + \Gamma^f_{\rm L}/\Gamma^s_{\rm L})$, in agreement with the findings by Belzig [125]. If for some reason the slow channel is disconnected from the right lead, $\Gamma^s_{\rm R} = 0$, the current becomes $I = e\Gamma^f_{\rm L} f^-_{\rm L}$. Similar calculations as for the current yield the Fano factor

$$F = 1 + \frac{2\Gamma^f_{\rm L}}{\Gamma^s_{\rm L} + \Gamma^s_{\rm R}}. \tag{5.38}$$

Notice that it always holds $F \geq 1$. The expression simplifies to $F = 1+2\Gamma_{\mathrm{L}}^{f}/\Gamma_{\mathrm{L}}^{s}$ for Coulomb blockade with large asymmetry [125] as well as a decoupled slow channel. One can show that in a situation where the state $|0\rangle$ has one electron more than $|f\rangle$ and $|s\rangle$ the Liouvillian and the current operators for the left lead are given again by Eqs. (5.35) and (5.36), respectively, upon exchanging $\mathrm{L} \leftrightarrow \mathrm{R}$ and $f_l^+ \leftrightarrow f_l^-$. This corresponds to hole transport. With the same exchanges the current and Fano factor are obtained from Eqs. (5.37) and (5.38), respectively. Notice that this result includes also external asymmeties $\Gamma_{\mathrm{L}} \neq \Gamma_{\mathrm{R}}$.

5.5.3 Single impurity Anderson model

A simple system with richer features is again the SU(2) single-impurity Anderson model (SIAM). The current in the sequential tunneling regime is shown in Fig. 5.5a for symmetric coupling $\Gamma_{\mathrm{L}} = \Gamma_{\mathrm{R}} = \Gamma$. The calculated Fano factor is shown in Fig. 5.5b. In the transport regime when only the ground state participates in transport the current and Fano factor are the one of the resonant level, e.g. $F = 1/2$ from Eq. (5.31). As soon as the excited state enters the bias window, the Fano factor also changes. Away from resonant lines the system can be approximated via a degenerate level such that the effective rate for tunneling in the QD is twice as large as the rate for tunneling out. This means that the equation for the Fano factor in the resonant level still holds with $\Gamma_{\mathrm{L}} = 2\Gamma_{\mathrm{R}} = \Gamma$ and yields the fractional Fano factor $F = 5/9$. In the Coulomb blockade regions with $N = 0$, $N = 2$ and small parts of $N = 1$ electrons, where no additional excited states lie in the bias window, it shows a value of $F = 1$. This is reasonable since the current is governed by thermal excitations of the trapped electrons which form the bottleneck processes of current in this situation. These processes are independent of each other and therefore result in a Poissonian noise with $F = 1$. Around $|eV_{\mathrm{b}}| \lesssim k_B T$ the Fano factor diverges again due to Johnson-Nyquist noise. Finally, deep inside the central Coulomb diamond the system resembles exactly the minimal system with one fast and one slow channel. Since all rates are the same, the Fano factor from Eq. (5.38) assumes the value $F = 2$. It is remarkable how many values of the Fano factor can already be explained using the simple resonant level or fast and slow channel models. In experiments the measurement of the shot noise can unravel the underlying transport mechanisms and for example give insight in the degeneracy of levels.

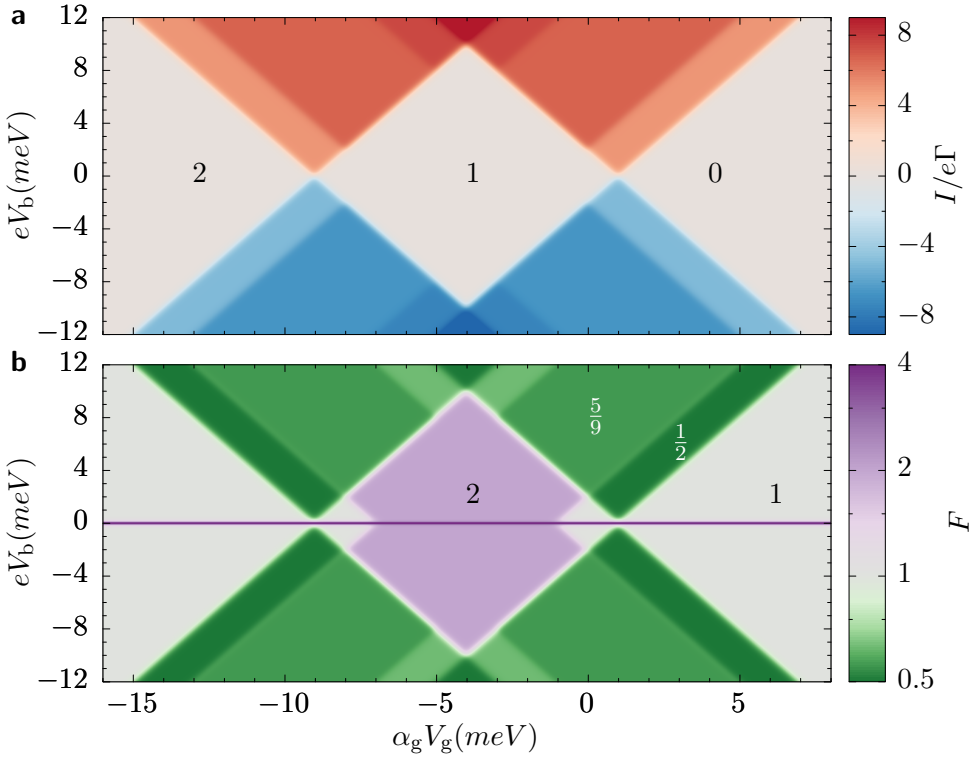

Figure 5.5: **a** Stability diagram of the SIAM with highlighed electron numbers in the Coulomb blockade regions. **b** Corresponding Fano map with certain Fano factor values being highlighted. The used parameters are $U = 8meV$, $\Delta\epsilon = 2meV$, $\hbar\Gamma_L = \hbar\Gamma_R = \hbar\Gamma = 10\mu eV$, $k_B T = 0.1meV$ and $\eta = 0.5$.

CHAPTER 6

Topological blockade in a dimer chain

Quantum electronics is governed by charging energies which give rise to Coulomb blockade in quantum dots [12] and conducting molecules [148]. When electron spins and phonons come into play, additional blockade phenomena may influence the current-voltage characteristics. For example, the Pauli exclusion principle may cause a spin blockade in double [149, 150] and triple quantum dots [151]. Moreover, an entering electron may emit a phonon and become trapped until it reabsorbs a phonon, which is known as phonon blockade [50, 152, 153]. Some blockade phenomena are less pronounced in the current, but have a strong impact on the current noise. Most prominently, the strong coupling of an electron in a molecular wire with a vibrational degree of freedom may lead to a switching between conducting and almost isolating configurations and cause Franck-Condon blockade. Then the transport becomes avalanche-like, which drastically enhances the shot noise [50, 154]. A similar effect occurs in capacitively coupled transport channels, where noise measurements reveal that a mutual channel blockade causes electron bunching [100, 155]. We propose a new blockade mechanism based on the interplay of strong Coulomb repulsion and a relatively new field in condensed matter physics: topology. Using the probably simplest model of a topological insulator, a one-dimensional array of quantum dots with alternating hopping elements, the so called Su-Schrieffer-Heeger (SSH) model, we show that topological edge states can emerge [156] which block the current even at large bias voltages.

The transition from a topologically trivial to a nontrivial regime is manifest in the shot noise properties as it is accompanied by a crossover from bunched electron transport to a Poissonian process. This makes noise measurements an ideal tool for mapping out a topological phase diagram. Experimental evidence for this edge-state blockade will be facilitated by a high tunability of the inter-dot tunneling. A possible way to achieve this is driving the conductor by an electric dipole field. Then for not too small frequencies, the driving essentially renormalizes the inter-dot tunnel coupling [157–160] and, thus, allows the emulation of a dimer chain with highly tunable tunneling. One expects a corresponding current suppression [161, 162] which has been measured in double quantum dots [42, 163]. Moreover, the driving may have significant impact on the shot noise [130]. Based on the recent finding that the topological properties of AC driven dimer chains can be controlled via the amplitude of a driving field [164–166], we find the topological phase diagram as a function of the driving parameters.

Large parts of this chapter were published in Benito *et al.* [P.1] and Niklas *et al.* [P.2].

6.1 Topology in condensed matter physics

Condensed matter physics deals with different phases of matter and how their physical properties are affected by different factors. Such phases are defined via their symmetries, as can be seen in the example of liquids and solids. While liquids are invariant under both translations and rotations, in solids these continuous symmetries are broken down to finite symmetries. This shows that transitions between these phases are accompanied by a change in the symmetry class. Another well known example of such a phase transition is the cooling down of a ferromagnet. Below the Curie temperature the spins line up and create a global magnetization and therefore the magnet changes from an unordered state into an ordered state. Hereby, the magnetization plays the role of an order parameter that can characterize this phase transition. In fact, all phase transitions can be described by an order parameter which suddenly changes from zero in the unordered phase to non-zero in the ordered phase. In the last decades a new family of phases of matter has drawn the interest of many physicists: topological phases. The concept of topology has been adopted to physics from mathematics where it describes properties

that are preserved under continuous transformations. This means that these topological phases go beyond the usual symmetry description as they cannot be characterized by an order parameter. They can undergo so called topological phase transitions even without breaking the corresponding symmetries. In condensed matter physics this is of special interest since effects that originate from topological phenomena are robust against perturbations and independent of the details of the system as long as the necessary symmetries are conserved: these effects are symmetry protected. This suggests an enormous potential for novel applications [167]. This concept has been applied to the established Bloch band theory for solids. In an insulator an energy gap separates the valence from the conduction bands. This ensemble can have trivial or twisted topological properties, the latter is often called an inverted band structure and is topological non-trivial. Such types of crystals are called topological insulators. The only possible way a topological phase transition can take place is the closing of the gap to change from a trivial to a non-trivial region. For the same reason, at the boundary between two materials with distinct topological phases the gap also has to close which leads to the formation of conducting surface states. Keeping in mind that the vacuum is like a topological trivial insulator shows that a piece of topological insulator is conducting on the surface while being an insulator in the bulk. This surface or edge states are usually protected against scattering by time-reversal symmetry. The most important concept in topological Bloch theory is the Berry phase [168–170]. The wave function of an electron in a solid is given by Bloch waves $\phi_{\nu,\boldsymbol{k}}(\boldsymbol{r}) = e^{i\boldsymbol{k}\boldsymbol{r}} u_{\nu,\boldsymbol{k}}(\boldsymbol{r})$, where ν is the band index and $u_{\nu,\boldsymbol{k}}(\boldsymbol{r}+\boldsymbol{a}) = u_{\nu,\boldsymbol{k}}(\boldsymbol{r})$ the periodic part of the Bloch wave. The Berry phase is then defined using the Fourier transform of the periodic part $|u_\nu(\boldsymbol{k})\rangle$ as the integral over the Berry potential or Berry connection $\boldsymbol{A}_\nu(\boldsymbol{k}) = i\langle u_\nu(\boldsymbol{k})|\nabla_{\boldsymbol{k}}|u_\nu(\boldsymbol{k})\rangle$ along a closed path $\mathscr{C}$ in momentum space

$$\gamma_\nu = i \oint_{\mathscr{C}} \mathrm{d}\boldsymbol{k}\ \langle u_\nu(\boldsymbol{k})|\nabla_{\boldsymbol{k}}|u_\nu(\boldsymbol{k})\rangle. \tag{6.1}$$

In one-dimensional systems the only possible closed loop is the entire Brillouin zone, in which case the Berry phase is also called the Zak phase [171]. In systems with spatial inversion symmetry this phase can only assume the values 0 and π [169, 172]. In higher dimensions the Berry curvature can be derived from the Berry connection as $\Omega_\nu(\boldsymbol{k}) = \nabla_{\boldsymbol{k}} \boldsymbol{A}_\nu(\boldsymbol{k})$ whose integration along a closed path results in the Chern number. This shows that in contrast

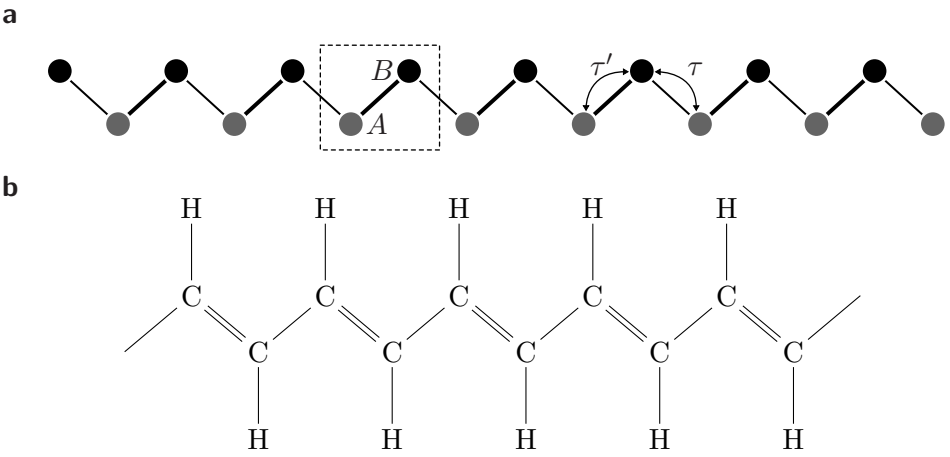

Figure 6.1: **a** Tight binding SSH model. The dashed box shows the unit cell with the two atomic basis A and B. Arrows show the inter- and intra-dimer tunneling, τ, τ', respectively. **b** Polyacetylene is an organic molecule that represents such a dimer chain.

to the "classical" phases identified via an order parameter the topological phases can be described using these topological indices. The probably simplest model that can undergo topological phase transitions is the one-dimensional Su-Shrieffer-Heeger model.

6.2 The Su-Shrieffer-Heeger model

A one-dimensional tight-binding model with alternating tunnel matrix elements represents a simple description of a dimerized polymer. It was originally used to study solitonic effects in polymers [173, 174] and is now named after its inventors as the Su-Schrieffer-Heeger (SSH) model. In Fig. 6.1 such a simple tight-binding model is pictured next to a molecular realization, polyacetylene. The Hamiltonian of this spinless chain of dimers is [173]

$$H_{\mathrm{SSH}} = \sum_{n=1}^{N-1} \tau_n d_{n+1}^{\dagger} d_n + \mathrm{h.c.}, \tag{6.2}$$

with the alternating tunnel matrix elements $\tau_n = \tau_0 + (-1)^n \delta\tau$ and the fermionic annihilation operator d_n at site n. The model consists of $N/2$ unit cells. We keep τ_0 constant and use $\delta\tau$ as a control parameter. This results in the inter-dimer hopping $\tau = \tau_0 + \delta\tau$ and intra-dimer hopping $\tau' = \tau_0 - \delta\tau$. The Schrödinger equation for the h-th unit cell in the two atomic basis with

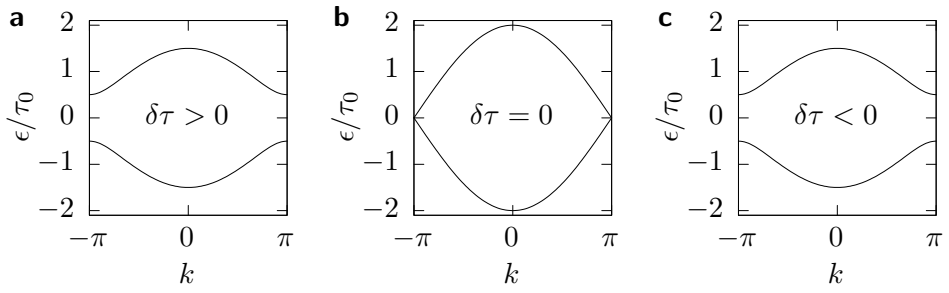

Figure 6.2: **a,b,c** Bands of the SSH model for different values of the hopping amplitudes. **a** $\tau = 2\tau' = \tau_0$, **b** $\tau = \tau' = \tau_0$ and **c** $2\tau = \tau' = \tau_0$.

$|\phi_h\rangle = \left(\phi^A_{2h}, \phi^B_{2h+1}\right)^T$, can be written as the set of coupled equations

$$\tau\sigma_+ |\phi_{h-1}\rangle + \tau'\sigma_x |\phi_h\rangle + \tau\sigma_- |\phi_{h+1}\rangle = \epsilon |\phi_h\rangle , \tag{6.3}$$

where σ_α are the Pauli matrices with $\sigma_\pm = (\sigma_x \pm i\sigma_y)/2$. For periodic boundary conditions we use the Bloch ansatz $|\phi_h\rangle \to |\phi_{h,k}\rangle = e^{ikh} |u_k\rangle$. Therefore, for an infinitely long chain this Hamiltonian describes two bands in momentum space

$$\begin{pmatrix} 0 & \tau e^{-ik} + \tau' \\ \tau e^{ik} + \tau' & 0 \end{pmatrix} |u_k\rangle = \epsilon(k)|u_k\rangle, \tag{6.4}$$

with the eigenenergies $\epsilon(k) = \pm\sqrt{\tau^2 + \tau'^2 + 2\tau\tau' \cos k}$. The band structure can be seen in Fig. 6.2 for various values of τ and τ'. The two bands are split by a band gap of $|2\delta\tau|$ as long as the hopping amplitudes are staggered $\delta\tau \neq 0$. At $\delta\tau = 0$ a topological phase transition happens as the gap closes. Using the eigenstates $|u_{k,\pm}\rangle = (e^{-i\vartheta(k)}, \pm 1)^T/\sqrt{2}$, where we defined $\tan\vartheta(k) = \tau \sin k/(\tau \cos k + \tau')$, we can calculate the Zak phase in these cases

$$Z = i \int_{-\pi}^{\pi} \mathrm{d}k \, \langle u_\pm(k)|\partial_k|u_\pm(k)\rangle = \pi\Theta(\delta\tau), \tag{6.5}$$

and see that the SSH model is non-trivial when $\delta\tau > 0$. This Zak phase has been measured recently [175].

6.2.1 Edge states

We have seen that at the boundaries of a topological non-trivial system surface states appear. In one-dimensional systems like the SSH model these edges are

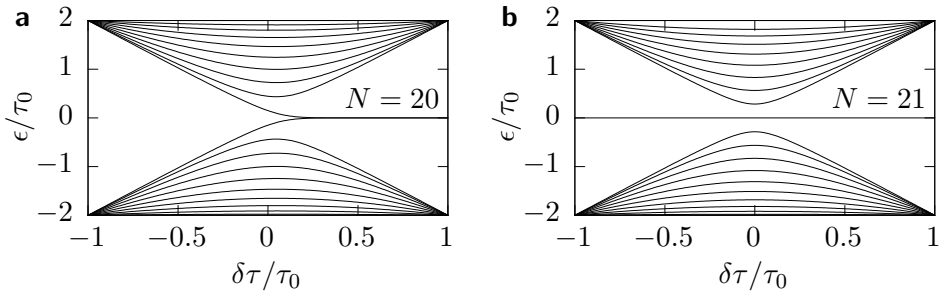

Figure 6.3: **a,b** Energy spectrum of a finite size SSH model as a function of the difference of hopping amplitudes. **a** A dimer chain with an even number of sites of length $N = 20$ shows two edge states appreading at $\delta\tau > 0$. **b** With an odd number of sites, $N = 21$, a transition happens from an edge state at the right end to one at the left end.

located at the ends. An edge state in a semi-infinite chain corresponds to a solution that vanishes at some site such that, e.g., $|\phi_{-1}\rangle = 0$. Then, we obtain from the Schrödinger equation and Eq. (6.4) the condition

$$\begin{pmatrix} 0 & \tau' \\ \tau e^{ik} + \tau' & 0 \end{pmatrix} |u_{k,\mathrm{edge}}\rangle = 0. \tag{6.6}$$

It possesses a nontrivial solution if $k = \pi + i \ln(\tau/\tau')$, which for $\delta\tau > 0$ is decaying as $|\phi_h\rangle \propto \exp(-\kappa h)$ with the exponent $\kappa = \ln(\tau/\tau')$ [156]. Close to the phase transition $|\delta\tau| \ll \tau_0$, it becomes $\kappa \approx 2\delta\tau/\tau_0$. Therefore, the overlap between the two edge states of a chain with $N/2$ dimers can be estimated as

$$\Delta \approx \tau_0 e^{-\delta\tau N/\tau_0}. \tag{6.7}$$

It agrees with the splitting of the interband doublet found in finite dimer chains [156]. In Fig. 6.3a we show the spectrum of a dimer chain of length $N = 20$ where these edge states appear at $\delta\tau > 0$. If the array consists of an odd number of sites, a monomer will remain forming an edge state. Thus, we witness a transition from a situation with an edge state at the right end of the chain ($\delta\tau < 0$) to one with an edge state at the left end ($\delta\tau > 0$) [167]. This transition, however, is not visible in the spectrum as seen in Fig. 6.3b for $N = 21$ sites.

6.2.2 Chiral symmetry

The topological properties of the SSH model stem from a chiral symmetry C which fulfills

$$C\hat{H}_{\mathrm{SSH}}C = -\hat{H}_{\mathrm{SSH}}. \tag{6.8}$$

This chiral symmetry operator has to be unitary and Hermitian $C^{-1} = C^{\dagger} = C$ with $C^2 = 1$. In second quantization, this symmetry operation can be written as

$$C = e^{i\pi \sum_n n d_n^{\dagger} d_n}, \tag{6.9}$$

which provides a minus sign for all creation and annihilation operators with an odd site number

$$C d_n C = (-1)^n d_n. \tag{6.10}$$

Consequently, all nearest-neighbor hoppings acquire a factor -1 which explains the mentioned chiral symmetry of $\hat{H}_{\mathrm{SSH}}$. The chiral symmetry is also called sublattice symmetry since it allows to define the orthogonal sublattice projectors $\mathcal{P}_A = (1+C)/2$ and $\mathcal{P}_B = (1-C)/2$. These projectors fulfill $\mathcal{P}_A + \mathcal{P}_B = 1$ and $\mathcal{P}_A \mathcal{P}_B = 0$. Since the SSH model only consideres nearest neighbor hopping it holds

$$\hat{H}_{\mathrm{SSH}} = \mathcal{P}_A \hat{H}_{\mathrm{SSH}} \mathcal{P}_B + \mathcal{P}_B \hat{H}_{\mathrm{SSH}} \mathcal{P}_A. \tag{6.11}$$

A consequence of the chiral symmetry is that the spectrum must be symmetric because for any state $|\psi_n\rangle$ with eigenenergy ϵ_n from $\hat{H}_{\mathrm{SSH}}|\psi_n\rangle = \epsilon_n|\psi_n\rangle$ it follows

$$\hat{H}_{\mathrm{SSH}} C|\psi_n\rangle = -C\hat{H}_{\mathrm{SSH}}|\psi_n\rangle = -\epsilon_n C|\psi_n\rangle. \tag{6.12}$$

Therefore, each state $|\psi_n\rangle$ has a chiral partner $C|\psi_n\rangle$ at opposite energy. This has interesting applications on the edge states which hold $\epsilon_{\mathrm{edge}} = 0$ from $\hat{H}_{\mathrm{SSH}}|\psi_{\mathrm{edge}}\rangle = 0$. Such states fulfill

$$\hat{H}_{\mathrm{SSH}}|\psi_{\mathrm{edge}}\rangle = \hat{H}_{\mathrm{SSH}} \left(|\psi_{\mathrm{edge}}\rangle \pm C|\psi_{\mathrm{edge}}\rangle\right) = 0, \tag{6.13}$$

which proves that the zero energy edge states are the chiral symmetric partners of themselves. The existence of edge states in the SSH model has interesting effects on transport when coupled to leads.

6.3 Edge state blockade

Our main focus is the behavior of the SSH model in transport, i.e. when coupled to biased leads acting as the electron source and drain with an applied

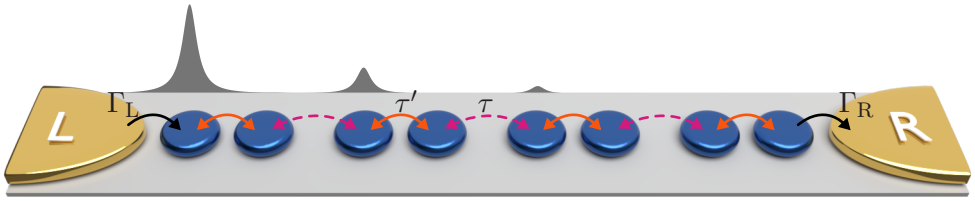

Figure 6.4: Scheme of a QD dimer chain with inter- and intra-dimer tunnel couplings $\tau = \tau_0 + \delta\tau$ and $\tau' = \tau_0 - \delta\tau$, respectively, connected to leads with tunneling rates $\Gamma_{L/R}$. The wave function depicts the stationary state in the topological regime. Electron trapping in the edge state at the left lead causes an edge-state blockade.

bias voltage V_b. While in principle the central system can be any dimerized structure like polyacetylene in Fig. 6.1b, we consider the idea of quantum dots in a row with alternating small and large distances between them. Such a model system can be seen in Fig. 6.4. In our model we allow only up to one spinless electron and we work in the weak coupling and high bias limit $\hbar\Gamma_{L/R}, \tau, \tau' \ll k_B T \ll eV_b$, such that the electron transport becomes unidirectional. Moreover, the array-lead tunneling becomes independent of the details of the array's level structure, which allows working in the local basis. Then the master equation (2.46) assumes the convenient Lindblad form even without the secular approximation

$$\dot{\rho} = \mathcal{L}\rho \equiv -\frac{i}{\hbar}[\hat{H}_{SSH}, \rho] + \Gamma_L \mathcal{D}(d_1^\dagger)\rho + \Gamma_R \mathcal{D}(d_N)\rho, \tag{6.14}$$

with the Lindblad operator $\mathcal{D}(x)\rho = (2x\rho x^\dagger - x^\dagger x\rho - \rho x^\dagger x)/2$ and the dot-lead rates $\Gamma_{L/R}$. Since the transport is unidirectional there exist only one current operator $\mathcal{J}^+\rho = \Gamma_R d_N \rho d_N^\dagger$.

Let us start by investigating a dimer chain in the case of an even number of sites for which the current in the different regimes is shown in Fig. 6.5a. We notice that in the monomer limit $\delta\tau = 0$, the current assumes an appreciable value. Towards both the topologically trivial and the nontrivial region, it decays. In the nontrivial region, the decay is faster despite the presence of interband states. The asymmetry is also found for the Fano factor in Fig. 6.5c which is super-Poissonian for $\delta\tau \lesssim 0$, while for $\delta\tau > 0$ it converges to the Poissonian value $F = 1$. This indicates that the transport relates to topology.

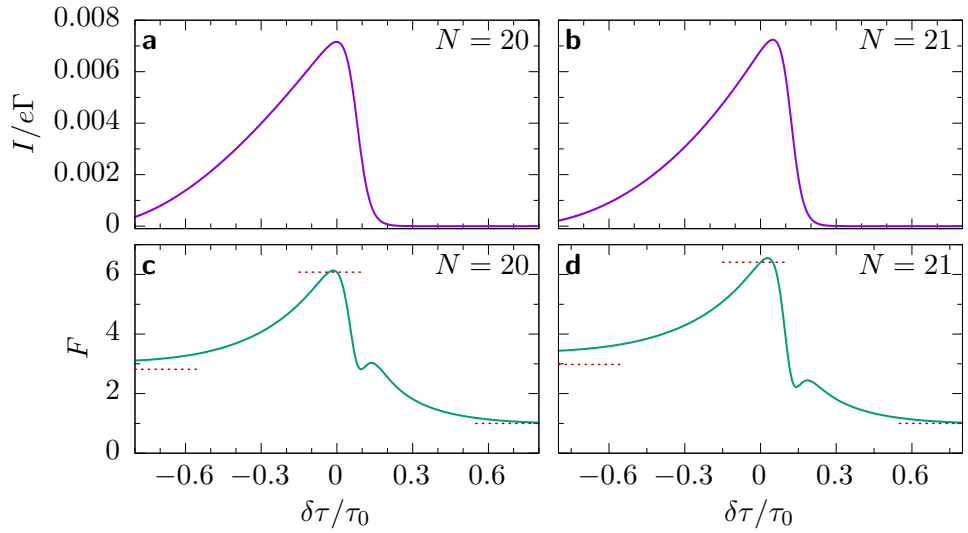

Figure 6.5: **a,b** Current and **c,d** Fano factor for an array of **a,c** $N = 20$ and **b,d** $N = 21$ sites as a function of the imbalance $\delta\tau/\tau_0$ and the lead couplings $\hbar\Gamma_\mathrm{L} = \hbar\Gamma_\mathrm{R} = \hbar\Gamma = 5\tau_0$. The dotted horizontal lines mark the analytically obtained limits. Despite the different single-particle spectra, the results for an even and odd number of sites are qualitatively the same.

6.3.1 Analytical limits

The current for the full model follows directly from the stationary solution of the master equation (6.14), i.e., from the Kernel of the Liouvillian $\mathcal{L}$. It can be computed analytically, which allows us to evaluate the expression for the current. We obtain

$$I_\mathrm{even} = \frac{e\Gamma_\mathrm{R}}{N + \frac{\Gamma_\mathrm{R}}{\Gamma_\mathrm{L}} + \frac{\hbar^2\Gamma_\mathrm{R}^2}{4\tau^2}\left[N - 2 + \left(\frac{\tau}{\tau'}\right)^N\right]}, \tag{6.15}$$

$$I_\mathrm{odd} = \frac{e\Gamma_\mathrm{R}}{\frac{\Gamma_\mathrm{R}}{\Gamma_\mathrm{L}} + \frac{\hbar^2\Gamma_\mathrm{R}^2(N-1)}{4\tau^2} + \left(\frac{\tau'}{\tau}\right)^2\left[N - 1 + \left(\frac{\tau}{\tau'}\right)^{N+1}\right]}. \tag{6.16}$$

Both expressions assume their maximum close to $\tau \approx \tau'$. For $\tau \gg \tau'$, i.e., in the region in which we find edge-state blockade, it decays $\propto (\tau'/\tau)^N$. In the opposite limit, $\tau \ll \tau'$, the decay is algebraic, $I \propto N^{-1}$. These behaviors are shown in Fig. 6.6. By contrast, computing the cumulants c_n with $n \geq 2$ requires not only the Kernel of the Liouvillian, but also its pseudoinverse or solutions of the non-homogeneous equations for X_n, which considerably complicates the analytical evaluation. To nevertheless find analytical results for the noise, below we develop a description with simplified master equations

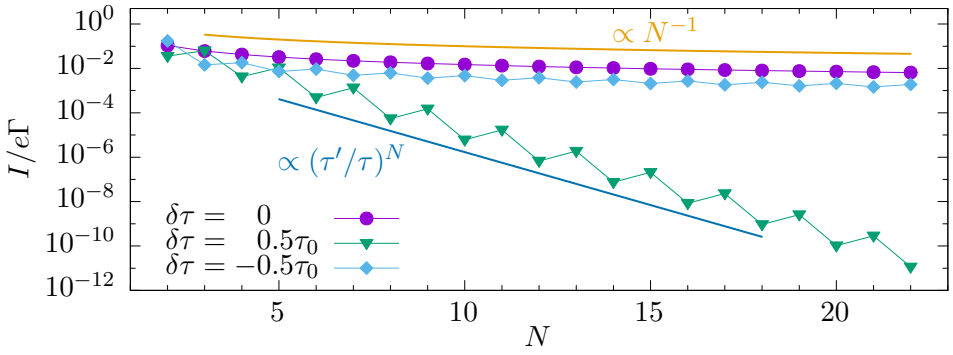

Figure 6.6: Stationary current as a function of the chain length for various values of $\delta\tau$. The dot-lead coupling is $\hbar\Gamma_\mathrm{R} = \hbar\Gamma_\mathrm{L} = \hbar\Gamma = 5\tau_0$.

for some limiting cases. For each region we find a dominating mechanism and capture it by a rate equation that provides analytical expressions for the current and the Fano factor which we then mark in Fig. 6.5.

6.3.1.1 Mutually exclusive channels

For the monomer chain realized at the transition point $\delta\tau = 0$ (for finite systems it is rather a crossover at $\delta\tau \approx \tau_0/N$ [156]), the eigenstates read $\phi_\ell(n) \propto \sin[\pi\ell n/(N+1)]$, where $\ell = 1, \ldots, N$, labels the solutions. We assume that each eigenstate forms a transport channel, where a strong Coulomb interaction leads to mutual exclusion of the channel occupation. The corresponding load and unload rates $\gamma_\ell^{L,R}$ are determined by the overlaps with the terminating sites, i.e., by $|\phi_\ell(1)|^2$ and $|\phi_\ell(N)|^2$. For a symmetric setup, $\gamma_\ell^L = \gamma_\ell^R \equiv \gamma_\ell$, states with $\ell \approx N/2$ are much stronger coupled to the leads than those with $\ell = 1$ or $\ell = N$ and, thus, most of the time, the strongly coupled states support a regular current. However, whenever a weakly coupled state becomes populated, an electron will remain there for the rather long time γ_ℓ^{-1} and thereby interrupt the transport process. Accordingly, we expect bunching as is indicated by a large Fano factor. A general model for transport via mutually exclusive channels ℓ that are weakly coupled to both leads with equal strength is sketched in Fig. 6.7a. It corresponds to the rate equation

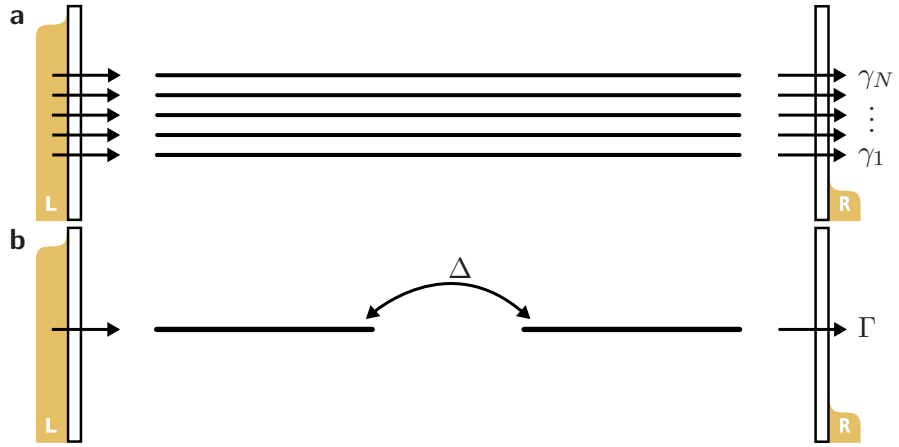

Figure 6.7: Sketch of the situations that we treat analytically with rate equations. **a** Mutually exclusive channels for the delocalized eigenstates of a monomer chain. The rates γ_ℓ reflect the overlap between the eigenstates and the first and the last site and obey $\sum_\ell \gamma_\ell = \Gamma$. **b** Two-state model for the edge states in the topological region. The intersite tunneling Δ is the exponentially small overlap between the edge states given in Eq. (6.7).

$$\dot{P} = \begin{pmatrix} -\Gamma & \gamma_1 & \dots & \gamma_N \\ \gamma_1 & -\gamma_1 & & 0 \\ \vdots & & \ddots & \vdots \\ \gamma_N & 0 & \dots & -\gamma_N \end{pmatrix} \begin{pmatrix} p_0 \\ p_1 \\ \vdots \\ p_N \end{pmatrix}, \tag{6.17}$$

where normalization is ensured by $\Gamma = \sum_\ell \gamma_\ell$. The rates γ_ℓ are determined by the overlap between the eigenstates ϕ_ℓ with the terminating sites. In a symmetric setup, the rates at the source and at the drain are equal, which is reflected by the symmetry of the matrix in Eq. (6.17). To be specific, for $\delta\tau = 0$ the eigenstates of the array are

$$\phi_\ell = \sqrt{\frac{2}{N+1}} \sin\Big(\frac{\pi \ell n}{N+1}\Big), \tag{6.18}$$

so that the rates become

$$\gamma_\ell = \frac{2\Gamma}{N+1} \sin^2\Big(\frac{\pi \ell}{N+1}\Big). \tag{6.19}$$

Then the stationary solution of Eq. (6.17) reads $P^\infty = (1, 1, ..., 1)^T/(N+1)$ and thus $I = e\Gamma/(N+1)$, which represents the weak coupling limit of Eq. (6.15). The second cumulant follows from evaluating the formal solution derived above

$$c_2 = c_1 + \frac{2\Gamma}{(N+1)^3}\left[\frac{\Gamma}{\tilde{\Gamma}} - N(N+1)\right], \tag{6.20}$$

where $\tilde{\Gamma}^{-1} = \sum_\ell \gamma_\ell^{-1}$ is dominated by the weakly coupled states owing to their small γ_ℓ. Inserting the rates and performing the iteration scheme also for the next two orders, we find

$$F_1 = \frac{N^2 - N + 3}{3\,(N+1)} = \frac{N-2}{3} + \mathcal{O}(N^{-1}) \equiv F_{\text{mono}}(N), \tag{6.21}$$

$$F_2 = \frac{N^2 - 5N + 8}{10} + \mathcal{O}(N^{-1}), \tag{6.22}$$

$$F_3 = \frac{4N^2 - 22N + 32}{21} + \mathcal{O}(N^{-1}). \tag{6.23}$$

Notice that all cumulant ratios grow with the length of the array as $F_n = c_{n+1}/c_n \propto N^2$. Since the effects are most noticeable in longer arrays, we ignore corrections of the order N^{-1}. Deep in the trivial region $\delta\tau < 0$, the central system consists of weakly coupled dimers. Then we can consider each dimer as one site and, thus, expect the behavior of a monomer array with $N/2$ sites. Therefore, without an explicit calculation, we can conclude that the Fano factor is $F = F_{\text{mono}}(N/2)$.

6.3.1.2 Two-site model

Finally, in the topological region $\delta\tau > 0$, the electrons mainly enter and leave the array via an edge state which is at zero energy. Since all other states are energetically far off, they merely mediate long-range tunneling with the exponentially small effective matrix element Δ given above. Then a proper simplified model is that of a two-level system with tunnel splitting Δ, as it is sketched in Fig. 6.7b. It can be captured by the master equation for the RDM $\rho = (|0\rangle\langle 0|, |L\rangle\langle L|, |R\rangle\langle R|, |L\rangle\langle R|, |R\rangle\langle L|)^T$ which reads

$$\dot{\rho} = \begin{pmatrix} -\Gamma_{\text{L}} & 0 & \Gamma_{\text{R}} & 0 & 0 \\ \Gamma_{\text{L}} & 0 & 0 & i\Delta/2 & -i\Delta/2 \\ 0 & 0 & -\Gamma_{\text{R}} & -i\Delta/2 & i\Delta/2 \\ 0 & i\Delta/2 & -i\Delta/2 & -\Gamma_{\text{R}}/2 & 0 \\ 0 & -i\Delta/2 & i\Delta/2 & 0 & -\Gamma_{\text{R}}/2 \end{pmatrix} \rho. \tag{6.24}$$

In the symmetric case $\Gamma_{\text{R}} = \Gamma_{\text{L}} = \Gamma$, the current and the Fano factor are

$$I = e\frac{\Gamma\Delta^2}{\Gamma^2 + 3\Delta^2}, \tag{6.25}$$

$$F = \frac{\Gamma^4 + 5\Delta^4 - 2\Gamma^2\Delta^2}{\left(\Gamma^2 + 3\Delta^2\right)^2}. \tag{6.26}$$

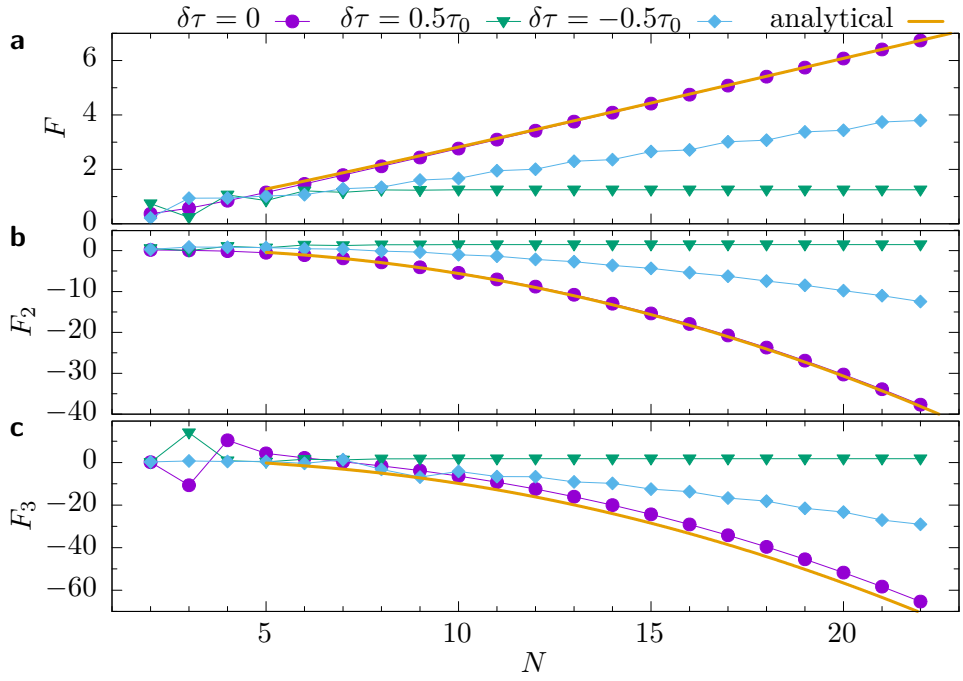

Figure 6.8: **a** Fano factor, **b** second cumulant ratio and **c** third cumulant ratio as a function of the chain length for various $\delta\tau$ and the lead coupling $\hbar\Gamma_{\mathrm{L}} = \hbar\Gamma_{\mathrm{R}} = \hbar\Gamma = 5\tau_0$.

In the limit $\Delta \ll \hbar\Gamma$, we expand the expressions for all cumulants to lowest order in Δ and find that all cumulants are equal to the current and therefore all cumulant ratios are one $F_n = 1$. This shows that the transport process is essentially Poissonian.

Since the separation of the Fano factors in the different regions grows with the length of the array, one may aim at an experimental realization with as many sites as possible. This, however, will raise the experimental difficulties drastically. Moreover, beyond a certain system size, the limit of a strong Coulomb blockade may no longer be realistic. Thus the length dependence of the Fano factors deserves a closer inspection. The data shown in Fig. 6.8a confirm our analytical results even down to rather small lengths. For an intermediate length $N \approx 10$, the Fano factors in the three regimes are already significantly different from each other. In particular, the differences are larger than the demonstrated resolution of mesoscopic noise measurements [176]. The data for cumulants of higher order presented in Figs. 6.8b,c support our conjecture of Poissonian transport in the topological phase.

The Fano factor of the full numerical calculation agrees rather well with the limits obtained analytically, see the horizontal lines in Fig. 6.5a. This provides evidence that the transport process in each region indeed follows the scenario sketched above.

6.3.2 Arrays with an odd number of sites

A further important observation is that the behavior of the shot noise for chains with an odd number of sites interpolates the behavior of dimer chains. In particular, we find that the current and the Fano factor as a function of $\delta\tau$ indeed are qualitatively the same as for even N as seen in Fig. 6.5b,d. For odd N, irrespective of the sign of $\delta\tau$, there always exists one edge state which has zero energy. Thus, the chain does not exhibit a transition between a topological and a nontopological phase. Nevertheless, the emergence of the edge state at one specific end of the chain can be explained in terms of the bulk-edge correspondence as follows. Let us consider a not too short chain with even N and $\delta\tau > 0$, such that the tunnel splitting $\Delta \sim \exp(-N\delta\tau/\tau_0)$ between the edge states is much smaller than the lead coupling Γ. Then decoherence will turn a possible superposition of both edge states into a mixture so that the edge state at the left lead will not be influenced by its counterpart at the drain. Then removing the last site of the chain will not have a major effect on the edge-state formation at the left lead. In this sense, also finite chains with odd N still exhibit some footprint of a topological transition that is found for infinite or semi-infinite dimer chains.

The common feature for even and for odd N is that only for $\delta\tau > 0$, does the chain possess an edge state at the left side. The relevance of its location at the source is visible in the behavior under inverting the applied bias: For even N, the chain is symmetric, so that only the direction of the current changes. Therefore, the Fano factor in Fig. 6.5c will remain the same. For odd N, by contrast, the inverted bias leads to a situation with an edge state at the drain but none at the source. Thus, bias inversion is equivalent to changing the sign of $\delta\tau$, which for odd N moves the edge state from one end of the chain to the other. Therefore, upon bias inversion, F in Fig. 6.5d becomes reflected at the y axis (not shown).

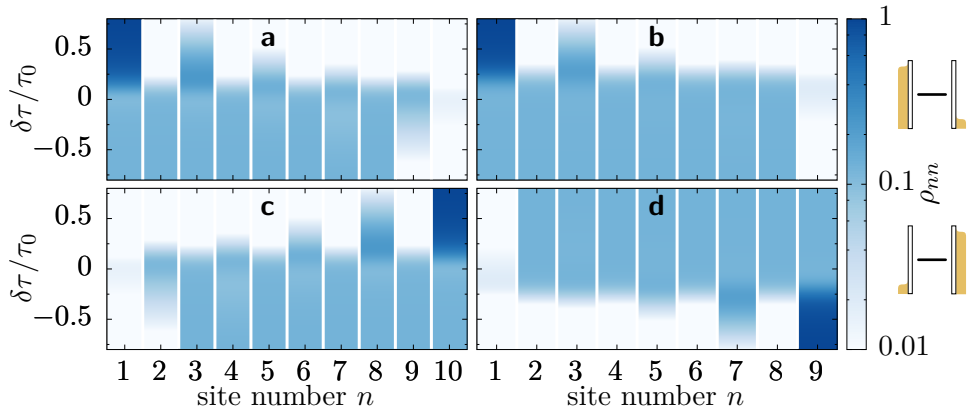

Figure 6.9: Population of the quantum dots in the stationary state for the array lengths **a,c** $N = 10$ and **b,d** $N = 9$ and the lead coupling $\hbar\Gamma_\mathrm{R} = \hbar\Gamma_\mathrm{L} = 5\tau_0$. The data in the lower row are with the source and drain interchanged, as indicated by the sketches at the right margin. They reveal that a current blockade emerges when the edge state at the left is strongly populated (dark blue areas). Comparing the upper row with the lower row highlights the reflection symmetry for even N, while for odd N the spatial reflection corresponds to inverting the sign of $\delta\tau$.

6.3.3 Blocking mechanism and localization

To underline the importance of the edge state and to develop a physical picture for the blockade, we consider the population of the sites in the stationary state of the open system in Fig. 6.9. For an even number of sites [Figs. 6.9a,c, where the latter is computed with interchanged bias direction], in the topological phase, $\delta\tau > 0$, the edge state at the source is predominantly populated. This is consistent with the scenario drawn above in which the transport occurs via weak long-range tunneling. Consequently, an electron becomes trapped in the edge state localized at the source, while once it is at the opposite side of the array, it leaves quickly to the drain.

For an odd number of sites, the behavior is similar. Outside the crossover region $|\delta\tau| \gg \tau_0$, one edge state always exists. For $\delta\tau > 0$, it is localized at site 1 and causes a current blockade. By contrast, for $\delta\tau < 0$, despite the emergence of an edge state at site N, an appreciable current flows.

To resolve this seeming contradiction, let us focus on an array with odd N and $\delta\tau < 0$ such that an edge state is formed at the drain. Nevertheless, a small overlap of the bulk states with the last site opens a way to circumvent the

edge state. Moreover, in rare cases in which an electron reaches the edge state, it will proceed quickly to the right lead, consequently, no relevant blockade occurs. For $\delta\tau > 0$, the edge state is located at the source and is mostly occupied, as seen in Fig. 6.9b. This situation results in topological blockade of the current arising from an interplay of edge-state formation at the source and the requirement of single occupation. The population for inverted bias direction is shown in Fig. 6.9d and confirms that the edge-state formation at the source is also decisive for trapping an electron when N is odd.

6.4 The driven SSH model

The exploration of topological phases in the SSH model requires a good experimental controllability of the inter- and intra-dimer hopping parameters. While this could be achieved via many gates the distance between two quantum dots has a natural effect on the wave function overlap of these dots and therefore also the hopping amplitude. This alone, however, does not allow the manipulation of the latter. Coupling the dimer chain to a time-dependent electric dipole field circumvents this problem and allows the perfect control of the topological phases via the driving parameters. Such an AC field affects the onsite energies of the QDs which oscillate in time with a position-dependent amplitude, see Fig. 6.10. This is described by the Hamiltonian of the driven chain

$$H(t) = H_{\mathrm{SSH}} + \hbar A \sum_{n=1}^{N} x_n d_n^\dagger d_n \cos(\omega t). \tag{6.27}$$

For convenience, we choose the origin in the middle of the chain such that

$$x_n = \begin{cases} -L/2 + (n-1)a/2 & \text{for } n \text{ odd} \\ -L/2 + (n-2)a/2 + b & \text{for } n \text{ even} \end{cases} \tag{6.28}$$

with the distances between two neighboring sites b and $a - b$, alternatively, which implies a unit cell of length a and a chain length $L = (N-2)a/2 + b$. The driving is determined by its frequency ω and amplitude $A = \Omega/L$ via the Rabi frequency Ω. We will mainly focus on chains with an even number of sites.

The time-dependent part of the Hamiltonian (6.27) consists of local terms $d_n^\dagger d_n$ which are invariant under the chiral transformation C. However, the sinusoidal driving allows us to obtain a minus sign via shifting the time by

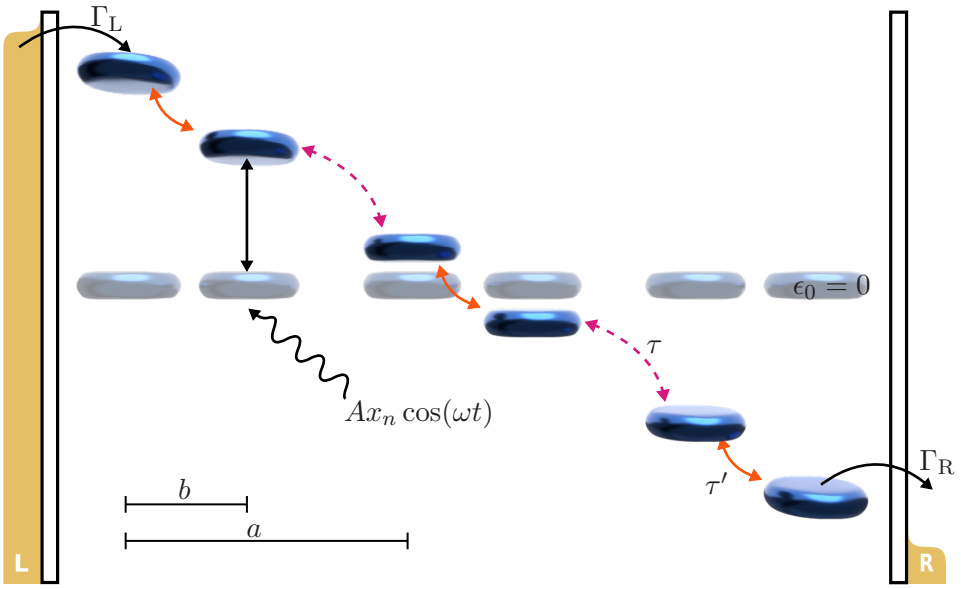

Figure 6.10: Dimer chain with intra- and inter-dimer tunnel coupling, τ' and τ respectively, connected to the leads with rates $\Gamma_{L/R}$. The applied external AC field generates an oscillation of the onsite energies with frequency ω which depends on the positions of the quantum dots, x_n, therefore the inter and intra dimer distances a and b, respectively, become relevant.

half a driving period, $t \to t + T/2$, where $T = 2\pi/\omega$. Formally, this can be expressed as

$$CH(t)C = -H(t + T/2). \tag{6.29}$$

We refer to this symmetry relation as "generalized chirality", owing to its resemblance to the generalized parity present in symmetric bistable potentials driven by a dipole force [157]. A consequence of the generalized chirality is that the propagator of the chain, $U(t, t')$, obeys the relation $U(t + T, t + T/2) = CU^{-1}(t + T/2, t)C$. Thus, the one-period propagator can be split in two symmetry-related parts, a fact that has been identified as a condition for non-trivial topological properties of a periodically driven system [177].

6.5 Transport in the high-frequency regime

The main energy scale of the SSH Hamiltonian (6.2) is the bandwidth τ_0. If it is much smaller than the energy quanta of the driving field, $\tau_0 \ll \hbar\omega$, one may employ a high-frequency approximation to derive an effective time-

independent Hamiltonian that captures the long-time-dynamics of the driven system. Including the the driving by means of the minimal coupling in the time-dependent Hamiltonian in momentum space

$$\hat{H}_k = \begin{pmatrix} 0 & \varrho(k) \\ \varrho(k)^* & 0 \end{pmatrix} \to \begin{pmatrix} 0 & \varrho(k,t) \\ \varrho(k,t)^* & 0 \end{pmatrix}, \tag{6.30}$$

with $\varrho(k) = \tau e^{ik(a-b)} + \tau' e^{-ikb} \to \varrho(k,t) = \tau e^{i(k+A\sin\omega t)(a-b)} + \tau' e^{-i(k+A\sin\omega t)b}$. For high frequencies this Hamiltonian is mainly given by its time averaged one. By using the definition of the zero-th order Bessel function of the first kind $J_0(x) = \int_0^T \exp(ix\sin t)\mathrm{d}t/T$ we find $\bar{\varrho}(k) = \int_0^T \varrho(k,t)\mathrm{d}t/T = \tau e^{ik(a-b)} J_0(A(a-b)/\omega) + \tau' e^{-ikb} J_0(Ab/\omega)$. This shows that in the high-frequency regime the driven SSH model becomes an effective static one with hopping parameters

$$\tau_{\mathrm{eff}}\boldsymbol{\prime} = J_0(Ab/\omega)\tau', \tag{6.31}$$

$$\tau_{\mathrm{eff}} = J_0(A(a-b)/\omega)\tau. \tag{6.32}$$

In a dimer chain driven by an external electric field, the intra- and inter-dimer spacings become relevant because they determine the dipole moments and, thus, appear in the renormalizations of the hopping amplitudes. In this way, the AC-driving offers a possibility for tuning system parameters. A classic example is the suppression of tunneling in bistable potentials [157, 158] and superlattices [159, 178] by the purely coherent influence of an AC field. For details of the calculation, see Gómez-León and Platero [164]. With these effective tunnel matrix elements, one can draw conclusions about the topological properties of the chain by a comparison with results for the time-independent SSH model [156, 171]. The main finding is a trivial topology for $\tau'_{\mathrm{eff}} > \tau_{\mathrm{eff}}$, while for $\tau'_{\mathrm{eff}} < \tau_{\mathrm{eff}}$ it becomes non-trivial with a Zak phase π. As a function of the driving parameters the Zak phase reads [164, 165]

$$Z = \pi\ \mathrm{sgn}\left[\tau^2 J_0^2(A(a-b)/\omega) - \tau'^2 J_0^2(Ab/\omega)\right]. \tag{6.33}$$

This Zak phase is shown in Fig. 6.13a. Similar influence of radiation on topology occurs also in higher dimensions [179–181]. The tunnel matrix elements (6.31) and (6.32) possess an interesting duality. By the replacement $(\delta\tau, b) \to (-\delta\tau, a-b)$, these matrix elements are interchanged. Then the topological properties are interchanged as well, while the bulk spectra remain the same. This motivated the choice of parameters used in Fig. 6.11.

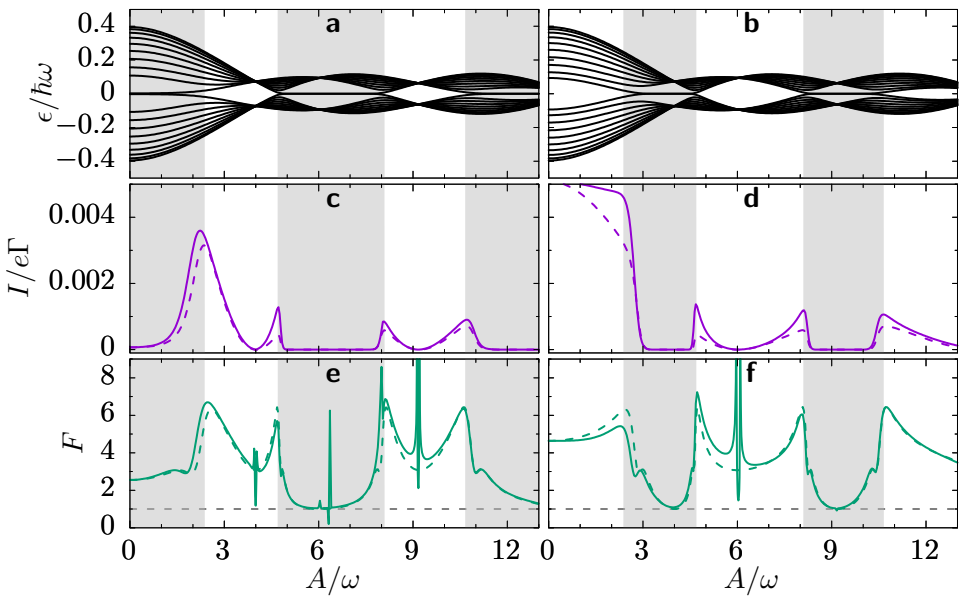

Figure 6.11: **a,b** Quasienergy spectrum as a function of the driving amplitude A for **a** $\delta\tau = 0.2\tau_0$, $b = 0.4a$ and **b** $\delta\tau = -0.2\tau_0$, $b = 0.6a$ for a chain with $N = 20$ sites. The parameters are chosen such that the bulk spectra in the thermodynamic limit are identical, while the topological properties depend on the sign of $\delta\tau$. Accordingly, we find edge-states at zero quasienergies in the regions marked by a grey background. **c,d** Time-averaged current. The dashed lines correspond to the high-frequency approximation result. The driving frequency is $\hbar\omega = 5\tau_0$, while the chain-lead coupling reads $\hbar\Gamma = 5\tau_0$. **e,f** Fano factor $F = |\bar{S}/e\bar{I}|$.

6.5.1 Current suppression and edge-state blockade

If the driving amplitude A is such that one of the Bessel functions in Eqs. (6.31) and (6.32) vanishes, the way from the electron source to the drain is practically interrupted, which significantly reduces the current. The data in Fig. 6.11 confirm this expectation and reveal a particular dependence on topology: It is best visible in a comparison of data for two parameter sets that are related by the transposition of inter- and intra-dimer coupling (left and right column, respectively, of this figure). Both choices lead to the same bulk properties, while the topological and the trivial regions are interchanged. This allows us to identify topological effects. The complementarity of the two cases is evident from the quasienergy spectra shown in Figs. 6.11a,b. Figures 6.11c,d show a remarkable dependence of the current suppression on the topology. In the

trivial region, the current is extensively reduced only when the effective inter dimer tunneling vanishes, i.e., for $\tau_{\text{eff}} \ll \tau_0$ ($A \approx 9\omega$ in Fig. 6.11a and $A \approx 6\omega$ in Fig. 6.11d). Close to the suppression, the current grows quadratically, such as for a driven double quantum dot [162]. By contrast, the current almost vanishes in the whole topological region, i.e., whenever the weaker condition $\tau'_{\text{eff}} < \tau_{\text{eff}}$ is fulfilled. Therefore, we can conclude that the physical origin of this current suppression is not a completely vanishing effective tunnel matrix element, but must be related to topology and the corresponding edge states formed at the source and at the drain. As compared to its counterpart in time-independent chains, this blockade is characterized by a broad region with vanishing current, while the suppression of current in the trivial region has a parabolic shape.

6.5.2 Shot noise and phase diagram

For less tunable static chains we have seen before that shot noise measurements are capable of characterising the topological properties of the SSH model. In particular, we found that the small current in the blockade regime obeys Poissonian statistics ($F \approx 1$), while the transport in the trivial regime is characterised by electron bunching. Figures 6.11e,f depict the shot noise for the driven case characterized by the Fano factor. It reveals a smeared crossover between Poissonian noise and super Poissonian values up to $F \approx 8$. The difficulty of performing an experiment on a chain with many sites raises the question about the necessary length to observe the edge state blockade. Thus we have calculated the Fano factor corresponding to the parameters in Fig. 6.11f for chains of different length. An advantage of using the external AC field to manipulate the topological phase is that the ideal Poissonian Fano factor $F \approx 1$ is always reached for a certain point in the blockade region, as shown in Fig. 6.12. This finding is in contrast to the static case, where $F \approx 1$ was found only in the limit of very long chains. However, Fig. 6.12 also shows that for a short chain the Fano factor also approaches unity at the suppression regions in the trivial regime, which does not allow distinguishing the this effect from the topological blockade. While in contrast to the static case, here the shape of the current suppression may be sufficient to identify edge-state blockade, it will turn out that the Fano factor exhibits clearer fingerprints of the topological phase diagram computed as by Gómez-León and Platero [164] and shown in Fig. 6.13a in terms of the Zak phase (6.33). The corresponding plot for the

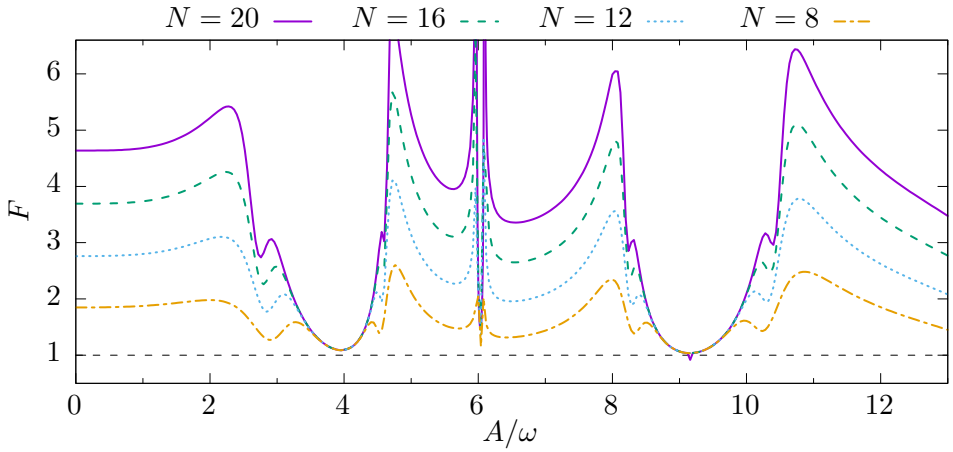

Figure 6.12: Fano factor as a function of the driving amplitude A for $\delta\tau = -0.2\tau_0$, $b = 0.6a$ for chains of various lengths. The driving frequency and the lead-chain coupling are $\hbar\omega = 5\tau_0$ and $\hbar\Gamma = 5\tau_0$, respectively.

current in Fig. 6.13b exhibits a richer structure stemming from the additional current suppressions in the trivial regions. Therefore the behavior of the current alone does not reflect the topological phase. The Fano factor in Fig. 6.13c, by contrast, provides clearer evidence, because $F \approx 1$ is found exclusively for non-trivial topology (black regions). We also find some additional structure in the trivial region as narrow lines at the trivial regions of zeros of the current. There, the Fano factor assumes even larger values which correspond to the sharp peaks in Figs. 6.11e,f. Thus, shot noise measurements represent an alternative to the direct observation of the Zak phase [175].

6.6 Robustness

The formation of edge states with exponentially small splitting is protected by sublattice or chiral symmetry present in our idealized SSH Hamiltonian (6.2). In a realistic experiment, however, it may be quite difficult to tune the system sufficiently well. Therefore, we check the robustness of the model against different types of perturbations.

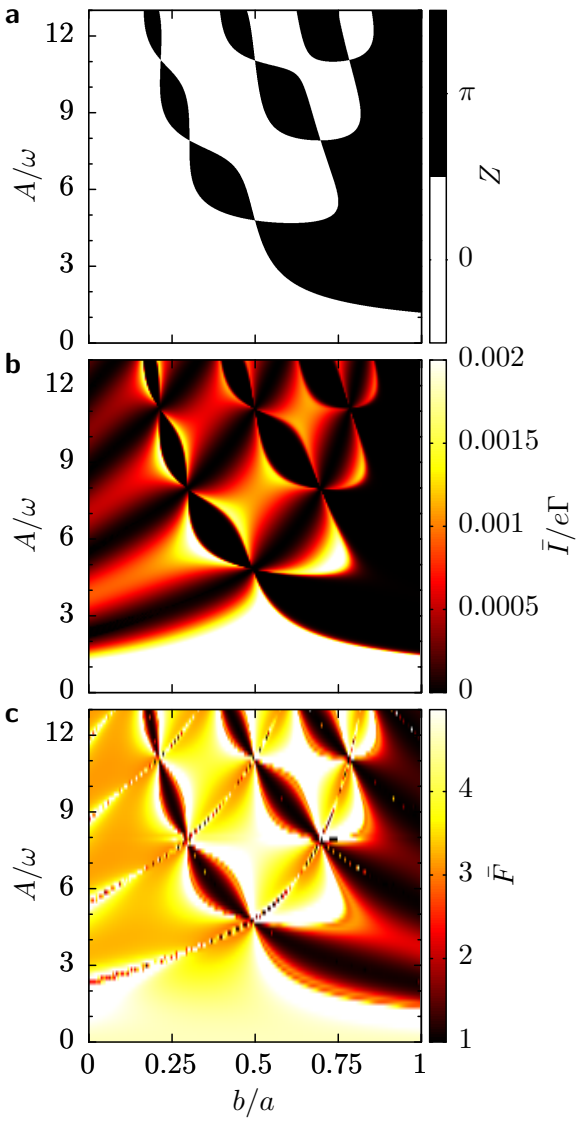

Figure 6.13: **a** Zak phase from Eq. (6.33) as a function of the intra dimer distance b and the driving amplitude A. Dark regions ($Z = \pi$) refer to a non-trivial topology, cf. the grey background in Fig. 6.11. All other parameters are as in the right column of Fig. 6.11. **b** Corresponding time-averaged current and **c** Fano factor.

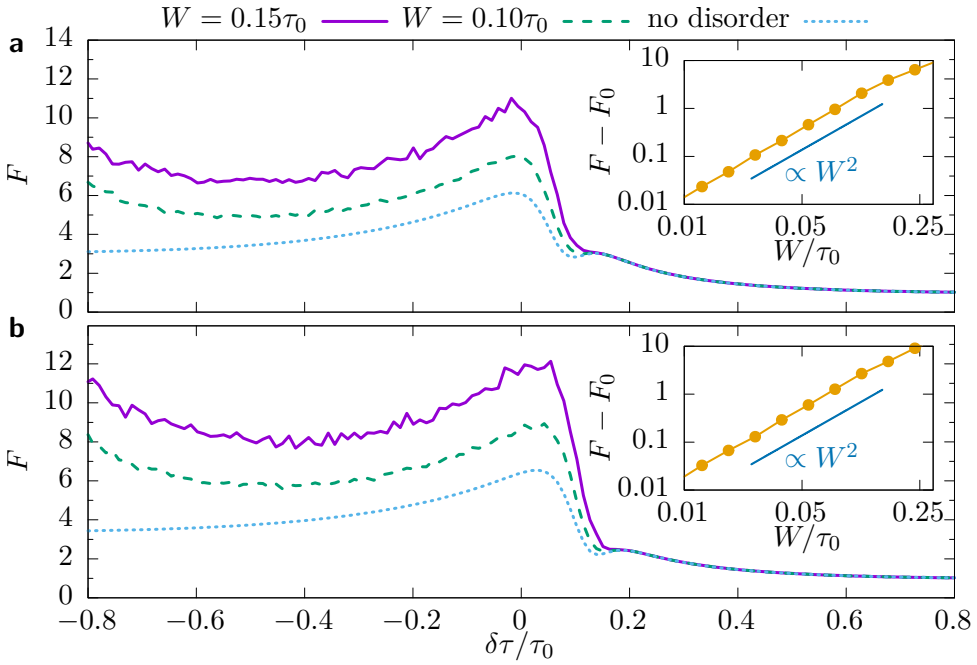

Figure 6.14: **a,b** Fano factor in the presence of disorder with strength W for a chain of lengths **a** $N = 20$ and **b** $N = 21$ with the parameters used in Fig. 6.11. Insets: Deviation of the averaged Fano factor from its value in the absence of disorder for $\delta\tau = -0.5\tau_0$.

6.6.1 Static disorder

To investigate the influence of imperfections, we consider disorder by adding random on-site energies to the static problem,

$$\hat{H}_{\mathrm{SSH}} \to \hat{H}_{\mathrm{SSH}} + W \sum_n \xi_n d_n^\dagger d_n, \tag{6.34}$$

where W is the disorder strength and ξ_n is taken from a normalized box distribution with $-1/2 \leq \xi_n \leq 1/2$. Figure 6.14 shows the resulting Fano factor which now is the ratio of the average noise and current. Comparing Figs. 6.14a,b, the behavior for an even and an odd number of sites again turns out to be practically the same. For $\delta\tau \lesssim 0$, we find that the Fano factor grows with increasing disorder. The enhancement is roughly $\propto W^2$, as can be appreciated in the inset. Notice that for larger values of W and much longer arrays, Anderson localization [182] becomes relevant and may change this behavior. For $\delta\tau > 0$, by contrast, disorder has almost no influence on the Fano factor. This finding is consistent with the physical picture drawn

above: The transport occurs via the two states localized at the ends of the array, while the other states are off-resonant and not populated. Since disorder even supports localization, the Poissonian behavior remains unaffected.

6.6.2 Quantum dissipation

Additionally we investigate the impact of a dynamic disorder stemming from the interaction of each site with a respective heat bath via the population operators $d_n^\dagger d_n$. For weak coupling, we use a simple description with a Lindblad operator [183] with equal coupling strengths and modify the Liouvillian according to

$$\mathcal{L} \to \mathcal{L} + \gamma \sum_n \mathcal{D}(d_n^\dagger d_n), \tag{6.35}$$

where $\mathcal{D}$ is the Lindblad operator defined after Eq. (6.14). Figs 6.15a,b depict how the current changes upon increasing the dissipation strength for two selected driving amplitudes. We focus on the two complementary parameter sets, used in Fig. 6.11, and select two particular driving amplitudes, one corresponding to trivial topology (solid lines), the other to non-trivial topology (dashed lines). For trivial topology, the current is rather insensitive to weak dissipation. The main reason for this is that in the trivial region, the transport occurs via the delocalized eigenstates of the chain while coherences between these states play a minor role. Accordingly, decoherence is not a relevant issue. For non-trivial topology, by contrast, the current grows with an increasing dissipation strength γ. A physical picture for this behavior is the direct transport between edge states. Since the splitting of the edge state doublet is exponentially small, the current is rather weak. Then dissipative transitions turn out to be rather beneficial for the electron transport. In contrast to the current, shot noise is affected by dissipation in the same way as can be appreciated in Figs. 6.15c,d. For both trivial and non-trivial topology, dissipation reduces the Fano factor which soon assumes value close to the Poissonian $F = 1$. This means that measuring the topological phase diagram via the Fano factor (see Fig. 6.13) will require samples with very good coherence properties such that $\gamma \lesssim 10^{-3}\tau_0$, a value that seems feasible with present quantum dot technology [42].

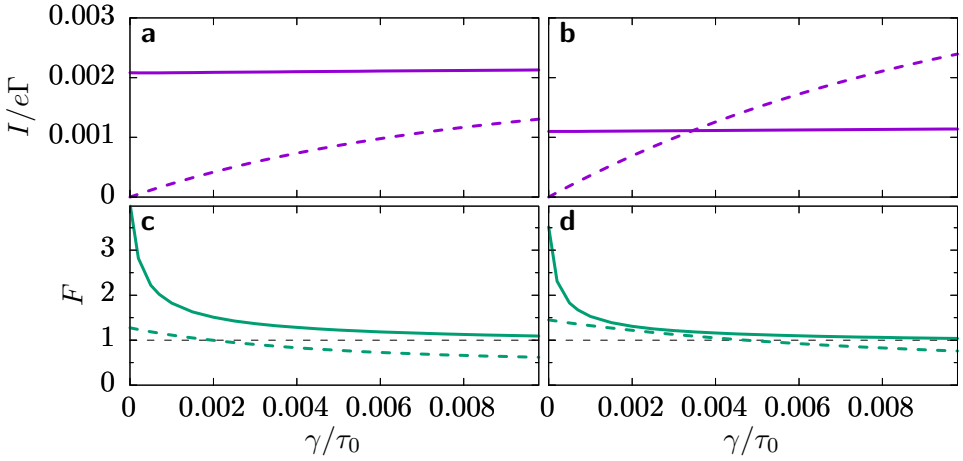

Figure 6.15: Influence of quantum dissipation. **a,b** Time-averaged currents as a function of the dissipation rate γ for the amplitudes $A = 3.5\omega$ and $A = 7\omega$. The left and right column corresponds to the respective column of Fig. 6.11, i.e., (**a**) $\delta\tau = 0.2\tau_0$ and $b = 0.4a$, while (**b**) correspond to the complementary case $\delta\tau = -0.2\tau_0$ and $b = 0.6a$. Solid lines mark topologically trivial cases, while dashed lines correspond to non-trivial topology. The driving frequency is $\hbar\omega = 5\tau_0$, while the chain-lead coupling reads $\hbar\Gamma = 5\tau_0$. **c,d** Corresponding Fano factors.

6.7 Conclusions

We have investigated a current blockade mechanism for a strongly biased contacted SSH model. It results from an interplay of single occupancy and edge-state formation which relates to a topological transition. Owing to their topological properties and the corresponding presence of edge states, such chains have potential applications in quantum information processing. The edge state at the left lead can trap an electron such that the resulting electron transport consists of rare long-distance tunneling events between a pair of edge states and exhibits a characteristic Poissonian behavior. By contrast, in the topologically trivial region, we find transport through delocalized states via many mutually exclusive channels and electron bunching with a super Poissonian shot noise. Since the edge state at the left lead turned out to be responsible, the effect can be observed also in chains with an odd number of sites in which a different but related transition occurs, namely, the displacement of the edge state from one end to the other. Clear experimental evidence for the transition between the different regions can be provided by shot noise

measurements. When driving the dimer chain with an AC field the topological properties can be controlled in a very flexible manner via driving frequency and amplitude. Within a high-frequency approximation, we have mapped the driven chain to an effective time-independent model whose tunnel matrix elements are dressed by Bessel functions. At the zeros of Bessel functions, the effective tunnel matrix elements and, thus, the current, vanish. As an interesting feature of driving-induced edge state blockade, not only the behavior of the Fano factor, but also the shape of the current suppressions depends on topology. Finally, map out the complete phase diagram of the driven SSH model. While we have demonstrated that the mechanisms on both sides of the transition are fairly insensitive to static disorder, a more realistic description of an implementation with molecular wires should consider also spin effects, vibrational degrees of freedom, and decoherence. Quantum dissipation, on the other hand, affects the noise properties strongly such that good, but achievable, samples are required.

The high tunability of the various types of quantum dots makes them natural candidates for the implementation of blockade effects in mesoscopic transport. For an experimental realization of our proposal, one may employ lateral quantum dots for which chains with seven dots have been realized [184]. While the nearest neighbor interaction is typically much larger than the inter-dot tunneling [13, 42], the magnitude of the long-range Coulomb repulsion is still to be determined. In general, the charging energy and the tunnel matrix elements are highly controllable by gate voltages. Thus it should be possible to tune them such that they meet the requirement of single occupancy, at least in not too long arrays. For double dots with an ac gating of a few GHz and amplitudes $A \lesssim 10\omega$, intra-dot excitations turned out to play a minor role [42]. A promising alternative are conducting polymers which are tunable by atomic force microscopy techniques [185] and, owing to their small size, possess a huge charging energy so that the one-electron regime should be easier to reach. Since this may also affect wire-lead tunneling rates, the visibility of the blockade in the Fano factor is a virtue since this quantity, in contrast to the current, depends only weakly on the wire-lead coupling.

CHAPTER 7

Dark states in a symmetric triple quantum dot

The interplay between Pauli principle and repulsive Coulomb interactions usually yields Poissonian and sub-Poissonian noise, corresponding to a Fano factor $F = 1$, and $F < 1$, respectively. For example, we have shown in Sec. 5.5.3 that in single quantum dot systems one finds Poissonian shot noise at Coulomb blockade with a chemical potential landscape as shown in Fig. 7.1a. Furthermore, sub-Poissonian noise with $1/2 < F < 1$, is found in the sequential transport regime [124, 186–190]. This is an indication that each tunneling barrier can be regarded as an independent source of Poissonian noise [191]. The enhancement of the shot noise, i.e. $F > 1$, requires a multilevel structure of the quantum dot [125, 191, 192] or complex multiple quantum dot devices [193–196] like in chapter 6. Independent of the details of the nanosystems, super-Poissonian noise implies the presence of slow and fast channels, and mechanisms which occasionally allow for charge transfer on a time scale much shorter than the average residence time in the slow channel state, see e.g. Figs. 7.1b,c. As shown in Sec. 5.5.2, these models have super-Poissonian noise which is a signature of fermionic bunching and in turn of subtle quantum correlations.

In chapter 4 we found dark states (DSs) in a carbon nanotube (CNT)-QD, based on the presence of a symmetry of the system yielding degenerate energy states and non-diagonal tunneling matrices in the basis associated to this symmetry. These DSs act as a slow channel and therefore are expected

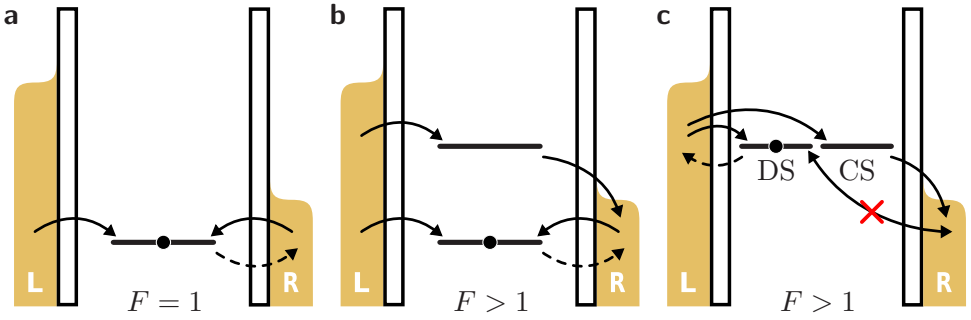

Figure 7.1: Chemical potential landscape models. **a** Single resonant level in Coulomb blockade regime with Fano factor $F = 1$. **b** If an excited state is present in the bias window of a Coulomb blockaded quantum dot, electron bunching through the excited state yields super-Possonian noise ($F > 1$). **c** Interference of degenerate orbitals gives rise to coupled (CS), and dark (DS) states, and in turn to super-Poissonian noise. Solid arrows show fast processes, dashed ones the dominant slow processes.

to support interesting noise properties. To additionally study the influence of interactions on the shot noise, we analyze in this chapter the smallest system that possesses DSs and allows to treat interactions exactly: a C_{3v} symmetric triangular triple quantum dot (TQD), as sketched in Fig. 7.2. We investigate the Fano stability diagram of this TQD, as a function of its occupation. The interplay of statistics, Coulomb interactions and geometry allows one the study of peculiar many-body effects such as super-exchange induced triplet-singlet transition [197], many-body interference [105, 106, 195], cellular automata phenomena [198], charge frustration [199–201], or channel blockade [202]. Indeed, a gated TQD features all the three dynamical situations sketched in Fig. 7.1. TQDs have been recently realized in lateral semiconducting heterostrucures [198, 199, 202, 203], which are tunable down to the few electron regime by means of plunger and depletion gates [203], and by means of atomic STM manipulation [204]. In the latter experiment, orbital degeneracy in a C_{3v} symmetric triangular dot could be demonstrated. So far, investigations of transport noise have been restricted to set-ups in which the C_{3v} symmetry of an isolated TQD is broken in various ways, e.g. by assuming unequal interdot hoppings and/or onsite energies [194, 195, 205–207]. These asymmetries remove orbital degeneracies and hence the possibility to observe current suppression due to the destructive orbital interference [208]. We show that the Fano map of a C_{3v} symmetric, weakly coupled TQD is characterized by regions of

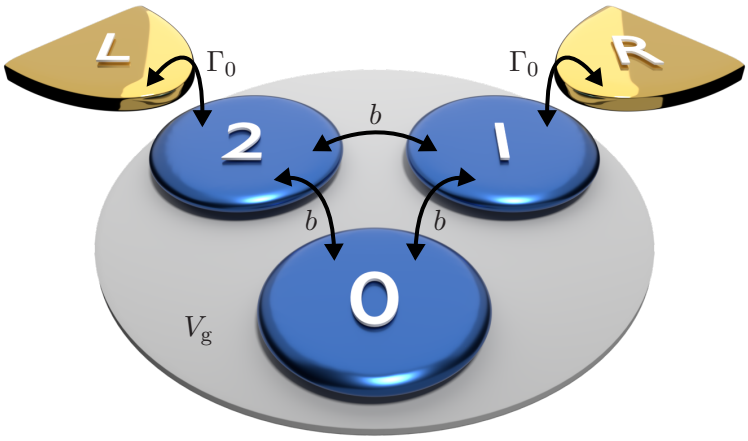

Figure 7.2: Model of a gated triangular triple quantum dot (TQD) with tunneling rates Γ_0 and inter-dot hopping b.

super-Poissonian noise outside the Coulomb blockade region, see Fig. 7.1c, with specific fractional values of the Fano factor being a signature of such many-body interference. By exploting an analytical solution for the TQD spectrum, the explicit form of the DSs is provided, including the most complex situation of half-filling. This is possible since we obtain the complete many-body spectrum analytically. Interestingly, the form of the DSs resembles the one found in chapter 4. The Lamb shift contributions lift the otherwise perfect blockade from the DSs and creates a smooth negative differential conductance behavior. We study this influence at an example transition using a minimal model.

Most content of this chapter was published in Niklas *et al.* [P.5].

7.1 Model and spectrum

The TQD spectrum derives from a three-site Hamiltonian with hopping $b < 0$, onsite Coulomb repulsion U and inter-site repulsion V,

$$\begin{aligned}\hat{H}_{\mathrm{TQD}} = \xi \sum_{i\sigma} n_{i\sigma} + b \sum_{i\neq j,\sigma} d^\dagger_{j\sigma} d_{i\sigma} + U \sum_i \left(n_{i\uparrow} - \frac{1}{2}\right)\left(n_{i\downarrow} - \frac{1}{2}\right) \\ + V \sum_{i<j} \left(n_i - 1\right)\left(n_j - 1\right), \end{aligned} \tag{7.1}$$

where $\xi = \varepsilon + \alpha_g V_g$ includes the onsite energy ε and the effects of an applied gate voltage V_g with level arm α_g. To not break the C_{3v} symmetry, the gate voltage is applied identical to all three QDs. Here, operators $d^\dagger_{i\sigma}$ and $d_{i\sigma}$

create and annihilate an electron with spin projection σ in dot $i = 0, 1, 2$, and $n_i = \sum_\sigma n_{i\sigma}$, $n_{i\sigma} = d^\dagger_{i\sigma} d_{i\sigma}$, cf. Fig. 7.2. The tunneling between the TQD and the leads is described by $\hat{H}_{\rm tun} = \sum_{lk\sigma i} t_{li} d^\dagger_{i\sigma} c_{lk\sigma} + {\rm h.c.}$. The single orbital approximation yields a realistic description of lateral TQD devices [198, 199, 202, 203] as long as $eV_{\rm b}$ and $eV_{\rm g}$ are of the order of the hopping parameter b [209]. In the following, we consider equal coupling to the left and right leads, and set $t_{L2} = t_{R1} = t$ and otherwise $t_{li} = 0$. We identify for later convenience ${\rm R} = 1$ and ${\rm L} = 2$, such that $d_{{\rm R}\sigma} = d_{1\sigma}$, $d_{{\rm L}\sigma} = d_{2\sigma}$. The single particle part of the TQD Hamiltonian in Eq. (7.1) is diagonalized in the basis of the angular momentum states

$$|\ell_z\rangle = \frac{1}{\sqrt{3}} \sum_{j=0}^{2} e^{-ij\ell_z 2\pi/3} |j\rangle, \tag{7.2}$$

where $\{\ell_z = 0, \pm 1\}$. This allows us to write the tunneling Hamiltonian in the single particle eigenbasis $\hat{H}_{\rm tun} = t \sum_{lk\sigma\ell_z} e^{-il\ell_z 2\pi/3} d^\dagger_{\ell_z\sigma} c_{lk\sigma} + {\rm h.c.}$. For comparison we construct the single particle rate matrix in both, position basis $i \in \{0, 1, 2\}$ and angular momentum basis $\ell_z \in \{0, +1, -1\}$, where it reads

$$\mathbf{\Gamma}_l = \Gamma_l \begin{pmatrix} 0 & 0 & 0 \\ 0 & \delta_{l{\rm R}} & 0 \\ 0 & 0 & \delta_{l{\rm L}} \end{pmatrix}_i = \Gamma_l \begin{pmatrix} 1 & e^{il2\pi/3} & e^{-il2\pi/3} \\ e^{-il2\pi/3} & 1 & e^{il2\pi/3} \\ e^{il2\pi/3} & e^{-il2\pi/3} & 1 \end{pmatrix}_{\ell_z}. \tag{7.3}$$

Here $\Gamma_l = 2\pi |t|^2 g_l/\hbar$ is the bare tunneling rate for lead l, proportional to the density of states at the Fermi energy g_l. In the following we assume identical leads, such that $\Gamma_{\rm L} = \Gamma_{\rm R} = \Gamma_0$, see Fig. 7.2.

Accounting for the spin degree of freedom σ, in the following we use this single particle basis to construct many-body states in the occupation number representation, where a generic vector $|n_{0\uparrow}, n_{1\uparrow}, n_{-1\uparrow}; n_{0\downarrow}, n_{1\downarrow}, n_{-1\downarrow}\rangle$ is fully characterized by the occupation numbers $n_{\ell_z\sigma}$. Finally, we use this many-body basis to diagonalize the TQD Hamiltonian and find its eigenvalues and eigenstates. Several symmetries have been exploited in the analytical diagonalization: $\hat{H}_{\rm TQD}$ commutes in fact with the total particle number operator $N = \sum_{\ell_z\sigma} n_{\ell_z\sigma}$, the total spin operator $S^2 = \sum_{i\ell_z\sigma\sigma'} (d^\dagger_{\ell_z\sigma} s^i_{\sigma\sigma'} d_{\ell_z\sigma'})^2$ (here is $s^i = \hbar\sigma^i/2$ and σ^i the i-th Pauli matrix), the spin projection $S_z = \hbar \sum_{\ell_z\sigma} \sigma n_{\ell_z\sigma}/2$, and the angular momentum operator $L_z = \hbar \sum_{\ell_z\sigma} \ell_z n_{\ell_z\sigma}|_{\rm mod\ 3}$ [105]. By ordering the many-body states according to the quantum numbers N, S, S_z and L_z associated to these operators, we could reduce the Hamiltonian into a block diagonal form

with blocks of maximal size 3×3, and then complete the diagonalization. For convenience we set $\hbar = 1$ in the quantum numbers. The set of quantum numbers listed above together with the energy E_{N_i}, of the i–th excited state with N electrons, fully characterize the eigenvectors of the interacting TQD Hamiltonian, a crucial knowledge for the forthcoming analysis. In the following we use the notation $|N, E; S, S_z, L_z\rangle$ or $|N, \alpha_i, L_z\rangle$, with $\alpha_i = \{E_{N_i}; S, S_z\}$, for a generic eigenvector. In particular, $S^2|N, E; S, S_z, L_z\rangle = \hbar^2 S(S+1)|N, E; S, S_z, L_z\rangle$ and, as usual, $-S \leq S_z \leq S$. All eigenvectors and the associated eigenenergies in the occupation number basis of the TQD Hamiltonian Eq. (7.1) are reported in Tables 7.1, 7.2 and 7.3. For simplicity the eigenenergies are presented without the term $N\xi$. Note that the energetic order of the states depends on the system parameters. We choose the ones we will use throughout this chapter $U = 5|b|$, $V = 2|b|$ and $b < 0$.

We notice that a classification of many-body states using the angular momentum quantum number L_z has been proposed by Kostyrko and Bułka [105] for the case of a symmetric triangular dot with intra-site repulsion only (i.e. $U \neq 0$, $V = 0$). Our analysis with $U \neq 0$, $V \neq 0$ thus generalizes that work and recovers the results reported by Korkusinski *et al.* [197], where a localized representation is used to discuss topological Hund rules and derive effective low energy spin Hamiltonians. For finite on-site and inter-site interactions U and V, the composition of the eigenstates is the result of a complex interplay between Pauli statistics and Coulomb repulsion, and we refer to the review by Hsieh *et al.* [209] for useful insights. For example, for double occupancy of the TQD, the configurations with $S = 1$ correspond to excited states with singly occupied dots, due to Pauli principle. The configurations with $S = 0$, however, contain both doubly occupied and singly occupied dots, with weight determined by the difference $U - V$. For $U = V$, the groundstate is in the occupation number representation the singlet $|100, 100\rangle$, with equal weights on single and doubly occupied sites, as seen in Table 7.1. The splitting between the sextuplet of excited states and the groundstate singlet is dominated by the hopping energy with a correction given by super-exchange processes due to the doubly occupied singlet configurations [197]. For a TQD with occupancy $N = 4$ (i.e. with two-holes), the ground state is always a triplet if $b < 0$, as in our work. Finally, of relevance for the discussion in the main part of the manuscript, the 3–particles and 5–particles ground states are a quadruplet due to orbital and spin degeneracy, while the associated first excited states are

N	Eigenenergy	S	S_z	L_z	Eigenstate
0	0	0	0	0	$\|000,000\rangle$
1	$-\frac{U}{2}-2V+2b$	$\frac{1}{2}$	$-\frac{1}{2}$	0	$\|000,100\rangle$
			$\frac{1}{2}$		$\|100,000\rangle$
	$-\frac{U}{2}-2V-b$	$\frac{1}{2}$	$-\frac{1}{2}$	-1	$\|000,001\rangle$
				1	$\|000,010\rangle$
			$\frac{1}{2}$	-1	$\|001,000\rangle$
				1	$\|010,000\rangle$
2	$-U-3V+b$ $+\frac{U-V}{2}-s_{-2}$	0	0	0	$\sin\phi_{-2}\left(\|010,001\rangle+\|001,010\rangle\right)/\sqrt{2}$ $-\cos\phi_{-2}\|100,100\rangle$
	$-U-3V+b$	1	-1	-1	$\|000,101\rangle$
				1	$\|000,110\rangle$
			0	-1	$\left(\|100,001\rangle-\|001,100\rangle\right)/\sqrt{2}$
				1	$\left(\|100,010\rangle-\|010,100\rangle\right)/\sqrt{2}$
			1	-1	$\|101,000\rangle$
				1	$\|110,000\rangle$
	$-U-3V-\frac{b}{2}$ $+\frac{U-V}{2}-s_1$	0	0	-1	$\sin\phi_1\left(\|100,001\rangle+\|001,100\rangle\right)/\sqrt{2}$ $-\cos\phi_1\|010,010\rangle$
				1	$\sin\phi_1\left(\|100,010\rangle+\|010,100\rangle\right)/\sqrt{2}$ $-\cos\phi_1\|001,001\rangle$
	$-U-3V-2b$	1	-1	0	$\|000,011\rangle$
			0		$\left(\|010,001\rangle-\|001,010\rangle\right)/\sqrt{2}$
			1		$\|011,000\rangle$
	$-U-3V-\frac{b}{2}$ $+\frac{U-V}{2}+s_1$	0	0	-1	$\cos\phi_1\left(\|100,001\rangle+\|001,100\rangle\right)/\sqrt{2}$ $+\sin\phi_1\|010,010\rangle$
				1	$\cos\phi_1\left(\|100,010\rangle+\|010,100\rangle\right)/\sqrt{2}$ $+\sin\phi_1\|001,001\rangle$
	$b-U-3V$ $+\frac{U-V}{2}+s_{-2}$	0	0	0	$\cos\phi_{-2}\left(\|010,001\rangle+\|001,010\rangle\right)/\sqrt{2}$ $+\sin\phi_{-2}\|100,100\rangle$

Table 7.1: Eigenenergies and eigenstates of a symmetric TQD. The ordering of the eigenergies depends on the TQD parameters b, U and V. We chose $U=5|b|$, $V=2|b|$ and $b<0$. We have defined $s_x=\sqrt{9x^2b^2+xb/2\,(U-V)+(U-V)^2}$ and $\phi_x=\arctan\left(2\sqrt{2}(U-V)/(U-V+9xb)\right)/2$.

N	Eigenenergy	S	S_z	L_z	Eigenstate
3	$-\frac{3}{2}U-3V+\epsilon_0$	$\frac{1}{2}$	$-\frac{1}{2}$	-1	$v_{0,1}\left\|100,101\right\rangle - v_{0,0}\left\|010,110\right\rangle - v_{0,-1}\left\|001,011\right\rangle$
				1	$v_{0,1}\left\|100,110\right\rangle + v_{0,0}\left\|001,101\right\rangle - v_{0,-1}\left\|010,011\right\rangle$
			$\frac{1}{2}$	-1	$v_{0,1}\left\|101,100\right\rangle - v_{0,0}\left\|110,010\right\rangle - v_{0,-1}\left\|011,001\right\rangle$
				1	$v_{0,1}\left\|110,100\right\rangle - v_{0,0}\left\|101,001\right\rangle + v_{0,-1}\left\|011,010\right\rangle$
	$-\frac{3}{2}U-3V$	$\frac{3}{2}$	$-\frac{3}{2}$	0	$\left\|000,111\right\rangle$
			$-\frac{1}{2}$		$\left(\left\|001,110\right\rangle - \left\|010,101\right\rangle + \left\|100,011\right\rangle\right)/\sqrt{3}$
			$\frac{1}{2}$		$\left(\left\|011,100\right\rangle - \left\|101,010\right\rangle + \left\|110,001\right\rangle\right)/\sqrt{3}$
			$\frac{3}{2}$		$\left\|111,000\right\rangle$
	$-\frac{3}{2}U-3V+\epsilon_1$	$\frac{1}{2}$	$-\frac{1}{2}$	-1	$v_{1,1}\left\|110,100\right\rangle - v_{1,0}\left\|101,001\right\rangle + v_{1,-1}\left\|011,010\right\rangle$
				1	$v_{1,1}\left\|100,110\right\rangle + v_{1,0}\left\|001,101\right\rangle - v_{1,-1}\left\|010,011\right\rangle$
			$\frac{1}{2}$	-1	$v_{1,1}\left\|101,100\right\rangle - v_{1,0}\left\|110,010\right\rangle - v_{1,-1}\left\|011,001\right\rangle$
				1	$v_{1,1}\left\|100,101\right\rangle - v_{1,0}\left\|010,110\right\rangle - v_{1,-1}\left\|001,011\right\rangle$
	$-\frac{3}{2}U-3V+(U-V)$	$\frac{1}{2}$	$-\frac{1}{2}$	0	$\left(\left\|001,110\right\rangle - \left\|100,011\right\rangle\right)/\sqrt{2}$
					$\left(\left\|001,110\right\rangle + 2\left\|010,101\right\rangle + \left\|100,011\right\rangle\right)/\sqrt{6}$
			$\frac{1}{2}$		$\left(\left\|110,001\right\rangle + 2\left\|101,010\right\rangle + \left\|011,100\right\rangle\right)/\sqrt{6}$
					$\left(\left\|110,001\right\rangle - \left\|011,100\right\rangle\right)/\sqrt{2}$
	$-\frac{3}{2}U-3V+\epsilon_{-1}$	$\frac{1}{2}$	$-\frac{1}{2}$	-1	$v_{-1,1}\left\|100,101\right\rangle - v_{-1,0}\left\|010,110\right\rangle - v_{-1,-1}\left\|001,011\right\rangle$
				1	$v_{-1,1}\left\|100,110\right\rangle + v_{-1,0}\left\|001,101\right\rangle - v_{-1,-1}\left\|010,011\right\rangle$
			$\frac{1}{2}$	-1	$v_{-1,1}\left\|101,100\right\rangle - v_{-1,0}\left\|110,010\right\rangle - v_{-1,-1}\left\|011,001\right\rangle$
				1	$v_{-1,1}\left\|110,100\right\rangle - v_{-1,0}\left\|101,001\right\rangle + v_{-1,-1}\left\|011,010\right\rangle$

Table 7.2: Eigenenergies and eigenstates of a symmetric TQD for occupation number $N = 3$. We have defined $a = (U-V)/(9b)$, $\theta = \arccos\left(\left[(3a^2)/(1+3a^2)\right]^{\frac{3}{2}}\right)/3$, $\lambda_\alpha = 2\sqrt{(1+a^2)/3}\cos\left(\theta+\alpha\frac{2\pi}{3}\right)$, $\epsilon_\alpha = 2(U-V)[1-\lambda_\alpha/2|a|)]/3$ and $v_{x,y} = (a-\lambda_x)|(a-\lambda_x)^2-1|/(a-\lambda_x-y)\sqrt{3(a-\lambda_x)^4+1}$.

N	Eigenenergy	S	S_z	L_z	Eigenstate
4	$+2b-U-3V$	1	-1	0	$\|100,111\rangle$
			0		$\left(\|101,110\rangle-\|110,101\rangle\right)/\sqrt{2}$
			1		$\|111,100\rangle$
	$-U-3V+\frac{b}{2}$ $+\frac{U-V}{2}-s_{-1}$	0	0	-1	$\sin\phi_{-1}\left(\|011,101\rangle+\|101,011\rangle\right)/\sqrt{2}$ $+\cos\phi_{-1}\|110,110\rangle$
				1	$\sin\phi_{-1}\left(\|011,110\rangle+\|110,011\rangle\right)/\sqrt{2}$ $-\cos\phi_{-1}\|101,101\rangle$
	$-U-3V-b$ $+\frac{U-V}{2}-s_2$	0	0	0	$\sin\phi_2\left(\|101,110\rangle+\|110,101\rangle\right)/\sqrt{2}$ $+\cos\phi_2\|011,011\rangle$
	$-U-3V-b$	1	-1	-1	$\|001,111\rangle$
				1	$\|010,111\rangle$
			0	-1	$\left(\|011,101\rangle-\|101,011\rangle\right)/\sqrt{2}$
				1	$\left(\|011,110\rangle-\|110,011\rangle\right)/\sqrt{2}$
			1	-1	$\|111,001\rangle$
				1	$\|111,010\rangle$
	$-U-3V+\frac{b}{2}$ $+\frac{U-V}{2}+s_{-1}$	0	0	-1	$\cos\phi_{-1}\left(\|011,101\rangle+\|101,011\rangle\right)/\sqrt{2}$ $-\sin\phi_{-1}\|110,110\rangle$
				1	$\cos\phi_{-1}\left(\|011,110\rangle+\|110,011\rangle\right)/\sqrt{2}$ $+\sin\phi_{-1}\|101,101\rangle$
	$-U-3V-b$ $+\frac{U-V}{2}+s_2$	0	0	0	$\cos\phi_2\left(\|101,110\rangle+\|110,101\rangle\right)/\sqrt{2}$ $-\sin\phi_2\|011,011\rangle$
5	$-\frac{U}{2}-2V+b$	$\frac{1}{2}$	$-\frac{1}{2}$	-1	$\|101,111\rangle$
				1	$\|110,111\rangle$
			$\frac{1}{2}$	-1	$\|111,101\rangle$
				1	$\|111,110\rangle$
	$-\frac{U}{2}-2V-2b$	$\frac{1}{2}$	$-\frac{1}{2}$	0	$\|011,111\rangle$
			$\frac{1}{2}$		$\|111,011\rangle$
6	0	0	0	0	$\|111,111\rangle$

Table 7.3: Eigenenergies and eigenstates of a symmetric TQD for electron numbers $N=4$–6. We have defined $s_x=\sqrt{9x^2b^2+xb/2\,(U-V)+(U-V)^2}$ and $\phi_x=\arctan\left(2\sqrt{2}(U-V)/(U-V+9xb)\right)/2$.

only spin degenerate.

The C_{3v} group of the TQD comprises also three reflection planes perpendicular to the system. In particular, we introduce the reflection operator σ_{v0} such that $\sigma_{v0} d^\dagger_{1\sigma} \sigma_{v0} = d^\dagger_{2\sigma}$ and $\sigma_{v0} d^\dagger_{0\sigma} \sigma_{v0} = d^\dagger_{0\sigma}$. The overall phase of the eigenstates is taken in such a way that $\sigma_{v0}|N, \alpha_i, 1\rangle = |N, \alpha_i, -1\rangle$.

7.2 Current and Fano maps

To compute the current and shot noise we use our master equation approach for the sequential tunneling limit in secular approximation from Eq. (2.38)

$$\mathcal{L}\rho^\infty = -\frac{i}{\hbar}\left[H_{\rm TQD} + H_{\rm LS}, \rho^\infty\right] + \mathcal{L}_t \rho^\infty = 0, \tag{7.4}$$

where $\mathcal{L}_t$ is the tunneling part of the Liouvillian. The Lamb shift Hamiltonian [106, 210] $H_{\rm LS}$ generates a precession dynamics within orbitally degenerate subspaces. Its explicit form is given in Sec. 7.4. The operatorial form of Eq. (7.4) fully accounts for interference effects captured in the off-diagonal elements of ρ^∞. The shot noise and ultimately the Fano factor are calculated using the iterative scheme from Eqs. (5.15) and (5.16). The stationary current is shown as a function of bias and gate voltage in Fig. 7.3a. For comparison, the same parameters as in the work by Donarini *et al.* [208] were used. Notice that the closed geometry of the TQD breaks the particle-hole symmetry otherwise present in linear triple dots [197]. The stability diagram displays Coulomb diamonds inside which current is exponentially suppressed (in second order in $H_{\rm tun}$) due to Coulomb blockade, but also regions outside the Coulomb diamonds with suppression due to orbital interference [106]. Coulomb diamonds are indicated with dotted lines when no longer visible due to the additional interference blockade. A measurement of the current alone, however, does not enable one to tackle down the different blockade mechanisms. In contrast, the Fano map, shown in Fig. 7.3b, displays a much richer structure than the current. In Fig. 7.3c we show the Fano factor F_{nv}, which is obtained by neglecting the Lamb shift term $H_{\rm LS}$ in Eq. (7.4). Clearly, the virtual transitions responsible for the Lamb shifts *blur* the otherwise poligonal Fano pattern.

At first glance one can observe a sub-Poissonian shot noise $1/2 < F < 1$ in the transport regime and both Poissonian, $F = 1$, and super-Poissonian, $F > 1$, shot noise in the regions of vanishing current. Furthermore, F diverges when $V_{\rm b} \to 0$ due to Johnson-Nyquist noise. Finally, vertical steps in the

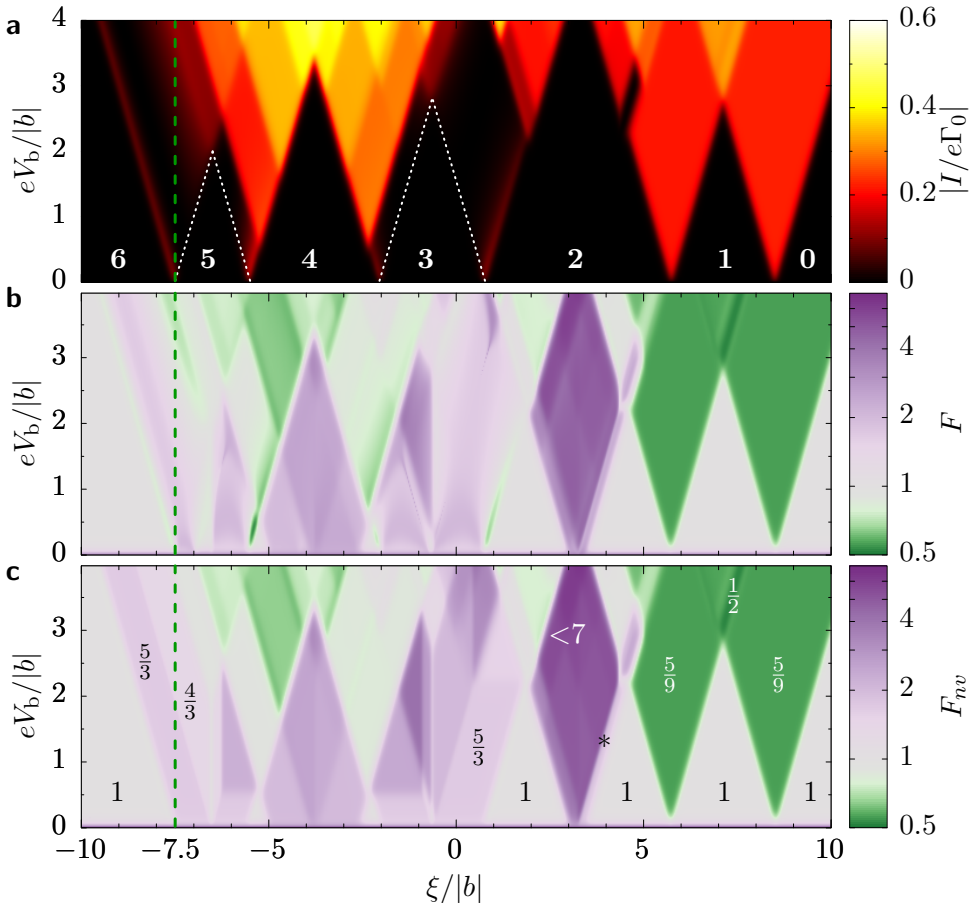

Figure 7.3: Current and Fano factors vs appplied gate and bias voltages. **a** Average current where the number of electrons in the blockade regions is displayed. The white dotted lines delimit regions where transport is inhibited due to Coulomb blockade. **b** Fano factor and **c** Fano factor without Lamb shifts due to virtual transitions. Some values discussed in the text are indicated. Parameters used for the simulations are $U = 5|b|$, $V = 2|b|$, $k_BT = 0.002|b|$, $k_BT = 20\Gamma$ and $b < 0$.

Fano factor are clearly visible at the center of the 3– and 5–particles Coulomb diamonds. At these positions the energy levels of the states with one electron more and less than the participating Coulomb- or interference-blocked state are aligned, and a little change in the gate voltage favors one or the other side in transport, leading to a sudden change in the statistics that is unaffected by the bias voltage [211, 212].

The complexity of the Fano pattern increases with growing electron filling,

so from right to left. The breaking of electron-hole symmetry is strikingly revealed in a Fano factor smaller (larger) than one, in the transport (blockade) regions involving the $N = 0\,(6)$ and $N = 1\,(5)$ ground states. Moreover, large values of F are observed for intermediate filling. The Fano map at low filling is easily understood by observing that the one-electron groundstates $\{|1, E_{1_0}; 1/2, \pm 1/2, 0\rangle\}$ are only spin degenerate. Then, in the region with zero and one electron occupation, the Fano map resembles the one of the SIAM, see Sec. 5.5.3, with $F = 5/9$ and $F = 1/2$ in the transport regions, and $F = 1$ at Coulomb blockade [190]. At larger filling $N \geq 2$, super-Poissonian noise signals the presence of fast (f) and slow (s) channels. In this situation the Fano factor can be described in terms of effective filling rates $\Gamma_l^p = R_l^p \Gamma_l$, $p = s, f$, as

$$F_{nv} = 1 + \frac{2\Gamma_{\rm L}^f}{\Gamma_{\rm L}^s + \Gamma_{\rm R}^s}, \quad \mu_{\rm L} > \mu_{\rm R}, \tag{7.5}$$

as shown in Sec. 5.5.2. The coefficients R_l^p weight the fast and slow channels, and account for both spin degeneracies and orbital interference. The latter is ubiquitous in our symmetric TQD. Hence, even at Coulomb blockade, the observed values of F and F_{nv} cannot be simply explained in terms of the channel blockade mechanism [125]. This requires a Coulomb blockaded level, and excited states in the transport window which provide a fast transport channel, see Fig. 7.1b. The larger the excited states degeneracy, the larger is the Fano factor. Consider the Coulomb diamond with $N = 2$ at the bias value indicated by the symbol * in Fig. 7.3c, where only the ground state $|2_0\rangle \equiv |2, E_{2_0}; 0, 0, 0\rangle$, and the first set of excited levels given by the sextuplet $\{|2, E_{2_1}; 1, S_z, \pm 1\rangle, S_z = 0, \pm 1\}$ enter the transport window. By applying Eq. (7.5) naively assuming that R_l^p is just the channel multiplicity ($R_l^s = 1$ and $R_l^f = 6$), one predicts $F_{nv} = 7$, which is bigger than the observed value $F_{nv} \approx 2$. At higher bias, transitions to the states $|2, E_{2_2}; 0, 0, \pm 1\rangle$ and $|3, E_{3_0}; 1/2, \pm 1/2, \pm 1\rangle$ enter the bias window and even larger values of F_{nv} are expected. This is not observed in our TQD, where $F_{nv} < 7$. However, the sheer amount of open transitions makes analytics practically impossible, especially since three of these states are orbitally degenerate.

At interference blockade, with the blocking state being decoupled at the right lead, cf. Fig. 7.1c, Eq. (7.5) holds with $\Gamma_{\rm R}^s = 0$. For transitions to the left lead through a coupled and decoupled state one would naively expect $R_{\rm L}^f = R_{\rm R}^s$ and therefore a Fano factor $F_{nv} = 3$, as found in many systems [125, 192–194]. The value $F_{nv} = 5/3$ observed e.g. at the resonance involving the ground

states $|2_0\rangle$ and $\{|3, E_{3_0}; 1/2, \pm 1/2, \pm 1\rangle\}$, see Fig. 7.3c, again indicates that the evaluation of the weights R_l^p requires a precise analysis of interference with its associated "dark states". In this respect we dedicate the next section to study the generic form of a dark state and give specific examples.

7.3 Dark states of a C_{3v} symmetric TQD

When a set of orbitally degenerate levels participate in transport, interference can inhibit the escape from one many-body state with N particles at one lead, such that electrons can leave this DS only via thermal activation through the other lead or via virtual excitations, see Fig. 7.1c. This yields current suppression. In the following we focus exemplarily on transitions blocked at the right lead and which involve an orbitally degenerate multiplet with N particles and a singlet with $N-1$ particles. We denote the latter state, which necessarily has $L_z = 0$, by $|N-1;0\rangle$, and define a DS through the requirement

$$\langle N-1;0|\, d_{\mathrm{R}\sigma}\, |N;\mathrm{DS}\rangle = 0. \tag{7.6}$$

We drop the additional degrees of freedom $\alpha_i = \{E_{N_i}; S, S_z\}$ that account for the energy and spin of the DS. Because a $L_z = 0$ state and $d_{\mathrm{R}\sigma}$ are invariant upon a reflection σ_{v1} which leaves the site 1 invariant and sends $2 \leftrightarrow 0$, such a blocking state must be antisymmetric under σ_{v1}. Expressing $d_{\mathrm{R}\sigma}$ in the angular momentum basis, we find for the DS the anti-bonding linear combination

$$|N;\mathrm{DS}\rangle = \frac{1}{\sqrt{2}}\left(e^{i2\pi/3}|N;1\rangle - e^{-i2\pi/3}|N;-1\rangle\right). \tag{7.7}$$

Thus, a DS is an anti-bonding combination of states with angular momentum $L_z = \pm 1$. This DS has exactly the form of the one found in a CNT-QD in Eq. (4.10), only now the phase is fixed to $2\pi/3$ by local tunneling. Note that this result is independent of spin degrees of freedom. Indeed this state fulfills

$$\begin{aligned}
&\langle N-1;0|d_{\mathrm{R}\sigma}|N;\mathrm{DS}\rangle = \\
&= \langle N-1;0|\sum_{\ell_z} e^{-i\ell_z 2\pi/3} d_{\ell_z\sigma}\left(e^{i2\pi/3}|N;1\rangle - e^{-i2\pi/3}|N;-1\rangle\right) \\
&= \langle N-1;0|d_{\ell_z=1\sigma}|N;1\rangle - \langle N-1;0|d_{\ell_z=-1\sigma}|N;-1\rangle \\
&= \langle N-1;0|d_{\ell_z=1\sigma}|N;1\rangle - \underbrace{\langle N-1;0|\sigma_{v0}}_{\langle N-1;0|}\underbrace{\sigma_{v0}d_{\ell_z=-1\sigma}\sigma_{v0}}_{d_{\ell_z=1\sigma}}\underbrace{\sigma_{v0}|N;-1\rangle}_{|N;1\rangle} \\
&= 0,
\end{aligned} \tag{7.8}$$

which shows that a transition is forbidden at the right lead. To the bonding linear combination it corresponds the coupled state $|N;\mathrm{CS}\rangle$. Expressing the dark states in position basis $\{n_{0\uparrow}, n_{1\uparrow}, n_{2\uparrow}; n_{0\downarrow}, n_{1\downarrow}, n_{2\downarrow}\}$ yields further insight into the blocking mechanism. Let us consider their composition for increasing electron filling. The dark state for the one–particle first excited state with $S_z = 1/2$, is

$$|1, E_{1_1}; \frac{1}{2}, \frac{1}{2}; \mathrm{DS}\rangle = \frac{1}{\sqrt{2}} \left(\quad - \quad \right), \tag{7.9}$$

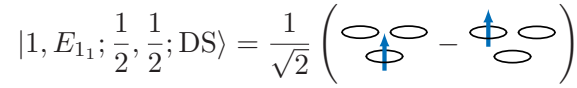

and similarly for the dark state with $S_z = -1/2$. Thus we recover the familiar result by Hsieh *et al.* [209], where the DS is a state without occupation of the right-coupled dot 1. On the other hand the vanishing of the matrix element in Eq. (7.8) also comes naturally from the fact that the DS (7.9) is *antisymmetric* under the operation σ_{v1} while both $d_{1\sigma}$ and the vacuum state $|0, \alpha_0; 0\rangle$ are symmetric. For the two–particle first excited state with $S_z = 1$ we obtain

$$|2, E_{2_1}, 1, 1; \mathrm{DS}\rangle = \frac{1}{\sqrt{6}} \left(\quad + \quad + 2 \quad \right), \tag{7.10}$$

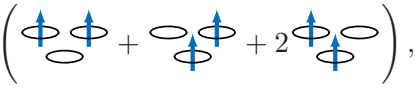

and similarly for $S_z = -1$. For the case $S_z = 0$ we find

$$|2, E_{2_1}; 1, 0; \mathrm{DS}\rangle = \frac{1}{2\sqrt{3}} \Big[\left(\quad - \quad \right) - \left(\quad - \quad \right) + 2 \left(\quad - \quad \right) \Big]. \tag{7.11}$$

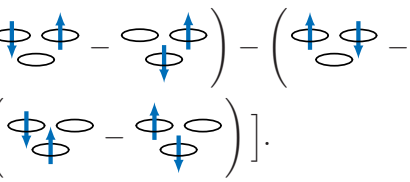

The composition of states shown in Eqs. (7.10)) and (7.11) is counterintuitive because they admit *finite* occupation of the dot 1. However, again the vanishing of the transition amplitude (7.8) results from the fact that the DS is antisymmetric with respect to the reflection σ_{v1} and the state $|1, \alpha_0, 0\rangle$ is symmetric. Notice that crucially the two contributions with single occupation of dot 1 give a contribution of opposite sign to the amplitude (7.8). The three–particles

ground state with $S_z = 1/2$ is given by the intricate superposition

$$|3, E_{3_0}; \frac{1}{2}, \frac{1}{2}; \mathrm{DS}\rangle = \frac{1}{3\sqrt{2}}\Big[(v_{0,1} - 2v_{0,0} + v_{0,-1}) \Big(+ \Big)$$
$$+ (2v_{0,1} - v_{0,0} - v_{0,-1}) \Big(+ \Big)$$
$$+ (v_{0,1} + v_{0,0} + v_{0,-1}) \Big(+ \Big)$$
$$+ (v_{0,1} + v_{0,0} - 2v_{0,-1}) \Big(+ \Big)$$
$$+2\,(v_{0,1} + v_{0,0} + v_{0,-1}) \Big], \tag{7.12}$$

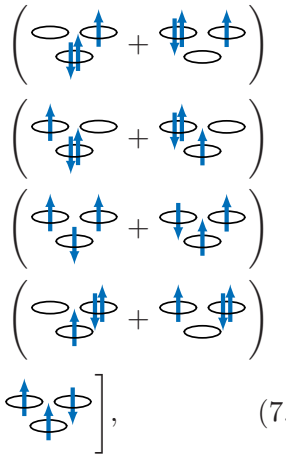

where $v_{x,y}$ is given in the caption of Tab. 7.2. Note that this state is anti-symmetric with respect to the reflection σ_{v1}, the plus signs are a result of the used ordering of the creation operators. Analogously the state with $S_z = -1/2$ can be constructed. Again the vanishing of the transition amplitude (7.8) results from a nontrivial quantum cancellation. To all these DSs there exist hole counterparts which, however, have different energetic ordering within the electron number. For example, in the 5–particle space the ground state features such a DS and the corresponding ground state interference.

7.4 Interference blockade at the $2_0 \leftrightarrow 3_0$ resonance

We apply the results above to investigate the bias region involving transitions among an N-particles ground state singlet, and an orbitally degenerate $(N+1)$-particles ground state. We exemplarily choose the $2_0 \leftrightarrow 3_0$ resonance where, as seen in Fig. 7.3c, $F_{nv} = 5/3$, but the results apply to other resonances as well. To this extent, let us observe that the stationary density matrix ρ^∞ has a block diagonal structure, with blocks $\rho^{NSS_z}(E)$ of definite N, S, S_z, and E [51]. The latter is possible since the tunneling rate is much small than all other energy scales in the system and therefore the secular approximation holds. Due to the equivalence of the configurations with different S_z for the dynamics, we introduce the matrices $(\rho_N)_{L_z L_z'}(E) := \sum_{S_z} (\rho^{NSS_z}(E))_{L_z L_z'}$. For example, since there exists only one configuration for the $N = 2$ ground state, ρ_2 is a number. On the other hand, $\rho_3(E_{3_0})$ is the 2×2 matrix associated to the 3–particles ground state quadruplet. By using the Wigner-Eckart theorem

[112] to calculate matrix elements of the operators, $d^\dagger_{l\sigma}$ and $d_{l\sigma}$, between states of different particle number and spin, and summing over σ, Eq. (7.4) yields for the case of unidirectional transport near the $2_0 \leftrightarrow 3_0$ resonance

$$\begin{aligned} 0 &= -\frac{i}{\hbar}\left[\hat{H}_{\rm LS}, \rho_3\right] + 2\Gamma\mathcal{R}_{\rm L}\rho_2 - \frac{\Gamma}{2}\left\{\mathcal{R}_{\rm R}, \rho_3\right\}, \\ 0 &= \Gamma\ {\rm tr}_{\rm TQD}\left\{\mathcal{R}_{\rm L}\rho_3\right\} - 4\Gamma\rho_2, \end{aligned} \tag{7.13}$$

which, together with ${\rm tr}_{\rm TQD}\{\rho\} = 1$, fully determines $\rho_2(E_{2_0})$ and $\rho_3(E_{3_0})$. This equation is exactly the same as for the minimal model in CNT-QDs in Eq. (4.15). We have split the many body rates into a prefactor Γ and the coherence matrices $\mathcal{R}_l$, which in the angular momentum basis have the form $(\mathcal{R}_l)_{\ell_z\ell'_z} = e^{il(\ell_z-\ell'_z)2\pi/3}$. The many body rate is directly related to the single particle tunneling rate from Eq. (7.3) such that the prefactor is given by $\Gamma = a\Gamma_0$ where $a = \sum_\sigma |\langle 3, E_{3_0}; \frac{1}{2}, -\sigma, 1|d^\dagger_{l\sigma}|2_0\rangle|^2/2$. The Lamb shift Hamiltonian can be cast, following Donarini *et al.* [106], into the form $\hat{H}_{\rm LS} = \hbar\sum_l \omega_{\rm L}\mathcal{R}_l/2$. The precession frequencies $\omega_{\rm L}$ account for virtual transitions from the 3–particles ground states to the states with 2 and 4 particles and are independent of S_z. We find

$$\begin{aligned} \omega_{\rm L} = \frac{\Gamma_0}{\pi}\sum_{\sigma,E} & p_l\left(E - E_{3_0}\right)\langle 3, E_{3_0}; \frac{1}{2}, S_z, L_z|d_{0\sigma}\mathcal{P}_{4,E}d^\dagger_{0\sigma}|3, E_{3_0}; \frac{1}{2}, S_z, -L_z\rangle \\ & + p_l\left(E_{3_0} - E\right)\langle 3, E_{3_0}; \frac{1}{2}, S_z, L_z|d^\dagger_{0\sigma}\mathcal{P}_{2,E}d_{0\sigma}|3, E_{3_0}; \frac{1}{2}, S_z, -L_z\rangle, \end{aligned} \tag{7.14}$$

where $\mathcal{P}_{NE} = \sum_{S_z,L_z}|N, E; S, S_z, L_z\rangle\langle N, E; S, S_z, L_z|$ is the projector on the N-particle subspace with energy E and spin S. Notice that one cannot diagonalize the two coherence matrices $\mathcal{R}_L$ and $\mathcal{R}_R$ simultaneously. In the basis spanned by $|3, {\rm DS}\rangle$ and $|3, {\rm CS}\rangle$ we get

$$\mathcal{R}_{\rm R} = \begin{pmatrix} 0 & 0 \\ 0 & 2 \end{pmatrix}, \qquad \mathcal{R}_{\rm L} = \frac{1}{2}\begin{pmatrix} 3 & -i\sqrt{3} \\ i\sqrt{3} & 1 \end{pmatrix}, \tag{7.15}$$

and $\rho_3(E_{3_0}) = p(I + \mathbf{n}\cdot\boldsymbol{\sigma})/2$, where $\boldsymbol{n}$ is the Bloch vector corresponding to the orbitally degenerate state, $\boldsymbol{\sigma}$ is the vector of Pauli matrices, $p = \rho_{dd} + \rho_{cc}$, and the decoupled state points along the z–axis. Neglecting the Lamb shift term, the matrix $\rho_3(E_{3_0})$ is diagonal, with elements $\rho_{dd} = 1$, $\rho_{cc} = 0$ at deep interference blockade. The diagonal elements 0, 2 and 3/2, 1/2 of $\mathcal{R}_\alpha$ correspond to the weights R^s_R, R^f_R, and R^s_L, R^f_L, respectively, entering Eq. (7.5). Notice that

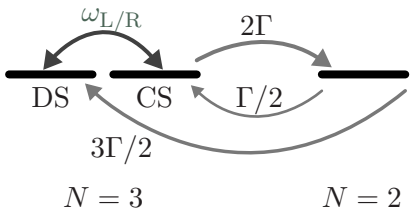

Figure 7.4: Level scheme and effective filling rates at the $2_0 \leftrightarrow 3_0$ resonance including the precession between the DS and CS.

this yields the counterintuitive result $R_L^f \neq R_L^s$. Using these values we find $F_{nv} = 5/3$. The level scheme and the effective rates are shown in Fig. 7.4. So far the effect of the Lamb shift Hamiltonian $\hat{H}_{\mathrm{LS}}$ has been neglected. An analytical treatment of the precessional dynamics is possible in the parameter region involving the $N = 5$ and $N = 6$ ground states as discussed below.

7.5 Interference blockade at the $5_0 \leftrightarrow 6_0$ resonance

The Lamb shift term describes a precession of the Bloch vector $\boldsymbol{n}$ around an axis set by the coherence matrices $\mathcal{R}_l$. The populations of the coupled and of the dark state are thus affected by partially coherent gain and loss, and the blockade is perfect only when $\omega_{\mathrm{L}} = 0$. We choose the $5_0 \leftrightarrow 6_0$ resonance at $\xi = -7.5|b|$, indicated by a green dashed line in Fig. 7.3, to study the effect of this precession.

7.5.1 Hole transport

The dynamics between the $N = 5$ and $N = 6$ ground states is easily described in terms of hole transport. Then, Eqs. (7.5), (7.13) and (7.15) apply upon exchange of $\mathrm{L} \leftrightarrow \mathrm{R}$ together with $3 \to 5$, $2 \to 6$, which yields

$$\begin{aligned} 0 &= -\frac{i}{\hbar}\left[\hat{H}_{\mathrm{LS}}, \rho_5\right] + 2\Gamma\mathcal{R}_{\mathrm{R}}\rho_6 - \frac{\Gamma}{2}\left\{\mathcal{R}_{\mathrm{L}}, \rho_5\right\}, \\ 0 &= \Gamma\ \mathrm{tr}_{\mathrm{TQD}}\left\{\mathcal{R}_{\mathrm{L}}\rho_5\right\} - 4\Gamma\rho_6, \end{aligned} \tag{7.16}$$

where we use $a = \sum_\sigma |\langle 5, E_{5_0}; \frac{1}{2}, -\sigma, 1|d_{l\sigma}|6\rangle|^2/2 = 1/3$ and $\Gamma = a\Gamma_0$.

Bias traces of currents and Fano factors at the gate voltage corresponding to $\xi = -7.5|b|$ are shown in Fig. 7.5a,b. The current I_{nv}, which does not account for the Lamb shifts, is exponentially suppressed in the voltage range

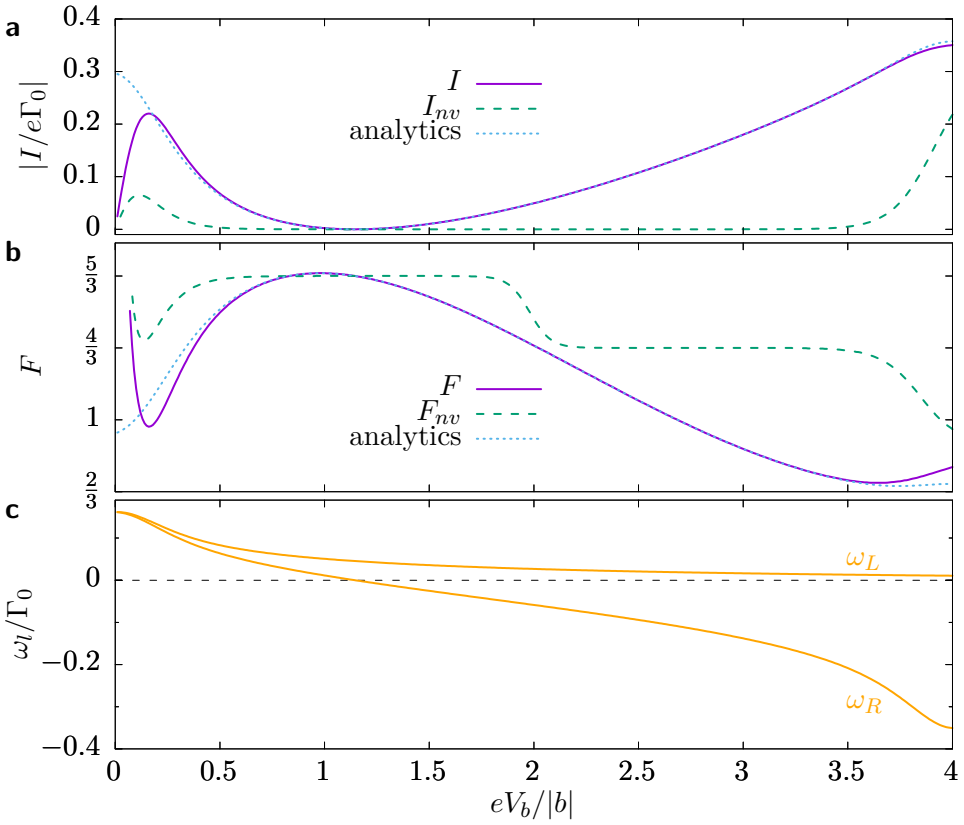

Figure 7.5: Bias trace of **a** current, **b** Fano factor and **c** precession frequencies $\omega_{\mathrm{L/R}}$ at $\xi = -7.5|b|$, corresponding to the green dashed line in Fig. 7.3. The numerical data well agree with analytical expressions from the text.

$0.5 < eV_\mathrm{b}/|b| < 3.5$. The associated Fano factor takes the values $F_{nv} = 5/3$ at low bias, and $F_{nv} = 4/3$ above $eV_\mathrm{b} = 2|b|$, when transitions from 5_0 to the 4–particle ground states $\{|4, E_{4_0}; 1, S_z, 0\rangle\}$ dominate the bottleneck process for transport, as shown in Sec. 7.5.3. Virtual transitions modify this picture: the current I (Fano factor F) varies with bias voltage and has a minimum (maximum) at $\omega_R \approx 0$. In the following we investigate how the Lamb shift Hamiltonian affects the dark state of the 5–particles ground states and the resulting Fano factor.

7.5.2 Interference dynamics

The precession frequencies ω_α from Eq. (7.14) account for virtual transitions from the 5–particles ground states to the state $|6_0\rangle \equiv |6, E_6; 0, 0, 0\rangle$ and to

levels with energies $E_{4_{0,1,2,3}}$. Their bias dependence is shown in Fig. 7.5c. The stationary density matrix in the basis $\{|5_0, \mathrm{DS}\rangle, |5_0, \mathrm{CS}\rangle, |6_0\rangle\}$, obtained as solution to Eq. (7.16) is

$$\rho^{\infty} = \frac{1}{D}\begin{pmatrix} D - 3\omega_{\mathrm{R}}^2 & -\sqrt{3}\omega_{\mathrm{R}}(\Gamma - i2(\omega_{\mathrm{L}} - \omega_{\mathrm{R}})) & 0 \\ -\sqrt{3}\omega_{\mathrm{R}}(\Gamma + i2(\omega_{\mathrm{L}} - \omega_{\mathrm{R}})) & 2\omega_{\mathrm{R}}^2 & 0 \\ 0 & 0 & \omega_{\mathrm{R}}^2 \end{pmatrix}, \tag{7.17}$$

with $D = 2\Gamma^2 + 8\omega_{\mathrm{L}}^2 - 12\omega_{\mathrm{L}}\omega_{\mathrm{R}} + 9\omega_{\mathrm{R}}^2$. The corresponding current is $I = e4\Gamma\omega_{\mathrm{R}}^2/3D$. For $\omega_{\mathrm{R}} \to 0$ the system gets quadratically stuck in the decoupled state and thus current is supressed. The resulting Fano factor is

$$F = \frac{5}{3} + 18\omega_{\mathrm{R}}\frac{\Gamma^2(32\omega_{\mathrm{L}} - 74\omega_{\mathrm{R}}) + 9(128\omega_{\mathrm{L}}^3 - 296\omega_{\mathrm{L}}^2\omega_{\mathrm{R}} + 252\omega_{\mathrm{L}}\omega_{\mathrm{R}} - 105\omega_{\mathrm{R}}^3)}{3D^2}, \tag{7.18}$$

therefore, the limit of $F = 5/3$ is recovered at complete blockade. Since $\omega_{\mathrm{L}} > 0$, the Fano factor is not maximal at $\omega_{\mathrm{R}} = 0$ but instead at a little lower bias voltage.

7.5.3 Including 4–particle ground states

A striking feature at the left side of the stability diagram, a Fano factor of $F_{nv} = 4/3$, cannot be obtained considering a minimal model using only the 5– and 6–particle states. It appears at bias and gate voltages where $f_{\mathrm{R}}^{-}(E_{5_0} - E_{4_0})$ overcomes $f_{\mathrm{R}}^{+}(E_6 - E_{5_0})$ and the transition to the triplet of ground states with 4 particles becomes the new bottleneck of transport. At $\xi = -7.5|b|$, this happens at $eV_{\mathrm{b}} = (E_6 - E_{4_0}) = V = 2|b|$. Similar to the model with slow and fast channels we write a minimal model in the basis $\{|6_0\rangle\langle 6_0|, |5_0, \mathrm{DS}\rangle\langle 5_0, \mathrm{DS}|, |5_0, \mathrm{CS}\rangle\langle 5_0, \mathrm{CS}|, |4_0\rangle\langle 4_0|\}$, where $|4_0\rangle$ is associated to the triplet $\{4, E_{4_0}; 1, S_z, 0\rangle\}$. The Liouvillian and current superoperators are

$$\mathcal{L} = \begin{pmatrix} -\Gamma_{\mathrm{R},65}^{c} - \Gamma_{\mathrm{R},65}^{d} & 0 & \Gamma_{\mathrm{L},65}^{c} & 0 \\ \Gamma_{\mathrm{R},65}^{d} & -\Gamma_{\mathrm{R},54}^{d} f_{\mathrm{R}}^{-} & 0 & \Gamma_{\mathrm{L},54}^{d} + \Gamma_{\mathrm{R},54}^{d} \\ \Gamma_{\mathrm{R},65}^{c} & 0 & -\Gamma_{\mathrm{L},65}^{c} & \Gamma_{\mathrm{L},54}^{c} + \Gamma_{\mathrm{R},54}^{c} \\ 0 & \Gamma_{\mathrm{R},54}^{d} f_{\mathrm{R}}^{-} & 0 & -\sum_{p,l}\Gamma_{l,54}^{p} \end{pmatrix},$$

$$\mathcal{J}^{+} = \begin{pmatrix} 0 & 0 & 0 & 0 \\ \Gamma_{\mathrm{R},65}^{d} & 0 & 0 & 0 \\ \Gamma_{\mathrm{R},65}^{c} & 0 & 0 & 0 \\ 0 & \Gamma_{\mathrm{R},54}^{d} f_{R}^{-} & 0 & 0 \end{pmatrix}, \qquad \mathcal{J}^{-} = \begin{pmatrix} 0 & 0 & 0 & 0 \\ 0 & 0 & 0 & \Gamma_{\mathrm{R},54}^{d} \\ 0 & 0 & 0 & \Gamma_{\mathrm{R},54}^{c} \\ 0 & 0 & 0 & 0 \end{pmatrix}, \tag{7.19}$$

where $f_{\rm R}^-$ is the Fermi function between the 5–particle and 4–particle ground states at the right lead and is responsible for the bottleneck process. The rates $\Gamma^p_{l,NN'}$ are the effective tunneling rates between particle numbers N and N' into or from the DS ($p=d$) and CS ($p=c$). To lowest order in this Fermi function, the current and Fano factor read

$$\begin{aligned} I &= e\Gamma^d_{\rm R,54} f_{\rm R}^- \frac{\Gamma^d_{\rm R,65}(\Gamma^d_{\rm L,54}+\Gamma^c_{\rm L,54}) + (\Gamma^c_{\rm L,54}+\Gamma^c_{\rm R,54})(\Gamma^d_{\rm R,65}+\Gamma^c_{\rm R,65})}{\Gamma^d_{\rm R,65}(\Gamma^c_{\rm L,54}+\Gamma^c_{\rm R,54}+\Gamma^d_{\rm L,54}+\Gamma^d_{\rm R,54})}, \\ F_{nv} &= \frac{\Gamma^c_{\rm L,54}\left(2(\Gamma^c_{\rm R,65})^2+5\Gamma^c_{\rm R,65}\Gamma^d_{\rm R,65}+4(\Gamma^d_{\rm R,65})^2\right)}{\Gamma^d_{\rm R,65}(\Gamma^c_{\rm L,54}(\Gamma^c_{\rm R,65}+2\Gamma^d_{\rm R,65})+\Gamma^c_{\rm R,54}(\Gamma^c_{\rm R,65}+\Gamma^d_{\rm R,65})+\Gamma^d_{\rm L,54}\Gamma^d_{\rm R,65})} \\ &\quad + \frac{+\Gamma^c_{\rm R,54}\left(2(\Gamma^c_{\rm R,65})^2+3\Gamma^c_{\rm R,65}\Gamma^d_{\rm R,65}+(\Gamma^d_{\rm R,65})^2\right)+\Gamma^d_{\rm L,54}(\Gamma^d_{\rm R,65})^2}{\Gamma^d_{\rm R,65}(\Gamma^c_{\rm L,54}(\Gamma^c_{\rm R,65}+2\Gamma^d_{\rm R,65})+\Gamma^c_{\rm R,54}(\Gamma^c_{\rm R,65}+\Gamma^d_{\rm R,65})+\Gamma^d_{\rm L,54}\Gamma^d_{\rm R,65})}. \end{aligned} \tag{7.20}$$

The many body rate matrix for the $5_0 \leftrightarrow 4_0$ transitions in the angular momentum basis reads $(\mathbf{\Gamma}_l)^{5_0\leftrightarrow 4_0}_{\ell_z\ell'_z} = \frac{1}{2}\sum_{\sigma,\tau}\langle 5, E_{5_0}; \frac{1}{2},\sigma,\ell_z|d^\dagger_{l\tau}\mathcal{P}_{4,E_{4_0}}d_{l\tau}|5,E_{5_0};\frac{1}{2},\sigma,\ell'_z\rangle$. Under the bias and gate voltage conditions considered here, the system still remains in the interference ground state blocking associated to the $5_0 \leftrightarrow 6$ transition. The corresponding coupled-decoupled basis introduced shortly above Eq. (7.15) is thus the most convenient representation. With the help of the eigenstates listed in Table 7.3 and the Wigner-Eckart theorem one calculates, $\Gamma^d_{l,\,54} = \frac{3}{2}\Gamma R^f_l$ and $\Gamma^c_{\alpha,\,54} = \frac{3}{2}\Gamma R^s_\alpha$ with $R^{f/s}_\alpha$ as given below Eq. (7.15). Finally, by substitution into Eq. (7.20), one obtains $I = e\Gamma f_R^-/4$ and $F = 4/3$.

7.6 Robustness

To check the influence of a weak perturbation which lifts degeneracies, we restrict ourself again to the $5_0 \leftrightarrow 6$ resonance. Then this perturbation changes the onsite energies of the orbitally degenerate $|5_0\rangle$ states and is given by a Hamiltonian $\hat{H}_\Delta = -\Delta E\sigma_z/2$ which, rotated to the coupled and decoupled basis, takes the form

$$\hat{H}_\Delta = \frac{1}{2}\begin{pmatrix} 0 & \Delta E \\ \Delta E & 0 \end{pmatrix}. \tag{7.21}$$

If one assumes weak coupling to the leads, $\hbar\Gamma \ll k_{\rm B}T$ and in addition also that $\Delta E \ll k_{\rm B}T$, the dissipative part of the unidirectional master equation is unaffected by the changes. Therefore, the master equation (7.4) holds with the substitution $\hat{H}_{\rm LS} \to \hat{H}_{\rm LS} + \hat{H}_\Delta$. The resulting current and Fano factor at

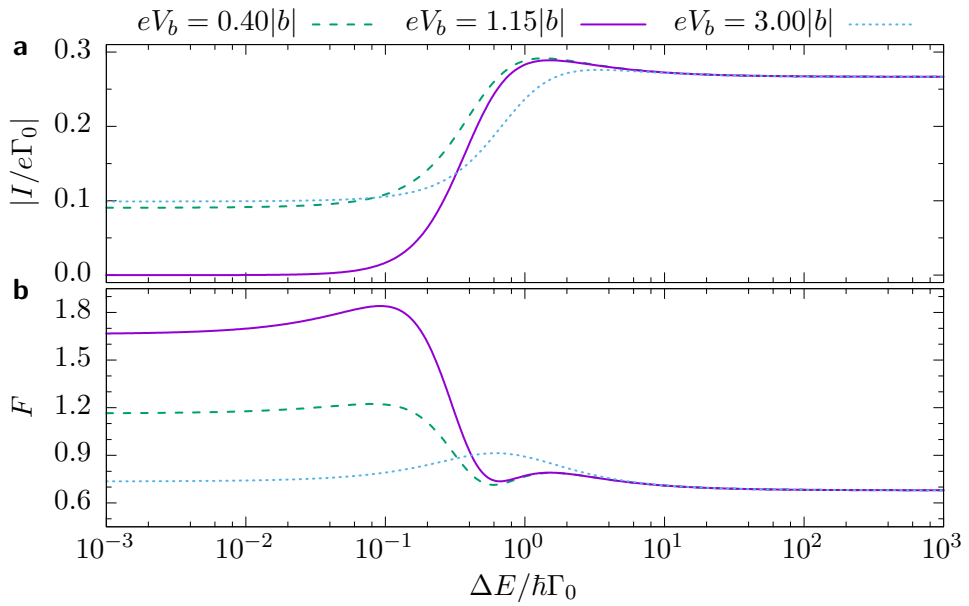

Figure 7.6: **a** Current and **b** Fano factor as a function of detuning at $V_g = -7.5|b|$ for different bias voltages. In the limit of large detuning where $\Delta E \gg \hbar\Gamma_0$ the current is $I = e4\Gamma_0/15$ and the Fano factor $F = 17/25$. For vanishing detuning $F = 5/3$ is recovered at full blockade ($eV_b \approx 1.15|b|$).

the $5_0 \leftrightarrow 6$ resonance is shown as a function of the detuning in Fig. 7.6. The results of this paper are robust for a perturbation strength up to the order of $\Delta E \lesssim 0.01\hbar\Gamma_0$. In the limit of large detuning where $k_B T \gg \Delta E \gg \hbar\Gamma_0$ the current is $I = e4\Gamma_0/15$ and the Fano factor $F = 17/25$. This Fano factor can be again explained by the one for a single resonant level (5.31) $F = \left(R_L^2 + R_R^2\right) / \left(R_L + R_R\right)^2$, where, due to the 4–fold degeneracy of $|5_0\rangle$, $R_L = 4R_R$.

7.7 Conclusions

Using a full counting statistics approach in Liouville space we obtained the Fano stability diagram of a C_{3v} symmetric TQD. In the region of current suppression the Fano factor helps unraveling the underlying blocking mechanisms. Poissonian statistics suggests "classical" Coulomb blockade, whereas super-Possonian noise points to the presence of fast and slow channels, the latter including dark states. A population redistribution between dark and coupled states, induced by virtual excitations in the Lamb shift Hamiltonian,

results in a nontrivial bias dependence of the current and Fano factor. The value attained by the Fano factor at specific gate and bias voltages further reveals the internal structure of the dark states. We have shown that such dark states persist under weak perturbations that change the otherwise perfect degeneracies of angular momentum states into quasi degeneracies with splittings smaller than the tunneling rates.

This work is focused on the impact of the C_{3v} symmetry on noise and thus restriction to sequential tunneling already yields interesting results. However, co-tunneling contributions [206, 207] might additionally influence the noise features and should be further investigated for a C_{3v} symmetric setup.

Conclusions and outlook

Throughout the first part of this thesis we have investigated transport in single-electron transistors (SETs) in and out of equilibrium. To calculate the current through such quantum dot (QD) devices, we use the Nakajima-Zwanzig projection operator formalism. We derive an equation for the reduced density matrix of the dot, based on superoperators. The resulting Kernel operator can be expanded in orders of the tunnel coupling. For weak coupling it is sufficient to cut this series at a certain order due to its perturbative origin. To lowest order, this derivation is equivalent to commonly used derivations. For the next leading order contribution, we showed that it reproduces the results, previously obtained by Koller [45]. The main reason behind the chosen derivation becomes clear when introducing the diagrammatic rules. Certain diagrams can be summed up analytically to all orders. This leads to a correction of the lowest order contribution, called generalized dressed second order (DSO^{+}), in the form of a self energy. It allows, to some extent, the description of transport at strong coupling. It is restricted to $U \gg \hbar\Gamma, k_{\mathrm{B}}T \gtrsim k_{\mathrm{B}}T_{\mathrm{K}}$ [53]. In the future one can think of including more and more diagrams into the resummation. For example, one could derive the resonant tunneling approximation (RTA) [51, 52, 213, 214] using the superoperator formalism.

We apply the derived master equation to analyze two experiments in carbon nanotube (CNT)-QDs. The first experiment uses the high tuneability of the coupling strength with a back gate in CNTs. This allows one to observe the Kondo effect on the hole side and co-tunneling on the electron side. Analyzing the $\mathrm{SU}(2) \otimes \mathrm{SU}(2)$ Kondo effect in CNTs requires knowledge of the symmetries present in the single particle part of the Hamiltonian. We find time-reversal-like ($\mathcal{T}$), particle-hole-like ($\mathcal{P}$) and chiral ($\mathcal{C}$) symmetries. All transitions in the excitation spectrum, starting from the ground state, can be labeled with the corresponding symmetry. Magnetotransport measurements allow one

to identify these transitions. Interestingly, we find that on the hole side $\mathcal{P}$ transitions are blocked while being present on the electron side. The SU(2) symmetries are created by pseudospin operators. DM-NRG calculations show that the Kondo ground state is a singlet with no net pseudospin, resulting from the antiferromagnetic coupling of the impurity pesudospin with the conduction electrons. This shows that only transitions are allowed that flip the pseudospin and therefore the $\mathcal{P}$ transition is forbidden. Future analysis might aim at explanation of the revival of this resonance under the presence of high magnetic field or asymmetries in the tunnel couplings. DM-NRG calculations including finite exchange interaction, not performed so far due to high numerical costs, might yield better results in the two electron valley.

The second experiment was performed on a CNT with negligible spin-orbit coupling (SOC) and valley mixing, resulting in valley (angular momentum) degeneracy. We find evidence for all-electric coherent population trapping (CPT) where the electrons become blocked in a dark state (DS). We obtain simple, analytic expressions for these DSs, which require an angular momentum dependent tunneling phase. Coupling to the leads results in precession between the dark and coupled states, mediated by the Lamb shift. This lifts the otherwise perfect blockade and supports a smooth current behavior. A minimal model for only $N = 0 \leftrightarrow 1$ transitions is solved analytically, which quantitatively fits the experiment. Finally, we justify the angular momentum dependent tunneling phase by showing that the single particle rate matrix is diagonal within the surface Γ–point approximation. Further studies can explore the possibility of finding constructive interference that can exceed the incoherent limit, whenever asymmetries in the tunnel couplings are present.

The second part explores the statistical properties of open quantum systems. We derive the full counting statistics in the master equation approach by introducing a counting variable and a generalized reduced density matrix (RDM). The current cumulants then follow as derivatives of this generalized RDM, with respect to the counting variable. As an important measure of the statistical properties we employ the Fano factor as ratio of the second current cumulant, called shot noise, and the current. We develop an iterative scheme to compute even higher order cumulants as well as an efficient method to compute them for driven systems. Already at the level of simple models one can see that the Fano factor assumes certain fractional values at plateaus of constant current.

We use this method to analyze systems consisting of multiple QDs, beyond the average current. First, we investigate the Su-Schrieffer-Heeger (SSH) model, built as a dimerized chain of QDs. The formation of topological edge states results in a topological blockade. Because also topological trivial blockading situations exist, we propose the Fano factor as an instrument to distinguish these two situations. The noise is Poissonian in topological non-trivial regions and super-Poissonian otherwise. Driving the system via an AC dipole field effectively renormalizes the inter-site hoppings. This allows for active control over the system's topological phase via the driving parameters. We use the Fano factor to map out a topological phase diagram. Additional work should go into the extension of this model to include the spin degree of freedom and allow for two or more electrons and study the effects of low driving frequencies.

In the last chapter we examine a C_{3v} symmetric triangular triple quantum dot (TQD). The single particle part of the Hamiltonian is diagonalized in the angular momentum basis. We calculate the stability diagram and the Fano map. Using the symmetries of the system allows us to find all many-body eigenstates in analytic form. We find DSs of the same simple form as in chapter 4. In position basis, these DSs turn out to be antisymmetric upon exchanging dots 0 and 2, and thus, feature a nodal plane at the right lead. We use their analytic form to study minimal models at the $2 \leftrightarrow 3$ and $5 \leftrightarrow 6$ transitions. Again, the Lamb shift creates precession between the dark and coupled states, which in turn is responsible for smooth current and Fano factor behavior. Further work might aim to include co-tunneling contributions and non-secular dynamics and to investigate their affect on the shot noise.

APPENDIX A

The rules of superoperators

In this appendix we give some insight into the calculation rules of superoperators and show some left out steps in the derivation of the quantum master equation in chapter 2.

Expansion of the Kernel

In this section we show the expansion of the Kernel in Eq. 2.14, which reads

$$K\rho^{\infty} = \lim_{\lambda\to 0^+} \mathrm{tr}_{\mathrm{B}} \left\{ \mathcal{L}_{\mathrm{tun}} \frac{1}{\lambda - \mathcal{L}_{\mathrm{S}} - \mathcal{L}_{\mathrm{B}} - \mathcal{Q}\mathcal{L}_{\mathrm{tun}}\mathcal{Q}} \mathcal{L}_{\mathrm{tun}} \rho^{\infty} \otimes \rho_B \right\}, \tag{A.1}$$

where the Laplace transform of the propagator $\bar{G}_{\mathcal{Q}}(t)$ enters

$$\tilde{G}_Q(\lambda) = \int_0^{\infty} \mathrm{d}t \; e^{(\mathcal{L}_{\mathrm{S}} + \mathcal{L}_{\mathrm{B}} + \mathcal{Q}\mathcal{L}_{\mathrm{tun}}\mathcal{Q} - \lambda)t} = \frac{1}{\lambda - \mathcal{L}_{\mathrm{S}} - \mathcal{L}_{\mathrm{B}} - \mathcal{Q}\mathcal{L}_{\mathrm{tun}}\mathcal{Q}}. \tag{A.2}$$

This can be expanded into a geometrical series

$$(x-y)^{-1} = (1 - x^{-1}y)^{-1}x^{-1} = \sum_{n=0}^{\infty} \left(x^{-1}y\right)^n x^{-1}, \tag{A.3}$$

where we expand around $y = \mathcal{Q}\mathcal{L}_{\mathrm{tun}}\mathcal{Q}$ and use $x^{-1} = \tilde{G}_0$, the Laplace transform of the free propagator $\tilde{G}_0 = \lim_{\lambda\to 0^+} \tilde{G}_0(\lambda) = \lim_{\lambda\to 0^+} [\lambda - \mathcal{L}_{\mathrm{S}} - \mathcal{L}_{\mathrm{B}}]^{-1}$. This gives the final result

$$K\rho^{\infty} = \mathrm{tr}_B \left\{ \mathcal{L}_{\mathrm{tun}} \sum_{n=0}^{\infty} \left(\tilde{G}_0 \mathcal{Q}\mathcal{L}_{\mathrm{tun}}\mathcal{Q}\right)^{2n} \tilde{G}_0 \mathcal{L}_{\mathrm{tun}} \rho^{\infty} \otimes \rho_B \right\}. \tag{A.4}$$

Since $\mathcal{P}\mathcal{L}_{\text{tun}}^{2n+1}\mathcal{P} = 0$ for $n \in \mathbb{N}$, only an even number of $\mathcal{L}_{\text{tun}}$ survives the trace and we can write the exponent $2n$. Notice that in this expression it seems as if we performed the limes of $\lambda \to 0^+$ in each free propagator, which is technically not correct, it has to be performed as one of the last steps. Therefore, we will keep the short hand notation of leaving 0^+ in the denominator of the propagators which is to be interpreted as a single limes.

Commutation rule for superoperators

For two fermionic operators X, Y, that fulfill $\{X, Y\} = 0$, we can deduce from the four possible superoperatorial combinations

$$\begin{aligned} X^+Y^+\rho &= XY\rho = -YX\rho = -Y^+X^+\rho, \\ X^+Y^-\rho &= X\rho Y = (X\rho)Y = Y^-(X\rho) = Y^-X^+\rho, \\ X^-Y^+\rho &= Y\rho X = Y(\rho X) = Y(X^-\rho) = Y^+X^-\rho, \\ X^-Y^-\rho &= \rho YX = -\rho XY = -Y^-X^-\rho, \end{aligned} \tag{A.5}$$

that the common commutation rule reads

$$X^\alpha Y^{\alpha'} = -\alpha\alpha' Y^{\alpha'} X^\alpha. \tag{A.6}$$

Notice that for commuting operators $[X, Y] = 0$, it simply holds $[X^\alpha, Y^{\alpha'}] = 0$.

Action of the system Liouvillian

The system Liouvillian is defined via

$$\mathcal{L}_{\text{S}} X = -\frac{i}{\hbar}\left(\hat{H}_{\text{S}} X - X\hat{H}_S\right), \tag{A.7}$$

therefore it is easy to see that

$$i\hbar\mathcal{L}_{\text{S}} X(\omega) = i\hbar\mathcal{L}_{\text{S}} \sum_E \Pi(E) X \Pi(E-\omega) = [E-(E-\omega)]X(\omega) = \omega X(\omega). \tag{A.8}$$

In the case of two operators, projected onto subspaces of fixed energy difference, we get

$$\begin{aligned} i\hbar\mathcal{L}_{\text{S}} X(\omega)Y(\omega') &= i\hbar\mathcal{L}_{\text{S}} \sum_{E,E'} \Pi(E)\ X\ \underbrace{\Pi(E-\omega)\Pi(E')}_{\Pi(E-\omega)\delta(E-E'-\omega)}\ Y\ \Pi(E'-\omega') \\ &= i\hbar\mathcal{L}_{\text{S}} \sum_E \Pi(E) X \Pi(E-\omega) Y \Pi(E-\omega-\omega') \\ &= (\omega+\omega') X(\omega) Y(\omega'). \end{aligned} \tag{A.9}$$

The same holds true for a system Liouvillian acting on any number of operators. Its action is simply the sum of all energy differences of these operators.

Wick's theorem for superoperators

We will show that Wick's theorem for fermionic operators of noninteracting particles can be easily extended to superoperators. The traditional version of Wick's theorem for the expectation value of four fermionic operators, reads $\langle c_3^\dagger c_2^\dagger c_1 c_0\rangle = \langle c_3^\dagger c_0\rangle \langle c_2^\dagger c_1\rangle - \langle c_3^\dagger c_1\rangle \langle c_2^\dagger c0\rangle$. This assumes $\{c_i^\dagger, c_j^\dagger\} = \{c_i, c_j\} = 0$, $\{c_i^\dagger, c_j\} = \delta_{ij}$ and a Hamiltonian diagonal in the basis spanned by these operators (as is the case for the bath operators in the derivation of the master equation of the main text). Using additionally $\langle c_i^\dagger c_j^\dagger\rangle = \langle c_i c_j\rangle = 0$ and $\langle c_j^\dagger c_j\rangle \propto \delta_{ij}$, one can generalize this theorem to any combination of four bath operators

$$\langle X_3 X_2 X_1 X_0\rangle = \langle X_3 X_2\rangle\langle X_1 X_0\rangle - \langle X_3 X_1\rangle\langle X_2 X_0\rangle + \langle X_3 X_0\rangle\langle X_2 X_1\rangle\,, \tag{A.10}$$

where X_i is either a creation, $c_i^\dagger$ or annihilation, c_i, operator. First, we use the cyclic property of the trace to show that the result must be independent of the first superoperator

$$\begin{aligned}\langle X_3^+ X_2^{\alpha_2} X_1^{\alpha_1} X_0^{\alpha_0}\rangle &= \mathrm{tr}\{X_3 X_2^{\alpha_2} X_1^{\alpha_1} X_0^{\alpha_0}\rho\} = \mathrm{tr}\{(X_2^{\alpha_2} X_1^{\alpha_1} X_0^{\alpha_0}\rho) X_3\}\\ &= \langle X_3^- X_2^{\alpha_2} X_1^{\alpha_1} X_0^{\alpha_0}\rangle\,.\end{aligned} \tag{A.11}$$

Then, choosing e.g. $\alpha_3 = +$, we show explicitly all eight remaining possibilities

$$\begin{aligned}
\langle X_3^+ X_2^+ X_1^+ X_0^+\rangle &= \langle X_3 X_2 X_1 X_0\rangle\\
&= \langle X_3^+ X_2^+\rangle\langle X_1^+ X_0^+\rangle - \langle X_3^+ X_1^+\rangle\langle X_2^+ X_0^+\rangle + \langle X_3^+ X_0^+\rangle\langle X_2^+ X_1^+\rangle\,,\\
\langle X_3^+ X_2^+ X_1^+ X_0^-\rangle &= \langle X_0 X_3 X_2 X_1\rangle\\
&= \langle X_0 X_3\rangle\langle X_2 X_1\rangle - \langle X_0 X_2\rangle\langle X_3 X_1\rangle + \langle X_0 X_1\rangle\langle X_3 X_2\rangle\\
&= \langle X_3^+ X_2^+\rangle\langle X_1^+ X_0^-\rangle - \langle X_3^+ X_1^+\rangle\langle X_2^+ X_0^-\rangle + \langle X_3^+ X_0^-\rangle\langle X_2^+ X_1^+\rangle\,,\\
\langle X_3^+ X_2^+ X_1^- X_0^+\rangle &= \langle X_1 X_3 X_2 X_0\rangle\\
&= \langle X_1 X_3\rangle\langle X_2 X_0\rangle - \langle X_1 X_2\rangle\langle X_3 X_0\rangle + \langle X_1 X_0\rangle\langle X_3 X_2\rangle\\
&= \langle X_3^+ X_2^+\rangle\langle X_1^- X_0^+\rangle + \langle X_3^+ X_1^-\rangle\langle X_2^+ X_0^+\rangle - \langle X_3^+ X_0^+\rangle\langle X_2^+ X_1^-\rangle\,,\\
\langle X_3^+ X_2^+ X_1^- X_0^-\rangle &= \langle X_1 X_0 X_3 X_2\rangle\\
&= \langle X_1 X_0\rangle\langle X_3 X_2\rangle - \langle X_1 X_3\rangle\langle X_0 X_2\rangle + \langle X_1 X_2\rangle\langle X_0 X_3\rangle\\
&= \langle X_3^+ X_2^+\rangle\langle X_1^- X_0^+\rangle + \langle X_3^+ X_1^-\rangle\langle X_2^+ X_0^+\rangle - \langle X_3^+ X_0^+\rangle\langle X_2^+ X_1^-\rangle\,,
\end{aligned} \tag{A.12}$$

and

$$\begin{aligned}
\langle X_3^+ X_2^- X_1^+ X_0^+ \rangle &= \langle X_2 X_3 X_1 X_0 \rangle \\
&= \langle X_2 X_3 \rangle \langle X_1 X_0 \rangle - \langle X_2 X_1 \rangle \langle X_3 X_0 \rangle + \langle X_2 X_0 \rangle \langle X_3 X_1 \rangle \\
&= \langle X_3^+ X_2^+ \rangle \langle X_1^- X_0^+ \rangle + \langle X_3^+ X_1^- \rangle \langle X_2^+ X_0^+ \rangle - \langle X_3^+ X_0^+ \rangle \langle X_2^+ X_1^- \rangle \,, \\
\langle X_3^+ X_2^- X_1^+ X_0^- \rangle &= \langle X_2 X_0 X_3 X_1 \rangle \\
&= \langle X_2 X_0 \rangle \langle X_3 X_1 \rangle - \langle X_2 X_3 \rangle \langle X_0 X_1 \rangle + \langle X_2 X_1 \rangle \langle X_0 X_3 \rangle \\
&= \langle X_3^+ X_2^+ \rangle \langle X_1^- X_0^+ \rangle + \langle X_3^+ X_1^- \rangle \langle X_2^+ X_0^+ \rangle - \langle X_3^+ X_0^+ \rangle \langle X_2^+ X_1^- \rangle \,, \\
\langle X_3^+ X_2^- X_1^- X_0^+ \rangle &= \langle X_2 X_1 X_3 X_0 \rangle \\
&= \langle X_2 X_1 \rangle \langle X_3 X_0 \rangle - \langle X_2 X_3 \rangle \langle X_1 X_0 \rangle + \langle X_2 X_0 \rangle \langle X_1 X_3 \rangle \\
&= \langle X_3^+ X_2^+ \rangle \langle X_1^- X_0^+ \rangle - \langle X_3^+ X_1^- \rangle \langle X_2^+ X_0^+ \rangle + \langle X_3^+ X_0^+ \rangle \langle X_2^+ X_1^- \rangle \,, \\
\langle X_3^+ X_2^- X_1^- X_0^- \rangle &= \langle X_2 X_1 X_0 X_3 \rangle \\
&= \langle X_2 X_1 \rangle \langle X_0 X_3 \rangle - \langle X_2 X_0 \rangle \langle X_1 X_3 \rangle + \langle X_2 X_3 \rangle \langle X_1 X_0 \rangle \\
&= \langle X_3^+ X_2^+ \rangle \langle X_1^- X_0^+ \rangle - \langle X_3^+ X_1^- \rangle \langle X_2^+ X_0^+ \rangle + \langle X_3^+ X_0^+ \rangle \langle X_2^+ X_1^- \rangle \,,
\end{aligned} \tag{A.13}$$

One finds that these equations can be combined such that the Wick's theorem for superoperators reads

$$\begin{aligned}
\langle X_3^{\alpha_3} X_2^{\alpha_2} X_1^{\alpha_1} X_0^{\alpha_0} \rangle = \langle X_3^{\alpha_3} X_2^{\alpha_2} \rangle \langle X_1^{\alpha_1} X_0^{\alpha_0} \rangle &- \alpha_1 \alpha_2 \langle X_3^{\alpha_3} X_1^{\alpha_1} \rangle \langle X_2^{\alpha_2} X_0^{\alpha_0} \rangle \\
&+ \alpha_1 \alpha_2 \langle X_3^{\alpha_3} X_0^{\alpha_0} \rangle \langle X_2^{\alpha_2} X_1^{\alpha_1} \rangle \,.
\end{aligned} \tag{A.14}$$

Diagrammatic rules

Similar to Koller [45] and Mantelli [53] we define diagrammatic rules that allow one to obtain all higher order contributions to the tunneling Kernel.

i

Draw a propagation line oriented right to left. On it fix $2n$ vertices, each associated to a superoperator index $\alpha \in \{+, -\}$. For example:

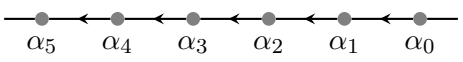

ii

Draw n fermionic lines all oriented from left to right, each labelled with a direction index p_i and an energy ϵ_i, connecting the $2n$ vertices in such a way

that the diagram cannot be cut into 2 pieces by cutting a single propagator line. Continuing the example from before:

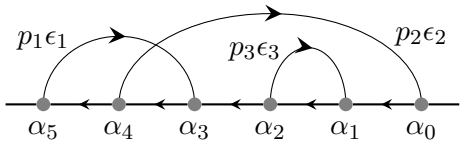

iii

Assign to each fermionic line the number $f_{b_i}^{p_i\alpha}(\epsilon_i)$, where α is the superoperator index of the rightmost vertex of the two vertices that this line connects.

iv

Assign to each vertex a system operator $D_{b_i}^{p_i,\alpha_j}$ or $D_{b_i}^{\bar{p}_i,\alpha_j}$, for incoming and outgoing fermionic lines, respectively. Notice that this operator has the dimension of energy.

v

Assign to each propagator line between vertices the operator

$$G_{\mathrm{S}}(\omega) = \frac{1}{\omega - i\hbar\mathcal{L}_{\mathrm{S}} + i0^+}.$$

vi

The energy in a vertex should be conserved:

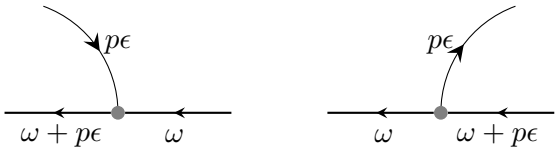

Carrying on with the previous example:

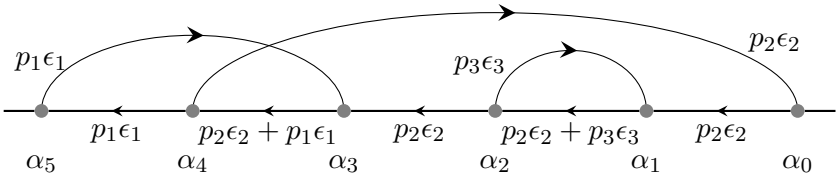

(A.15)

vii

Write the product of the vertex operators and the propagators from left to right, respecting the order of the graph.

viii

Multiply by a prefactor

$$-\frac{i}{\hbar}(-1)^{P(\{\alpha_i\})}\prod_i \alpha_i,$$

where $P(\{\alpha_i\})$ is the number of permutations of *equal* vertices, necessary to recast the graph into a completely reducible form

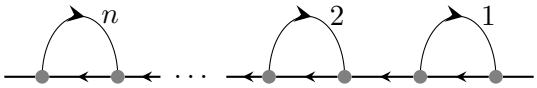

and respecting the time ordering of the contractions (the direction of the fermionic lines).

ix

Sum over all internal degrees of freedom, i.e.

$$\sum_{\{\alpha_i\}}\sum_{\{p_i\}}\sum_{\{b_i\}} \to \sum_{\{\alpha_i\}}\sum_{\{p_i\}}\sum_{\{l_i\}\in\{\mathrm{L,R}\}}\sum_{\{\sigma_i\}}\int \mathrm{d}\epsilon_i\ g_{l_i\sigma_i}(\epsilon_i),$$

where $l = \mathrm{L/R}$ represents the different leads and σ the spin. $g_{l\sigma}(\epsilon)$ is the density of states.

Example

The diagram in Eq. (A.15) then yields the expression

$$\begin{aligned}-\frac{i}{\hbar}\sum_{\{\alpha_i\}}\sum_{\{p_i\}}\sum_{\{l_i\}}\sum_{\{\sigma_i\}}\int \mathrm{d}\epsilon_1\ g_{l_1\sigma_1}(\epsilon_1)\int \mathrm{d}\epsilon_2\ g_{l_2\sigma_2}(\epsilon_2)\int \mathrm{d}\epsilon_3\ g_{l_3\sigma_3}(\epsilon_3)(-1)^{P(\{\alpha_i\})}\\ \left(\prod_{i=0}^{5}\alpha_i\right) f_{l_1}^{p_1\alpha_3}(\epsilon_1) f_{l_2}^{p_2\alpha_0}(\epsilon_2) f_{l_3}^{p_3\alpha_1}(\epsilon_3) D_{l_1\sigma_1}^{\bar{p}_1,\alpha_5}\frac{1}{p_1\epsilon_1 - i\hbar\mathcal{L}_\mathrm{S} + i0^+} D_{l_2\sigma_2}^{\bar{p}_2,\alpha_4}\\ \frac{1}{p_2\epsilon_2 + p_1\epsilon_1 - i\hbar\mathcal{L}_\mathrm{S} + i0^+} D_{l_1\sigma_1}^{p_1,\alpha_3}\frac{1}{p_2\epsilon_2 - i\hbar\mathcal{L}_\mathrm{S} + i0^+} D_{l_3\sigma_3}^{\bar{p}_3,\alpha_2}\\ \frac{1}{p_2\epsilon_2 + p_3\epsilon_3 - i\hbar\mathcal{L}_\mathrm{S} + i0^+} D_{l_3\sigma_3}^{p_3,\alpha_1}\frac{1}{p_2\epsilon_2 - i\hbar\mathcal{L}_\mathrm{S} + i0^+} D_{l_2\sigma_2}^{p_2,\alpha_0}.\end{aligned} \tag{A.16}$$

APPENDIX B

Additional checks of Kondo blockade

In this appendix we report additional checks of emergent Kondo blockade reported in chapter 3. In the single shell in the hole side in the main text we found that the particle-hole like $\mathcal{P}$ transitions get blocked due to antiferromagnetic correlations. The corresponding ground state is a singlet state with net zero pseudospin. A first check is to look at neighboring shells.

Magnetospectrum of other quartets

Up to now, we only considered one selected quartet for holes and electrons lying respectively in the CNT valence and conduction bands. Here we show that comparable conclusions regarding the suppression of $\mathcal{P}$ channels due to Kondo screening can be drawn for other quartets, showing the generality of the analysis depicted in the main text.

In the co-tunneling regime, observed for electrons lying in the conduction band, the CNT transport characteristics has been thoroughly investigated by magnetospectroscopy for different electron fillings. Fig. B.1 depicts part of the measurements, which display the same qualitative behavior as the studies in Fig. 3.5 of the main text, highlighting the robustness of the energy level spectrum, reproducible for several electron quartets. The data discussed in the main text correspond to the quadruplet N_e with $4N_e$ total electrons in the conduction band.

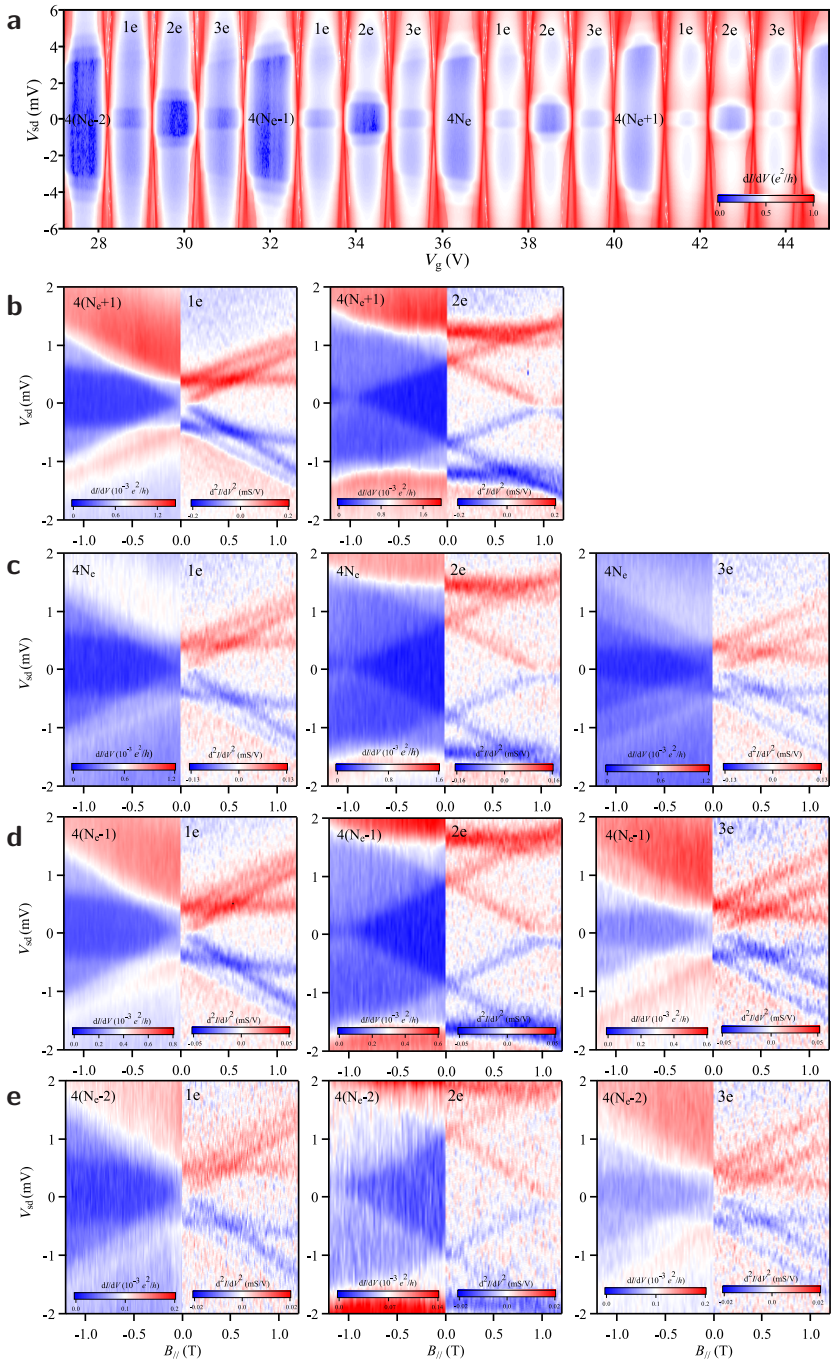

Figure B.1: **a** Stability diagram on the electron side at $B = 0$. **b-e** Magnetotransport measurements of the $1-3$e charge states (from left to right) for electrons in the quadruplets $N_e + 1$ (**b**), N_e (**c**), $N_e - 1$ (**d**) and $N_e - 2$ (**e**).

	shell	$\Delta_{\mathrm{SO}}(meV)$	$\Delta_{\mathrm{KK'}}(meV)$	$\mu_{\mathrm{orb}}(meV/T)$	$J(meV)$
electrons	$N_\mathrm{e}+1$	-0.40	0.04	0.37	-1.05
	N_e	-0.40	0.04	0.40	-1.30
	$N_\mathrm{e}-1$	-0.40	0.04	(1e, 3e) 0.45 (2e) 0.32	-1.00
	$N_\mathrm{e}-2$	-0.42	0.04	0.48	-1.80
holes	$N_\mathrm{h}+2$	-0.21	(2h) 0.30 (3h) 0.35	0.43	-1.10
	$N_\mathrm{h}+1$	-0.21	0.08	0.48	-1.10
	N_h	-0.21	0.08	(1h) 0.55 (2h, 3h) 0.51	-1.30
	$N_\mathrm{h}-1$	(1h, 2h) -0.21 (3h) -0.27	(1h) 0.27 (2h, 3h) 0.38	(1h) 0.70 (2h) 0.53 (3h) 0.60	-1.30 -1.65

Table B.1: The parameters used to fit the transport spectra of the CNT at various shells and filling numbers. The experimental data show an offset in V_b of $0.28meV$ ($0.12meV$) and are tilted in the magnetic field by $-0.06meV/T$ ($-0.05meV/T$) at the electron (hole) side. The hole side has an offset of the magnetic field of $0.06T$.

Analogously, the strongly correlated regime has been investigated for various hole shell numbers in Fig. B.2. By tuning the gate voltage it is possible to follow the system evolution over the full transition from the $SU(4)$ to $SU(2)$ transport regimes in a controllable way [66, 68]. In the present study, we are more interested in checking the robustness of the suppression of the $\mathcal{P}$ lines by inspecting the magnetic field evolution in different quadruplets. In general, neither in the quadruplets with stronger Kondo correlations (shells $N_\mathrm{h}+1$ and $N_\mathrm{h}+2$) nor in the one with a weaker Kondo effect (shell $N_\mathrm{h}-1$), the $\mathcal{P}$ transition can be resolved from an analysis of the excitation spectrum, as exemplarily shown in Fig. B.3. Notice that due to gate voltage instability we do not report on the magnetic field evolution in the 1h valley of the $N_\mathrm{h}+1$ and $N_\mathrm{h}+2$ quadruplets.

Finally, Tab. B.1 summarizes the CNT parameters which optimize the fit between excitation spectrum and the experimental data for all of the considered electron and hole quadruplets.

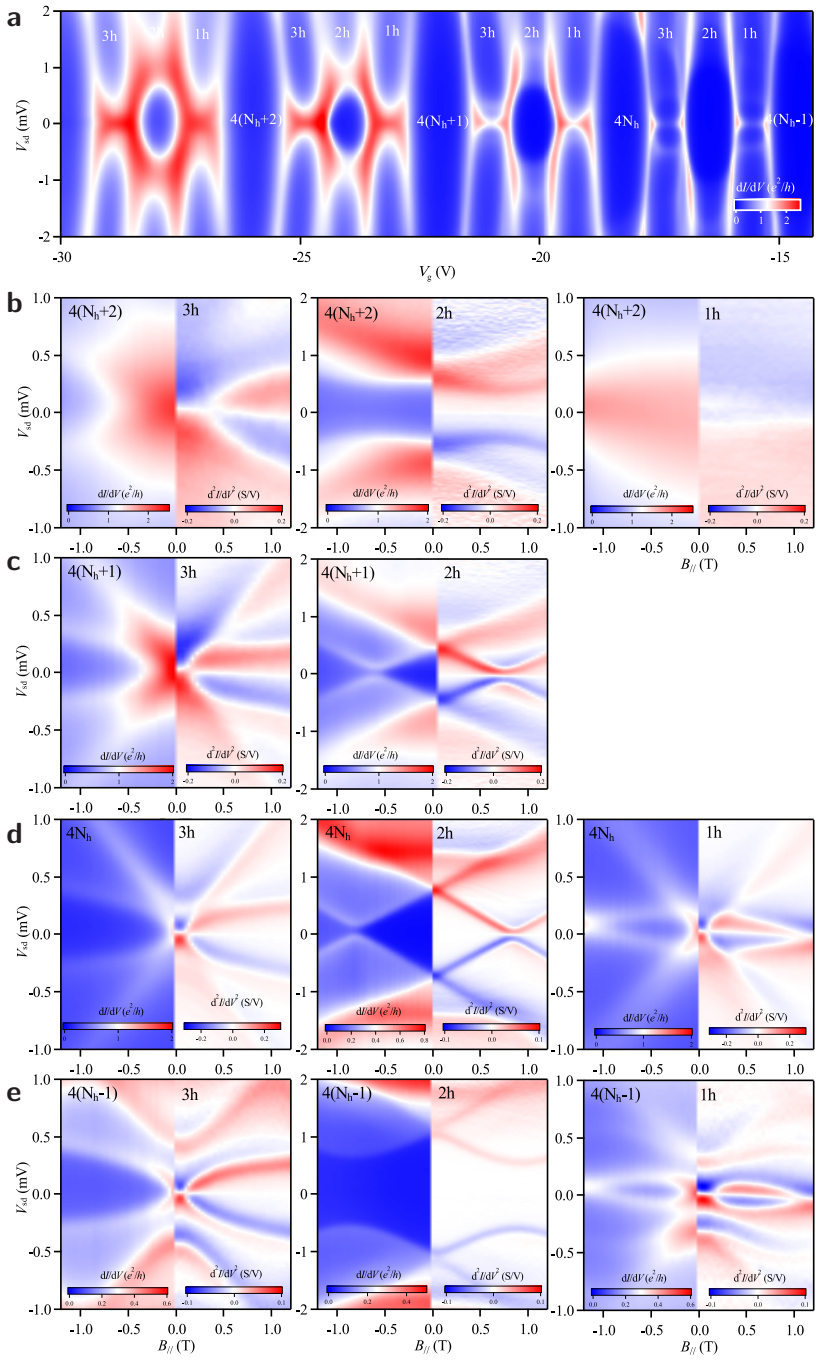

Figure B.2: **a** Stability diagram on the hole side at $B = 0$. **b-e** Magnetotransport measurements of the $3-1$h charge states (from left to right) for electrons in the quadruplets $N_\mathrm{h}+2$ (**b**), $N_\mathrm{h}+1$ (**c**), N_h (**d**) and $N_\mathrm{h}-1$ (**e**). For odd fillings similar conclusions regarding the blocking of the $\mathcal{P}$ resonance can be drawn.

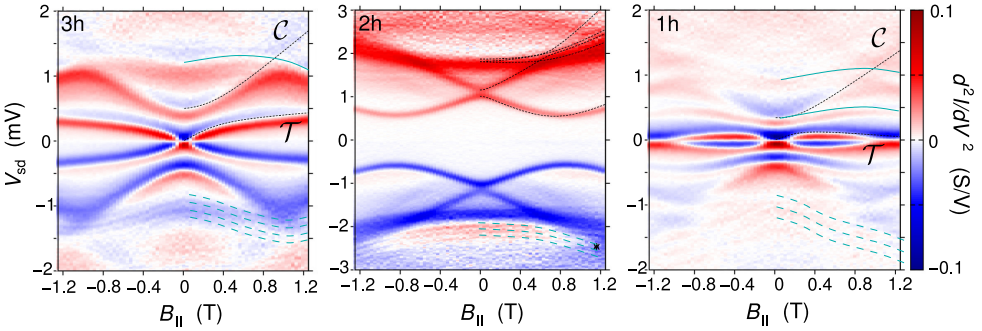

Figure B.3: An analysis of the excitation spectrum of the $N_{\rm h}$ quadruplet allows us to identify the low energy $\mathcal{T}$ and $\mathcal{C}$ resonances at 1h and 3h filling. Additional harmonic excitations are also seen, which are not captured by our model Hamiltonian, for all hole fillings (dashed and solid lines).

Differential conductance traces

Experimental bias traces are compared to KEA predictions in the Fig. B.4. An overall qualitative agreement between theoretical and experimental prediction is observed. A quantitative agreement is found regarding the position of the $\mathcal{T}$ and $\mathcal{C}$ resonances. Clearly, the $\mathcal{P}$ resonance, whose expected position is indicated by vertical lines, is not resolved at low fields. Signatures of the re-emergence of such transition are observed at fields of the order of $0.9T$, a shoulder in panels c and d. However, higher magnetic fields, not accessible to the experiment, would be necessary to track the evolution of this shoulder at even higher bias voltages. In our calculations the temperature was set to zero and we have chosen a source drain voltage V^* such that $G(T=0,V=V^*)=0.8G(T=0,V=0)$. At this voltage, the dynamics is still universal and V^* is proportional to the Kondo voltage. E.g. for our symmetric set-up with $\Gamma_{li}=\Gamma$ we find $V^*=0.41V_{\rm K}$ with $eV_{\rm K}=k_{\rm B}T_{\rm K}$. We have also checked the evolution of this relation at finite temperatures. For temperatures $T=0.13\Delta/k_{\rm B}$, similar to the experiment, we found $G(T,V=V^{**})=0.8G(T,V=0)$ with $V^{**}=0.59V_{\rm K}$. To allow for comparison, the experimental data are scaled by a bias voltage $V^*_{\rm exp}=0.0842mV$ for which $G(T,V=V^*_{\rm exp})=0.8G(T,V=0)$ for both the 1h and 3h valleys.

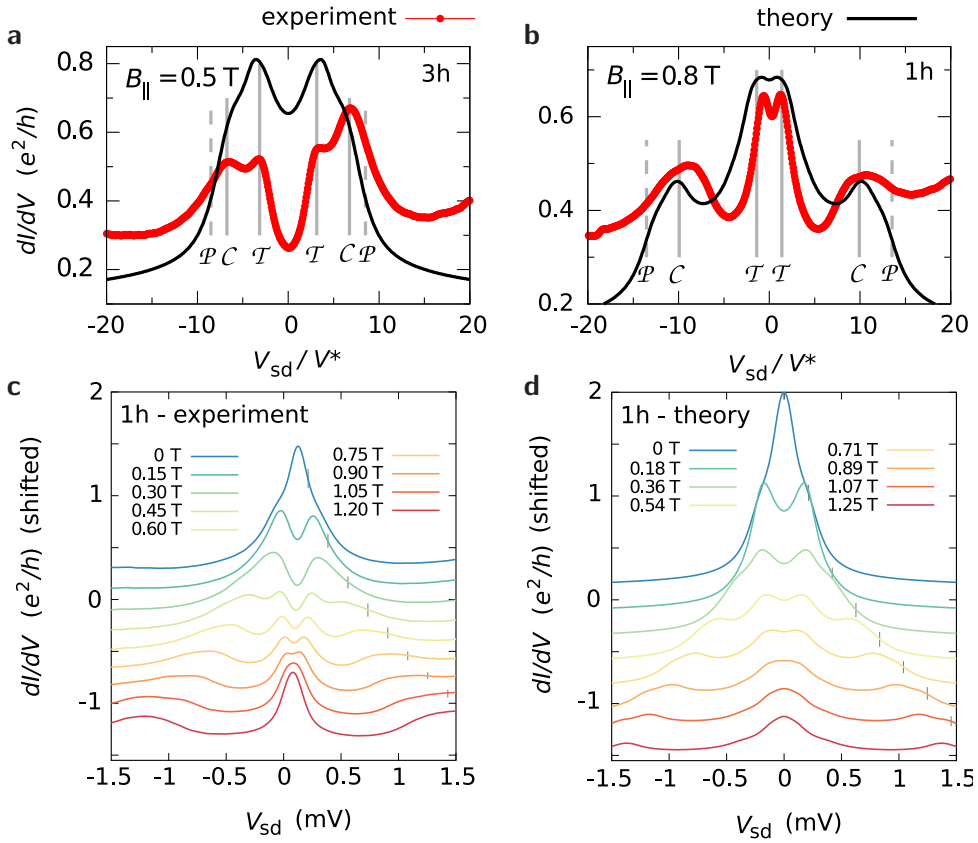

Figure B.4: Bias traces of the differential conductance at various magnitudes of an applied axial magnetic field in the valence shell $N_h = 6$. **a,b** Traces for the 3h and 1h valleys, respectively. The bias voltage is scaled by the voltage V^* at which the differential conductance at zero applied field reaches 0.8 of the conductance at zero bias. The vertical lines denote the position of the $\mathcal{P}$ and $\mathcal{C}$ resonances as expected from the addition spectrum. **c,d** Experimental and theoretical bias traces for different values of the magnetic field. The qualitative evolution of the bias traces is similar in the theory and experiment, despite the shapes differ. The short vertical lines denoted the expected position of the $\mathcal{P}$ resonance, which is not visible at low fields, neither in the theoretical nor in the experimental traces. However, a signature of such resonance is observed at fields of about $0.9T$, indicating that Kondo screening has been weakened by the bias voltage necessary to induce a $\mathcal{P}$ transition.

APPENDIX C

Carbon nanotube eigenstates

In this appendix we show the eigenstates of a CNT-QD with three shells $m = 0, 1, 2$ and including exchange interaction given by the Hamiltonian

$$\hat{H}_{\mathrm{CNT}} = \sum_{m\ell_z} m\varepsilon_0 \hat{n}_{m\ell_z} + \frac{U}{2}\hat{N}^2 + J\sum_{m}\left(\hat{\mathbf{S}}_{m\ell}\cdot\hat{\mathbf{S}}_{m-\ell} + \frac{1}{4}\hat{n}_{m\ell}\hat{n}_{m-\ell}\right), \quad \text{(C.1)}$$

where we have neglected the gate voltage contribution. The first few eigenenergies and eigenstates with filling $N = 0$ are shown in Tab. C.1. For $N = 1$, see Tabs. C.2 and C.3, for $N = 2$ see Tab. C.4. Finally the eigenstates for $N = 3$ can be found in Tabs. C.5 and C.6. We consider only states up to an energy $\varepsilon_0 \pm J$ above the ground states, which would correspond to the first excited state for vanishing exchange interaction. In the numerics this is done via a cut-off at $1.5\varepsilon_0$. All states are defined over a reference state $|0\rangle$ where the shell $m = 0$ is completely full, and the upper two shells $m = 1, 2$ completely empty. The $N = 0$ ground state is therefore

$$|0\rangle = \quad . \quad \text{(C.2)}$$

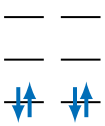

We fix the energy of this state to be E_0. The energy of the ground state with 4 electrons is $E_0 + 4\varepsilon_0 + 8U + J$. From the many-body energies, addition energies $E_N^{\mathrm{add}} = \mu(N+1) - \mu(N) = E_{N+1} - 2E_n + E_{N-1}$ are easily calculated. We find $E_0^{\mathrm{add}} = \varepsilon_0 + U - J/2$, $E_1^{\mathrm{add}} = U - J/2$, $E_2^{\mathrm{add}} = U + 3J/2$ and $E_3^{\mathrm{add}} = U - J/2$, which in turn define the heights of the Coulomb diamonds.

$N = 0$

ΔE	S	S_z	L_z	Eigenstate
0	0	0	0	
$\varepsilon_0 - \frac{J}{2}$	0	0	0	
				
	1	1	0	
		0		
		−1		
	0	0	2ℓ	
	1	1	2ℓ	
		0		
		−1		
	0	0	-2ℓ	
	1	1	-2ℓ	
		0		
		−1		

Table C.1: First few eigenstates of a three shell CNT Hamiltonian with $N = 0$ electrons above the reference state. ΔE is the energy above the ground state with energy E_0.

$N = 1$

ΔE	S	S_z	L_z	Eigenstate
0	$\frac{1}{2}$	$\frac{1}{2}$	ℓ	
		$-\frac{1}{2}$		
	$\frac{1}{2}$	$\frac{1}{2}$	$-\ell$	
		$-\frac{1}{2}$		
$\varepsilon_0 - J$	$\frac{1}{2}$	$\frac{1}{2}$	ℓ	
		$-\frac{1}{2}$		
	$\frac{1}{2}$	$\frac{1}{2}$	$-\ell$	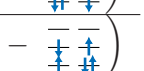
		$-\frac{1}{2}$		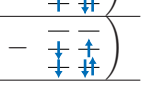
$\varepsilon_0 - \frac{J}{2}$	$\frac{1}{2}$	$\frac{1}{2}$	3ℓ	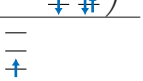
		$-\frac{1}{2}$		
	$\frac{1}{2}$	$\frac{1}{2}$	ℓ	
		$-\frac{1}{2}$		
	$\frac{1}{2}$	$\frac{1}{2}$	$-\ell$	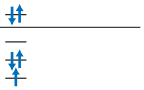
		$-\frac{1}{2}$		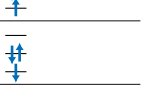
	$\frac{1}{2}$	$\frac{1}{2}$	-3ℓ	
		$-\frac{1}{2}$		

Table C.2: First few eigenstates of a three shell CNT Hamiltonian with $N = 1$ electrons above the reference state. ΔE is the energy above the ground state with energy $E_1 = E_0 + \varepsilon_0 + U/2$.

$N = 1$

ΔE	S	S_z	L_z	Eigenstate
ε_0	$\frac{1}{2}$	$\frac{1}{2}$	ℓ	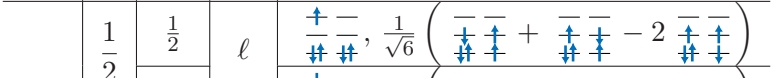
		$-\frac{1}{2}$		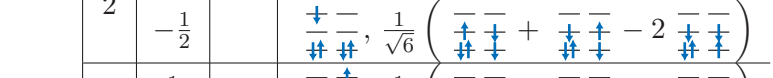
	$\frac{1}{2}$	$\frac{1}{2}$	$-\ell$	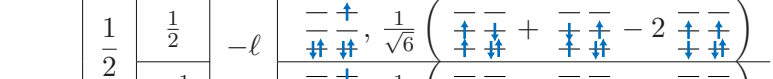
		$-\frac{1}{2}$		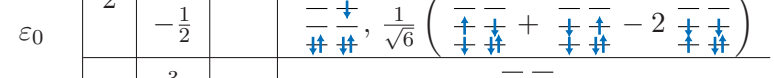
	$\frac{3}{2}$	$\frac{3}{2}$	ℓ	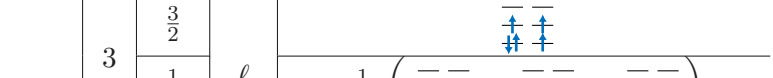
		$\frac{1}{2}$		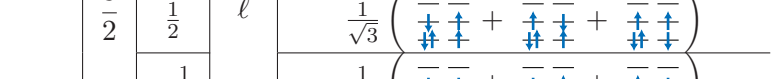
		$-\frac{1}{2}$		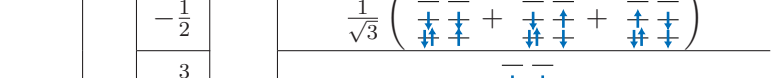
		$-\frac{3}{2}$		
	$\frac{3}{2}$	$\frac{3}{2}$	$-\ell$	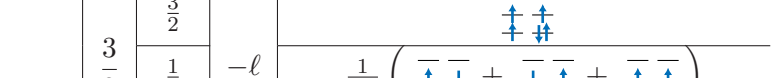
		$\frac{1}{2}$		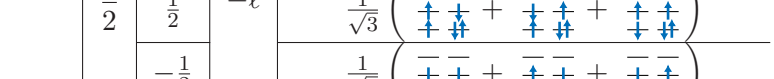
		$-\frac{1}{2}$		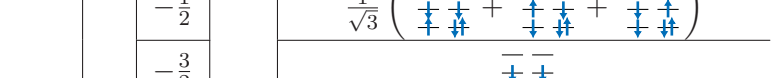
		$-\frac{3}{2}$		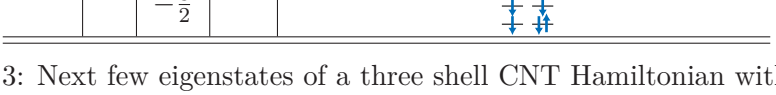

Table C.3: Next few eigenstates of a three shell CNT Hamiltonian with $N = 1$ electrons above the reference state. ΔE is the energy above the ground state with energy $E_1 = E_{40} + \varepsilon_0 + U/2$.

$N = 2$

ΔE	S	S_z	L_z	Eigenstate
0	0	0	0	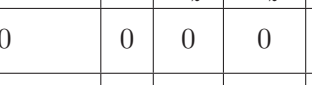
$\frac{J}{2}$	0	0	2ℓ	
			-2ℓ	
J	1	1	0	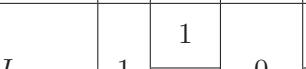
		0		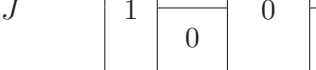
		-1		
$\varepsilon_0 + \frac{J}{2}$	0	0	2ℓ	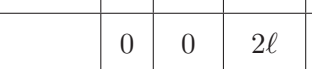
	1	1	2ℓ	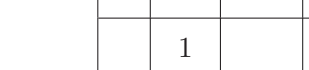
		0		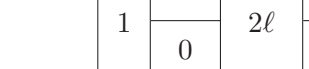
		-1		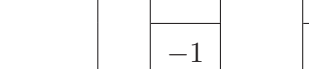
	0	0	0	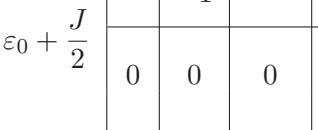
	1	1	0	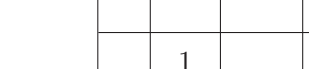
		0		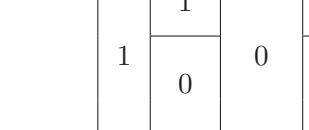
		0		
	0	0	-2ℓ	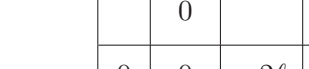
	1	1	-2ℓ	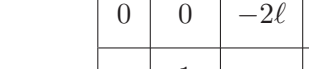
		0		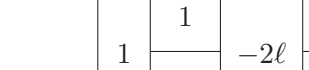
		-1		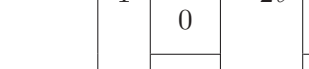

Table C.4: First few eigenstates of a three shell CNT Hamiltonian with $N = 2$ electrons above the reference state. ΔE is the energy above the ground state with energy $E_2 = E_0 + 2\varepsilon_0 + 2U - J/2$.

$N = 3$

ΔE	S	S_z	L_z	Eigenstate
0	$\frac{1}{2}$	$\frac{1}{2}$	ℓ	
		$-\frac{1}{2}$		
	$\frac{1}{2}$	$\frac{1}{2}$	$-\ell$	
		$-\frac{1}{2}$		
$\varepsilon_0 - J$	$\frac{1}{2}$	$\frac{1}{2}$	ℓ	
		$-\frac{1}{2}$		
	$\frac{1}{2}$	$\frac{1}{2}$	$-\ell$	
		$-\frac{1}{2}$		
$\varepsilon_0 - \frac{J}{2}$	$\frac{1}{2}$	$\frac{1}{2}$	3ℓ	
		$-\frac{1}{2}$		
	$\frac{1}{2}$	$\frac{1}{2}$	ℓ	
		$-\frac{1}{2}$		
	$\frac{1}{2}$	$\frac{1}{2}$	$-\ell$	
		$-\frac{1}{2}$		
	$\frac{1}{2}$	$\frac{1}{2}$	-3ℓ	
		$-\frac{1}{2}$		

Table C.5: First few eigenstates of a three shell CNT Hamiltonian with $N = 3$ electrons above the reference state. ΔE is the energy above the ground state with energy $E_3 = E_0 + 3\varepsilon_0 + 9U/2 + J/2$.

$N = 3$

ΔE	S	S_z	L_z	Eigenstate
ε_0	$\frac{1}{2}$	$\frac{1}{2}$	ℓ	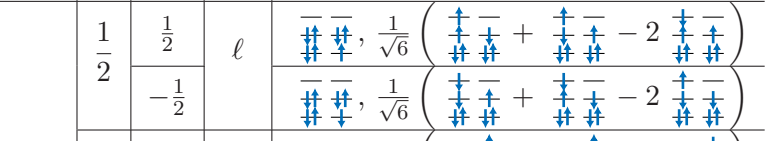
		$-\frac{1}{2}$		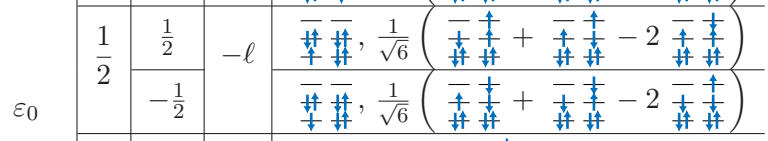
	$\frac{1}{2}$	$\frac{1}{2}$	$-\ell$	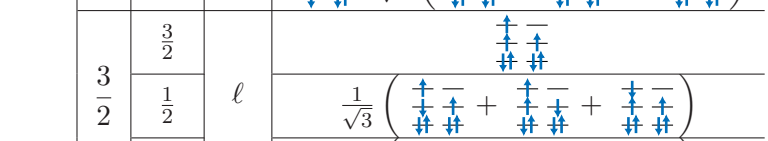
		$-\frac{1}{2}$		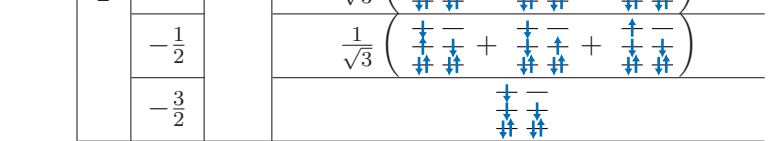
	$\frac{3}{2}$	$\frac{3}{2}$	ℓ	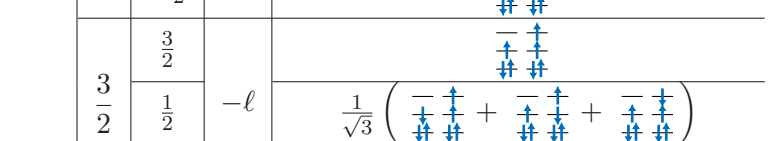
		$\frac{1}{2}$		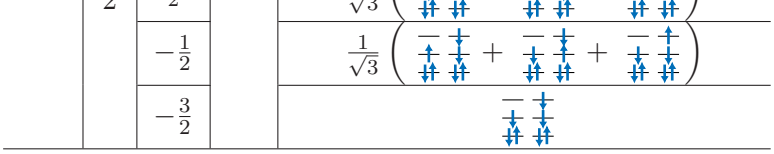
		$-\frac{1}{2}$		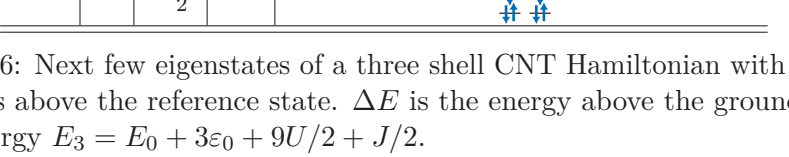
		$-\frac{3}{2}$		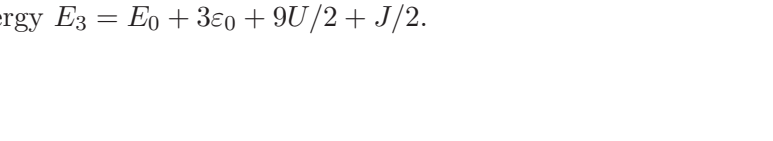
	$\frac{3}{2}$	$\frac{3}{2}$	$-\ell$	
		$\frac{1}{2}$		
		$-\frac{1}{2}$		
		$-\frac{3}{2}$		

Table C.6: Next few eigenstates of a three shell CNT Hamiltonian with $N = 3$ electrons above the reference state. ΔE is the energy above the ground state with energy $E_3 = E_0 + 3\varepsilon_0 + 9U/2 + J/2$.

APPENDIX D

Rate matrix of a ring-metal complex

In this appendix we calculate the single particle rate matrix for a ring of N carbon atoms with radius R. To study the effects of the orientation of the ring with respect to the surface, we study three different configurations. In the first one (**case a**), the ring is lying parallel to the surface of the lead, at a distance d from it, as shown in Fig. D.1a; in the second one (**case b**) it is standing on the $x-y$ plane perpendicular to the lead plane like shown in Fig. D.1b; in the third one (**case c**) it is also standing but now in a way that two atoms are equally distant from the lead, as shown in Fig. D.1c. The

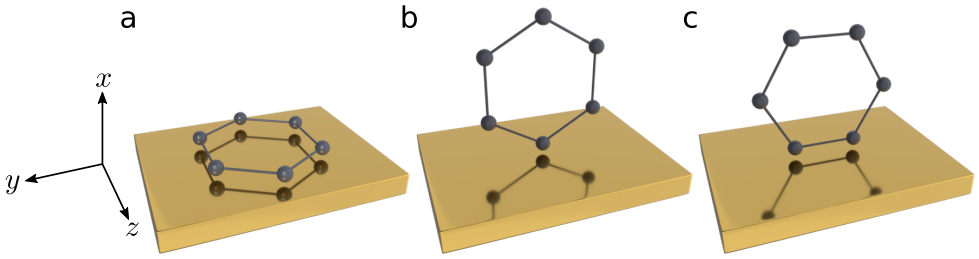

Figure D.1: Tunneling configurations for a ring-lead complex. **a** The ring lies flat on the lead surface. All atoms of the ring are equidistant from the surface. **b** The benzene ring is standing perpendicular to the lead with only one carbon atom closest to the surface. **c** Similar to the previous case, the ring is standing perpendicular to the surface but rotated such that two carbon atoms are equidistant from the lead.

rate matrix for the ring follows easily from the general expression Eq. (4.28) upon dropping the shell index m. Similar to the CNT, the ring has a C_N symmetry and its single particle eigenstates can be classified in terms of angular momentum, ℓ_z, and spin, σ, degrees of freedom. The linear combination of atomic orbitals (LCAO) coefficients follow from the diagonalization of the ring Hamiltonian, and have the form $c_j(\ell_z) = \langle j|\ell_z\rangle = \frac{1}{\sqrt{N}} e^{i\frac{2\pi}{N} j\ell_z}$. Eq. (4.28) yields then for the ring the rate matrix

$$\begin{aligned}(\mathbf{\Gamma}_l)_{\ell_z\ell_z'}(\Delta E) &= \frac{2\pi}{\hbar}\frac{\varepsilon^2}{N}|a|^2 \sum_{jj'} e^{-i\frac{2\pi}{N}(j\ell_z - j'\ell_z')} \sum_{\boldsymbol{k}} \psi_{l\boldsymbol{k}}(\boldsymbol{R}_j)\psi^*_{l\boldsymbol{k}}(\boldsymbol{R}_{j'})\delta(\xi_{l\boldsymbol{k}} - \Delta E) \\ &= \frac{2\pi}{\hbar}\frac{\varepsilon^2}{N}\frac{|a|^2}{L_x} \sum_{jj'} e^{-i\frac{2\pi}{N}(j\ell_z - j'\ell_z')} \sum_{\boldsymbol{k}} \psi^{\parallel}_{l\boldsymbol{k}_\parallel}(\boldsymbol{R}_j)\psi^{\parallel *}_{l\boldsymbol{k}_\parallel}(\boldsymbol{R}_{j'}) \\ &\quad \times e^{-\kappa_x(X_j + X_{j'})}\delta(\xi_{l\boldsymbol{k}} - \Delta E). \end{aligned} \tag{D.1}$$

To further simplify the calculation we consider in the following a plane wave behavior for the parallel wave function, $\psi^{\parallel}_{l\boldsymbol{k}_\parallel}(\boldsymbol{R}) = e^{i\boldsymbol{k}_\parallel\cdot\boldsymbol{R}}/\sqrt{S}$, with S a normalization constant.

Case a

Let us consider the first case where the ring is lying planar on top of the lead at a distance $X_j = d$. The rate matrix then reads

$$(\mathbf{\Gamma}_l)_{\ell_z\ell_z'}(\Delta E) = \frac{2\pi}{\hbar}\frac{\mathcal{C}\varepsilon^2}{N} \sum_{jj'} e^{-i\frac{2\pi}{N}(j\ell_z - j'\ell_z')} \sum_{\boldsymbol{k}} e^{i\boldsymbol{k}_\parallel\cdot(\boldsymbol{R}_j - \boldsymbol{R}_{j'})} e^{-2\kappa_x d}\delta(\xi_{l\boldsymbol{k}} - \Delta E), \tag{D.2}$$

where $\mathcal{C} := |a|^2/(SL_x)$. It is convenient to express $j' = j' - j + j := -\Delta j + j$ and to observe that $|\boldsymbol{R}_j - \boldsymbol{R}_{j'}| := R_{\Delta j}$ only depends on the relative distance Δj but not on the position j. This suggests to transform the sum over momentum into an integral, and to express this integral in cylindrical coordinates $k_y, k_z \to \varphi, k_\parallel$. This results in

$$\begin{aligned}(\mathbf{\Gamma}_l)_{\ell_z\ell_z'}(\Delta E) &= \frac{2\pi}{\hbar}\frac{\mathcal{C}\varepsilon^2}{N} \overbrace{\sum_{j} e^{-i\frac{2\pi}{N} j(\ell_z - \ell_z')}}^{N\delta_{\ell_z\ell_z'}} \sum_{\Delta j} e^{-i\frac{2\pi}{N}\Delta j\ell_z'} \int \mathrm{d}\varphi \int \mathrm{d}k_\parallel \int \mathrm{d}k_x \\ &\quad \times k_\parallel e^{ik_\parallel R_{\Delta j}\cos\varphi} e^{-2\kappa_x d}\delta(\xi_{l\boldsymbol{k}} - \Delta E). \end{aligned} \tag{D.3}$$

The integration over the angle φ results in a real function of $k_\parallel$. Similarly, in the sum over Δj for each finite positive Δj there is a negative counterpart.

This leaves us with the diagonal and real rate matrix

$$\mathbf{\Gamma}_l = \Gamma_l \begin{pmatrix} 1 & 0 \\ 0 & 1 \end{pmatrix}, \tag{D.4}$$

which therefore does not support dark states. The absolute value of the diagonal parts is not important in this consideration. For simplicity and homogeneity with the other cases we have kept the δ approximation for the p_z functions. The description of a CNT "slice" would rather require to consider the orbital structure of the radially distributed p orbitals. Eq. (D.4) is obtained, though, also out of more fundamental symmetry arguments:

$$\begin{aligned}
(\mathbf{\Gamma}_l)_{\ell_z\ell'_z} &= \frac{2\pi}{\hbar}\varepsilon_m^2 \sum_{\boldsymbol{k}} \langle m\ell_z|l\boldsymbol{k}\rangle\langle l\boldsymbol{k}|m\ell'_z\rangle \\
&= \frac{2\pi}{\hbar}\varepsilon_m^2 \sum_{\boldsymbol{k}} \langle m\ell_z|\,\hat{C}_N^\dagger\hat{C}_N\,|l\boldsymbol{k}\rangle\langle l\boldsymbol{k}|\,\hat{C}_N^\dagger\hat{C}_N\,|m\ell'_z\rangle \\
&= \frac{2\pi}{\hbar}\varepsilon_m^2 e^{i\frac{2\pi}{N}(\ell'_z-\ell_z)} \sum_{\boldsymbol{k}} \langle m\ell_z|l\boldsymbol{k}\rangle\langle l\boldsymbol{k}|m\ell'_z\rangle \\
&= e^{i\frac{2\pi}{N}(\ell'_z-\ell_z)}(\mathbf{\Gamma}_l)_{\ell_z\ell'_z},
\end{aligned} \tag{D.5}$$

where $\hat{C}_N$ is the rotation of $2\pi/N$ around the x axis and the isotropy of the leads is assumed. Eq. (D.5) implies $\mathbf{\Gamma}_l$ is diagonal. The form in Eq. (D.4) follows by requiring time reversal symmetry.

Case b

In the second case the result is quite different. The rate matrix for the standing ring is

$$\begin{aligned}
(\mathbf{\Gamma}_l)_{\ell_z\ell'_z}(\Delta E) = \frac{2\pi}{\hbar}\frac{\mathcal{C}\varepsilon^2}{N} \sum_{jj'} e^{-i\frac{2\pi}{N}(j\ell_z - j'\ell'_z)} \\
\times \sum_{\boldsymbol{k}} e^{ik_y(Y_j-Y_{j'})-\kappa_x(X_j+X_{j'})}\delta(\xi_{l\boldsymbol{k}}-\Delta E),
\end{aligned} \tag{D.6}$$

where $\mathcal{C} := |a|^2/(SL_x)$. One can see immediately that the trick used in the previous case **a** does not work here, due to the dependence on j (j') of the variables X_j (X'_j). An estimation of $\kappa_x = \sqrt{\frac{2m_{\rm el}}{\hbar^2}(E_F^l+\phi_0^l) - k_x^2} \geq \sqrt{\frac{2m_{\rm el}}{\hbar^2}\phi_0^l} = \mathcal{O}(\text{Å}^{-1})$ for typical work functions $\phi_0 = \mathcal{O}(eV)$ tells that the contribution to the rate matrix shrinks by one order of magnitude for a distance of 1Å of the atom to the lead surface. This suggests that perfect local tunneling to the atom

closest to the lead $j = j' = J$ at distance $X_J = d$ is a good approximation. We then obtain

$$(\mathbf{\Gamma}_l)_{\ell_z \ell'_z} = \frac{2\pi}{\hbar} \frac{\mathcal{C}\varepsilon^2}{N} e^{-iJ\frac{2\pi}{N}(\ell_z - \ell'_z)} \sum_{\boldsymbol{k}} 2\kappa_x e^{-2\kappa_x^{\alpha} d} \delta(\xi_{l\boldsymbol{k}} - \Delta E), \tag{D.7}$$

and finally

$$\mathbf{\Gamma}_l = \Gamma_l \begin{pmatrix} 1 & e^{2i\phi_l} \\ e^{-2i\phi_l} & 1 \end{pmatrix}. \tag{D.8}$$

Thus the single atom contact yields a rate matrix with maximal coherence, like in the surface Γ-point approximation discussed in the previous subsection.

Case c

In the third case the ring is rotated in a way that tunneling can occur through two atoms J and J' which are both in contact with the lead ($X_J = X_{J'} = d$). The rate matrix reads

$$(\mathbf{\Gamma}_l)_{\ell_z \ell'_z}(\Delta E) = \frac{2\pi}{\hbar} \frac{\mathcal{C}\varepsilon^2}{N} \sum_{jj' \in (J,J')} e^{-i\frac{2\pi}{N}(j\ell_z - j'\ell'_z)} \sum_{\boldsymbol{k}} e^{ik_y(Y_j - Y_{j'}) - 2\kappa_x d} \delta(\xi_{l\boldsymbol{k}} - \Delta E). \tag{D.9}$$

The diagonal and off-diagonal elements of the rate matrix can be simplified to

$$\begin{aligned}(\mathbf{\Gamma}_l)_{\ell\ell}(\Delta E) = \frac{4\pi}{\hbar} \frac{\mathcal{C}\varepsilon^2}{N} \sum_{\boldsymbol{k}} \left[1 + \cos\left(\frac{2\pi}{N}\ell(J - J')\right) \cos\left(k_y \Delta Y\right)\right] \\ \times e^{-2\kappa_x d} \delta(\xi_{l\boldsymbol{k}} - \Delta E),\end{aligned} \tag{D.10}$$

$$\begin{aligned}(\mathbf{\Gamma}_l)_{\ell-\ell}(\Delta E) = \frac{4\pi}{\hbar} \frac{\mathcal{C}\varepsilon^2}{N} e^{-i\frac{2\pi}{N}\ell(J+J')} \sum_{\boldsymbol{k}} \left[\cos\left(\frac{2\pi}{N}\ell(J - J')\right) + \cos\left(k_y \Delta Y\right)\right] \\ \times e^{-2\kappa_x d} \delta(\xi_{l\boldsymbol{k}} - \Delta E),\end{aligned} \tag{D.11}$$

with $\Delta Y = Y_J - Y_{J'}$. We used the fact that the sum over $\boldsymbol{k}$ is isotropic and therefore $\sin(k_y \Delta Y) \to 0$. One can see directly that for $\Delta Y = 0$ the result of case **b** is recovered. For $\Delta Y \neq 0$ the amplitude of the off-diagonal terms in $\mathbf{\Gamma}_l$ is smaller than the diagonal values since it holds in general $1 + \cos x \cos y - \cos x - \cos y = (\cos x - 1)(\cos y - 1) \geq 0$. We obtain a rate matrix intermediate to cases **a** and **b**

$$\mathbf{\Gamma}_l = \Gamma_l \begin{pmatrix} 1 & he^{2i\phi_l} \\ he^{-2i\phi_l} & 1 \end{pmatrix}, \quad 0 \leq h \leq 1. \tag{D.12}$$

In all three cases this results in $\mathbf{\Gamma}_l = \Gamma_l \mathcal{R}_l$ where the coherence matrices fulfill $|(\mathcal{R}_l)_{\ell_z \ell_z}| = 1$ and $0 \leq |(\mathcal{R}_l)_{\ell_z - \ell_z}| \leq 1$.

List of Figures

List of Tables

Acronyms

CNT carbon nanotube. xi, xii, 5, 6, 11–13, 18, 20–33, 37, 62, 68, 69, 71–74, 76, 78, 83–87, 91–93, 95, 97–99, 106–113, 159, 170, 173, 181, 182, 191, 193, 197–203, 206, 207

CPT coherent population trapping. 89–92, 95, 100–102, 112, 113, 182

CS coupled state. 91, 99, 101, 102, 111, 112, 174, 177

CVD chemical vapor deposition. 92

DM-NRG stands for density matrix–numerical renormalization group. Our transport program is based on the open access Budapest code [90] and allows for the calculation of linear conductance ($V_\mathrm{b} = 0$) for large coupling strength Γ. The main responsibility lies with Davide Mantelli. 59, 78–80, 85, 87, 182

DS dark state. 90–93, 95, 98, 99, 101, 102, 110–112, 159–161, 170–172, 174, 177, 182, 183

DSO$^+$ generalized dressed second order. 57–59, 181

FCS full counting statistics. 117, 119, 120, 126

KEA is the Keldysh effective action approach, recently developed mainly by Sergey Smirnov [74, 88]. It is based on a slave boson field integral formulation, where a truncation of the effective action to terms quadratic in the slave boson fields enables us to evaluate the tunneling density of state of the Kondo quantum dot in analytic form. 78, 81, 83, 87, 88, 195

KinEq is the kinetic equation solver, a code written by Sonja Koller which calculates transport including first and second order contributions of the tunneling rates Γ [48]. 49, 65, 75

LCAO linear combination of atomic orbitals. 108–110, 206

MOKE magneto-optic Kerr effect. 92

MOSFET metal-oxide-semiconductor field-effect transistor. 12

PT perturbation theory. 75, 76, 78, 81, 82

QD quantum dot. 11–20, 28, 29, 35–39, 50, 61, 62, 64, 67–69, 71–73, 76, 84, 87, 89–92, 95, 97, 112, 120, 130, 140, 148, 159, 161, 170, 173, 181, 183, 197

RDM reduced density matrix. 38, 40–43, 45–47, 51, 53, 54, 59, 61, 66, 121, 122, 124, 126, 144, 182

RTA resonant tunneling approximation. 181

SET single-electron transistor. 12–17, 28, 35, 36, 50, 59, 120, 126, 128, 181

SIAM single-impurity Anderson model. 62, 63, 66, 69, 70, 130, 131, 169

SOC spin-orbit coupling. 27, 28, 30, 68, 71–73, 79, 86, 87, 93, 95, 108, 112, 182

SSH Su-Schrieffer-Heeger. 133, 136, 137, 139, 148–150, 152, 153, 156, 158, 183

STM scanning tunneling microscope. 160

TQD triangular triple quantum dot. 160–166, 169, 178, 183

Bibliography

[1] T. Young, *A course of lectures on natural philosophy and the mechanical arts: Volume 1* (London : Printed for J. Johnson, 1807).

[2] A. Einstein, Ann. Phys. **322**, 132 (1905).

[3] A. Einstein and L. Infeld, *The Evolution of Physics: The Growth of Ideas from Early Concepts to Relativity and Quanta* (Cambridge University Press, 1938).

[4] R. Bach, D. Pope, S.-H. Liou, and H. Batelaan, New J. Phys. **15**, 033018 (2013).

[5] L. de Broglie, Nature **112**, 540 (1923).

[6] S. Eibenberger, S. Gerlich, M. Arndt, M. Mayor, and J. Tuxen, Phys. Chem. Chem. Phys. **15**, 14696 (2013).

[7] E. Schrödinger, Phys. Rev. **28**, 1049 (1926).

[8] A. Pérot and C. Fabry, Astrophys. J. **9**, 87 (1899).

[9] C. Fabry and A. Pérot, Ann. Chim. Phys. **16**, 115 (1899).

[10] W. Liang, M. Bockrath, D. Bozovic, J. H. Hafner, M. Tinkham, and H. Park, Nature **411**, 665 (2001).

[11] A. Dirnaichner, M. del Valle, K. J. G. Götz, F. J. Schupp, N. Paradiso, M. Grifoni, C. Strunk, and A. K. Hüttel, Phys. Rev. Lett. **117**, 166804 (2016).

[12] W. G. van der Wiel, S. De Franceschi, J. M. Elzerman, T. Fujisawa, S. Tarucha, and L. P. Kouwenhoven, Rev. Mod. Phys. **75**, 1 (2002).

[13] D. Taubert, D. Schuh, W. Wegscheider, and S. Ludwig, Rev. Sci. Instrum. **82**, 123905 (2011).

[14] D. Loss and D. P. DiVincenzo, Phys. Rev. A **57**, 120 (1998).

[15] J. M. Elzerman, R. Hanson, L. H. W. van Beveren, B. Witkamp, L. M. K. Vandersypen, and L. P. Kouwenhoven, Nature **430**, 431 (2004).

[16] R. Landauer, Nature **392**, 658 (1998).

[17] B. Peng, M. Locascio, P. Zapol, S. Li, S. L. Mielke, G. C. Schatz, and H. D. Espinosa, Nature Nanotech. **3**, 626 (2008).

[18] G. Pastorin, Pharm. Res. **26**, 746 (2009).

[19] L. Yu, C. Shearer, and J. Shapter, Chem. Rev. **116**, 13413 (2016).

[20] K. Mizuno, J. Ishii, H. Kishida, Y. Hayamizu, S. Yasuda, D. N. Futaba, M. Yumura, and K. Hata, Proc. Nat. Acad. Sci. **106**, 6044 (2009).

[21] Y. Meir, N. S. Wingreen, and P. A. Lee, Phys. Rev. Lett. **66**, 3048 (1991).

[22] V. Pribiag, S. Nadj-Perge, S. Frolov, J. van den Berg, I. van Weperen, S. Plissard, E. Bakkers, and L. Kouwenhoven, Nature Nanotech. **8**, 170 (2013).

[23] L. Kouwenhoven and T. Oosterkamp, Science **278**, 1788 (1997).

[24] S. Sapmaz, P. Jarillo-Herrero, J. Kong, C. Dekker, L. Kouwenhoven, and H. van der Zant, Phys. Rev. B **71**, 153402 (2005).

[25] M. Leijnse, M. R. Wegewijs, and M. H. Hettler, Phys. Rev. Lett. **103**, 156803 (2009).

[26] D. R. Schmid, P. L. Stiller, C. Strunk, and A. K. Hüttel, New J. Phys. **14**, 083024 (2012).

[27] D. Tománek and S. G. Louie, Phys. Rev. B **37**, 8327 (1988).

[28] M. Margańska, P. Chudzinski, and M. Grifoni, Phys. Rev. B **92**, 075433 (2015).

[29] M. del Valle, M. Margańska, and M. Grifoni, Phys. Rev. B **84**, 165427 (2011).

[30] M. Gmitra, S. Konschuh, C. Ertler, C. Ambrosch-Draxl, and J. Fabian, Phys. Rev. B **80**, 235431 (2009).

[31] T. Ando, J. Phys. Soc. Jap. **69**, 1757 (2000).

[32] G. A. Steele, F. Pei, E. A. Laird, J. M. Jol, H. B. Meerwaldt, and L. P. Kouwenhoven, Nat. Commun. **4**, 1573 (2013).

[33] E. A. Laird, F. Kuemmeth, G. A. Steele, K. Grove-Rasmussen, J. Nygård, K. Flensberg, and L. P. Kouwenhoven, Rev. Mod. Phys. **87**, 703 (2015).

[34] F. Kuemmeth, S. Ilani, D. C. Ralph, and P. L. McEuen, Nature **452**, 448 (2008).

[35] T. S. Jespersen, K. Grove-Rasmussen, J. Paaske, K. Muraki, T. Fujisawa, J. Nygård, and K. Flensberg, Nat. Phys. **7**, 348 (2011).

[36] K. Grove-Rasmussen, S. Grap, J. Paaske, K. Flensberg, S. Andergassen, V. Meden, H. I. Jørgensen, K. Muraki, and T. Fujisawa, Phys. Rev. Lett. **108**, 176802 (2012).

[37] W. Izumida, R. Okuyama, and R. Saito, Phys. Rev. B **91**, 235442 (2015).

[38] M. Niklas, "Electronic spectra of ultra-clean carbon nanotubes in a magnetic field," Bachelor thesis (2013), supervisor: Prof. Dr. M. Grifoni.

[39] L. Mayrhofer and M. Grifoni, Eur. Phys. J. B **63**, 43 (2008).

[40] A. Secchi and M. Rontani, Phys. Rev. B **80**, 041404 (2009).

[41] C. Sommer, "Effects of exchange interaction in Carbon Nanotubes," Bachelor thesis (2014), supervisor: Prof. Dr. M. Grifoni.

[42] C. Forster, "Exchange effects in interacting carbon nanotubes," Master thesis (2014), supervisor: Prof. Dr. M. Grifoni.

[43] S. Nakajima, Prog. Theo. Phys. **20**, 948 (1958).

[44] R. Zwanzig, J. Chem. Phys. **33**, 1338 (1960).

[45] S. Koller, *Spin phenomena and higher order effects in transport across interacting quantum-dots*, Ph.D. thesis, Universität Regensburg (2009), supervisor: Prof. Dr. M. Grifoni.

[46] D. Darau, G. Begemann, A. Donarini, and M. Grifoni, Phys. Rev. B **79**, 235404 (2009).

[47] M. Leijnse and M. R. Wegewijs, Phys. Rev. B **78**, 235424 (2008).

[48] S. Koller, M. Grifoni, M. Leijnse, and M. R. Wegewijs, Phys. Rev. B **82**, 235307 (2010).

[49] A. Donarini, A. Yar, and M. Grifoni, Eur. Phys. J. B **85**, 316 (2012).

[50] J. Koch and F. von Oppen, Phys. Rev. Lett. **94**, 206804 (2005).

[51] J. König, J. Schmid, H. Schoeller, and G. Schön, Phys. Rev. B **54**, 16820 (1996).

[52] J. König, H. Schoeller, and G. Schön, Phys. Rev. Lett. **76**, 1715 (1996).

[53] D. Mantelli, *Analytical and numerical study of quantum impurity systems in the intermediate and strong coupling regimes*, Ph.D. thesis, Universität Regensburg (2016), supervisor: Prof. Dr. M. Grifoni.

[54] J. Kern and M. Grifoni, Eur. Phys. J. B **86** (2013), 10.1140/epjb/e2013-40618-9.

[55] H. K. Onnes, Commun. Phys. Lab. Univ. Leiden. **12**, 120 (1911).

[56] W. Meissner and R. Ochsenfeld, Naturwissenschaften **21**, 787 (1933).

[57] W. de Haas, J. de Boer, and G. van dën Berg, Physica **1**, 1115 (1934).

[58] J. Kondo, Prog. Theo. Phys. **32**, 37 (1964).

[59] D. Goldhaber-Gordon, H. Shtrikman, D. Mahalu, D. Abusch-Magder, U. Meirav, and M. A. Kastner, Nature **391**, 156 (1998).

[60] S. M. Cronenwett, T. H. Oosterkamp, and L. P. Kouwenhoven, Science **281**, 540 (1998).

[61] J. Schmid, J. Weis, K. Eberl, and K. v. Klitzing, Physica B **256-258**, 182 (1998).

[62] A. C. Hewson, *The Kondo Problem to Heavy Fermions* (Cambridge University Press, 1993).

[63] M.-S. Choi, R. López, and R. Aguado, Phys. Rev. Lett. **95**, 067204 (2005).

[64] P. Jarillo-Herrero, J. Kong, H. S. van der Zant, C. Dekker, L. P. Kouwenhoven, and S. D. Franceschi, Nature **434**, 484 (2005).

[65] P. Jarillo-Herrero, J. Kong, H. S. J. van der Zant, C. Dekker, L. P. Kouwenhoven, and S. De Franceschi, Phys. Rev. Lett. **94**, 156802 (2005).

[66] A. Makarovski, A. Zhukov, J. Liu, and G. Finkelstein, Phys. Rev. B **75**, 241407 (2007).

[67] F. B. Anders, D. E. Logan, M. R. Galpin, and G. Finkelstein, Phys. Rev. Lett. **100**, 086809 (2008).

[68] J. P. Cleuziou, N. V. N'Guyen, S. Florens, and W. Wernsdorfer, Phys. Rev. Lett. **111**, 136803 (2013).

[69] M. Ferrier, T. Arakawa, T. Hata, R. Fujiwara, R. Delagrange, R. Weil, R. Deblock, R. Sakano, A. Oguri, and K. Kobayashi, Nat. Phys. **12**, 230 (2015).

[70] T.-F. Fang, W. Zuo, and H.-G. Luo, Phys. Rev. Lett. **101**, 246805 (2008).

[71] T.-F. Fang, W. Zuo, and H.-G. Luo, Phys. Rev. Lett. **104**, 169902 (2010).

[72] M. R. Galpin, F. W. Jayatilaka, D. E. Logan, and F. B. Anders, Phys. Rev. B **81**, 075437 (2010).

[73] Y.-W. Lan, K. Aravind, C.-S. Wu, C.-H. Kuan, K.-S. Chang-Liao, and C.-D. Chen, Carbon **50**, 3748 (2012).

[74] D. R. Schmid, S. Smirnov, M. Margańska, A. Dirnaichner, P. L. Stiller, M. Grifoni, A. K. Hüttel, and C. Strunk, Phys. Rev. B **91**, 155435 (2015).

[75] J. Nygård, D. H. Cobden, and P. E. Lindelof, Nature **408**, 342 (2000).

[76] S. Sasaki, S. Amaha, N. Asakawa, M. Eto, and S. Tarucha, Phys. Rev. Lett. **93**, 017205 (2004).

[77] C. H. L. Quay, J. Cumings, S. J. Gamble, R. d. Picciotto, H. Kataura, and D. Goldhaber-Gordon, Phys. Rev. B **76**, 245311 (2007).

[78] S. Grap, S. Andergassen, J. Paaske, and V. Meden, Phys. Rev. B **83**, 115115 (2011).

[79] G. C. Tettamanzi, J. Verduijn, G. P. Lansbergen, M. Blaauboer, M. J. Calderón, R. Aguado, and S. Rogge, Phys. Rev. Lett. **108**, 046803 (2012).

[80] J. Cao, Q. Wang, and H. Dai, Nature Mat. **4**, 745 (2005).

[81] J. R. Schrieffer and P. A. Wolff, Phys. Rev. **149**, 491 (1966).

[82] H. Grabert and M. H. Devoret, eds., *Single Charge Tunneling* (Springer US, 1992).

[83] J. König, J. Schmid, H. Schoeller, and G. Schön, Phys. Rev. B **54**, 16820 (1996).

[84] J. N. Pedersen and A. Wacker, Phys. Rev. B **72**, 195330 (2005).

[85] A. Dirnaichner, M. Grifoni, A. Prüfling, D. Steininger, A. K. Hüttel, and C. Strunk, Phys. Rev. B **91**, 195402 (2015).

[86] L. Borda, G. Zaránd, W. Hofstetter, B. I. Halperin, and J. von Delft, Phys. Rev. Lett. **90**, 026602 (2003).

[87] D. Mantelli, C. P. Moca, G. Zaránd, and M. Grifoni, Physica E **77**, 180 (2016).

[88] S. Smirnov and M. Grifoni, Phys. Rev. B **87**, 121302 (2013).

[89] A. V. Kretinin, H. Shtrikman, and D. Mahalu, Phys. Rev. B **85**, 201301 (2012).

[90] A. I. Tóth, C. P. Moca, Ö. Legeza, and G. Zaránd, Phys. Rev. B **78**, 245109 (2008).

[91] J. S. Lim, M.-S. Choi, M. Y. Choi, R. López, and R. Aguado, Phys. Rev. B **74**, 205119 (2006).

[92] L. Borda, G. Zaránd, W. Hofstetter, B. I. Halperin, and J. von Delft, Phys. Rev. Lett. **90**, 026602 (2003).

[93] E. Minamitani, N. Tsukahara, D. Matsunaka, Y. Kim, N. Takagi, and M. Kawai, Phys. Rev. Lett. **109**, 086602 (2012).

[94] A. J. Keller, S. Amasha, I. Weymann, C. P. Moca, I. G. Rau, J. A. Katine, H. Shtrikman, G. Zaránd, and D. Goldhaber-Gordon, Nat. Phys. **10**, 145 (2013).

[95] A. Crippa, M. L. V. Tagliaferri, D. Rotta, M. De Michielis, G. Mazzeo, M. Fanciulli, R. Wacquez, M. Vinet, and E. Prati, Phys. Rev. B **92**, 035424 (2015).

[96] E. Arimondo and G. Orriols, Lett. Nuovo Cimento **17**, 333 (1976).

[97] R. M. Whitley and C. R. Stroud, Phys. Rev. A **14**, 1498 (1976).

[98] T. Brandes and F. Renzoni, Phys. Rev. Lett. **85**, 4148 (2000).

[99] T. Brandes, Phys. Rep. **408**, 315 (2005).

[100] R. Sánchez, C. López-Monís, and G. Platero, Phys. Rev. B **77**, 165312 (2008).

[101] G. Alzetta, A. Gozzini, L. Moi, and G. Orriols, Il Nuovo Cimento B **36**, 5 (1976).

[102] B. Michaelis, C. Emary, and C. W. J. Beenakker, Europhys. Lett. **73**, 677 (2006).

[103] C. Emary, Phys. Rev. B **76**, 245319 (2007).

[104] C. Pöltl, C. Emary, and T. Brandes, Phys. Rev. B **80**, 115313 (2009).

[105] T. Kostyrko and B. R. Bułka, Phys. Rev. B **79**, 075310 (2009).

[106] A. Donarini, G. Begemann, and M. Grifoni, Nano Lett. **9**, 2897 (2009).

[107] M. Busl, R. Sánchez, and G. Platero, Physica E **42**, 830 (2010).

[108] R. Sánchez, F. Gallego-Marcos, and G. Platero, Phys. Rev. B **89**, 161402 (2014).

[109] M. H. Hettler, W. Wenzel, M. R. Wegewijs, and H. Schoeller, Phys. Rev. Lett. **90**, 076805 (2003).

[110] G. Begemann, D. Darau, A. Donarini, and M. Grifoni, Phys. Rev. B **77**, 201406 (2008).

[111] M. Braun, J. König, and J. Martinek, Phys. Rev. B **70**, 195345 (2004).

[112] A. Messiah, *Quantum Mechanics - Volume 2* (North Holland Physics Publishing, 1961).

[113] M. Dresselhaus, G. Dresselhaus, and A. Jorio, *Group Theory: Application to the Physics of Condensed Matter*, SpringerLink: Springer e-Books (Springer Berlin Heidelberg, 2007).

[114] J. Tersoff and D. R. Hamann, Phys. Rev. B **31**, 805 (1985).

[115] N. Lambert, F. Nori, and C. Flindt, Phys. Rev. Lett. **115**, 216803 (2015).

[116] C. M. Guédon, H. Valkenier, T. Markussen, K. S. Thygesen, J. C. Hummelen, and S. J. van der Molen, Nat. Nanotech. **7**, 305 (2012).

[117] H. Vazquez, R. Skouta, S. Schneebeli, M. Kamenetska, R. Breslow, L. Venkataraman, and M. Hybertsen, Nat. Nanotech. **7**, 663 (2012).

[118] K. G. L. Pedersen, M. Strange, M. Leijnse, P. Hedegård, G. C. Solomon, and J. Paaske, Phys. Rev. B **90**, 125413 (2014).

[119] M.-C. Harabula, V. Ranjan, R. Haller, G. Fülöp, and C. Schönenberger, Phys. Rev. B **97**, 115403 (2018).

[120] C. Beenakker and C. Schönenberger, Phys. Today **56(5)**, 37 (2003).

[121] M. Büttiker, Phys. Rev. B **46**, 12485 (1992).

[122] L. S. Levitov and G. B. Lesovik, JETP Lett. **58**, 230 (1993).

[123] Y. Blanter and M. Büttiker, Phys. Rep. **336**, 1 (2000).

[124] D. A. Bagrets and Y. V. Nazarov, Phys. Rev. B **67**, 085316 (2003).

[125] W. Belzig, Phys. Rev. B **71**, 161301 (2005).

[126] D. K. C. Macdonald, Rep. Progr. Phys. **12**, 56 (1949).

[127] N. G. van Kampen, *Stochastic processes in physics and chemistry* (North-Holland, Amsterdam, 1992).

[128] W. Schottky, Ann. Phys. **362**, 541 (1918).

[129] X. Jehl, M. Sanquer, R. Calemczuk, and D. Mailly, Nature **405**, 50 (2000).

[130] S. Camalet, J. Lehmann, S. Kohler, and P. Hänggi, Phys. Rev. Lett. **90**, 210602 (2003).

[131] L. Fricke, M. Wulf, B. Kaestner, V. Kashcheyevs, J. Timoshenko, P. Nazarov, F. Hohls, P. Mirovsky, B. Mackrodt, R. Dolata, T. Weimann, K. Pierz, and H. W. Schumacher, Phys. Rev. Lett. **110**, 126803 (2013).

[132] B. Kaestner and V. Kashcheyevs, Rep. Prog. Phys. **78**, 103901 (2015).

[133] A. Croy and U. Saalmann, Phys. Rev. B **93**, 165428 (2016).

[134] M. Kataoka, N. Johnson, C. Emary, P. See, J. P. Griffiths, G. A. C. Jones, I. Farrer, D. A. Ritchie, M. Pepper, and T. J. B. M. Janssen, Phys. Rev. Lett. **116**, 126803 (2016).

[135] C. Flindt, T. c. v. Novotný, A. Braggio, M. Sassetti, and A.-P. Jauho, Phys. Rev. Lett. **100**, 150601 (2008).

[136] C. Flindt, T. c. v. Novotný, A. Braggio, and A.-P. Jauho, Phys. Rev. B **82**, 155407 (2010).

[137] S. A. Gurvitz and Y. S. Prager, Phys. Rev. B **53**, 15932 (1996).

[138] B. Kubala, J. Ankerhold, and A. D. Armour, "Electronic and photonic counting statistics as probes of non-equilibrium quantum dynamics," (2016), arXiv:1606.02200 .

[139] J. Cerrillo, M. Buser, and T. Brandes, Phys. Rev. B **94**, 214308 (2016).

[140] T. Novotný, A. Donarini, C. Flindt, and A.-P. Jauho, Phys. Rev. Lett. **92**, 248302 (2004).

[141] D. Kambly, C. Flindt, and M. Büttiker, Phys. Rev. B **83**, 075432 (2011).

[142] D. Kambly and C. Flindt, J. Comput. Electron. **12**, 331 (2013).

[143] F. Forster, M. Mühlbacher, R. Blattmann, D. Schuh, W. Wegscheider, S. Ludwig, and S. Kohler, Phys. Rev. B **92**, 245422 (2015).

[144] R. Hannes and T. Frank, *The Fokker-Planck equation*, 2nd ed., Springer Series in Synergetics, Vol. 18 (Springer, Berlin, 1989).

[145] C. Flindt, C. Fricke, F. Hohls, T. Novotný, K. Netočný, T. Brandes, and R. J. Haug, Proc. Natl. Acad. Sci. USA **106**, 10116 (2009).

[146] J. B. Johnson, Phys. Rev. **32**, 97 (1928).

[147] H. Nyquist, Phys. Rev. **32**, 110 (1928).

[148] J. C. Cuevas and E. Scheer, *Molecular electronics: An introduction to theory and experiment*, World scientific series in nanoscience and nanotechnology: Volume 1 (New Jersey [u.a.] : World Scientific, 2010).

[149] D. Weinmann, W. Häusler, and B. Kramer, Phys. Rev. Lett. **74**, 984 (1995).

[150] K. Ono, D. G. Austing, Y. Tokura, and S. Tarucha, Science **297**, 1313 (2002).

[151] M. Busl, G. Granger, L. Gaudreau, R. Sánchez, A. Kam, Pioro-Ladrière, S. A. Studenikin, P. Zawadzki, Z. R. Wasilewski, A. S. Sachrajda, and G. Platero, Nature Nanotech. **8**, 261 (2013).

[152] E. M. Weig, R. H. Blick, T. Brandes, J. Kirschbaum, W. Wegscheider, M. Bichler, and J. P. Kotthaus, Phys. Rev. Lett. **92**, 046804 (2004).

[153] H. Hübener and T. Brandes, Phys. Rev. B **80**, 155437 (2009).

[154] R. Leturcq, C. Stampfer, K. Inderbitzin, L. Durrer, C. Hierold, E. Mariani, M. G. Schultz, F. von Oppen, and K. Ensslin, Nat. Phys. **5**, 327 (2009).

[155] P. Barthold, F. Hohls, N. Maire, K. Pierz, and R. J. Haug, Phys. Rev. Lett. **96** (2006), 10.1103/physrevlett.96.246804.

[156] P. Delplace, D. Ullmo, and G. Montambaux, Phys. Rev. B **84** (2011), 10.1103/physrevb.84.195452.

[157] F. Grossmann, T. Dittrich, P. Jung, and P. Hänggi, Phys. Rev. Lett. **67**, 516 (1991).

[158] F. Großmann and P. Hänggi, Europhys. Lett. **18**, 571 (1992).

[159] M. Holthaus, Z. Phys. B **89**, 251 (1992).

[160] C. E. Creffield and G. Platero, Phys. Rev. B **65**, 113304 (2002).

[161] G. Platero and R. Aguado, Phys. Rep. **395**, 1 (2004).

[162] S. Kohler, J. Lehmann, and P. Hänggi, Phys. Rep. **406**, 379 (2005).

[163] J. Stehlik, Y. Dovzhenko, J. R. Petta, J. R. Johansson, F. Nori, H. Lu, and A. C. Gossard, Phys. Rev. B **86**, 121303 (2012).

[164] A. Gómez-León and G. Platero, Phys. Rev. Lett. **110**, 200403 (2013).

[165] V. Dal Lago, M. Atala, and L. E. F. Foa Torres, Phys. Rev. A **92**, 023624 (2015).

[166] M. Bello, C. E. Creffield, and G. Platero, Sci. Rep. **6** (2016), 10.1038/srep22562.

[167] B. Bernevig and T. Hughes, *Topological Insulators and Topological Superconductors* (Princeton University Press, 2013).

[168] M. V. Berry, Proc. R. Soc. Lond. A **392**, 45 (1984).

[169] D. Xiao, M.-C. Chang, and Q. Niu, Rev. Mod. Phys. **82**, 1959 (2010).

[170] M. Z. Hasan and C. L. Kane, Rev. Mod. Phys. **82**, 3045 (2010).

[171] J. Zak, Phys. Rev. Lett. **62**, 2747 (1989).

[172] S. Ryu, A. P. Schnyder, A. Furusaki, and A. W. W. Ludwig, New J. Phys. **12**, 065010 (2010).

[173] W. P. Su, J. R. Schrieffer, and A. J. Heeger, Phys. Rev. Lett. **42**, 1698 (1979).

[174] W. P. Su, J. R. Schrieffer, and A. J. Heeger, Phys. Rev. B **22**, 2099 (1980).

[175] M. Atala, M. Aidelsburger, J. T. Barreiro, D. Abanin, T. Kitagawa, E. Demler, and I. Bloch, Nat. Phys. **9**, 795 (2013).

[176] G. Kießlich, E. Schöll, T. Brandes, F. Hohls, and R. J. Haug, Phys. Rev. Lett. **99**, 206602 (2007).

[177] J. K. Asbóth, B. Tarasinski, and P. Delplace, Phys. Rev. B **90**, 125143 (2014).

[178] G. Platero and R. Aguado, Appl. Phys. Lett. **70**, 3546 (1997).

[179] N. H. Lindner, G. Refael, and V. Galitski, Nat. Phys. **7**, 490 (2011).

[180] A. G. Grushin, Á. Gómez-León, and T. Neupert, Phys. Rev. Lett. **112**, 156801 (2014).

[181] G. Usaj, P. M. Perez-Piskunow, L. E. F. Foa Torres, and C. A. Balseiro, Phys. Rev. B **90**, 115423 (2014).

[182] P. W. Anderson, Phys. Rev. **109**, 1492 (1958).

[183] H.-P. Breuer and F. Petruccione, *Theory of open quantum systems* (Oxford University Press, Oxford, 2003).

[184] R. K. Puddy, L. W. Smith, H. Al-Taie, C. H. Chong, I. Farrer, J. P. Griffiths, D. A. Ritchie, M. J. Kelly, M. Pepper, and C. G. Smith, Appl. Phys. Lett. **107**, 143501 (2015).

[185] N. Kocić, P. Weiderer, S. Keller, S. Decurtins, S.-X. Liu, and J. Repp, Nano Lett. **15**, 4406 (2015).

[186] S. Hershfield, J. H. Davies, P. Hyldgaard, C. J. Stanton, and J. W. Wilkins, Phys. Rev. B **47**, 1967 (1993).

[187] U. Hanke, Y. M. Galperin, K. A. Chao, and N. Zou, Phys. Rev. B **48**, 17209 (1993).

[188] A. N. Korotkov, Phys. Rev. B **49**, 10381 (1994).

[189] A. Nauen, I. Hapke-Wurst, F. Hohls, U. Zeitler, R. J. Haug, and K. Pierz, Phys. Rev. B **66**, 161303 (2002).

[190] A. Thielmann, M. H. Hettler, J. König, and G. Schön, Phys. Rev. B **68**, 115105 (2003).

[191] E. V. Sukhorukov, G. Burkard, and D. Loss, Phys. Rev. B **63**, 125315 (2001).

[192] A. Cottet and W. Belzig, Europhys. Lett. **66**, 405 (2004).

[193] G. Kießlich, A. Wacker, and E. Schöll, Phys. Rev. B **68**, 125320 (2003).

[194] C. W. Groth, B. Michaelis, and C. W. J. Beenakker, Phys. Rev. B **74**, 125315 (2006).

[195] C. Pöltl, C. Emary, and T. Brandes, Phys. Rev. B **80**, 115313 (2009).

[196] G. Schaller, G. Kießlich, and T. Brandes, Phys. Rev. B **80**, 245107 (2009).

[197] M. Korkusinski, I. P. Gimenez, P. Hawrylak, L. Gaudreau, S. A. Studenikin, and A. S. Sachrajda, Phys. Rev. B **75**, 115301 (2007).

[198] H. Pan, M. G. House, X. Hao, and H. W. Jiang, Appl. Phys. Lett. **100**, 263109 (2012).

[199] M. Seo, H. K. Choi, S.-Y. Lee, N. Kim, Y. Chung, H.-S. Sim, V. Umansky, and D. Mahalu, Phys. Rev. Lett. **110**, 046803 (2013).

[200] S. Andergassen, Nature **495**, 321 (2013).

[201] S.-Y. Lee and Y. Chung, Phys. Rev. B **87**, 045302 (2013).

[202] M. Kotzian, F. Gallego-Marcos, G. Platero, and R. J. Haug, Phys. Rev. B **94**, 035442 (2016).

[203] L. Gaudreau, S. A. Studenikin, A. S. Sachrajda, P. Zawadzki, A. Kam, J. Lapointe, M. Korkusinski, and P. Hawrylak, Phys. Rev. Lett. **97**, 036807 (2006).

[204] H. H. Weitering, Nature Nanotech. **9**, 499 (2014).

[205] F. Domínguez, G. Platero, and S. Kohler, Chem. Phys. **375**, 284 (2010).

[206] I. Weymann, B. R. Bułka, and J. Barnaś, Phys. Rev. B **83**, 195302 (2011).

[207] K. Wrześniewski and I. Weymann, Phys. Rev. B **92**, 045407 (2015).

[208] A. Donarini, G. Begemann, and M. Grifoni, Phys. Rev. B **82**, 125451 (2010).

[209] C.-Y. Hsieh, Y.-P. Shim, M. Korkusinski, and P. Hawrylak, Rep. Prog. Phys. **75**, 114501 (2012).

[210] M. G. Schultz and F. von Oppen, Phys. Rev. B **80**, 033302 (2009).

[211] F. Bodoky, W. Belzig, and C. Bruder, Phys. Rev. B **77**, 035302 (2008).

[212] W. Belzig and A. Bednorz, Phys. Status Solidi B **251**, 1945 (2014).

[213] H. Schoeller and G. Schön, Phys. Rev. B **50**, 18436 (1994).

[214] H. Schoeller and G. Schön, Phys. B: Cond. Mat. **203**, 423 (1994).